LINEAR SYNCHRONOUS MOTORS

Transportation and Automation Systems

Jacek F. Gieras
and
Zbigniew J. Piech

CRC Press
Boca Raton London New York Washington, D.C.

Library of Congress Cataloging-in-Publication Data

Linear synchronous motors : transportation and automation systems /
edited by Jacek F. Gieras, Zbigniew J. Piech
p. cm.
Includes bibliographical references and index.
ISBN 0-8493-1859-9 (alk. paper)
1. Electric motors, Linear. 2. Electric motors, Synchronous.
3. Permanent magnet motors. 4. Magnetic levitation vehicles.
5. Automation. I. Gieras, Jacek, F. II. Piech, Zbigniew J.
TK2537.L56 1999
621.46—dc21 99-38333
CIP

This book contains information obtained from authentic and highly regarded sources. Reprinted material is quoted with permission, and sources are indicated. A wide variety of references are listed. Reasonable efforts have been made to publish reliable data and information, but the author and the publisher cannot assume responsibility for the validity of all materials or for the consequences of their use.

Neither this book nor any part may be reproduced or transmitted in any form or by any means, electronic or mechanical, including photocopying, microfilming, and recording, or by any information storage or retrieval system, without prior permission in writing from the publisher.

The consent of CRC Press LLC does not extend to copying for general distribution, for promotion, for creating new works, or for resale. Specific permission must be obtained in writing from CRC Press LLC for such copying.

Direct all inquiries to CRC Press LLC, 2000 N.W. Corporate Blvd., Boca Raton, Florida 33431.

Trademark Notice: Product or corporate names may be trademarks or registered trademarks, and are used only for identification and explanation, without intent to infringe.

Visit the CRC Press Web site at www.crcpress.com

© 2000 by CRC Press LLC

No claim to original U.S. Government works

International Standard Book Number 0-8493-1859-9
Library of Congress Card Number 99-38333
Printed in the United States of America 2 3 4 5 6 7 8 9 0
Printed on acid-free paper

Contents

Preface

1 Topology and Selection
- 1.1 Definitions, Geometry and Thrust Generation
- 1.2 Linear Synchronous Motor Topologies
  - 1.2.1 Permanent Magnet Motors with Active Reaction Rail
  - 1.2.2 PM Motors with Passive Reaction Rail
  - 1.2.3 Motors with Electromagnetic Excitation
  - 1.2.4 Motors with Superconducting Excitation System
  - 1.2.5 Variable Reluctance Motors
  - 1.2.6 Stepping Motors
  - 1.2.7 Switched Reluctance Motors
- 1.3 Calculation of Forces
- 1.4 Linear Motion
  - 1.4.1 Speed-Time Curve
  - 1.4.2 Thrust-Time Curve
  - 1.4.3 Dynamics
  - 1.4.4 Traction
- 1.5 Selection of Linear Motors

2 Materials and Construction
- 2.1 Materials
- 2.2 Laminated Ferromagnetic Cores
  - 2.2.1 Electrotechnical Sheet-steels
  - 2.2.2 High-Saturation Ferromagnetic Alloys
  - 2.2.3 Permalloys
  - 2.2.4 Amorphous Materials
  - 2.2.5 Solid Ferromagnetic Materials
  - 2.2.6 Soft Magnetic Powder Composites
- 2.3 Permanent Magnets
  - 2.3.1 Demagnetization Curve
  - 2.3.2 Magnetic Parameters
  - 2.3.3 Magnetic Flux Density in the Airgap
  - 2.3.4 Properties of Permanent Magnets
- 2.4 Conductors
- 2.5 Principles of Superconductivity
- 2.6 Laminated Stacks
- 2.7 Armature Windings of Slotted Cores
- 2.8 Slotless Armature Systems
- 2.9 Electromagnetic Excitation Systems
- 2.10 Permanent Magnet Excitation Systems
- 2.11 Superconducting Excitation Systems
- 2.12 Hybrid Linear Stepping Motors

3 Theory of Linear Synchronous Motors
- 3.1 Permanent Magnet Synchronous Motors
  - 3.1.1 Magnetic Field of the Armature Winding
  - 3.1.2 Form Factors and Reaction Factors
  - 3.1.3 Synchronous Reactance
  - 3.1.4 Voltage Induced
  - 3.1.5 Electromagnetic Power and Thrust

©2000 CRC Press LLC

    - 3.1.6 Thrust Ripple
    - 3.1.7 Direct Calculation of Thrust
- 3.2 Motors with Superconducting Excitation Coils
- 3.3 Variable Reluctance Motors
- 3.4 Permanent Magnet Hybrid Motors
    - 3.4.1 Finite Element Approach
    - 3.4.2 Reluctance Network Approach
    - 3.4.3 Experimental Investigation
- 3.5 Switched Reluctance Motors

4 Motion Control

- 4.1 Control of a.c. Motors
- 4.2 EMF and Thrust of PM Synchronous and Brushless Motors
    - 4.2.1 Sine-Wave Motors
    - 4.2.2 Square Wave (Trapezoidal) Motors
- 4.3 Dynamic Model of a PM Motor
- 4.4 Thrust and Speed Control of PM Motors
    - 4.4.1 Open Loop Control
    - 4.4.2 Closed Loop Control
    - 4.4.3 Zero Direct Axis Current Control
    - 4.4.4 Flux- Weakening Control
    - 4.4.5 Direct Thrust Control
    - 4.4.6 Fuzzy Control
- 4.5 Control of Hybrid Stepping Motors
    - 4.5.1 Microstepping
    - 4.5.2 Electronic Controllers
- 4.6 Precision Linear Positioning

5 Sensors

- 5.1 Linear Optical Sensors
    - 5.1.1 Incremental Encoders
    - 5.1.2 Absolute Encoders
- 5.2 Linear Magnetic Encoders
    - 5.2.1 Construction
    - 5.2.2 Noise Cancellation
    - 5.2.3 Signal Interpolation Process
    - 5.2.4 Transmission of Speed and Position Signals

6 High Speed Maglev Transport

- 6.1 Electromagnetic and Electrodynamic Levitation
- 6.2 Transrapid System (Germany)
    - 6.2.1 Background
    - 6.2.2 Propulsion, Support and Guidance
    - 6.2.3 Guideway
    - 6.2.4 Power Supply
    - 6.2.5 Vehicle
    - 6.2.6 Control System of Electromagnets
    - 6.2.7 The Future of Transrapid System
    - 6.2.8 History of Transrapid Maglev System in Germany
- 6.3 Yamanashi Maglev Test Line in Japan
    - 6.3.1 Background
    - 6.3.2 Location of Yamanashi Maglev Test Line
    - 6.3.3 Principle of Operation
    - 6.3.4 Guideway
    - 6.3.5 Vehicle
    - 6.3.6 Superconducting Electromagnet

©2000 CRC Press LLC

        - 6.3.7 Power Conversion Substation
        - 6.3.8 Brakes
        - 6.3.9 Boarding System
        - 6.3.10 Control System
        - 6.3.11 Communication System
        - 6.3.12 Experiments
        - 6.3.13 History of Superconducting Maglev Transportation Technology in Japan
    - 6.4 Swissmetro
        - 6.4.1 Assumptions
        - 6.4.2 Pilot Project
    - 6.5 Marine Express

7 Building and Factory Transportation Systems
    - 7.1 Elevator Hoisting Machines
        - 7.1.1 Linear Motor Driven Elevator Cars
        - 7.1.2 Elevator with Linear Motor in the Pit
        - 7.1.3 Linear Motor in Counterweight
        - 7.1.4 Conventional versus Linear Motor Driven Elevator
    - 7.2 Ropeless Elevators
        - 7.2.1 Vertical Transport in Ultra-High Buildings
    - 7.3 Assessment of Hoist Performance
        - 7.3.1 Construction of Ropeless Elevators
        - 7.3.2 Operation
        - 7.3.3 First Prototypes
        - 7.3.4 Brakes
    - 7.4 Horizontal Transportation Systems
        - 7.4.1 Guidelines for Installation
        - 7.4.2 Construction
        - 7.4.3 Applications

8 Industrial Automation Systems
    - 8.1 Automation of Manufacturing Processes
    - 8.2 Casting processes
        - 8.2.1 Metal Casting Machines
        - 8.2.2 2D Orientation of Plastic Films
    - 8.3 Machining Processes
    - 8.4 Welding and Thermal Cutting
        - 8.4.1 Friction Welding
        - 8.4.2 Welding Robots
        - 8.4.3 Thermal Cutting
    - 8.5 Surface Treatment and Finishing
        - 8.5.1 Electrocoating
        - 8.5.2 Laser Scribing Systems
    - 8.6 Material Handling
        - 8.6.1 Monorail Material Handling System
        - 8.6.2 Semiconductor Wafer Transport
        - 8.6.3 Capsule Filling Machine
    - 8.7 Testing
        - 8.7.1 Surface Roughness Measurement
        - 8.7.2 Generator of Vibration
    - 8.8 Industrial Laser Applications

A Magnetic Circuits with Permanent Magnets
    - A.1 Approximation of Demagnetization Curve and Recoil Line
    - A.2 Operating Diagram
        - A.2.1 Construction of the Operating Diagram

A.2.2 Magnetization without Armature
A.2.3 Magnetization with Armature
A.2.4 Equivalent Magnetic Circuit

B Calculations of Permeances
B.1 Field Plotting
B.2 Dividing the Magnetic Field into Simple Solids
B.3 Prisms and Cylinders Located in an Open Space

C Performance Calculations for PM LSMs

Symbols and Abbreviations

References

©2000 CRC Press LLC

Preface

There are pessimistic opinions expressed by some educators and attitudes of students and young generation of electrical engineers that electric motors are an old-fashioned area of electrotechnology and research. Current trends in the electrical engineering industry and related areas show that the development of electric motors has by no means been stopped. Electric motors are the most popular machines of everyday life and the number of their types increases with the development of science and technology, e.g., switched reluctance motors, ultrasonic motors, various hybrid motors, transverse flux motors, linear motors, etc. Progress in electric motor technology is now stimulated by

- material engineering, i.e., NdFeB permanent magnets (PMs), high temperature superconductors, high temperature insulating materials, amorphous laminations, sintered powders, wires with heat activated adhesive overcoats, piezoelectric ceramics (ultrasonic motors), magnetostrictive alloys with 'giant' strains;
- impact of power electronics (development of variable speed drives and switched reluctance motor drives);
- impact of new control strategies, e.g., self-tuning drives, 'intelligent' drives, sentient technology (self learning/thinking);
- new areas of applications, e.g., computers, robotics, electric cars, aerospace technology, consumer goods, microdrives, large electric drives, naval applications, bullet trains, linear metro, light rail-ways, maglev trains, *etc.;*
- need for energy saving (energy efficient motors);
- demand on high speed gearless motor drives, e.g., for compressors;
- demand on high torque, direct gearless drives, e.g., electric vehicles, gearless elevators;
- application of magnetic bearings and development of bearingless motors;
- reliability demands, e.g., elimination of brush sliding contact, fault-tolerant motor drives;
- applications of the finite element method (FEM) to computer aided design (CAD);
- applications of new optimization methods in CAD, e.g., genetic algorithm.

This book is an example of new emerging technology: linear synchronous motors (LSMs) and their impact on transportation and automation systems.

Construction and practical application of LSMs became possible due to the availability of rare earth PMs, superconductors and solid switched devices. These new electrical machines were practically not recognized until the early 1980s. LSMs have better performance and higher power density than their induction counterparts [38] and, what is very important, they can operate with larger air gap (mechanical clearance) between the stationary and moving part.

It is necessary to emphasize enormous role in the development of LSMs played by Japanese research institutions (Musashi Institute of Technology, Shinshu University, University of Tokyo, Kyushu University, Railway Technical Research Institute) and both Japanese and United States industry.

The authors have tried to pay equal attention to the design and applications of LSMs. The authors hope that this book itself will provide a useful help to electrical, mechanical and civil engineers, graduate students, researchers and scientists and all enthusiasts of linear motors.

Jacek F. Gieras
Zbigniew J. Piech

Connecticut, July 1999

©2000 CRC Press LLC

chapter 1

Topology and Selection

1.1 Definitions, Geometry and Thrust Generation

Linear electric motors can drive a linear motion load without intermediate gears, screws or crank shafts. A *linear synchronous motor* (LSM) is a linear motor in which the mechanical motion is in synchronism with the magnetic field, i.e. the mechanical speed is the same as the speed of travelling magnetic field. The thrust (propulsion force) can be generated as an action of

- travelling magnetic field produced by a polyphase winding and an array of magnetic poles N, S,...N, S or a variable reluctance ferromagnetic rail (LSMs with a.c. armature windings);
- magnetic field produced by electronically switched d.c. windings and an array of magnetic Poles N, S,...N, S or variable reluctance ferromagnetic rail (linear stepping or switched reluctance motors).

The part producing the travelling magnetic field is called the *armature* or *forcer.* The part which provides the d.c. magnetic flux or variable reluctance is called the *field excitation system* (if the excitation system exists) or *salient-pole rail, reaction rail* or *variable reluctance platen.* The terms *primary* and *secondary* should rather be avoided, as they are only justified for linear induction motors [38] or transformers. The operation of a LSM does not depend which part is movable and which one is stationary.

Traditionally, a.c. polyphase synchronous motors are motors with d.c. electromagnetic excitation, the propulsion force of which has two components: (1) due to the travelling magnetic field and d.c. current magnetic flux (synchronous component) and (2) due to the travelling magnetic field and variable reluctance in *d* and *q* axis (reluctance component). Replacement of d.c. electromagnets by permanent magnets (PMs) is common, except for LSMs for magnetically levitated vehicles. PM brushless LSMs can be divided into two groups:

- PM LSMs in which the input current waveforms are sinusoidal and produce a travelling magnetic field;
- PM d.c. linear brushless motors (LBMs) with. position feedback, in which the input rectangular or trapezoidal current waveforms are precisely synchronized with the speed and position of the moving part.

Construction of magnetic and electric circuits of LSMs belonging to both groups is the same (Fig. 1.1). In d.c. brushless motors the information about the position of the moving part is usually provided by an absolute position sensor. This control scheme corresponds to an *electronic commutation,* functionally equivalent to the mechanical commutation in d.c. commutator motors. Therefore, motors with square (trapezoidal) current waveforms are called *d. c. brushless motors.*

Instead of d.c. or PM excitation, the difference between the *d* and *q*-axis reluctances and the travelling magnetic field can generate the reluctance component of the thrust. Such a motor is called the a.c. *variable reluctance* LSM. Different reluctances in the *d* and q-axis can be created by making salient ferromagnetic poles, using ferromagnetic and non-ferromagnetic materials or using anisotropic ferromagnetic materials. The operation of LBMs can be regarded as a special case of the operation of LSMs.

In the case of LSMs operating on the principle of the travelling magnetic field, the speed *v* of the moving part

$$\upsilon = \upsilon_s = 2f\tau = \frac{\omega}{\pi}\tau \qquad (1.1)$$

©2000 CRC Press LLC

is equal to the *synchronous speed* v_s of the travelling magnetic field depends only on the input frequency f (angular input frequency $\omega = 2\pi f$) and pole pitch τ . It does not depend on the number of poles $2p$.

The polyphase (usually three-phase) armature winding can be distributed in slots, made in the form of concentrated-parameter coils or made as a coreless (air cored) winding layer. PMs are the most popular excitation systems for short travelling distances (less than 10 m), e.g., factory transportation or automation systems. A long PM rail would be expensive. Electromagnetic excitation is used in high-speed passenger transportation systems operating on the principle of magnetic levitation (maglev). The German system, *Transrapid,* uses vehicle mounted steel core excitation electromagnets and stationary slotted armatures. Japanese MLX001 test trainsets use on board superconducting air-cored electromagnets and a stationary three-phase air-cored armature winding distributed along the guidaway (Yamanashi Maglev Test Line).

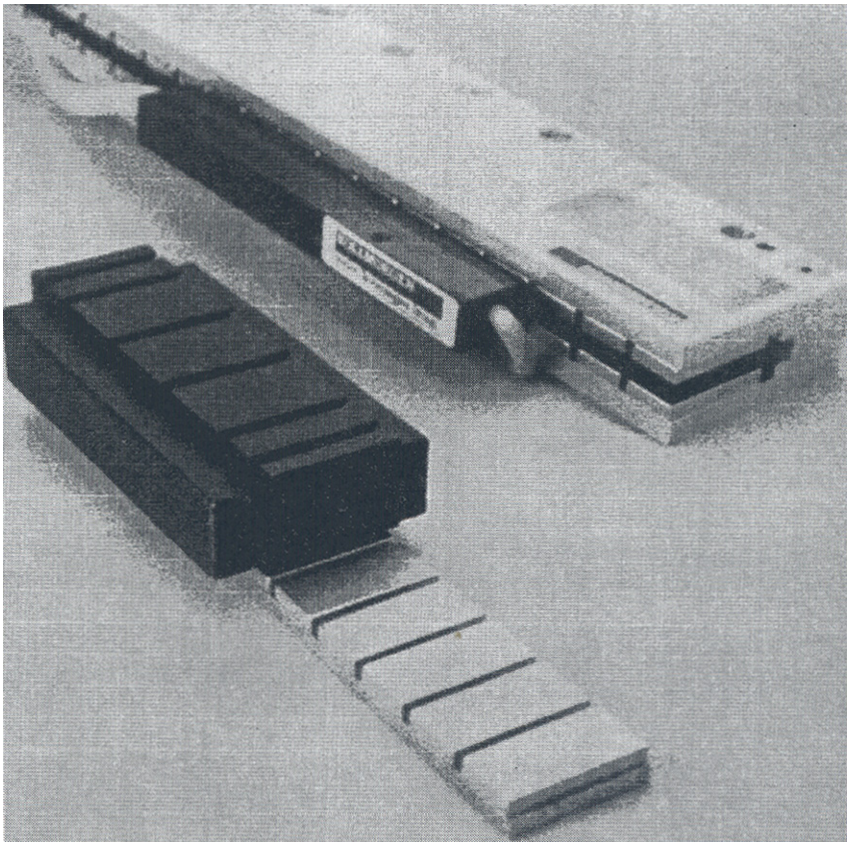

Figure 1.1 Three-phase PM linear motors. Photo courtesy of *Kollmorgen,* Radford, VA, U.S.A.

©2000 CRC Press LLC

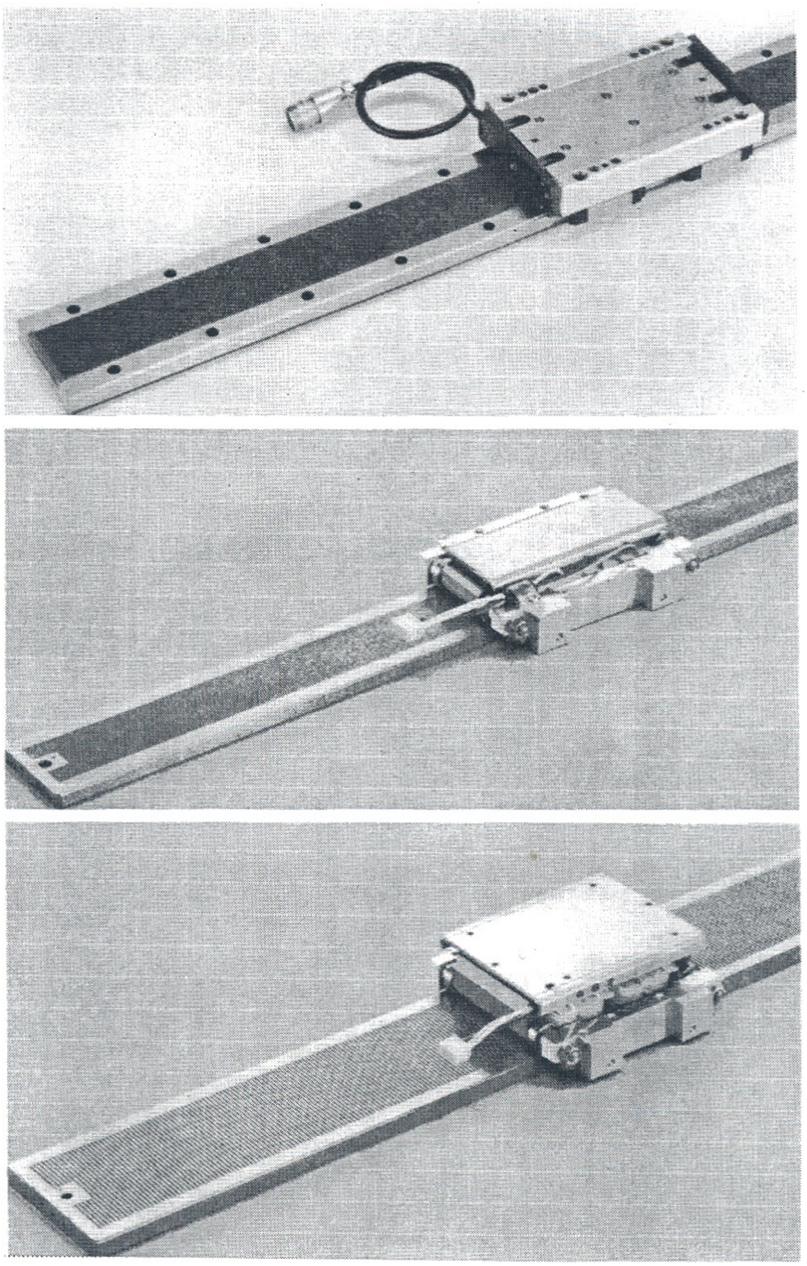

Figure 1.2 PM linear stepping motors. Photo courtesy of *Tokyo Aircraft Instrument, Co.,* Ltd., Japan.

A *linear stepping motor* has a concentrated armature winding wound on salient poles and PM excitation rail or variable reluctance platen (Fig. 1.2). The thrust is generated as an action of the armature magnetic flux and PM flux (active platen) or the armature magnetic flux and salient ferromagnetic poles (variable reluctance platen). Stepping motors have no position feedback.

©2000 CRC Press LLC

The topology of a linear switched reluctance motor is similar to that of a stepping motor with variable reluctance platen. In addition, it is equipped with position sensors. The *turn-on* and *turn-off* instant of the input current is synchronized with the position of the moving part. The thrust is very sensitive to the turn-on and turn-off instant.

In the case of a linear stepping or linear switched reluctance motor, the speed υ of the moving part is:

$$\upsilon = \upsilon_s = f_{sw}\tau \tag{1.2}$$

where f_{sw} is the fundamental switching frequency in one armature phase winding and τ is the pole pitch of the reaction rail. For a rotary stepping or switched reluctance motor $f_{sw} = 2p_r n$ where $2p_r$ is the number of rotor poles and n is rotational speed in rev/s.

1.2 Linear Synchronous Motor Topologies

LSMs can be classified according to whether they are

- flat (planar) or tubular (cylindrical);
- single sided or double sided;
- slotted or slotless;
- iron-cored or air-cored;
- transverse flux or longitudinal flux.

The above topologies are possible for nearly all types of excitation systems. LSMs operating on the principle of the travelling magnetic field can have the following excitation systems:

- PMs in the reaction rail;
- PMs in the armature (passive reaction rail);
- electromagnetic excitation system (with winding);
- superconducting excitation system;

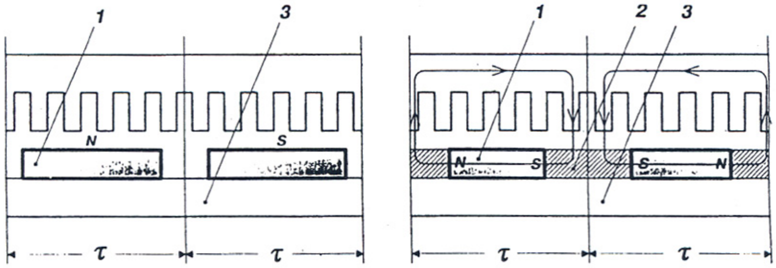

Figure 1.3 Single sided flat PM LSMs with slotted armature core and: (a) surface PMs, (b) buried PMs. 1 -PM, 2 - mild steel pole, 3 - yoke.

- passive reaction rail with saliency and neither PMs nor windings (variable reluctance motors).

LSMs with electronically switched d.c. armature windings are designed either as linear stepping motors or linear switched reluctance motors.

©2000 CRC Press LLC

1.2.1 Permanent Magnet Motors with Active Reaction Rail

Fig. 1.3a shows a single-sided flat LSM with the armature winding located in slots and surface PMs. Fig. 1.3b shows a similar motor with buried type PMs. In surface arrangement of PMs the yoke (back iron) of the reaction rail is ferromagnetic and PMs are magnetized in the normal direction (perpendicular to the active surface). Buried PMs are magnetized in the direction of travelling magnetic field and the yoke is non- ferromagnetic, e.g. made of aluminum. Otherwise, the bottom leakage flux would be greater than the linkage flux, as shown in Fig. 1.4. The same effect occurs in buried type PM rotors of rotary machines in which the shaft must also be non-ferromagnetic [40].

The so called *Halbach array* of PMs also does not require any ferromagnetic yoke and excites stronger magnetic flux density and closer to the sinusoids than a conventional PM array [45]. The key concept of the Halbach array is that the magnetization vector should rotate as a function of distance along the array (Fig. 1.5).

It is recommended to furnish a PM LSM with a *damper*. A rotary synchronous motor has a cage damper winding embedded in pole shoe slots. When the speed is different than the synchronous speed, electric currents are induced in damper circuits. The action of the armature magnetic field and damper currents allows for asynchronous starting, damps the oscillations and helps to return to synchronous operation when the speed decreases or increases. Also, a damper circuit reduces the backward travelling magnetic field. It would be rather difficult to furnish PMs with a cage winding so that the damper of PM LSMs has

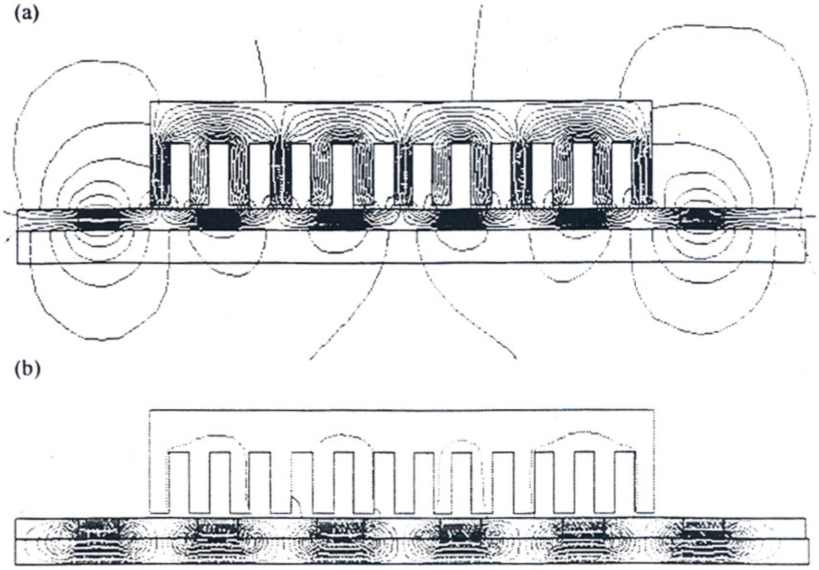

Figure 1.4 Magnetic flux distribution in the longitudinal sections of buried-type PM LSMs: (a) non-ferromagnetic yoke, (b) ferromagnetic yoke (back iron).

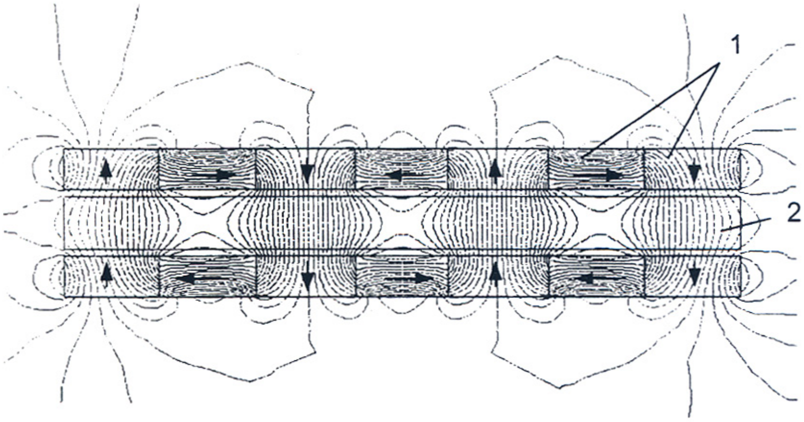

Figure 1.5 Double sided LSM with Halbach array of PMs. 1 - PMs, 2 - coreless armature winding.

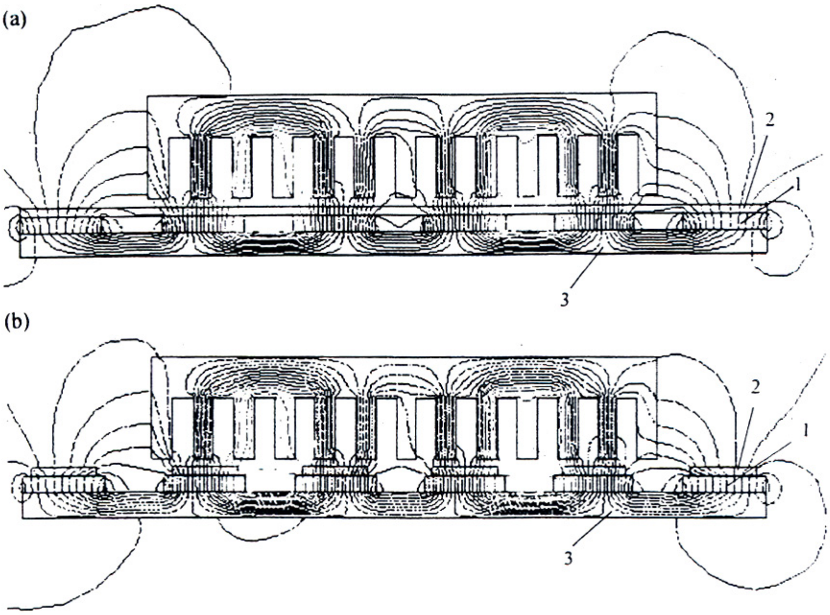

Figure 1.6 Dampers of surface-type PM LSMs: (a) aluminum cover (shield), (b) solid steel pole shoes. 1 - PM, 2 - damper, 3 - yoke.

the form of an aluminum cover (Fig. 1.6a) or solid steel pole shoes (Fig. 1.6b). In addition, steel pole shoes or aluminium cover (shield) can protect brittle PMs against mechanical damage.

©2000 CRC Press LLC

The *detent force*, i.e., attractive force between PMs and armature slotted core, force ripple and some higher space harmononics can be reduced with the aid of skewed assembly of PMs. Skewed PMs can be arranged in one row (Fig. 1.7a), two rows (Fig. 1.7b) or even more rows.

Specification data of flat, single sided PM LBMs manufactured by *Anorad* are shown in Table 1.1 [8] and motors manufactured by *Kollmorgen* are shown in Table 1.2 [69]. The temperature 25° C, 125°C or 130°C for the thrust, current, resistance and power loss is the temperature of the armature winding.

The armature constant κ_E in Tables 1.1 and 1.2 for sinusoidal operation is defined according to equation expressing the EMF (induced voltage) excited by PMs without the armature reaction, i.e.,

$$E_f = c_E \Phi_f \upsilon_s = k_E \upsilon_s \tag{1.3}$$

where Φ_f is the magnetic flux of the excitation system and $k_E = c_E \Phi_f$. Thus, the armature constant k_E multiplied by the synchronous speed υ_s gives the EMF E_f.

Table 1.1 Flat three-phase, single-sided PM LBMs with natural cooling systems manufactured by *Anorad*, Hauppage, NY, U.S.A.

Parameter	LCD-T-1	LCD-T-2-P	LCD-T-3-P	LCD-T-4-P
Continuous thrust at 25°C, N	163	245	327	490
Continuous current at 25°C, A	4.2	6.3	8.5	12.7
Continuous thrust at 25°C, N	139	208	277	416
Continuous current at 25°C, A	3.6	5.4	7.2	10.8
Peak thrust (0.25 s), N	303	455	606	909
Peak current (0.25 s), A	9.2	13.8	18.4	27.6
Peak force (1.0 s), N	248	373	497	745
Peak current (1.0 s), A	7.3	11.0	14.7	22.0
Continuous power losses at 125°C, W	58	87	115	173
Armature constant, k_E, Vs/m	12.9			
Thrust constant (three phases), k_F N/A	38.6			
Resistance per phase at 25°C, Ω	3.2	2.2	1.6	1.1
Inductance, mH	14.3	9.5	7.1	4.8
PM pole pitch, mm	23.45			
Maximum winding temperature, °C	125			
Armature assembly mass, kg	1.8	2.4	3.6	4.8
PM assembly mass, kg/m	6.4			
Normal attractive force, N	1036	1555	2073	3109

©2000 CRC Press LLC

Table 1.2 Flat three-phase, single-sided PM LBMs with natural cooling systems manufactured by *Kollmorgen,* Radford, VA, U.S.A.

Parameter	IC11-030	IC11-050	IC11-100	IC11-200
Continuous thrust at 130°C, N	150	275	600	1260
Continuous current at 130°C, A	4.0	4.4	4.8	5.0
Peak thrust, N	300	500	1000	2000
Peak current, A	7.9	7.9	7.9	7.9
Continuous power losses at 130°C, W	64	106	210	418
Armature constant, at 25°c, k_E , Vs/m	30.9	51.4	102.8	205.7
Thrust constant, at (three phases) 25°C, k_F , N/A	37.8	62.9	125.9	251.9
Resistance, line-to-line, at 25°C, Ω	1.9	2.6	4.4	8.0
Inductance, line-to-line, mH	17.3	27.8	54.1	106.6
Electrical time constant, ms	8.9	10.5	12.3	13.4
Thermal resistance winding-to-external structure, °C/W	1.64	0.99	0.55	0.25
Maximum winding temperature, °C	130			
Armature assembly mass, kg	2.0	3.2	6.2	12.2
PM assembly mass, kg	5.5	7.6	12.8	26.9
Normal attractive force, N	1440	2430	4900	9850

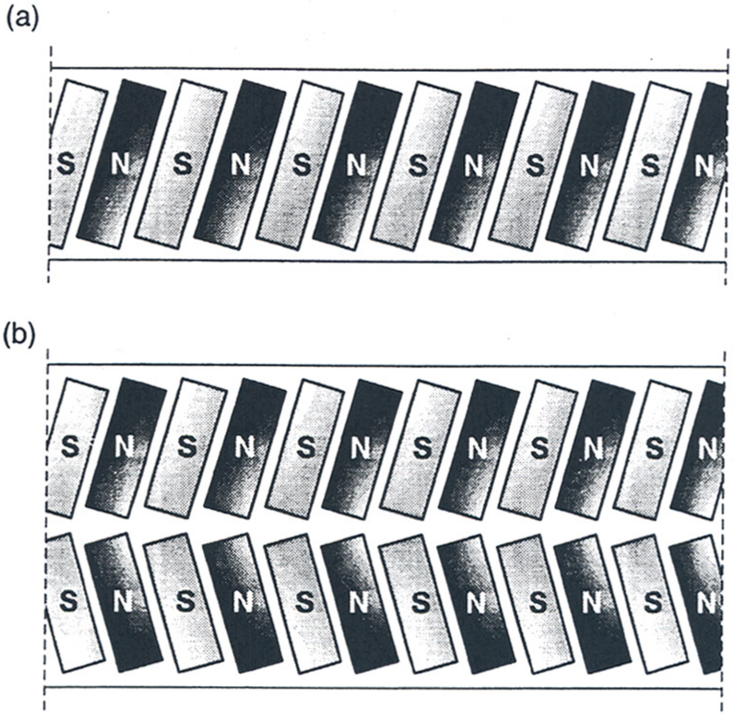

Figure 1.7 Skewed PMs in flat LSMs: (a) one row, (b) two rows.

©2000 CRC Press LLC

Table 1.3 Slotted versus slotless LSMs.

Quantity	Slotted LSM	Slotless LSM
Higher thrust density	X	
Higher efficency in the lower speed range	X	
Higher efficency in the higher speed range		X
Lower input current	X	
Less PM material	X	
Lower winding cost		X
Lower thrust pulsations		X
Lower acoustic noise		X

Table 1.4 Flat double sided PM LBMs with inner three-phase air-cored series-coil armature winding manufactured by *Trilogy Systems Corporation,* Webster, TX, U.S.A.

Parameter	310-2	310-4	310-6
Continuous thrust, N	111.2	209.1	314.9
Continuous power for sinusoidal operation, W	87	152	230
Peak thrust, N	356	712	1068
Peak power, W	900	1800	2700
Peak/continuous current, A	10.0/2.8	10.0/2.6	10.0/2.6
Thrust constant k_F for sinusoidal operation N/A	40.0	80.0	120.0
Thrust constant k_F for trapezoidal operation with Hall sensors, N/A	35.1	72.5	109.5
Resistance per phase, Ω	8.6	17.2	25.8
Inductance $\pm$ 0.5 mH	6.0	12.0	18.0
Heat dissipation constant for natural cooling, W/°C	1.10	2.01	3.01
Heat dissipation constant for forced air cooling W/°C	1.30	2.40	3.55
Heat dissipation constant for liquid cooling W/°C	1.54	2.85	4.21
Number of poles	2	4	6
Coil length, mm	142.2	264.2	386.1
Coil mass, kg	0.55	1.03	1.53
Mass of PM excitation systems, kg/m	12.67 or 8.38		

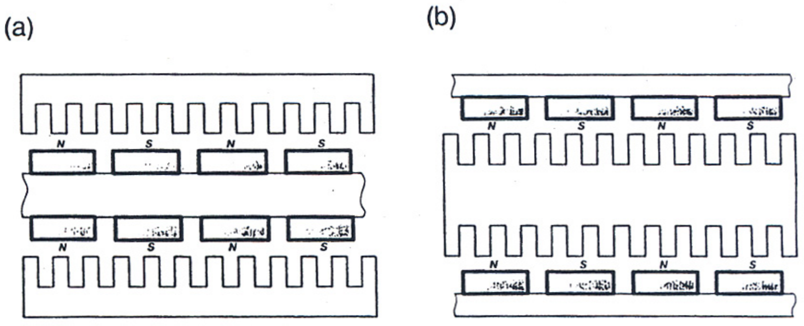

Figure 1.8 Double sided flat PM LSMs with: (a) two external armature systems, (b) one internal armature system.

©2000 CRC Press LLC

The thrust constant k_F in Tables 1.1 and 1.2 is defined according to simplified equation for the electromagnetic thrust, i.e.,

$$F_{dx} = \frac{m_1}{2} c_F \Phi_f I_a \cos\Psi = k_F I_a \cos\Psi \tag{1.4}$$

for a sinusoidally excited LSM with equal reluctances in the d and q-axis and for the angle between the armature current I_a and the q-axis $\Psi = 0°$ ($\cos\Psi$ = 1). Thus, the thrust constant k_F = $0.5 m_1 c_F \Phi_f$ times the armature current I_a gives the thrust. Derivations of eqns (1.3) and (1.4) are given in Chapter 4.

Double sided, flat PM LSMs consist of two external armature systems and one internal excitation system (Fig. 1.8a) or one internal armature system and two external excitation systems (Fig. 1.8b). In the second case a linear Gramme's armature winding can be used.

In *slotless motors* the primary winding is uniformly distributed on a smoooth armature core or does not have any armature core. Slotless PM LSMs are detent force free motors, provide lower torque ripple and at high input frequency can achieve higher efficiency than slotted LSMs. On the other hand, larger non-ferromagnetic airgap requires more PM material and the thrust density (thrust per mass or volume) is lower than that of slotted motors (Table 1.3). The input current is higher as synchronous rectances in the *d* and *q*-axis can decrease to a low undesired value due to absence of teeth. Fig. 1.9a shows a single sided flat slotless motor with armature core and Fig. 1.9b shows a double sided slotless motor with innner air-cored armature winding (moving coil motor).

Table 1.4 contains performance specifications of double sided PM LBMs with innner three-phase air-cored armature winding manufactured by *Trilogy Systems Corporation,* Webster, TX, U.S.A. [132]. *Trilogy* also manufactures motors with parallel wound coils as well as miniature motors and high force motors (up to 9000 N continuous thrust).

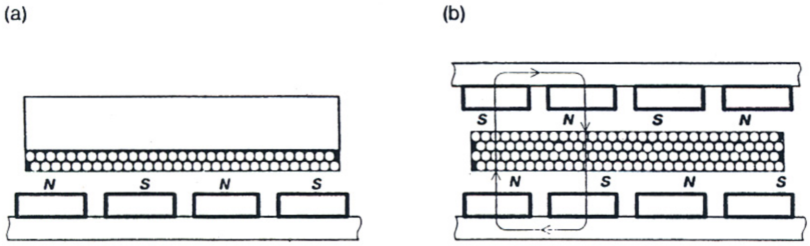

Figure 1.9 Flat slotless PM LSMs: (a) single sided with armature core, (b) double sided with inner air-cored armature winding.

©2000 CRC Press LLC

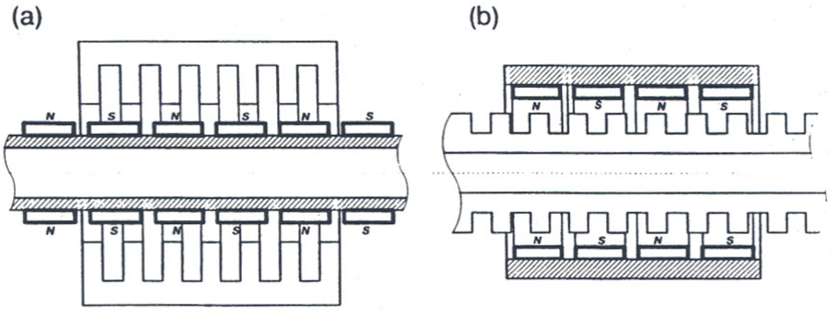

Figure 1.10 Single sided slotted tubular PM LSMs: (a) with external armature system, (b) with external excitation system.

By rolling a flat LSM around the axis parallel to the direction of the travelling magnetic field, i.e. parallel to the direction of thrust, a tubular (cylindrical) LSM can be obtained (Fig. 1.10). A tubular PM LSM can also be designed as a double-sided motor or slotless motor.

Tubular single-sided LSMs LinMoT(R)[1] with movable internal PM excitation system (slider) and stationary external armature are manufactured by *Sulzer Electronics AG*, Zürich, Switzerland (Table 1.5). All active motor parts, bearings, position sensors and electronics have been integrated into a rigid metal cylinder [79].

All the above mentioned PM LSMs are motors with *longitudinal magnetic flux,* the lines of which lie in the plane parallel to the direction of the travelling magnetic field. LSMs can also be designed as *transverse magnetic flux* motors, in which the lines of magnetic flux are perpendicular to the direction of the travelling field. Fig. 1.11 shows a single-sided transverse flux LSM in which PMs are arranged in two rows. A pair of parallel PMs creates a two pole flux excitation system. A double sided configuration of transverse flux motor is possible; however, it is complicated and expensive.

Table 1.5 Data of tubular LSMs LinMot(R) manufactured by *Sulzer Electronics AG,* Zürich, Switzerland.

Parameter	P01 23x80	P01 23x160	P01 37x120	P01 37x240
Number of phases	2			
Permanent magnets	0.210	0.340	1.400	1.460
Maximum stroke, m	33	60	122	204
Maximum force, N	280	350	247	268
Maximum acceleration, m/s^2	2.4	4.2	4.0	3.1
Maximum speed, m/s	0.177	0.257	0.227	0.347
Stator (armature) length, m	23	23	37	37
Stator outer diameter, mm	0.265	0.450	0.740	1.385
Stator mass, kg	12	12	20	20
Slider diameter, mm	12	12	20	20
Maximum temperature of the armature winding, °C	90			

1.2.2 PM Motors with Passive Reaction Rail

The drawback of PM LSMs is the large amount of PM material which must be used to design the excitation system. Normally, expensive rare earth PMs are requested. If a small PM LSM uses, say, 10 kg of NdFeB per 1m of the reaction rail, and 1 kg of good quality NdFeB costs US$ 200, the cost of the reaction rail without assembly amounts to US$ 2000 per 1 m. This price cannot be acceptable, e.g., in passenger transportation systems.

---

[1] LinMot(R) is a registered trademark of *Sulzer Electronics AG,* Zürich, Switzerland

©2000 CRC Press LLC

A cheaper solution is to apply the PM excitation system to the short armature which magnetizes the long reaction rail and creates magnetic poles in it. Such a linear motor is called the *homopolar* LSM.

The homopolar LSM as described in [32, 115] is a double sided a.c. linear motor which consists of two polyphase armature systems connected mechanically and magnetically by a ferromagnetic U-type yoke (Fig. 1.12). Each armature consists of a typical slotted linear motor stack with polyphase armature winding and PMs located between the stack and U-type yoke. Since the armature and excitation systems are combined together, the armature stack is oversized as compared with a conventional steel-cored 1SM. The PMs can also be replaced by electromagnets [115, 120]. The variable reluctance reaction rail is passive. The saliency is created by using ferromagnetic (solid or laminated) cubes separated by a nonferromagnetic material. The reaction rail poles are magnetized by the armature PMs through the airgap. The travelling magnetic field of the polyphase armature winding and salient poles of the reaction rail produce the thrust. Such a homopolar LSM has been proposed for the propulsion of maglev trains of *Swissmetro* [115].

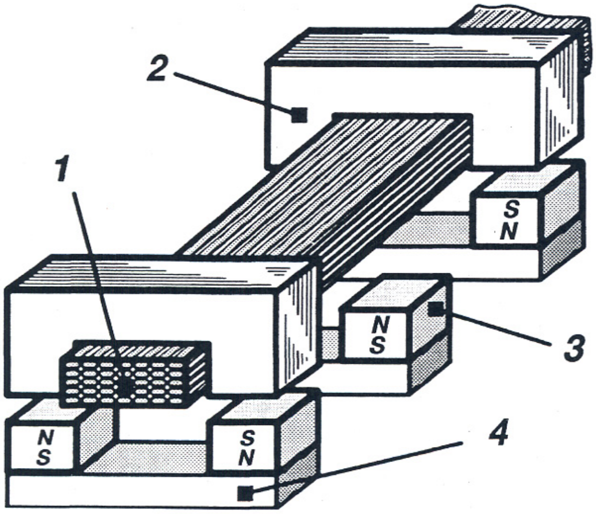

Figure 1.11 Transverse flux PM LSM. 1-armature winding, 2 – armature laminated core, 3 - PM, 4 - back ferromagnetic core.

Further simplification of the double sided configuration can be made obtain a single sided PM LSM shown in Fig. 1.13.

1.2.3 Motors with Electromagnetic Excitation

The electromagnetic excitation system of a LSM is similar to the salient pole rotor of a rotary synchronous motor. Fig. 1.14 shows a fiat single sided LSM with salient ferromagnetic poles and d. c. *field excitation winding*. The poles and pole shoes can be made of solid steel, laminated steel or sintered powder. If the electromagnetic excitation system is integrated with the moving part, the d.c. current can be delivered with the aid of brushes and contact bars, inductive power transfer (IPT) systems [137], linear transformers or linear brushless exciters.

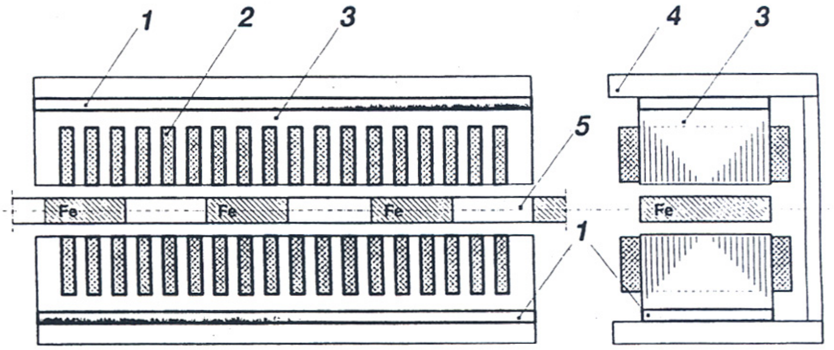

Figure 1.12 Double sided homopolar PM LSM with passive reaction rail.1 - PM, 2 - armature winding, 3 - armature stack, 4 - yoke, 5 – reaction rail.

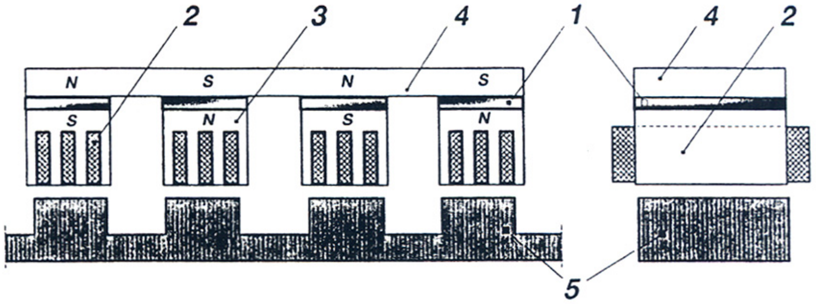

Figure 1.13 Single sided PM LSM with a passive reaction rail. 1 - PM, 2 - armature winding, 3 - armature stack, 4 - yoke, 5 – ferromagnetic reaction rail.

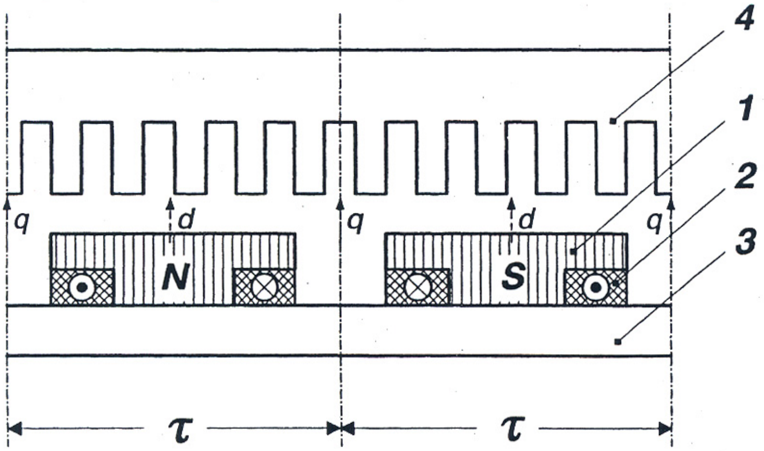

Figure 1.14 Electromagnetic excitation system of a flat single sided iron-cored LSM. 1 - salient pole, 2 - d.c. excitation winding, 3 – ferromagnetic rail (yoke), 4 - armature system.

©2000 CRC Press LLC

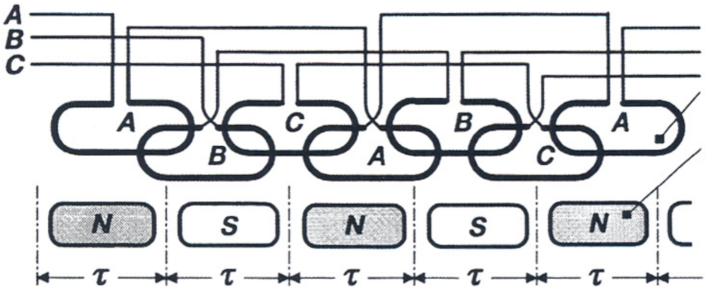

Figure 1.15 Three-phase air-cored LSM with superconducting excitation system. 1 - armature coils, 2 - superconducting excitation coils.

1.2.4 Motors with Superconducting Excitation System

In large power LSMs the electromagnets with ferromagnetic core that produce the excitation flux can be replaced by coreless *superconducting electromagnets.* Since the magnetic flux density produced by the superconducting electromagnet is greater than the saturation magnetic flux density of the best laminated alloys ($B_{sat} \approx 2.4$ T for cobalt alloy), there is no need to use the armature ferromagnetic core. A LSM with superconducting excitation system is a totally air-cored machine (Fig. 1.15).

1.2.5 Variable Reluctance Motors

The simplest construction of a *variable reluctance* LSM is that shown in Fig. 1.14 with d.c. excitation winding being removed. However, the

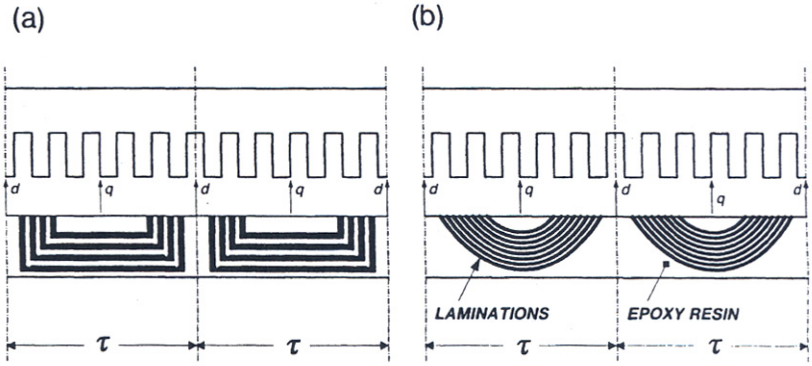

Figure 1.16 Variable reluctance LSMs with: (a) flux barriers (b) steel laminations.

©2000 CRC Press LLC

thrust of such a motor would be low as the ratio of *d*-axis permeance to *q*-axis permeance is low. Better performance can be obtained when using *flux barriers* [117] or steel laminations 1821. To make flux barriers, any non-ferromagnetic materials can be used. To obtain high permeance (low reluctance) in the d axis and low permeance in the q axis, steel laminations should be oriented in such a way as to create high permeance for the *d*-axis magnetic flux.

Fig. 1.16a shows a variable reluctance platen with flux barriers and Fig. 1.16b shows how to arrange steel laminations to obtain different reluctances in the *d* and *q* axis. The platen can be composed of segments the length of which is equal to the pole pitch τ . Each segment consists of semicircular *lamellas* cut out from electrotechnical sheet. A filling, e.g., epoxy resin is used to make the segment rigid and robust. By putting the segments together, a platen of any desired length can be obtained [46].

1.2.6 Stepping Motors

So far, only stepping linear motors of hybrid construction (PM, winding and variable reluctance airgap) have found practical applications.

The *hybrid linear stepping motor* (HLSM), as shown in Fig. 1.17, consists of two parts: the *forcer* (also called the *slider*) and the variable reluctance platen [21]. Both of them are evenly toothed and made of high permeability steel. This is an early design of the HLSM, the so called Sawyer linear motor [52]. .The forcer is the moving part with two rare earth magnets and two concentrated parameter windings. The tooth pitch of the forcer matches the tooth pitch on the platen. However, the tooth pitches on the forcer poles are spaced 1/4 or 1/2 pitch from one pole to the next. This arrangement allows for the PM flux to be controlled at any levels between minimum and maximum level by the winding so that the forcer and the platen lines up at a maximum permeance position. The HLSM is fed with two phase currents (90^{0} out of phase), similarly as a rotary stepping motor. The forcer moves ¼ tooth pitch per each full step .

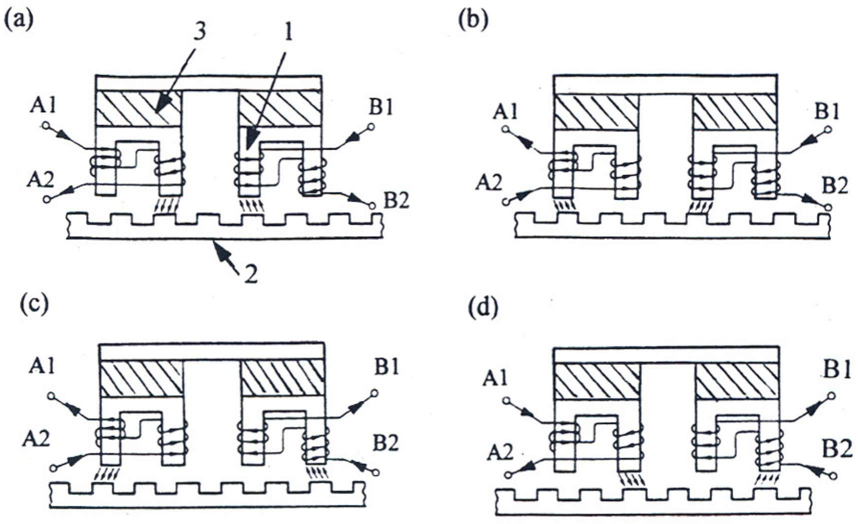

Figure 1.17 Principle of operation of a HLSM: (a) initial position, (b) ¼ tooth pitch displacement of the forcer, (c) 2/4 tooth pitch displacement (d) 3/4 tooth pitch displacement. 1 - forcer, 2 - platen, 3 - PM.

There is a very small airgap between the two parts which is maintained by strong air flow produced by an air compressor [61]. The average air pressure is about 300 to 400 kpa and depends on how many phases are excited.

Table 1.6 shows specification data of HLSMs manufactured by *Tokyo Aircraft Instrument Co., Ltd.*, Tokyo, Japan [78]. The *holding force* is the amount of external force required to break the forcer away from its rest position at rated current applied to the motor. The step-to-step *accuracy* is a measure of the maximum deviation from the true position in the length of each step. This value is different for full step and microstepping drives. The *maximum start-stop speed* is the maximum speed that can be used when starting or stopping the motor without ramping that does not cause the motor to fall out of synchronism or lose steps. The *maximum speed* is the maximum linear speed that can be achieved without the motor stalling or falling out of synchronism. The *maximum load mass* is the maximum allowable mass applied to the forcer against the scale that does not result in mechanical damage. The *full step resolution* is the position increment obtained when the currents are switched from one winding to the next winding. This is the typical resolution obtained with full step drives and it is strictly a function of the motor construction. The *microstepping resolution* is the position increment obtained when the full step resolution is divided electronically by proportioning the currents in the two windings (Chapter 4). This resolution is typically 10 to 250 times smaller than the full step resolution [78].

Table 1.6 Data of Data of HLSMs manufactured by *Tokyo Aircraft Instrument Co., Ltd.,* Tokyo, Japan.

Parameter	LP02-20a	LP04-20A	LP04-30A	LP60-20A
Driver	Bi-Polar Chopper			
Voltage, V	24 d.c			
Resolution, mm	0.2	0.4	0.4	0.423
Holding Force, N	20	20	29.5	20
Step-to-step Accuracy, mm	±0.03			
Cumulative Accuracy, mm	±0.2			
Maximum start-stop speed, mm/s	60	120	120	127
Maximum speed, mm/s	400	600	500	600
Maximum load mass, kg	3.0	3.0	5.0	3.0
Effective stroke, mm	330	300	360	310
Mass, kg	1.4	1.2	2.8	1.4

HLSMs are regarded as an excellent solution to positioning systems that require a high accuracy and rapid acceleration. With a microprocessor controlled *microstepping mode* (Chapter 4), a smooth operation with standard resolution of a few hundred steps/mm can be obtained. The advantages such as high efficiency, high throughput, mechanical simplicity, high reliability, precise open-loop operation, low inertia of the system, etc. have made these kind of motors more and more attractive in such applications as factory automation, high speed positioning, computer peripherals, facsimile machines, numerically controlled machine tools, automated medical equipment, automated laboratory equipment and welding robots. This motor is especially suitable for machine tools, printers, plotters and computer controlled material handling in which a high positioning accuracy and repeatability are the key problems.

©2000 CRC Press LLC

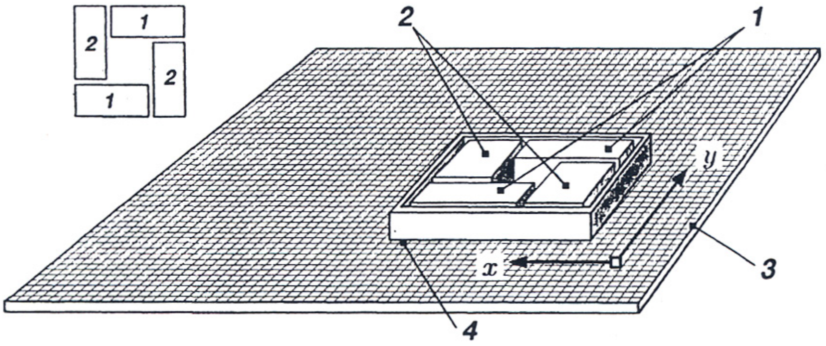

Figure 1.18 HLSM with a four-unit forcer to obtain the *x* -*y* motion: 1 –forcers for the *x*-direction, 2 - forcers for the *y* direction, 3- platen, 4 – air pressure.

Table 1.7 Data of *x* - *y* HLSMs manufactured by *Normag Northern Magnetics, Inc*., Santa Clarita, CA, U.S.A.

Parameter	4XY0602-2-0	4XY2002-2-0	4XY2004-2-0	4XY2504-2-0
Number of force unites per axis	1	1	2	2
Number of phases	2	2	2(4)	2(4)
Static thrust, N	13.3	40.0	98.0	133.0
Thrust at 1m/s,N	11.1	31.1	71.2	98.0
Normal Attractive Force, N	160.0	400.0	1440.0	1800.0
Resistance Per phase, Ω	2.9	3.3	1.6	1.9
Inductance Per phase, mH	1.5	4.0	2.0	2.3
Input phase Current, A	2.0	2.0	4.0	4.0
Airgap, mm	0.02			
Maximum Temperature, °C	110			
Mass, kg	3.2	0.72	2.0	1.5
Repeatability, mm	0.00254			
Resolution, mm	0.00254			
Bearing type	Air			

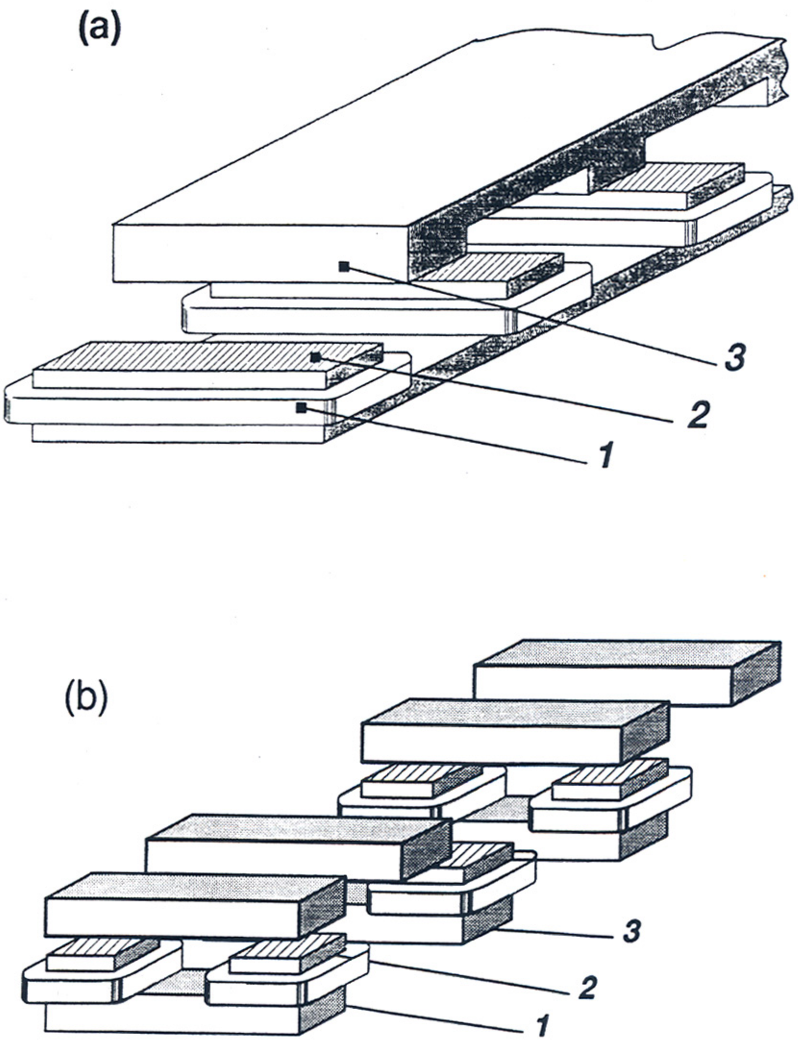

Figure 1.19 Linear switched reluctance motor configurations: (a) longitudinal flux design, (b) transverse flux design. 1 - armature winding, 2 – armature stack, 3 - platen. .

When two or four forcers mounted at 90° and a special grooved platen ('waffle plate') are used, the x-y motion in a single plane is obtained (Fig.1.18). Specification data of the x-y HLSMs manufactured by *Normag Northern Magnetics, Inc.*, Santa Clarita, CA, U.S.A. are given in Table 1.7 [105].

1.2.7 Switched Reluctance Motors

A *linear switched reluctance motor* has a doubly salient magnetic circuit with a polyphase winding on the armature. Longitudinal and transverse flux designs are shown in Fig. 1.19. A linear switched reluctance motor allows precise speed and position-controlled linear motion at low speeds, and is not subject to design constraints (minimum speed limited by minimum feasible pole pitch) of linear a.c. motors [4].

1.3 Calculation of Forces

Neglecting the core loss and nonlinearity, *the energy stored in the magnetic field* is

$$W = \frac{1}{2}\Phi F = \frac{1}{2}\Phi Ni \qquad \mathbf{J} \tag{1.5}$$

where the MMF $F = Ni$. Introducing the reluctance $\Re = F / \Phi$ the field energy is

$$W = \frac{1}{2}\Re\Phi^2 = \frac{1}{2}\frac{F^2}{\Re} \qquad \mathbf{J} \tag{1.6}$$

The self-inductance

$$L = \frac{N\Phi}{i} \tag{1.7}$$

is constant for $\Re = const$. Hence,

$$W = \frac{1}{2}Li^2 \tag{1.8}$$

In a magnetic circuit with the airgap $g > 0$, most of the MMF is expended on the airgap and most of the energy is stored in the airgap with its volume Ag where A is the cross section area of the airgap. Working in B and H units, the field energy per volume is

$$\omega = \frac{W}{Ag} = \frac{1}{2}B_g H = \frac{1}{2}\frac{B_g^2}{\mu_o} \qquad \mathbf{J}/\mathrm{m}^3 \tag{1.9}$$

where B_g is the magnetic flux density in the airgap.

Table 1.8 Electric and corresponding magnetic quantities.

Electric circuit	Unit	Magnetic circuit	Unit
Electric voltage, $V = \int_l Edl$	V	Magnetic voltage $V_\mu = \int_l Hdl$	A
EMF	V	MMF, F	A
Current, I	A	Magnetic flux, Φ	Wb
Current density, J	A/M^2	Magnetic flux density, B	Wb/m^2=T
Resistance, R	Ω	Reluctance , $\Re$	1/H
Conductance, G	S	Permeance, G	H
Electric conductivity, ρ	S/M	Magnetic permeability, μ	H/m

The magnetic quantities corresponding to electric quantities are listed in Table 1.8.

The *force* F_i *associated with any linear motion* defined by a variable S_i of a device employing a magnetic field is given by

$$F_i = \frac{\delta W}{\delta s_i} \tag{1.10}$$

©2000 CRC Press LLC

where W is the field energy in Joules according to eqn (1.5), F_i denotes the $F_x F_y F_z$ force component and s_i denotes the x, y or z coordinate.

For a singly excited device

$$F_i = \frac{1}{2}\Phi^2 \frac{d\Re}{ds_i} = \frac{1}{2} i^2 \frac{dL}{ds_i} \tag{1.11}$$

where the magnetic flux $\Phi = const$ and electric current $i = const$.

Eqn (1.11) can be used to find the attractive force between two poles separated by an airgap z = g. Let us consider a linear electromagnetic actuator, electromagnet or relay mechanism. The following assumptions are usually made: (a) leakage flux paths are neglected, (b) nonlinearities are neglected and (c) all the field energy is stored in the airgap ($\mu_o \mu_r >> \mu_o$) where the magnetic permeability of free space $\mu_o = 0.4\pi \times 10^{-6}$ and μ_r is the relative permeability. The volume of the airgap is Az and the stored field energy is $W = 0.5\left(B_g^2 / \mu_o\right)Az$. With the displacement dz of one pole the new airgap is $z + dz$, new stored energy is $W + dW = 0.5\left(B_g^2 / \mu_o\right)A(z + dz)$ change in stored energy is $0.5\left(B_g^2 / \mu_o\right)Adz$, work done $F_z dz$ and the force

$$F_z = \frac{dW}{dz} = \frac{1}{2}\frac{B_g^2}{\mu_o}A = \frac{1}{2}\frac{\mu_o (Ni)^2}{g^2}A \tag{1.12}$$

where $B_g = \mu_o H = \mu_o \left(Ni / z\right), z = g, i$ is the instantaneous electric current and A is the cross section of the airgap (surface of a single pole shoe). Eqn (1.12) is used to find the normal (attractive) force between the armature core and reaction rail of linear motors.

For a doubly excited device

$$F_i = \frac{1}{2} i_1^2 \frac{dL_{11}}{ds_i} + \frac{1}{2} i_2^2 \frac{dL_{22}}{ds_i} + i_1 i_2 \frac{dL_{12}}{ds_i} \tag{1.13}$$

where L_{11} is the self inductance of the winding with current i_1, L_{22} is the self inductance of the winding with current i_2 and L_{12} is the mutual inductance between coils 1 and 2. In simplified calculations the first two terms are commonly zero.

1.4 Linear Motion

1.4.1 Speed-Time Curve

The *speed-time curve* is a graph which shows the variation of the linear speed versus time (Fig. 1.20a). In most cases both the acceleration and deceleration are linear functions of time. Thus, the speed-time curve of a moving object is most often approximated by a trapezoidal function (Fig. 1.20a). The acceleration time is

$$t_1 = \frac{\upsilon_{const}}{a} \tag{1.14}$$

where υ_{const} is the constant (steady state) speed. Similarly the retardation time is

©2000 CRC Press LLC

$$t_3 = \frac{\upsilon_{const}}{d} \qquad (1.15)$$

where d is the deceleration. The time t_2 for a constant-speed running depends both on acceleration and deceleration, i.e.,

$$t_2 = t - t_1 - t_3 = t - \upsilon_{const}\left(\frac{1}{a} + \frac{1}{d}\right) \qquad (1.16)$$

where the total time of run $t = t_1 + t_2 + t_3$. The total distance of run can be found on the basis of Fig. 1.20a, i.e.,

$$s = \frac{1}{2}\upsilon_{const}t_1 + \upsilon_{const}t_2 + \frac{1}{2}\upsilon_{const}t_3 = \upsilon_{const}t - \frac{\upsilon^2 const}{2}\left(\frac{1}{a} + \frac{1}{d}\right) \qquad (1.17)$$

or

$$k\upsilon_{const}^2 - t\upsilon_{const} + s = 0 \qquad (1.18)$$

where

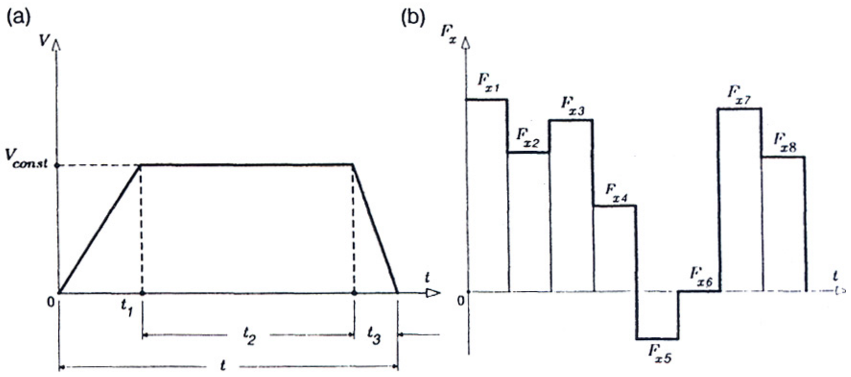

Figure 1.20 typical speed and thrust profiles: (a) speed-time curve, (b) thrust-time curve.

$$k = \frac{1}{2}\left(\frac{1}{a}\frac{1}{d}\right) \qquad (1.19)$$

The above quadratic eqn (1.18) allows one to find the constant speed as a function of the total time of run, acceleration, deceleration and total distance of run, i.e.,

$$\upsilon_{const} = \frac{t}{2k} - \sqrt{\left(\frac{t}{2k}\right)^2 - \frac{s}{k}} \qquad (1.20)$$

Table 1.9 compares basic formulae describing linear and rotational motions. There are two components of the linear acceleration: tangential $a = \alpha r$ and centripetal $a_r = \Omega^2 r$ where r is the radius.

©2000 CRC Press LLC

1.4.2 Thrust-Time Curve

The *thrust-time curve* is a graph which shows the variation of the thrust versus time (Fig. 1.20b). The rms thrust (force in the x direction) is based on the given duty cycle, i.e.,

$$F_{xrms}^2 \sum t_i = \sum F_{xi}^2 t_i$$

$$F_{xrms} = \sqrt{\frac{F_{x1}^2 t_1 + F_{x2}^2 t_2 + F_{x3}^2 t_3 + \ldots + F_{xn}^2 t_n}{t_1 + t_2 + t_3 + \ldots + t_n}} \tag{1.21}$$

Similarly, in electric circuits the rms or effective current is

$$I_{rms} = \sqrt{\frac{1}{T}\int_0^T i^2 dt}$$

Table 1.9 Basic formulae for linear and rotational motions.

Linear motion			Rotational motion		
Quantity	Formula	Unit	Quantity	Formula	Unit
Linear displacement	$s = \theta r$ r =radius	m	Angular displacement	θ	rad
Linear velocity	v=ds/dt $v = \Omega r$	m/s	Angular velocity	$\Omega = d\theta / dt$	rad/s or 1/s
Linear acceleration	a=dv/dt $a = \alpha r$ $a_r = \Omega^2 r$ $= v^2 / r$	m/s^2	Angular acceleration	$\alpha = d\Omega / dt$	rad / s^2 or $1 / s^2$
Mass	m	Kg	Moment of inertia	J	kgm^2
Force	$F = ma$	N	Torque	$T = J\alpha$	Nm
Work	dw=Fds	Nm	Work	$dW = Td\theta$	Nm
Kinetic energy	$E_k = 0.5mv^2$	J or Nm	Kinetic energy	$E_k = 0.5J\Omega^2$	J
Power	P=dW/dt $= Fv$	W	Power	P=dW/dt $= T\Omega$	W

since the average power delivered to the resistor R is

$$P = \frac{1}{T}\int_0^T i^2 R dt = R\frac{1}{T}\int_0^T i^2 dt = RI_{rms}^2$$

1.4.3 Dynamics

Fig. 1.21 shows the mass m sliding at velocity υ with a viscous friction coefficient μ_υ on a surface. The applied instantaneous force is f_x and the spring constant is k_s. According to d' Alembert's principle

©2000 CRC Press LLC

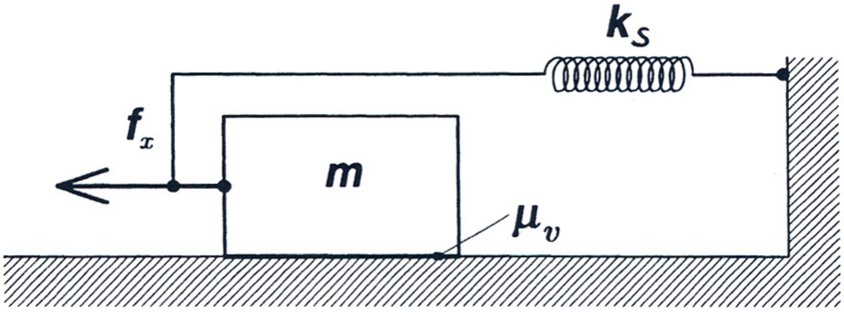

Figure 1.21 A simple linear mechanical system.

$$m\frac{dv}{dt}+\mu_v v+k_s\int vdt = f_x \tag{1.22}$$

The form of eqn (1.22) is similar to Kirchhoff's voltage equation for the RLC series circuit, i.e.,

$$L\frac{di}{dt}+Ri+\frac{1}{C}\int idt = e \tag{1.23}$$

where e is the instantaneous induced voltage (EMF) and i is the instantaneous current. Since

$$v=\frac{dx}{dt} \text{ and } i=\frac{dq}{dt}$$

where q is the electrical charge, eqns (1.22) and (1.23) can be rewritten to the forms

$$m\frac{d^2x}{dt^2}+\mu_v\frac{dx}{dt}+k_s x = f_x \tag{1.24}$$

$$L\frac{d^2q}{dt^2}+R\frac{dq}{dt}+\frac{1}{C}q = e \tag{1.25}$$

Analogous systems are described by the same integro-differential equation or set of equations, e.g., mechanical and electrical systems.

In the mechanical system, energy stored in the mass is given by the kinetic energy $0.5mv^2$. Energy storage occurs in a spring from the displacement $x=\int vdt$ due to a force. This force is expressed in terms of a spring constant k_s, as $f_x = k_s x = k_s\int vdt$.

Assuming a linear force-displacement relation, the work done is

©2000 CRC Press LLC

$$W = \frac{1}{2} f_x x = \frac{1}{2}\frac{1}{k_s} f_x^2 \qquad \mathbf{J} \tag{1.26}$$

A viscous friction element, such as a *dashpot*, is an energy dissipating element. In the *mass-inductance analogy*, the inductance has stored electromagnetic energy $0.5Li^2$ Application of a voltage to a capacitance causes a proportional storage of charge, $q = \int idt$, and the voltage component is $\left(1/C\right)\int idt$.

Similarly, in the mass-capacitance analogy, the energy stored in a capacitance is $0.5Ce^2$. The energy storage of a spring, $0.5\left(1/k_s\right)f_x^2$ is analogous to that in inductance $0.5Li^2$, whence inductance becomes the analogue of spring compliance $\left(1/k_s\right)$.

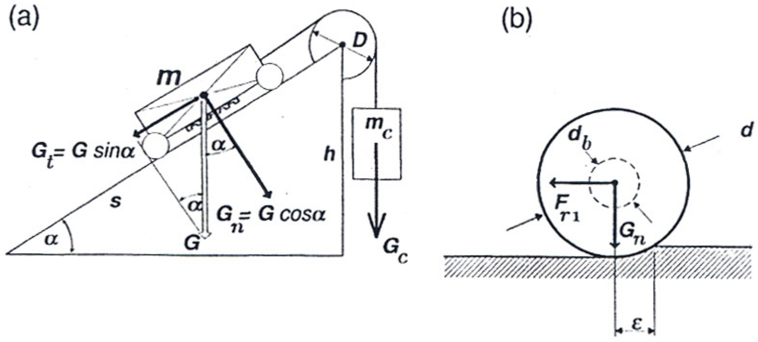

Figure 1.22 Linear motor driven mechanism: (a) slope, (b) sketch for calculating the rolling resistance.

1.4.4 Traction

Let us consider a mechanism driven by a linear motor (Fig. 1.22a). The mechanism consists of a moving part, i.e., a linear motor driven car with the total mass m on a slope, a pulley, a cable and a counterweight with its mass m_c. The efficiency of the system is η. The inertia of pulley and mass of cable is neglected.

For the steady-state linear motion

$$\eta\left(F_x + m_c g\right) = mg\sin\alpha + \mu mg\cos\alpha \tag{1.27}$$

where $mg\sin\alpha$ is the force due to the gradient resistance is the force due to the friction resistance and $g = 9.81\ m/s^2$ is the gravitational acceleration. The coefficient of friction μ is approximately 0.2 for steel on dry steel, 0.06 for steel on oiled steel (viscous friction), 0.005 for linear bearings with rollers and 0.002...0.004 for linear bearings with balls. Thus, the steady-state thrust (force produced by the linear motor) is

$$F_x = \frac{1}{\eta}\left(m\sin\alpha + \mu m\cos\alpha - m_c\right)g \tag{1.28}$$

©2000 CRC Press LLC

When the moving part runs up the gradient with an acceleration a the acceleration thrust is higher since the term $(m+m_c)a$ is added, i.e.,

$$F_{xpeak} = \frac{1}{\eta}\left[(m\sin\alpha + \mu m\cos\alpha - m_c)g + (m+m_c)a\right] \tag{1.29}$$

The thrust according to eqn (1.29) is often called the peak thrust. Similarly, if the car runs up with a deceleration d, the braking force is

$$F_{xb} = \eta\left[(m\sin\alpha + \mu m\cos\alpha - m_c)g - (m+m_c)a\right] \tag{1.30}$$

Note that for the braking mode the counterbalancing force is $1/\eta\,(F_{xb} + m_c g)$.

The linear motor driven car is furnished with wheels. The rolling force (Fig. 1.22b)

$$F_{r1} = \frac{\in G\cos\alpha}{0.5d}$$

where $G\cos\alpha = G_n = mg\cos\alpha$. Including friction in wheel-axle bearings

$$F_{r2} = F_{r1} + \frac{0.5d_{b\mu}G\cos\alpha}{0.5d} = \frac{\in +0.5\mu d_b}{0.5d}G\cos\alpha$$

where d_b is the diameter of bearing journal. An additional resistance due to uneven track and hunting can be added by introducing a coefficient $\beta > 1$. Thus, the total rolling force

$$F_r = k_r G \tag{1.31}$$

where

$$k_r = \mu\frac{(\in +0.5\mu d_b)\cos\alpha}{0.5d} \tag{1.32}$$

In railway engineering, the coefficient k_r is called the *specific rolling resistance*. For speeds up to 200 km/h and steel wheels on steel rails k_r = 0.002 to 0.012.

Eqn (1.28) in which $m_c = 0$ and $\eta \approx 1$ is known in railway engineering as *traction effort equation* and has the following form

$$F_x = (k_r + k_g + k_a)G \tag{1.33}$$

The *specific gradient resistance* is

$$k_g = \pm\sin\alpha = \pm\frac{h}{s} \tag{1.34}$$

since the force due to gravity is $G_t = G\sin\alpha$. The '$+$' sign is for a car moving up the gradient and the '$-$' sign is for a car moving down the gradient. Neglecting the inertia of rotating masses of the car, the *specific acceleration resistance* is

$$k_a = \frac{a}{g}$$

where a is the linear acceleration or deceleration.

For a curvelinear track, the *specific curve resistance* should be taken into account, i.e. ,

$$k_c = \frac{0.153S + 0.1b}{R_c} \tag{1.36}$$

where S is the circumference of wheel in meters, b is the mean value of all fixed wheel bases with $b < 3.3S$ in meters and R_c is the track curve radius in meters. For example, if the wheel radius is R = 0.46 m, wheel base is b = 3 m and the track curve radius is $R_c = 5$ km, the circumference of wheel $S = 2\pi R = 2\pi \times 0.46 = 2.89$ m and the specific curve resistance is $k_c = {(0.153 \times 2.89 + 0.1 \times 3.0)}/{5000} = 0.148 \times 10^{-3}$.

For high speed trains the air resistance force

$$F_{air} = 0.5 C \rho \upsilon^2 A \quad \text{N} \tag{1.37}$$

should be added to eqn (1.33). The coefficient C = 0.2 for cone or wedge shaped nose, C = 2.1 for flat front trains and C = 0.75 for automobiles. The air density is ρ, the speed v is in m/s and the front surface area A is in m^2. At 20°C and 1 atm the air density is ρ = 1.21. kg/m^3. For example if C = 0.2, v = 200 km/h = 200/3.6 = 55.55 m/s and A = 4x3 = 12 m^2, the air resistance force is F_{air} = 0.5 x 0.2 x 1.21 x (55.55)^2 X 12 = 4480.6 N. Eqn (1.37) gives too small values of the air resistance force for high speed maglev trains with wedge shaped front cars.

1.5 Selection of Linear Motors

Given below are numerical examples that show how to calculate basic parameters of linear motion drives and how to choose a linear electric motor with appropriate ratings. This is a simplified selection of linear motors and more detailed calculation of parameters, especially the thrust, is recommended (Chapter 3).

When designing a linear motor drive, it is always necessary to consider its benefits in comparison with traditional drives with rotary motors and mechanical gears or ball screws transferring rotary motion into translatory motion 138]. *The authors take no responsibility for any financial losses resulting from wrong decisions and impractical designs* .

Example 1.1

A moving part of a machine is driven by a linear motor. The linear speed profile can be approximated by a trapezoidal curve (Fig. 1.20a). The total distance of run s = 1.8 m is achieved in t = 0.5 s with linear acceleration a = 4g at starting and linear deceleration d = 3g at braking. Find the steady state speed v_{const}, acceleration-time t_1, acceleration distance s_1, constant speed time t_2, constant speed distance s_2, deceleration time t_3 and deceleration distance s_3.

Solution

According to eqn (1.19)

$$k = \frac{1}{2}\left(\frac{1}{4g} + \frac{1}{3g}\right) = 0.02973 \quad s^2/m$$

The constant speed according to eqn (1.20)

©2000 CRC Press LLC

$$v_{const} = \frac{0.5}{2\times 0.02973} - \sqrt{\left(\frac{0.5}{2\times 0.02973}\right)^2 - \frac{1.8}{0.02973}} = 5.22 \text{ m/s} = 18.8 \text{ km/h}$$

The time of acceleration

$$t_1 = \frac{5.22}{4g} = 0.133 \text{ s}$$

The distance corresponding to acceleration

$$s_1 = \frac{1}{2} 5.22 \times 0.133 = 0.347 \text{ m}$$

The time of deceleration

$$t_3 = \frac{5.22}{3g} = 0.177 \text{ s}$$

The distance corresponding to deceleration

$$s_3 = \frac{1}{2} 5.22 \times 0.177 = 0.462 \text{ m}$$

The time corresponding to the steady state speed

$$t_2 = 0.5 - 0.133 - 0.177 = 0.19 \text{ s}$$

The distance corresponding to the steady state speed

$$s_2 = 5.22 \times 0.19 = 0.991 \text{ m}$$

and

$$s_1 + s_2 + s_3 = 0.347 + 0.991 + 0.462 = 1.8 \text{ m}$$

Example 1.2

The specification data of a mechanism with linear motor shown in Fig. 1.22a are as follows: m = 500 kg, m_c = 225 kg , η = 0.85, α = 30^0, $\in$ = 0.00003 m, μ = 0.005, d = 0.03m; d_b = 0.01 m and β = 1.3. The car is moving up the slope. Find the thrust of the .linear motor for: (a) steady state, (b) starting with acceleration $a = 1$ m/s^2, (c) braking with deceleration d = 0.75 m/s^2. The mass of the cable, pulley and gears is neglected.

Solution

The weight of the car

$$G = 500 \times 9.81 = 4905 \text{ N}$$

The specific rolling resistance according to eqn (1.32)

$$k_r = 1.3 \frac{0.00003 + 0.5 \times 0.005 \times 0.01}{0.5 \times 0.03} \cos 30° = 0.00412$$

The steady state thrust according to eqn (1.28)

©2000 CRC Press LLC

$$F_x = \frac{1}{\eta}\left(\sin\alpha + k_r - \frac{m_c}{m}\right)G = \frac{1}{0.85}\left(\sin 30° + 0.00412 - \frac{225}{500}\right)\times 4905 = 312.3 \text{ N}$$

At starting with acceleration a = 1 m/s^2 – eqn (1.29)

$$F_{xpeak} = \frac{1}{0.85}\left[\left(\sin 30° + 0.00412 - \frac{225}{500}\right)\times 4905 + (500+225)\times 1.0\right] = 1165.2 \ N$$

The peak thrust of the linear motor should not be lower than the above value.

At braking with deceleration a = 0.75 m/s^2 – eqn (1.30)

$$F_{xb} = 0.85\left[\left(\sin 30° + 0.00412 - \frac{225}{500}\right)\times 4905 - (500+225)\times 0.75\right] = -236.6 \ N$$

Example 1.3

A 1.5-kW, 1.5 m/s linear electric motor operates with almost constant speed and with the following thrust profile: 1600 N for $0 \le t \le 3s$, 1200 N for $3 \le t \le 10 \ \ s$, 700 N for $10 \le t \le 26 \ \ s$, 500 N for $26 \le t \le 38 \ \ s$. The overload capacity factor $F_{x\max}/F_{xr}$ = 2. Find the thermal utilization coefficient of the motor.

Solution

The rated thrust produced by the linear motor

$$F_{xr} = \frac{P_{out}}{v} = \frac{1500}{1.5} = 1000 \ \ N$$

The linear motor has been properly selected since the maximum load for the given thrust profile 1600 N is less than the maximum thrust determined by the overload capacity factor, i.e.,

$$F_{x\max} = 2F_{xr} = 2\times 1000 = 2000 \ \ N$$

The rms thrust based on the given duty cycle

$$F_{xrms} = \sqrt{\frac{\sum F_{xi}^2 t_i}{\sum t_i}} = \sqrt{\frac{1600^2\times 3 + 1200^2\times 7 + 700^2\times 16 + 500^2\times 12}{3+7+16+12}} = 867.54 \ \ Nm$$

The coefficient of thermal utilization of the motor

$$\frac{F_{xrms}}{F_{xr}}\times 100\% = \frac{867.54}{1000.0}\times 100\% = 86.7\%$$

The linear motor, e.g., IC11-200 (Table 1.2) with continuous thrust 1260 *N* (F_{xrms} = 867.54 < 1260 N) and peak thrust 2000 N can be selected.

©2000 CRC Press LLC

Example 1.4

In a factory transportation system, linear motor driven containers with steel wheels run on steel rails. Each container is driven by a set of 2 linear motors. The loaded container runs up the gradient and accelerates from v = 0 to v_{const} = 18 km/h in t_1 = 5 s, then it runs with constant speed 18 km/h and finally it decelerates from v = 18 km/h to v = 0 in t_3 = 5 s. The total time of running is t = 20 s. Then containers are unloaded within minimum 10 s and they run back to the initial position where they are loaded again. The time of loading is minimum 20 s. The speed and force curves of unloaded containers running down the gradient are the same as those of loaded containers, i.e., acceleration in 5 s to v_{const} = 18 k/h, run with constant speed and deceleration in 5 s to v = 0. The mass of each container including the load and linear motor is m_c = 1200 kg, without load $m_c^{'}$ = 300 kg. The rise in elevation is h = 3 m and specific rolling resistance is k_r = 0.0025. The efficiency of the system can be assumed 100%. Find the length of the track, thrust curve and rms thrust.

Solution

The movement of the container can be approximated by a trapezoidal speed-time curve (Fig. 1.20a). The linear acceleration

$$a = \frac{v_{const} - 0}{t_1 - 0} = \frac{18/3.6}{5} = 1 \text{ m/s}^2$$

The linear deceleration

$$d = \frac{0 - v_{const}}{(t_1 + t_2 + t_3) - (t_1 + t_2)} = \frac{-v_{const}}{t_3} = \frac{-18/3.6}{5} = -1 \text{ m/s}^2$$

where $t = t_1 + t_2 + t_3 = 20$ s is the total time of run.

The time of running with constant speed

$$t_2 = t - t_1 - t_3 = 20 - 5 - 5 = 10 \text{ s}$$

The total distance of run is equal to the length of the track. According to eqn (1.17)

$$s = \frac{1}{2}vt_1 + vt_2 + \frac{1}{2}vt_3 = \frac{1}{2}\frac{18}{3.6}5 + \frac{18}{3.6}10 + \frac{1}{2}\frac{18}{3.6}5 = 75 \text{ m}$$

The specific gradient resistance

$$k_g = \pm\frac{h}{s} = \pm\frac{3}{75} = \pm 0.04$$

The specific acceleration and deceleration resistances

$$k_a = \frac{a}{g} = \frac{1.0}{9.81} = 0.102 \qquad k_a^{'} = \frac{d}{g} = \frac{-1.0}{9.81} = -0.102$$

The weight of loaded and empty container

$$G = m_c g = 1200 \times 9.81 = 11772 \text{ N}$$

$$G^{'} = m_c^{'} g = 300 \times 9.81 = 2943 \text{ N}$$

©2000 CRC Press LLC

The thrust produced by linear motors when the loaded container moves up the gradient

- the loaded container accelerates (t_1 = 5 s)

$$F_{xpeak} = \left(k_r + k_g + k_a\right)G = \left(0.0025 + 0.04 + 0.102\right)\times 11,772 \approx 1701 \text{ N}$$

or 1701/2 = 850.5 N per one linear motor;

- the loaded container runs with constant speed (t_2 = 10 s)

$$F_x = \left(k_r + k_g\right)G = \left(0.0025 + 0.04\right)\times 11,772 = 500.3 \text{ N}$$

or 500.3/2 ≈ 250.2 N per one linear motor

- the loaded container decelerates (t_3 = 5 s)

$$F_{xb} = \left(0.0025 + 0.04 - 0.102\right)\times 11,772 = -700.43 \text{ N}$$

or each linear motor should be able to produce a braking force - 700.43/2 ≈ -350.2 N during the last 5 s of run.

The thrust produced by linear motors when the unloaded container moves down the gradient

- the unloaded container accelerates (5 s)

$$F_x' = \left(k_r - k_g + k_a\right)G' = \left(0.0025 - 0.04 + 0.102\right)\times 2943 = 189.8 N$$

or 189.8/2 = 94.9 N per one linear motor;

- the unloaded container runs with constant speed (10 s)

$$F_x'' = \left(k_r - k_g\right)G' = \left(0.0025 - 0.04\right)\times 2943 = -110.4 N$$

or one linear motor should produce -110.4/3 = 55.2 N braking force

- the unloaded container decelerates (5 s)

$$F_x''' = \left(0.0025 - 0.04 - 0.102\right)\times 2943 = -410.55 \text{ N}$$

or each linear motor should produce a braking force of -410.55/2 ≈ 205.3 N.

©2000 CRC Press LLC

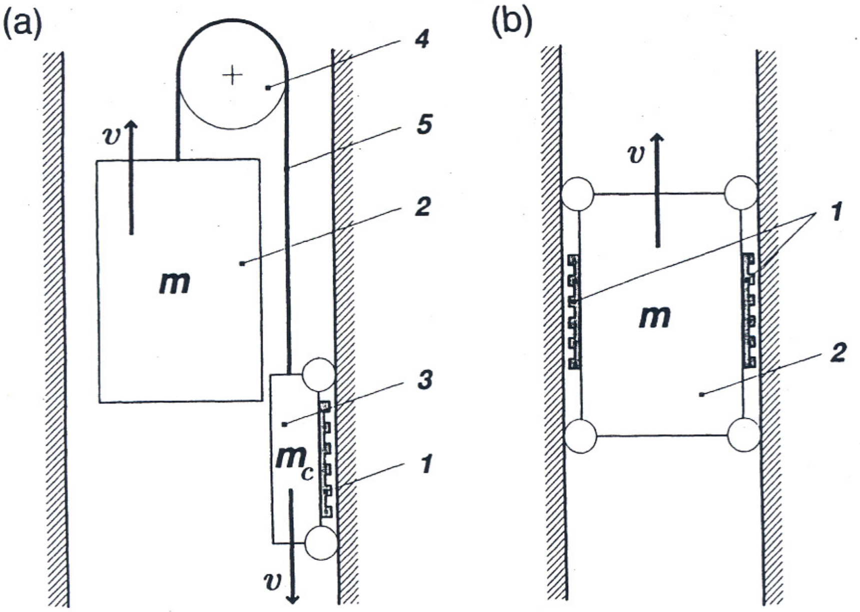

Figure 1.23 Linear electric motor driven elevators: (a) with a rope, (b) ropeless. 1 - armature of a linear motor, 2 - car (load), 3 - counterweight, 4 - sheave, 5 - rope.

The rms thrust developed by two linear motors

$$F_{rms} = \frac{(1701^2\times5+500.3^2\times10+700.43^2\times5+0+189.8^2\times5+110.4^2\times10+410.55^2\times5+0)^{\frac{1}{2}}}{(5+10+5+10+5+10+5+20)^{\frac{1}{2}}} = 542.1N$$

The overload capacity factor

$$\frac{F_{xpeak}}{F_{rms}} = \frac{1701.0}{542.1} \approx 3.14$$

It will probably be difficult to find a linear motor with 3.14 peak-to-rms thrust ratio. If no such linear motor is available, the selected linear motor should develop the peak thrust minimum 1701/2 = 850.5 N and its rated thrust can be higher than 542.1/2 ≈ 271.1 N

Example 1.5

A linear motor driven rope elevator is shown in Fig. 1.23a. The linear motor is built in the counterweight. The mass of the car with load is m =819 kg, the mass of counterweight is m_c =1187.5 kg, the steady state speed is v = 1.0 m/s, the acceleration at starting is a = 1.0 m/s^2 and the linear motor efficiency is η = 0.6. Neglecting the friction, rope mass and sheave mass, find the steady state and peak thrust developed by the linear motor and its power consumption at steady state.

Solution

The efficiency of the hoistway is assumed to be η = 100%. The thrust at steady state speed when the car is going up can be found on the basis of eqn (1.28) in which α = 90^0, i.e.,

$$F_x + m_c g = mg$$

$$F_x = (m - m_c)g = (819 - 1187.5)\times9.81 = -3615 \text{ N}$$

©2000 CRC Press LLC

The car is retarded when going up and the linear motor should produce a steady state braking force -3615 N. In the case of the drive failure, the elevator car will be moving up, not down, because $m_c > m$

The peak force at starting − compare eqn (1.29) for $\alpha = 90°$

$$F_{xpeak} = (m - m_c)g + (m + m_c)a = (819 - 1187.5)\times 9.81 + (819 + 1187.5)\times 1.0 = -1608.5 \text{ N}$$

The ratio $F_{xpeak} / F_x = 1608.5 / 3615 \approx 0.445$ The linear motor mounted in counterweight produces smaller braking force at starting than at steady state speed.

When the car is going down the thrust and the peak thrust are, respectively

$$F_X = (m_c - m)g = (1187.5 - 819.0)\times 9.81 = 3615 \text{ N}$$

$$F_{xpeak} = (m_c - m)g + (m + m_c)a = (1187.5 - 819.0)\times 9.81 + (819.0 + 1187.5)\times 1.0 = 5621.5 \text{ N}$$

The output power of the linear motor at steady-state speed

$$P_{out} = F_x \upsilon = 3615.0 \times 1.0 = 3615 \text{ W}$$

The electric power absorbed by the linear motor

$$P_{in} = \frac{P_{out}}{\eta} = \frac{3615}{0.6} = 6025 \text{ W}$$

Example 1.6

Consider a ropeless version of the elevator (Fig. 1.23b). The rope sheave and counterweight have been eliminated and the linear motor built in the counterweight has been replaced by car mounted linear motors. Assuming the mass of the loaded car m = 4583 kg, a= 1.1 m/s^2, υ = 10.0 m/s, linear motor efficiency η = 0.97 and 2 linear motors per car find the output and input power of linear motors.

Solution

The efficiency of hoistway is assumed to be η = 100%. When the car is going up, the requested steady state thrust is

$$F_x = mg = 4583.0 \times 9.81 = 44{,}960.0 \text{ N}$$

The requested peak thrust

$$F_{xpeak} = m(g + a) = 4583.0(9.81 + 1.1) \approx 50{,}000.0 \text{ N}$$

The ratio $F_{xpeak} / F_x = 50{,}000 / 44{,}960 = 1.112$ The steady state output power of linear motors

$$P_{out} = F_x \upsilon = 44{,}960.0 \times 10.0 = 449{,}600.0 \text{ W}$$

or 449,600.0/2 = 224,800.0 W per one linear motor. It is recommended to choose two linear motors rated at minimum 225 kW each and developing the steady state thrust 44.96/2 ≈ 22.5 kN at 10.0 m/s and peak thrust 50.0/2 = 25.0 kN.

When the car is going down the steady state breaking force is

$$F_{xb} = -mg = -4583.0 \times 9.81 = -44{,}960.0 \text{ N}$$

and the transient braking force is smaller

$$F'_{xb} = -mg + ma = -4583.0 \times 9.81 = 4583.0 \times 1.1 = -39{,}518.8 N$$

©2000 CRC Press LLC

The following power can be recovered when regenerative braking is applied

$$P_b = \eta F_{xb}\upsilon = 0.97 \times |\, 44,960.0 \,| \times 10.0 = 436,112.0 \text{ W}$$

Example 1.7

The MLX01 three-car maglev trainset with a superconducting LSM runs on a practically horizontal guidaway with the specific gradient resistance k_g = 0. The mass of the loaded train is m = 84 t, the front car is w = 2.9 m wide and h = 3.28 m high with a wedge shaped front nose. The following experimental test results on Yamanashi Maglev Test Line are available [72]: (1) LSM propulsion force 200 kN at υ = 350 km/h and (2) acceleration a = 0.2g. Assuming the air density p = 1.21 kg/m^3 at 20°C and 1 atm, find the specific 'rolling' resistance for a maglev train.

Solution

The weight of the trainset

$$G = mg = 84,000 \times 9.81 = 824.04 \text{ kN}.$$

The required output power of the LSM at constant speed υ = 350 km/h is

$$P_{out} = F_x \upsilon = 200 \times 10^3 \frac{350}{3.6} = 19,444,444 W \approx 19.45 MW$$

For a wedge shaped nose the coefficient of proportionality in the air resistance force equation (1.37) is C ≈ 0.2. The air resistance force at υ = 350 km/h

$$F_{air} = 0.5 C^2 wh = 0.5 \times 0.2 \times 1.21 \times (\frac{350}{3.6})^2 \times 2.9 \times 3.28 = 10,879 \text{ N}$$

The air resistance force obtained from eqn (1.37) seems to be too small because the air resistance due to longitudinal surfaces of the train has not been taken into account. Also, the air resistance due to tunnels has been neglected. The air resistance for MLX01 maglev train will probably be similar to that estimated for *Transrapid* maglev train, i.e., about 35 kN.

The specific acceleration resistance

$$k_a = \frac{a}{g} = \frac{0.2g}{g} = 0.2$$

On the basis of the traction effort equation (1.33)

$$k_r = \frac{1}{G}(F_X - F_{air}) - k_a = \frac{1}{824.04 \times 10^3}(200 \times 10^3 - 35 \times 10^3) - 0.2 = 0.000233$$

This is rather a very rough estimation of K_r. This resistance corresponds to the 'rolling' resistance of wheel-on-rail trains and it is due to braking forces of electrodynamic nature, i.e., interaction of the magnetic field of on board superconducting electromagnets and induced currents in levitation and guidance coils.

©2000 CRC Press LLC

chapter 2

Materials and Construction

2.1 Materials

All materials used in the construction of electric al machines can be divided into three groups:

- active materials, i.e., electric conductors, superconductors, electrotechnical steels, sintered powders and PMs;
- insulating materials;
- construction materials.

All current conducting materials (with high electric conductivity) and magnetic flux conducting materials (with high magnetic permeability) are called *active materials.* They serve for the excitation of EMF and MMF, concentrate the magnetic flux in the desired place or direction and help to maximize the electrodynamic forces. The ferromagnetic materials are divided into *soft ferromagnetic materials,* i.e., with a narrow hysteresis loop and *hard ferromagnetic materials* or *permanent magnets,* i.e., with a wide hysteris loop.

The *insulating materials* isolate electrically the current-conductors from the other parts of electrical machines.

There are no insulating materials for the magnetic flux. Leakage fluxes can only be reduced by a proper shaping of the magnetic circuit or using electromagnetic or electrodynamic screens (shielding).

The *construction materials* are necessary for structural purposes intended for the transmission and withstanding of mechanical loads and stresses. In electrical machine industry mild carbon steel, alloyed steel, cast iron, wrought iron, non-ferromagnetic steel, non-ferromagnetic metals and their alloys, and plastic materials are used as construction materials.

2.2 Laminated Ferromagnetic Cores

From the electromagnetic point of view, *laminated ferromagnetic cores* are used to improve the propagation of electromagnetic waves in conductive ferromagnetic materials. In thin ferromagnetic sheets, i.e., with their thicknesses below 1 mm, the *skin effect* at power frequencies 50 to 60 Hz practically does not exist. The damping effect of the electromagnetic field by eddy currents is substantially reduced. The alternating magnetic flux occurs in the whole sheet cross section and its distribution is practically uniform inside the laminated stack. Considering the skin effect, stacking factor, hysteresis losses, eddy-current losses, reactive power (magnetizing current) and easy stamping, the best thickness is 0.5 to 0.6 mm for 50-Hz electrical machines and 0.2 to 0.35 mm for 400-Hz electrical machines [135].

The *main losses* in a ferromagnetic core with its mass m_c at any frequency f and any magnetic flux density B are calculated as

$$\Delta P_{Fe} = k_{Fe} \Delta p_{1/50} \left(\frac{f}{50} \right)^{4/3} B^2 m_c \qquad (2.1)$$

©2002 CRC Press LLC

where $k_{Fe} > 1$ is the coefficient for including the difference in the distribution of the magnetic field in the core and in the sample in which the specific core losses have been measured and for including the losses due to rotational magnetic reversal and the 'work hardening' during stamping, $\Delta p_{1/50}$ is the specific core loss at f = 50 Hz and B = 1 T, f is the frequency of the magnetic field, and B is the magnetic flux density.

Better results are obtained if the losses are divided into *hysteresis losses* and *eddy-current losses,* i.e.,

$$\Delta P_{Fe} = \Delta P_h + \Delta P_e = \left[k_{Feh} c_h \left(\frac{f}{50} \right) B^2 + k_{Fee} c_e \left(\frac{f}{50} \right)^2 B^2 \right] m_c \tag{2.2}$$

where k_{Feh} = 1...2, k_{Fee}= 2...3, c_h= 2...5 $Ws/\left(T^2 kg\right)$ is the hysteresis constant, and c_e = 0.5...23 $Ws^2/T^2kg)$ is the eddy-current constant. The thicker the sheet, the higher the constants c_h and c_e. Eqn (2.2) can only be used if accurate values of c_h and c_e are known.

The external surfaces of electrotechnical steel sheets are covered with a thin layer of ceramic materials or oxides to electrically insulate the adjacent laminations in a stack. This insulation limits the eddy currents induced in the core due to a.c. magnetic fluxes. The thickness of the insulation is expressed with the aid of the *stacking* factor (insulation factor):

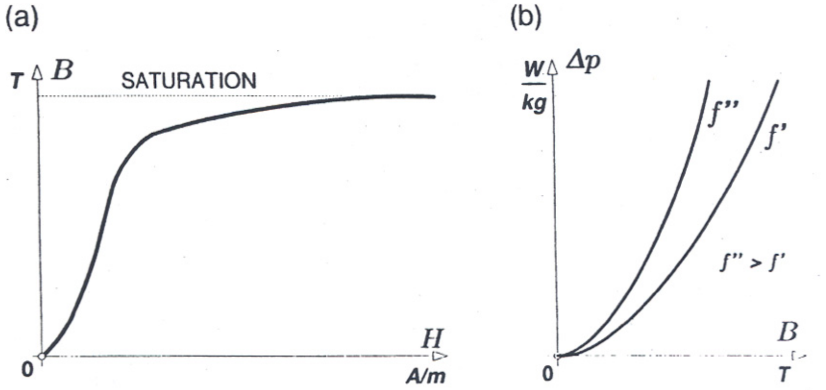

Figure 2.1 Typical characteristics of electrotechnical steel sheets: (a) magnetization curve *B-H*, (b) specific core loss curves $\Delta p - B$ at f = *const.*

$$k_i = \frac{\sum_{i=1}^{n} d_i}{\sum_{i=1}^{n} \left(d_i + 2\Delta_i \right)} < 1 \tag{2.3}$$

where d_i is the thickness of the *i*th lamination and Δ_i is the thickness of the insulation layer of the ith lamination measured on one side. For the stack consisting of laminations of equal thickness d with the thickness of the insulation layer Δ (one side), the stacking factor is

$$k_i = \frac{d}{d + 2\Delta} \tag{2.4}$$

©2002 CRC Press LLC

2.2.1 Electrotechnical Sheet-steels

Typical magnetic circuits of electrical machines and electromagnetic devices are laminated and are mainly made of *cold-rolled* electrotechnical steel sheets, i.e.,

- oriented (anisotropic) textured,
- nonoriented with silicon content,
- nonoriented without silicon.

Nowadays, *hot-rolled* electrotechnical steel sheets are almost never used. Electrotechnical steel sheets have crystal structure. *Oriented steel sheets* are used for the ferromagnetic cores of transformers, transducers and large synchronous generators. *Nonoriented steel sheets* are used for construction of large, medium, and low-power rotary electrical machines, micromachines, small transformers and reactors, electromagnets, and magnetic amplifiers. Silicon content increases the maximum magnetic permeability corresponding to critical magnetic field intensity, reduces the area of the hysteresis loop, increases the resistivity, and practically excludes the ageing (increase in the steel losses with time). Thus, owing to the silicon contents, the specific core losses are substantially reduced. On the other hand, silicon reduces somewhat the permeability in strong fields (saturation magnetic flux density) and makes the mechanical working more difficult (fast wear of the punching die). Fig. 2.1 shows a typical. magnetization curve *B-H* and specific core loss curve $\Delta p - B$ of electrotechnical steel sheets. The *B-H* curves are obtained by increasing the magnetic field intensity H from zero in a virgin sample (never magnetized before) as a set of top points of hysteresis loops. Specific core loss curves $\Delta p - B$ are measured with the aid of Epstein's apparatus. The shape of curve as that in Fig. 2.1b is only valid for steel sheets with crystal structure. Table 2.1 contains magnetization curves *B-H* and specific core loss curves $\Delta p - B$ of three types of cold-rolled, nonoriented electrotechnical steel sheets, i.e., Dk66, thickness d = 0.5 mm, k_i = 0.96, 7740 kg/m^3 (*Surahammars Bruk AB,* Sweden), H-9, d = 0.35 mm, k_i = 0.96, 7650 kg/m^3 (*Nippon Steel Corporation,* Japan) and DI-MAX EST20, d = 0.2 mm; k_i = 0.94, 7650 kg/m^3 (*Terni-Armco,* Italy).

Table 2.1 Magnetization and specific core loss characteristics of three types of cold-rolled, nonoriented electrotechnical steel sheets, i.e., Dk66, thickness 0.5 mm, k_i = 0.96 (Sweden), H-9, thickness 0.35 mm, k_i = 0.96 (Japan) and DI-MAX EST20, thickness 0.2 mm, k_i = 0.94, (Italy).

B T	H, A/m			Specific core losses $\Delta p, W/kg$				
	Dk66	H9	DI-MAX EST20	Dk66	H9		DI-MAX EST20	
				50Hz	50Hz	60Hz	50Hz	400Hz
0.1	55	13	19	0.15	0.02	0.02	0.08	0.30
0.2	65	20	28	0.24	0.06	0.10	0.15	0.70
0.4	85	30	37	0.50	0.15	0.20	0.25	2.40
0.6	110	40	48	0.90	0.35	0.45	0.42	6.00
0.8	135	55	62	1.55	0.60	0.75	0.63	
1.0	165	80	86	2.40	0.90	1.10	0.85	
1.2	220	160	152	3.30	1.30	1.65	1.25	
1.4	400	500	450	4.25	1.95	2.45	1.70	
1.5	700	1500	900	4.90	2.30	2.85	1.95	
1.6	1300	4000	2400		2.65	3.35	2.20	
1.7	4000	6500	6500					
1.8	8000	10,000	17,000					
1.9	15,000	16,000						
2.0	22,000	24,000						
2.1	35,000							

For cold-rolled electrotechnical steel sheets the stacking factor is k_i = 0.95 to 0.98, for hot-rolled sheets this factor is smaller.

©2002 CRC Press LLC

2.2.2 High-Saturation Ferromagnetic Alloys

Cobalt-iron alloys have the highest known saturation magnetic flux density. They are the natural choice for applications where mass and space saving are of prime importance. The nominal composition is up to 50% Co (cobalt), 2% V (vanadium) and the rest is Fe (iron). Curie temperature is from 940 to 980°C and specific mass density is from 7950 to 8150 kg/m^3. Cold-rolled strips are 0.1, 0.2 and 0.35 mm thick and up to 250 mm wide. Hardness is about 315 in Vicker's scale. Table 2.2 shows the magnetization characteristic *B*-*H* and specific core loss characteristics $\Delta p - B$ of cobalt alloy laminations at heat treatment temperature 920°C.

2.2.3 Permalloys

Small electrical machines and micromachines working in humid or chemical active atmospheres must have stainless ferromagnetic cores. The best corrosion-resistant ferromagnetic material is *permalloy* (Ni-Fe-Mn), but on the other hand, its saturation magnetic flux density is lower than that of electrotechnical steel sheets. Permalloy is also a good ferromagnetic material for cores of small transformers used in electronic devices and in electromagnetic A/D converters, where rectangular hysteresis loop is needed.

Table 2.2 Magnetization. curve and specific core loss curves of cobalt alloy laminations.

Magnetization curve		Specific core losses, W/kg	
Magnetic flux density, B, T	Magnetic field intensity, H, A/m	0.5mm	0.1mm
0.10	20	0.4	0.30
0.20	25	1.4	0.65
0.30	28	3.0	1.30
0.40	32	5.0	2.20
0.50	34	8.0	3.20
0.60	36	13.0	4.40
0.70	38	19.0	5.00
0.80	40	24.0	6.60
0.90	42	30.0	7.50
1.00	44	37.0	9.90
1.20	48	54.0	10.10
1.40	54	74.0	12.20
1.60	65	95.0	17.50
1.80	105	120.0	18.50
2.00	240	150.0	23.00
2.10	320		
2.20	600		
2.30	1500		
2.35	3500		
2.40	16,000		

©2002 CRC Press LLC

Table 2.3 Physical properties of iron based METGLAS amorphous alloy ribbons *(AlliedSignals, Inc., Morristown, NJ, U.S.A.).*

Quantity	2605CO	2605SAI
Saturation magnetic flux density, T	1.8	1.59 annealed 1.57 cast
Specific core losses at 50 Hz and 1 T, W/kg	less than 0.28	about 0:125
Specific density, kg/m3	7560	7200 annealed 7190 cast
Electric conductivity, S/m	0.813 x 10^6 S/m	0.769 x 10^6 S/m
Hardness in Vicker's scale	810	900
Elastic modulus, GN/m^2	100...110	100...110
Stacking factor	less than 0.75	less than 0.79
Crystallization temperature,^{0}C	430	507
Curie temperature, ^{0}C	415	392
Maximum service temperature, °C	125	150

2.2.4 Amorphous Materials

Core losses can be substantially reduced by replacing standard electrotechnical steels with *amorphous magnetic alloys.* Amorphous ferro-magnetic sheets, in comparison with electrotechnical sheets with crystal structure, do not have arranged in order, regular inner crystal structure (lattice). Table 2.3 shows physical properties and Table 2.4 shows specific core loss characteristics of commercially available iron-based METGLAS(R)[1] amorphous ribbons 2605C0 and 2605SA2 [92].

METGLAS amorphous alloy ribbons are produced by rapid solidification of molten metals at cooling rates of about 10^6 ^{0}C/s. The alloys solidify before the atoms have a chance to segregate or crystallize. The result is a metal alloy with a glass-like structure, i.e., a non-crystalline frozen liquid. METGLAS alloys for electromagnetic applications are based on alloys of iron, nickel and cobalt. Iron based alloys combine high saturation magnetic flux density with low core losses and economical price. Annealing can be used to alter *magnetostriction* to develop hysteresis loops ranging from flat to square.

Table 2.4 Specific core losses of iron based METGLAS amorphous alloy ribbons *(AlliedSignals, Inc., Morristown, NJ, U.S.A.).*

Magnetic flux density, *B* T	Specific core losses, Δp, W/kg			
	2605CO		2605SA1	
	50Hz	60Hz	50Hz	60Hz
0.05	0.0024	0.003	0.0009	0.0012
0.10	0.0071	0.009	0.0027	0.0035
0.20	0.024	0.030	0.0063	0.008
0.40	0.063	0.080	0.016	0.02
0.60	0.125	0.16	0.032	0.04
0.80	0.196	0.25	0.063	0.08
1.00	0.274	0.35	0.125	0.16

---

[1] (R) METGLAS is a registered trademark of *AlliedSignal, Inc*

Table 2.5 Magnetization curves of solid ferromagnetic materials: 1 - carbon steel (0.27%C), 2 - cast iron.

Magnetic flux density, *B*	Magnetic field intensity, *H*	
	Mild carbon steel 0.27% C	Cast iron
T	A/m	A/m
0.2	190	900
0.4	280	1600
0.6	320	3000
0.8	450	5150
1.0	900	9500
1.2	1500	18,000
1.4	3000	28,000
1.5	4500	
1.6	6600	
1.7	11,000	

Owing to very low specific core losses, amorphous alloys are ideal for power and distribution transformers, transducers, and high frequency apparatus. Application to the mass production of motors is limited by hardness, up to 1100 in Vicker's scale. Standard cutting methods as a guillotine or blank die are not suitable. The mechanically stressed amorphous material cracks. Laser and EDM cutting methods melt the amorphous material and cause undesirable crystallization. In addition, these methods make electrical contacts between laminations which contribute to the increased eddy-current and additional losses. *General Electric* cut amorphous materials in the early 1980s using chemical methods but these methods were very slow and expensive [95] Recently, the problem of cutting hard amorphous ribbons has been overcome by using a liquid jet [125]. This method makes it possible to cut amorphous materials in ambient temperature without cracking, melting, crystallization and electric contacts between isolated ribbons. The face of the cut is very smooth. It is possible to cut amorphous materials on profiles which are suitable for manufacturing laminations for rotary machines, linear machines, chokes and any other electromagnetic apparatus.

2.2.5 Solid Ferromagnetic Materials

Solid ferromagnetic materials as cast steel and cast iron are used for salient poles, pole shoes, solid rotors of special induction motors and reaction rails (platens) of linear motors. Table 2.5 shows magnetization characteristics B- H of a mild carbon steel and cast iron.

Electrical conductivities of carbon steels are from 4.5×10^6 to 7.0×10^6 S/m at 20°C.

2.2.6 Soft Magnetic Powder Composites

Powder metallurgy is used in production of ferromagnetic cores of small electrical machines or ferromagnetic cores with complicated shapes. The components of *soft magnetic powder composites* are iron powder, dielectric (epoxy resin) and filler (glass or carbon fibers) for mechanical strengthening. Powder composites can be divided into [141]:

- dielectromagnetics and magnetodielectrics,
- magnetic sinters.

Dielectromagnetics and magnetodielectrics are names referring to materials consisting of the same basic components: ferromagnetic (mostly iron powder) and dielectric (mostly epoxy resin) material [141]. The main tasks of the dielectric material is insulation and binding of ferromagnetic particles. In practice, composites containing up to 2% (of their mass) of dielectric materials are considered as *dielectromagnetics.* Those of higher content of dielectric material are considered as *magnetodielectrics*[141].

©2002 CRC Press LLC

Table 2.6 Magnetization and specific core loss characteristics of non-sintered *Accucore, Magnetics International, Inc.,* Burns Harbor, IN, U.S.A.

Magnetization curve		Specific core loss curves		
Magnetic flux density, *B*	Magnetic field intensity, *H*	60Hz	100Hz	400Hz
T	A/m	W/kg	W/kg	W/kg
0.10	152	0.132	0.242	1.058
0.20	233	0.419	0.683	3.263
0.30	312	0.772	1.323	6.217
0.40	400	1.212	2.072	9.811
0.50	498	1.742	2.976	14.088
0.60	613	2.315	3.968	18.850
0.70	749	2.954	5.071	24.295
0.80	909	3.660	6.305	30.490
0.90	1107	4.431	7.650	37.346
1.00	1357	5.247	9.039	44.489
1.10	1677	60129	10.582	52.911
1.20	2101	7.033	12.214	61.377
1.30	2687	7.981	13.845	70.151
1.40	3525	8.929	15.565	79.168
1.50	4763	9.965	17.394	90.302
1.60	6563	10.869	19.048	99.671
1.70	9035	11.707	20.635	109.880
1.75	10,746	12.125	21.407	

Magnetics International, Inc., Burns Harbor, IN, U.S.A., has recently developed a new soft powder material, *Accucore,* which is competitive to traditional steel laminations [1]. The magnetization curve and specific core loss curves of the non-sintered *Accucore* are given in Table 2.6. When sintered, *Accucore* has higher saturation magnetic flux density than the non-sintered material. The specific density is 7550 to 7700 kg/m^3.

2.3 Permanent Magnets

2.3.1 Demagnetization Curve

A *permanent magnet* (PM) can produce magnetic flux in an airgap with no exciting winding and no dissipation of electric power. As any other ferromagnetic material, a PM can be described by its B-H hysteresis loop. PMs are also called *hard magnetic materials,* which mean ferromagnetic materials with a wide hysteresis loop.

©2002 CRC Press LLC

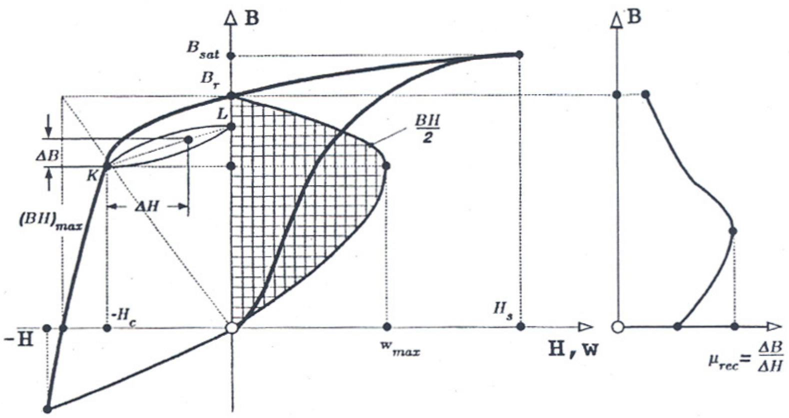

Figure 2.2 Demagnetization curve, recoil loop, energy of a PM, and recoil magnetic permeability.

The basis for the evaluation of a PM is the portion of its hysteresis loop located in the upper left-hind quadrant, called the *demagnetization curve* (Fig. 2.2). If a reverse magnetic field intensity is applied to a previously magnetized, say, toroidal specimen, the magnetic flux density drops down to the magnitude determined by the point K. When the reversal magnetic flux density is removed, the flux density returns to the point L according to a minor hysteresis loop. Thus, the application of a reverse field has reduced the *remanence,* or *remanent magnetism.* Reapplying a magnetic field intensity will again reduce the flux density, completing the minor hysteresis loop by returning the core to approximately the same value of flux density at the point K as before. The minor hysteresis loop may usually be replaced with little error by a straight line called the *recoil line.* This line has a slope called the *recoil permeability* μ_{rec} .

As long as the negative value of applied magnetic field intensity does not exceed the maximum value corresponding to the point K, the PM may be regarded as being reasonably permanent. If, however, a greater negative field intensity H is applied, the magnetic flux density will be reduced to a value lower than that at point K. On the removal of H, a new and lower recoil line will be established.

The general relationship between the magnetic flux density B, intrinsic magnetization B_{in} due to the presence of the ferromagnetic material, and magnetic field intensity H may be expressed as [85, 108]

$$B = \mu_0 H + B_{in} = \mu_0 \left(H + M \right) = \mu_0 \left(1 + \chi \right) H = \mu_0 \mu_r H \tag{2.5}$$

in which $\vec{B}, \vec{H}, \vec{B}_{in}$ and $\vec{M}$ are parallel or antiparallel vectors, so that the eqn (2.5) can be written in a scalar form. The magnetic permeability of free space μ_0 = 0.47π X 10^{-6} H/m. The relative magnetic permeability of ferromagnetic materials μ_r = 1 + χ > > 1. The magnetization vector $\vec{M}$ = χ $\vec{H}$ is proportional to the magnetic susceptibility χ of the material. The flux density μ_0 H would be present within, say, a toroid if the ferromagnetic core were not in place. The flux density B_{in} is the contribution of the ferromagnetic core.

A PM is inherently different from an electromagnet. If an external field H_a is applied to the PM, as was necessary to obtain the hysteresis loop of Fig. 2.2, the resultant magnetic field is

$$H = H_a + H_d \tag{2.6}$$

where $-H_d$ is a potential existing between the poles, 180^0 opposed to B_{in}, proportional to the intrinsic magnetization B_{in}. In a closed magnetic circuit, e.g., toroidal circuit, the magnetic field intensity resulting from the intrinsic magnetization H_d = 0. If the PM is removed from the magnetic circuit.

$$H_d = -\frac{M_b B_{in}}{\mu_0}$$

where M_b is the coefficient of demagnetization dependent on geometry of a specimen. Usually $M_b < 1$, see Appendix B.

2.3.2 Magnetic Parameters

PMs are characterized by the parameters listed below.

Remanent magnetic flux density B_r, or *remanence*, is the magnetic flux density corresponding to zero magnetic field intensity.

Coercive field strength H_c, or *coercivity*, is the value of demagnetizing field intensity necessary to bring the magnetic flux density to zero in a material previously magnetized.

Saturation magnetic flux density B_{sat} corresponds to high values of the magnetic field intensity, when an increase in the applied magnetic field produces no further effect on the magnetic flux density. In the *saturation region* the alignment of all the *magnetic moments of domains* is in the direction of the external applied magnetic field.

Recoil magnetic permeability μ_{rec} is the ratio of the magnetic flux density to magnetic field intensity at any point on the demagnetization curve, i.e.,

$$\mu_{rec} = \mu_o \mu_{rrec} = \frac{\Delta B}{\Delta H} \tag{2.8}$$

where the *relative recoil permeability* $\mu_{rrec} = 1...3.5$.

Maximum magnetic energy per unit produced by a PM in the external space is equal to the maximum magnetic energy density per volume, i.e.,

$$w_{max} = \frac{(BH)_{max}}{2} \quad J/m^3 \tag{2.9}$$

where the product $(BH)_{\max}$ corresponds to the maximum energy density point on the demagnetization curve with coordinates $B_{\max}$ and $H_{\max}$ (Fig. 2.2).

Form factor of the demagnetization curve characterizes the concave shape of the demagnetization curve, i.e.,

$$\gamma = \frac{(BH)_{max}}{B_r H_c} = \frac{B_{max} H_{max}}{B_r H_c} \tag{2.10}$$

For a square demagnetization curve $\gamma = 1$ and for a straight line (rare earth PM) $\gamma = 0.25$.

Owing to the leakage fluxes, PMs used in electrical machines are subject to non uniform demagnetization. Therefore, the demagnetization curve is not the same for the whole volume of a PM. To simplify the calculation, in general, it is assumed that the whole volume of a PM is described by one demagnetization curve with B_r and H_c about 5 to 10% lower than those for uniform magnetization.

The leakage flux causes the magnetic flux to be distributed nonuniformly along the height $2h_M$ of a PM. As a result, the MMF produced by the PM is not constant. The magnetic flux is higher in the neutral cross section and lower at the ends, but the behavior of the MMF distribution is the opposite (Fig. 2.3).

The PM surface is not equipotential. The magnetic potential at each point on the surface is a function of the distance to the neutral, zone. To simplify the calculation, the magnetic flux which is a function of the MMF distribution along the height h_M per pole is replaced by an equivalent flux. This equivalent flux goes

©2002 CRC Press LLC

through the whole height h_M and exits from the surface of the poles. To find the equivalent leakage flux and the whole flux of a PM, the equivalent magnetic field intensity needs to be found, i.e.,

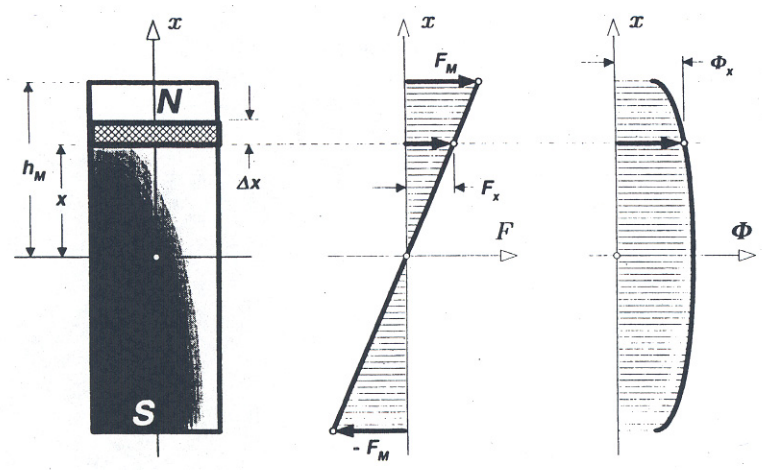

Figure 2.3 Distribution of the MMF and magnetic flux along the height h_M of a rectangular PM.

$$H = \frac{1}{h_M}\int_0^{h_M} H_x dx = \frac{F_M}{h_M} \qquad (2.11)$$

where H_x is the magnetic field intensity at a distance x from the neutral cross section and F_M is the MMF of the PM per pole (MMF = 2 F_M per pole pair).

The equivalent magnetic field intensity (2.11) allows the equivalent leakage flux of the PM to be found, i.e.,

$$\Phi_{iM} = \Phi_M - \Phi_g \qquad (2.12)$$

where Φ_M is the full equivalent flux of the PM and Φ_g is the air gap magnetic flux. The *coefficient of leakage flux* of the PM,

$$\sigma_{iM} = \frac{\Phi_M}{\Phi_g} = 1 + \frac{\Phi_{iM}}{\Phi_g} > 1 \qquad (2.13)$$

simply allows the air gap magnetic flux to be expressed as $\Phi_g = \Phi_M / \sigma_{iM}$.

The following leakage permeance expressed in the flux Φ-MMF coordinate system corresponds to the equivalent leakage flux of the PM:

$$G_{iM} = \frac{\Phi_{iM}}{F_M} \qquad (2.14)$$

An accurate estimation of the leakage permeance G_{iM} is the most difficult task in calculating magnetic circuits with PMs (Appendix A). This problem exists only in the circuital approach since using the field approach and, e.g., the finite element method (FEM) the leakage per-meance can be found fairly accurately.

©2002 CRC Press LLC

The average equivalent magnetic flux and equivalent MMF mean that the magnetic flux density and magnetic field intensity are assumed to be the same in the whole volume of a PM. The full energy produced by the magnet in the outer space is

$$W = \frac{BH}{2} V_M \qquad \text{J} \tag{2.15}$$

where V_M is the volume of the PM or a system of PMs.

2.3.3 Magnetic Flux Density in the Air gap

Let us consider a simple PM circuit with rectangular cross section consisting of a PM with height per pole , width , length , two mild steel yokes with average length and an air gap of thickness g. From the Ampere's circuital law

$$2H_M h_M = H_g g + 2H_{Fe} l_{Fe} = H_g g \left(1 + \frac{2H_{Fe} l_{Fe}}{H_g g} \right)$$

where $, H_g, H_{Fe}$ and h_M are the magnetic field intensities in the air gap, mild steel yoke, and PM, respectively. Since $\Phi_g \sigma_{iM} = \Phi_M$ or $B_g S_g = B_M S_M / \sigma_{iM}$, where B_g is the air gap magnetic flux density, B_M is the PM magnetic flux density, S_g is the cross section area of the air gap, and $S_M = w_M l_M$ is the cross section area of the PM, the following equation can be written

$$\frac{V_M}{2h_M} \frac{1}{\sigma_{iM}} B_M = \mu_o H_g \frac{V_g}{g}$$

where $V_g = S_g \; g$ is the volume of the air gap and $V_M = 2h_M \; S_M$ is the volume of the PM. The fringing flux in the air gap has been neglected. Multiplying through the equation for magnetic voltage drops and for magnetic flux, the air gap magnetic flux intensity is found as

$$B_g = \mu_o H_g = \sqrt{\frac{\mu_o}{\sigma_{iM}} \left(1 + \frac{2H_{Fe} l_{Fe}}{H_g g} \right)^{-1} \frac{V_M}{V_g} B_M H_M}$$

$$\approx \sqrt{\mu_o \frac{V_M}{V_g} B_M H_M} \tag{2.16}$$

For a PM circuit the magnetic flux density B_g in a given air gap volume V_g is directly proportional to the square root of the energy product $\left(B_M H_M \right)$ and the volume of magnet $V_M = 2h_M w_M l_M$.

Following the trend to smaller packaging, smaller mass and higher efficiency, the material research in the field of PMs has focused on finding materials with high values of the maximum energy product $(BH)_{\max}$.

The air gap magnetic flux density B_g can be estimated analytically on the basis of the demagnetization curve and air gap and leakage permeance lines and recoil lines (Appendix A). Approximately, for a LSM with armature ferromagnetic stack and surface configuration of PMs it can be found on the basis of the balance of magnetic voltage drops that

©2002 CRC Press LLC

$$\frac{B_r}{\mu o\mu_{rrec}} h_M = \frac{B_g}{\mu o\mu_{rrec}} h_M + \frac{B_g}{\mu o} g$$

where μ_{rrec} is the relative permeability of the PM (relative recoil permeability). Hence,

$$B_g = \frac{B_r h_M}{h_M + \mu_{rrec} g} \approx \frac{B_r}{1 + \mu_{rrec} g / h_M} \tag{2.17}$$

The air gap magnetic flux density is proportional to the remanent magnetic flux density B_{Υ} and decreases as the air gap g increases. Eqn (2.17) can only be used for preliminary calculations.

2.3.4 Properties of Permanent Magnets

In electric motors technology, the following PM materials are used:

- Alnico (AI, Ni, Co, Fe);
- Ferrites (ceramics), e.g., barium ferrite $\mathrm{BaO} \times 6\mathrm{Fe}_2\mathrm{O}_3$ and $\mathrm{SrO} \times 6\mathrm{Fe}_2\mathrm{O}_3$ strontium ferrite
- Rare-earth materials, i.e., samarium-cobalt SmCo and neodymium iron-boron NdFeB.

Demagnetization curves of the above PM materials are given in Fig. 2.4.

The main advantages of *Alnico* are its high magnetic remanent flux density and low temperature coefficients. The temperature coefficient of B_r is 0.02%/?C and maximum service temperature is 520°C. These advantages allow a quite high air gap flux density and high operating temperatures. Unfortunately, coercive force is very low and the demagnetization curve is extremely non-linear. Therefore, it is very easy not only to magnetize but also to demagnetize Alnico. Sometimes, Alnico PMs are protected from the armature flux, and consequently from demagnetization, using additional soft-iron pole shoes. Alnico magnets dominated the PM machines industry from the mid 1940s to about 1970 when ferrites became the most widely used materials [108].

Barium and strontium *ferrites* were invented in the 1950s. A ferrite has a higher coercive force than that of Alnico, but at the same time has a lower remanent magnetic flux density. Temperature coefficients

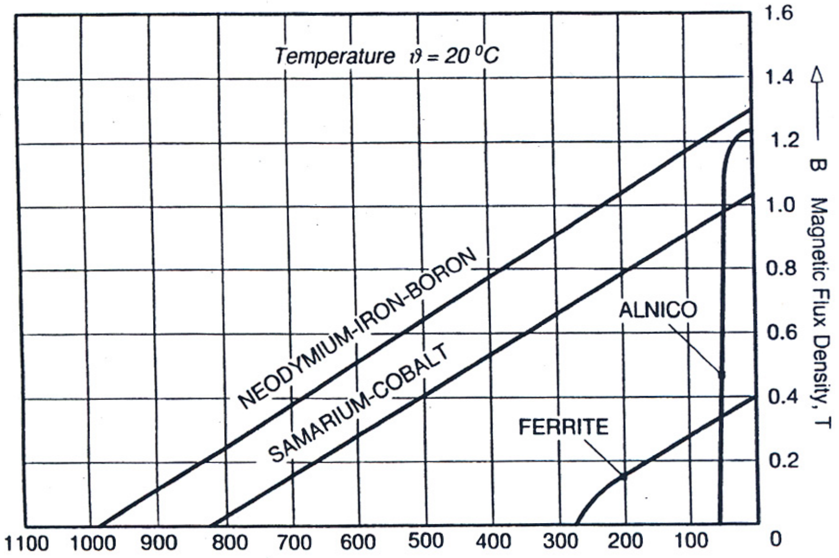

Figure 2.4 Demagnetization curves for different permanent magnet materials

©2002 CRC Press LLC

are relatively high, i.e., the coefficient of B_r is 0.20%/?C and the coefficient of is 0.27%/?C. The maximum service temperature is 400°C.The main advantages of ferrites are their low cost and very high electric resistance, which means no eddy-current losses in the PM volume. Barium ferrite PMs are commonly used in small d.c. commutator motors for automobiles (blowers, fans, windscreen wipers, pumps, etc.) and electric toys. Ferrites are produced by powder metallurgy. Their chemical formulation may be expressed as , $\mathrm{MO}\times 6(\mathrm{Fe_2O_3})$ where M is Ba, Sr, or Pb. Strontium ferrite has a higher coercive force than barium ferrite. Lead ferrite has a production disadvantage from an environmental point of view. Ferrite magnets are available in *isotropic* and *anisotropic* grades.

During the last three decades great progress regarding available energy density $(BH)_{\max}$ has been achieved with the development of *rare-earth* PMs. The rare-earth elements are in general not rare at all, but their natural minerals are widely mixed compounds. To produce one particular rare-earth metal, several others, for which no commercial application exists, have to be refined. This limits the availability of these metals. The first generation of these new alloys were invented in the 1960s and based on the composition $SmCo_5$ which has been commercially produced since the early 1970s. Today it is a well established hard magnetic material. $SmCo_5$ has the advantage of high remanent flux density, high coercive force, high energy product, linear demagnetization curve and low temperature coefficient. The temperature coefficient

Table 2.7 Magnetic characteristics of sintered NdFeB PMs manufactured in China.

Grade	Remanent magnetic flux density B_r ,T	Coercivity H_c kA/m	Intrinsic coercive force $i\,H_c$ kA/m	Maximum energy product $(BH)_{\max}$, kJ/m^3
N27	1.02...1.10	764...836	≥ 955	199...223
N30	1.08...1.15	796...860	≥ 955	223...247
N33	1.13...1.17	844...884	≥ 955	247...263
N35	1.17...1.21	876...915	≥ 955	263...286
N38	1.20...1.28	899...971	≥ 955	286...302
N27M	1.02...1.10	764...836	≥ 1194	199...223
N30M	1.08...1.15	796...860	≥ 1194	223...247
N33M	1.13...1.17	844...884	≥ 1194	247...263
N35M	1.17...1.21	876...915	≥ 1194	263...286
N27H	1.02...1.10	764...836	≥ 1353	199...223
N30H	1.08...1.15	796...860	≥ 1353	223...247.
N33H	1.13...1.17	844...884	≥ 1353	247...263
N35H	1.17...1.21	876...915	≥ 1353	263...286
N27SH	1.02...1.10	764...836	≥ 1592	199...223
N30SH	1.08...1.15	796...860	≥ 1592	223...247
N33SH	1.13...1.17	844...884	≥ 1592	247...263
N35SH	1.16...1.22	876...915	≥ 1592	263...279
N25UH	0.97...1.05	748...812	≥ 1910	183...207
N27UH	1.02...1.10	764...836	≥ 1910	199...223

©2002 CRC Press LLC

Table 2.8 Physical properties of sintered NdFeB PMs manufactured in China.

Grade	Operating temperature °C	Temperature coefficient for B_r %/°C	Curie temp. °C	Specific mass density g/cm^3	Recoil permeability
N27	≤ 80	-0.11	310	7.4...7.5	1.1
N30	≤ 80	-0.11	310	7.4...7.5	1.1
N33	≤ 80	-0.11	310	7.4...7.5	1.1
N35	≤ 80	-0.11	310	7.4...7.5	1.1
N38	≤ 80	-0.11	310	7.4...7.5	1.1
N27M	≤ 100	-0.11	320	7.4...7.5	1.1
N30M	≤ 100	-0.11	320	7.4...7.5	1.1
N33M	≤ 100	-0.11	320	7.4...7.5	1.1
N35M	≤ 100	-0.11	320	7.4...7.5	1.1
N27H	≤ 120	-0.10	340	7.4...7.5	1.1
N30H	≤ 120	-0.10	340	7.4...7.5	1.1
N33H	≤ 120	-0.10	340	7.4...7.5	1.1
N35H	≤ 120	-0.10	340	7.4...7.5	1.1
N27SH	≤ 150	-0.10	340	7.4...7.5	1.1
N30SH	≤ 150	-0.10	340	7.4...7.5	1.1
N33SH	≤ 150	-0.10	340	7.4...7.5	1.1
N35SH	≤ 150	-0.10	340	7.4...7.5	1.1
N25UH	≤ 170	-0.10	340	7.4...7.5	1.1
N27UH	≤ 170	-0.10	340		1.1

Table 2.9 Magnetic characteristics of bonded NdFeB PMs manufactured in China.

Grade	Remanent magnetic flux density B_r ,T	Coercivity H_c kA/m	Intrinsic coercive force iH_c kA/m	Maximum energy product $(BH)_{\max}$, kJ/m^3
N36G	≥ 0.70	≥ 170	≥ 210	32...40
N44Z	≥ 0.47	≥ 360	≥ 540	40...48
N52Z	≥ 0.55	≥ 360	≥ 500	48...56
N60Z	≥ 0.58	≥ 380	≥ 680	56...64
N68G	≥ 0.60	≥ 410	≥ 1120	64...72
N76Z	≥ 0.65	≥ 400	≥ 720	70...80
N84Z	≥ 0.70	≥ 450	≥ 850	80...88

Table 2.10 Physical properties of bonded NdFeB PMs manufactured in China.

Grade	Maximum Operating temperature °c	Temperature coefficient for B_{Υ} %/°c	Curie temp. °c	Specific mass density g/cm^3
N36G	70	≤ -0.13	300	6.0
N44Z	110	≤ -0.13	350	6.0
N52Z	120	≤ -0.13	350	6.0
N60Z	120	≤ -0.13	350	6.0
N68G	150	≤ -0.13	305	6.0
N76G	150	≤ -0.13	360	6.0
N48Z	150	≤ -0.13	360	6.0

©2002 CRC Press LLC

of B_{Υ} is -0.03 to -0.045%/ °C, and the temperature coefficient of H_c is -0.14 to -0.40%/ °C. Maximum service temperature is 250 to 300°C. It is well suited to build motors with low volume and consequently high specific power and low moment of inertia. The cost is the only drawback. Both Sm and Co are relatively expensive due to their supply restrictions.

With the discovery in the recent years of a second generation of rare-earth magnets on the basis of cost effective neodymium (Nd) and iron, a remarkable progress with regard to lowering raw material costs has been achieved. This new generation of rare-earth PMs was announced by *Sumitomo Special Metals,* Japan, in 1983 at the 29th Annual Conference of Magnetism and Magnetic Materials held in Pittsburg. The Nd is a much more abundant rare-earth element than Sm. NdFeB magnets, which are now produced in increasing quantities have better magnetic properties than those of SmCo, but unfortunately only at room temperature. The demagnetization curves, especially the coercive force, are strongly temperature dependent. The temperature coefficient of B_r is -0.095 to -0.15%/ °C and the temperature coefficient of H_c is -0.40 to -0.70%/ °C. The maximum service temperature is 170°C and Curie temperature is 300 to 360°C. The NdFeB is also susceptible to corrosion. NdFeB magnets have great potential for considerably improving the *performance-to-cost ratio* for many applications. For this reason they have a major impact on the development and application of PM apparatus.

According to the manufacturing processes, rare earth NdFeB PMs are classified into *sintered* PMs (Tables 2.7 and 2.8) and *bonded* PMs (Table 2.9 and 2.10).

2.4 Conductors

Armature windings of electric motors are made of solid *copper conductor wires* with round or rectangular cross sections. When the price or mass of the motor are paramount, e.g., long armature LSMs for transportation systems, magnetically levitated vehicles, hand tools, etc., *aluminum conductor wires* can be better.

The *electric conductivity* at 20°C of copper wires is 57 x 10^6 = σ_{20} = 56 x 10^6 S/m. For aluminum wires $\sigma_{20} \approx 33\text{x}10^6$ S/m. The electric conductivity is temperature dependent and up to 150°C can be expressed as

$$\sigma = \frac{\sigma_{20}}{1+\alpha\left(\theta - 20^0\right)} \tag{2.18}$$

where σ is the *temperature coefficient of electric resistance*. For copper wires σ = 0.00393 1/ °C and for aluminum wires σ = 0.00403 1/ °C.

The *maximum temperature rise* for the windings of electrical machines is determined by the temperature limits of insulating materials. The maximum temperature rise in Table 2.11 assumes that the temperature of the cooling medium $v_c \leq 40$°C. The maximum temperature of windings can be

$$v_{\max} = v_c + \Delta v \tag{2.19}$$

where Δv is the maximum temperature rise according to Table 2.11. Polyester-imide and polyamide-imide coat can provide operating temperature 200°C. The highest operating temperatures (over 600°C) can be achieved using *nickel clad copper or palladium-silver* conductor wires and ceramic insulation.

After coils are wound, they must be somehow secured in place, so as to avoid conductor movement. Two standard methods are used to secure the conductors of electrical machines in place:

- *dipping* the whole component into a varnish-like material, and then baking off its solvent,
- *trickle impregnation* method, which uses heat to cure a catalyzed resin which is dripped onto the component.

©2002 CRC Press LLC

As impregnating materials for treatment of stator or rotor windings polyester, epoxy or silicon resins are used most often. Silicon resins of high thermal endurance are able to withstand $v_{\max}$ >225°c.

Recently, a new method of conductor securing that does not require any additional material, and uses very low energy input, has emerged [84].The solid conductor wire (usually copper) is coated with a *heat and/or solvent activated adhesive.* The adhesive which is usually a polyvinyl butyral, utilizes a low temperature thermoplastic resin [84]. This means that the bonded adhesive can come apart after certain minimum temperature is reached, or it again comes in contact with the solvent. Normally this temperature is much lower than the thermal rating of the base insulation layer. The adhesive is activated by either passing the wire through a solvent while winding or heating the finished coil as a result of passing electric current through it.

Table 2.11 Maximum temperature rise Δv for armature windings of electrical machines according to IEC and NEMA (based on 40° ambient temperature).

Rated power of machines, length of core and voltage	Insulation class				
	A °c	E °c	B °c	F °c	H °c
lEC a.c. machines < 5000 kVA (resistance method)	60	75	80	100	125
lEC a.c. machines ≥ 5000 kVA or length of core ≥ 1 m (embedded detector method)	60	70	80	100	125
NEMA a.c. machines ≤1500 hp (embedded detector method)	70	-	90	115	140
NEMA a.c. machines > 1500 hp and ≤ 7 kV (embedded detector method)	65	-	85	110	135

The conductor wire with a heat activated adhesive overcoat costs more than the same class of non-bondable conductor. However, less than two second current pulse is required to bond the heat activated adhesive layer and bonding machinery costs about half as much as trickle impregnation machinery [84].

2.5 Principles of Superconductivity

In power electrical engineering *superconductivity* finds its practical application in large turbo alternators, d.c. machines, LSMs, energy storages, magnetic levitation trains, transmission cables, fault-current limiters and HTS filters. The use of superconductivity in electrical machines reduces the excitation losses, increases the magnetic flux density, eliminates ferromagnetic cores, and reduces the synchronous reactance (in synchronous machines).

The apparent electromagnetic power is proportional to electromagnetic loadings, i.e., the stator line current density and the air gap magnetic flux density. High magnetic flux density increases the output power or reduces the size of the machine.

Superconductivity was discovered in 1911 by H. Kammerlingh-Onnes when he tried to liquefy helium. The electric resistance of some metals drops to zero or becomes unmeasurably small at a temperature close to the absolute zero point, where helium liquefies.

Superconductors are able to carry a large direct current without any resistance and to exclude a static magnetic flux from its interior. The second property is known as *Meissner effect* (1933), that distinguishes a superconductor from merely being a perfect conductor (which conserves the magnetic flux in its interior). A superconductor will not allow any magnetic field to freely enter it. If a PM was placed on the top of a bulk superconductor when the superconductor was above its critical temperature, and then it was cooled down to below the critical temperature, the superconductor would then exclude the magnetic field of the PM. The PM itself is repelled and, if its weight does not exceed the repulsion force, it levitates above the superconductor.

The first satisfactory theory of superconductivity was developed in 1957 by J. Bardeen, L.N. Cooper and J.R. Schrieffer (they shared the 1972 Nobel Physics Prize).

Superconductivity takes place only when the temperature diminishes below the so-called *critical temperature* T_c which ranges from 1 to 130K. However, there are two other critical quantities to be considered: the critical magnetic flux density B_c and the critical current density J_c (Table 2.12). These critical values must not be exceeded at any case and are dependent one on the others (Fig. 2.5). When T_c J_c and B_c are exceeded, the material loses its superconductivity and generates the electrical resistance (*quench effect*). A quench is the most dangerous failure of superconducting equipment. Time dependent currents or fields cause eddy currents, hysteresis, and coupling losses. A second source of danger are *a.c. losses*. With regard to a.c. losses, it is obvious to use superconducting material first of all for d.c. windings.

Superconducting windings can replace traditional windings in power generators and large motors. The high intensity magnetic field is produced by much less electrical energy and cost. In synchronous machines superconducting windings are used as d.c. excitation windings. The excitation system does not have any ferromagnetic core because the magnetic flux density exceeds the saturation magnetic flux density of even the best ferromagnetic materials (about 2.4 T, see Table 2.2). The armature winding is made in a traditional way (copper or aluminum) as a slotless winding. The armature ferromagnetic core (external yoke) is used only to provide a magnetic shielding. Under normal operating

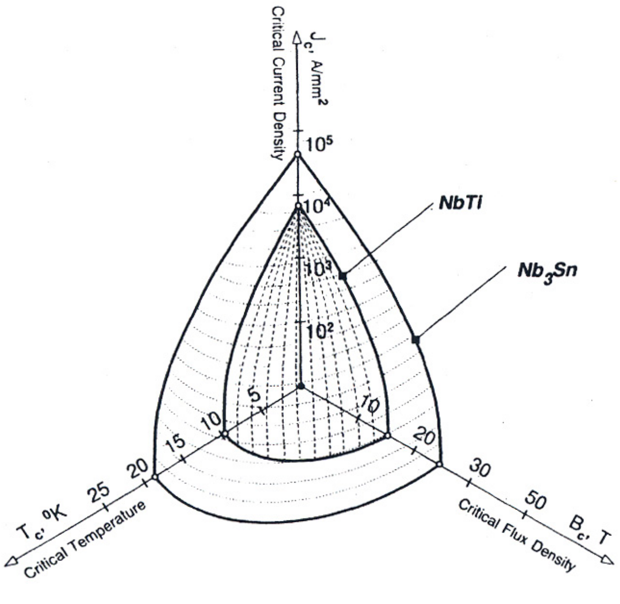

Figure 2.5 Phase space for the superconducting alloys niobium-titanium NbTi and niobium tin Nb_3Sn . The material is superconducting inside the volume of phase space indicated.

conditions the armature magnetic field is in synchronism with the field produced by the d.c. excitation system. Any unbalance in the polyphase armature winding gives rise to negative sequence currents which counterrotate at twice the synchronous speed. The armature time-varying fields of other than the synchronous frequency induce currents in the field excitation system. These currents heat the d.c. superconducting winding and structural support. This effect can be reduced if electrodynamic shields are inserted between the armature and excitation windings. In superconducting generators, there are two types of electro-dynamic shields: (a) *cold shield* (neighboring with the superconducting winding) and (b) *warm shield* (between the cold shield and air gap) which damps also mechanical oscillations.

Early superconductors were *low temperature superconductors* (LTS) with $1 \leq T_c \leq 20$ K. The LTS, e.g., NbTi (niobium-titanium) requires liquid helium cooling and its thermal margin is small, about 6 K. Thus, in synchronous generators, the shielding system must be carefully designed to minimize a.c. heating of the LTS excitation system, prevent degradation of the critical current and magnetic field capability [16].

In 1986, the first superconductor (ceramic compounds of lanthanum, barium, copper and oxygen $\mathrm{La_2 \times Ba_x CuO_o}$) with higher T_c than that for metallic superconductors was discovered by K.A. Müller and J.G. Bednorz (1987 Nobel Prize) at the IBM Research Laboratory in Zürich, Switzerland. This material becomes superconducting at 35 K and was called *high temperature superconductor* (HTC). Another team soon found superconductivity in a related material, a compound of yttrium, barium, copper and oxygen $\mathrm{YBa_2Cu_3O_7}$ at 93 K (Table 2.13), well above the temperature at which nitrogen liquefies. Liquid nitrogen is about 50 times cheaper than helium.

Table 2.12 Critical T_c, B_c, and J_c for some superconducting materials (Ba = barium, Nb = niobium, Sn = tin, Ti = tytanium, Y = ytrium).

Composition of material	T_c B_c=0, J_c=0	B_c J_c=0	J_c
NbTi	9k	12 T at 4.2 K	900 A/mm^2 at 8 T and 4.2 K
$\mathrm{Nb_3Sn}$	18k	26 T at 4.2 K	up to 1400 A/mm^2 at 11 T and 4.2 K
$\mathrm{YBa_2Cu_3O_7}$	93k	18 T at 77 K 75 T at 4.2 K	7 A/mm^2 at 0 T and 77 K

At 60 to 80 K thermal properties become more friendly and cryogenics can be 40 times more efficient than at 4.2 K. An HTS winding would be inherently more stable than an LTS winding. Operating an HTS winding in a liquid nitrogen environment would further improve the overall thermal stability. Another advantage is greater tolerance for a.c. losses because larger temperature intervals are tolerated during a.c. transients.

U.S. companies such as *Intermagnetics General Co.* and *American Superconductor Co.,* and the Japanese company *Sumitomo Electric Industries, Ltd.* are producing silver sheathed BSCCO-2223 HTS tape. The numerals indicate the number of atoms of each type in the $\mathrm{(Bi,Pb)_2\,Sr_2Ca_2Cu_3O_x}$ molecule. The best HTS winding (1997 technology), using BSCCO-2223,has demonstrated nearly 3 T magnetic flux density at 30 to 35 K [16].

2.6 Laminated Stacks

Most LSMs use laminated armature stacks with rectangular semi-open or open slots. In low-speed industrial application the frequency of the armature current is well below the power frequency 50 or 60 Hz so that from electromagnetic point of view, laminations can be thicker than 0.5

©2002 CRC Press LLC

Table 2.13 Critical T_c for high temperature cuprates and oxycarbonates

Composition of material	Critical temperature T_c K
$YBa_2Cu_3O_{7+\delta}$	93
$Hg_{0.4}CeO_5Sr_{2.5}Ca_{0.5}Cu_{2.1}O_7$	51
$Hg_{0.3}Pb_{0.7}Sr_2Ca_{0.7}Nd_{0.3}Cu_{2.1}O_7$	100
$Hg_{0.4}TI_{1.6}Ba_2Ca_2Cu_3O_{10-\delta}$	130
$Hg_{0.7}V_{0.3}Sr_{2-x}La_xCuO_{4+\delta}$	50
$Bi_{2-x}Pb_xSr_{3.5}Cu_2(CO_3)O_8$	30
$TIBa_2Sr_2Cu_2(CO_3)O_7$	62
$Bi_{0.5}Ti_{0.5}Sr_4Cu_2(CO_3)O_7$	55
$Pb_{0.5}TI_{0.5}Sr_4Cu_2(CO_3)O_7$	70
$YCaBa_4Cu_5(CO_3)_{1-x}(NO_3)_x O_{11}$	82

or 0.6 mm (typical thickness for 50 or 60 Hz, respectively). The laminations are cut to dimensions using stamping presses in mass production or laser cutting machines when making prototypes of LSMs. If the stack is thicker than 50 mm, it is recommended to group laminations into 20 to 40 mm thick packets separated by 4 to 8 mm wide longitudinal cooling ducts. Each of the two external laminations should be thicker than internal laminations to prevent the expansion (swelling) of the stack at toothed edges. The slot pitch of a flat armature core is

$$t_1 = b_{11} + c_1 = 2p\tau / z_1 \tag{2.20}$$

where b_{11} is the width of rectangular slot, c_1 is the width of tooth, $2p$ is the number of poles, τ is the pole pitch and z_1 is the number of slots totally filled with conductors. The shapes of armature slots of flat LSMs are shown in Fig. 2.6.

The laminations are kept together with the aid of seam welds (Fig.2.7), spot welds or using bolts and bars pressing the stack Fig. 2.8.

Stamping and stacking can be simplified by using rectangular laminations, as in Fig. 2.9 [136]. When making a prototype, the laminated stack of a polyphase LSM can also be assembled of E-shaped laminations, the same as those used in manufacturing small single phase transformers.

For slot less windings, armature stacks are simply made of rectangular strips of electro technical steel.

LSMs for heavy duty applications are sometimes furnished with finned heat exchangers or water-cooled cold plates which are attached to the yoke of the armature stack.

Armature stacks of tubular motors can be assembled in the following three ways by using:

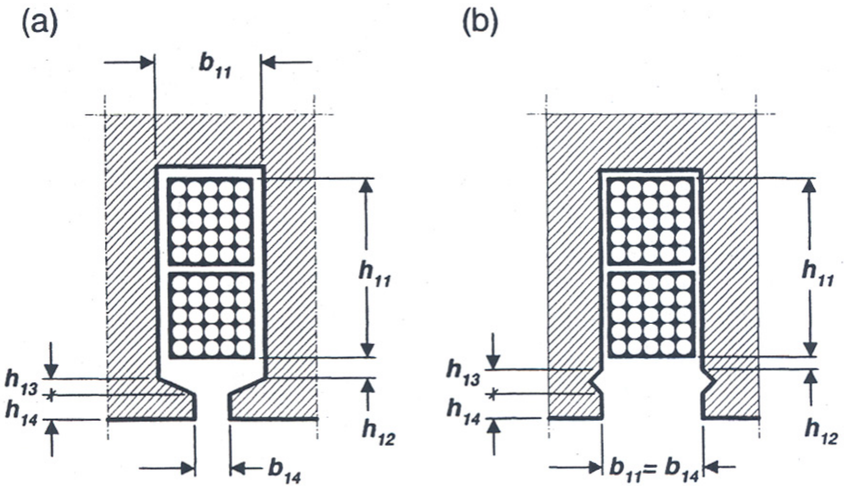

Figure 2.6 Armature slots of flat LSMs: (a) semi-open, (b) open.

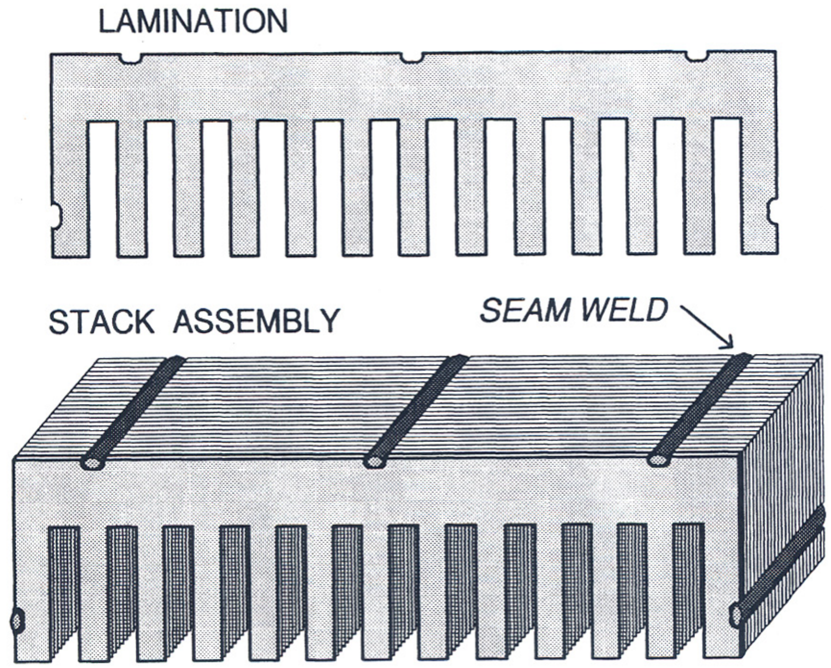

Figure 2.7 Laminated stack assembled with the aid of seam welds.

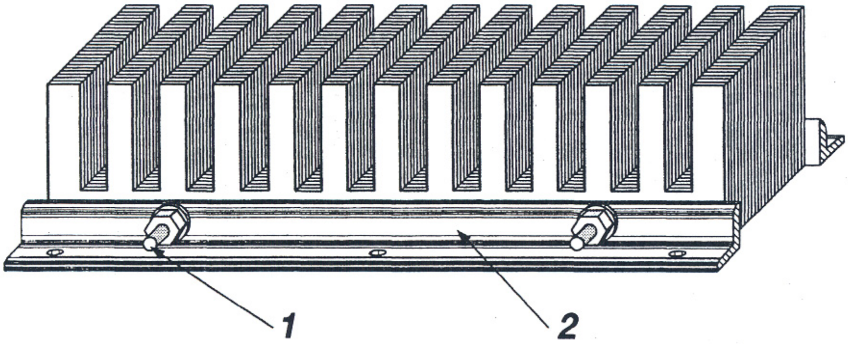

Figure 2.8 Laminated stack assembled by using: 1 - bolts, and 2 - pressing angle bars.

©2002 CRC Press LLC

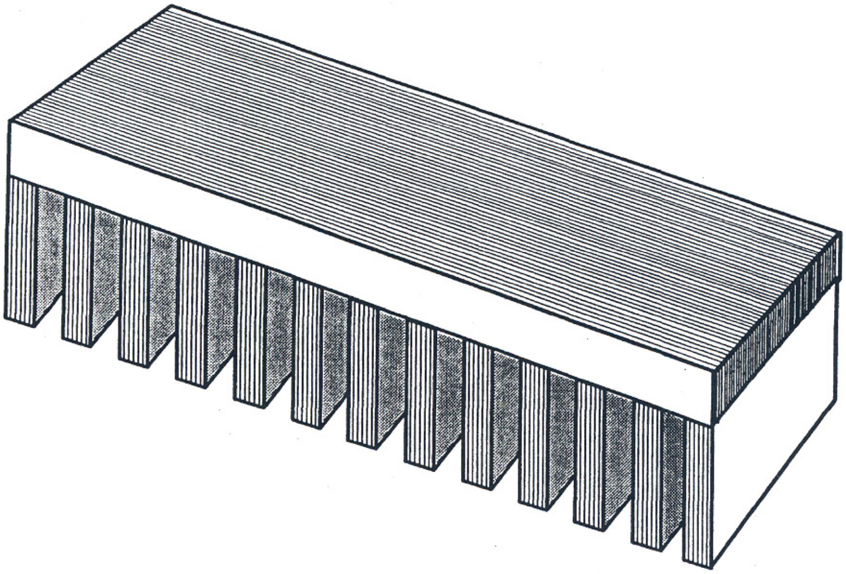

Figure 2.9 Slotted armature stack of an a.c. linear motor assembled of rectangular laminations.

- star ray arranged long flat slotted stacks of the same dimensions which embrace the excitation system;
- modules of ring laminations with inner different diameters for teeth and for slots;
- sintered powders.

The last method seems to be the best from the performance of the magnetic circuit point of view.

2.7 Armature Windings of Slotted Cores

Armature windings are usually made of insulated copper conductors. The cross section of conductors can be circular or rectangular. Some-times, to obtain a high power density, a direct water cooling system has to be used and consequently hollow conductors.

It is difficult to make and shape armature coil if the round conductor is thicker that 1.5 mm. If the current density is too high, parallel conductor wires of smaller diameter are rather recommended than one thicker wire. Armature windings can also have parallel current paths.

The armature windings can be either *single-layer or double layer*. Fig.2.10 shows a three-phase, four-pole winding configured both as double-layer and single-layer. In Fig. 2.10a the number of slots z_1 = 24 assumed for calculations is equal to the number of slots totally filled with conductors, i.e. 19 plus 50% of half filled slots, i.e., 19 + 0.5 x 10 = 24. The total number of slots is [38]:

$$z_1^{/} = \frac{1}{2p}\left(2p + \frac{w_c}{\tau}\right)z_1 = \frac{1}{4}\left(4 + \frac{5}{6}\right)24 = 29$$

where $w_c \le T$ is the coil pitch.

The resistance of a flat armature winding as a function of the winding parameters, dimensions and electric conductivity is expressed as

$$R_1 = \frac{2\left(L_i^{/} k_{1R} + l_{1e}\right) N_1}{\sigma s_1 a_p a} \qquad (2.21)$$

©2002 CRC Press LLC

where N_1 is the number of series turns per phase, L'_i is the length of the laminated stack including cooling ducts, l_{1e} is the average length of a single end connection, k_{1R} is the skin effect coefficient (k_{1R} ˜ 1for round conductors with diameter less than 1 mm), σ is the electric conductivity of the conductor at the operating temperature - eqn (2.18), s_1 is the cross section of the armature conductor wire, a_p is the number of parallel conductors and a is the number of parallel current paths. For tubular LSMs l_{1e} = 0 and 2 L'_i in the numerator should be replaced by an average

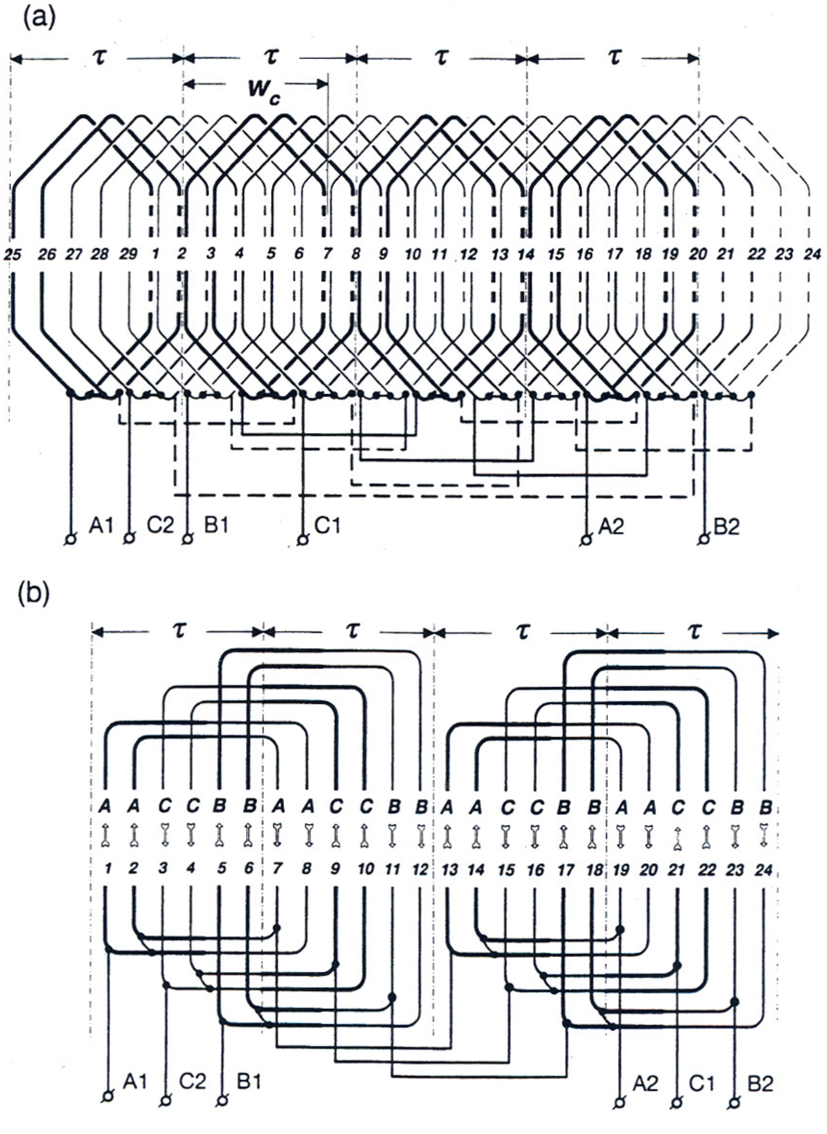

Figure 2.10 Three-phase, four-pole (2p = 4) full pitch windings of a LSM distributed in 24 slots totally filled with conductors: (a) double-layer winding, (b) single-layer winding.

length of turn $l_{1av} = \pi\left(D_{1in} + h_1\right)l_{1av} = \pi\left(D_{1out} - h_1\right)$, where h_1 is the height of the concentrated primary coil, D_{1in} is the inner diameter of the armature stack and D_{1out} is the outer diameter of the armature stack.

©2002 CRC Press LLC

A more accurate method of calculating the armature resistance of a tubular a.c. linear motor is given below. For a ring-shaped coil consisting of n layers of rectangular conductor with its height $h_{wir} = h_1/\mathrm{n}$, the length of the conductor per coil is expressed by the following arithmetic series

$$
\begin{aligned}
&2\pi(r+h_{wir})+2\pi(r+2h_{wir})+2\pi(r+3h_{wir})+\ldots+2\pi(r+nh_{wir})\\
&=2\pi rn+2\pi(h_{wir}+2h_{wir}+3h_{wir}+\ldots+nh_{wir})\\
&=2\pi n\left(r+h_{wir}\frac{1+n}{2}\right)
\end{aligned}
$$

where the sum of the arithmetic series is $S_n = n(a_1 + a_n)/2$, the first term $a_1 = h_{wir}$, the last term $a_n = nh_{wir}$ and the inner radius of the coil is

$$
r = \frac{D_{1in} + 2(h_{14} + h_{13} + h_{12})}{2} \qquad (2.22)
$$

where h_{14} is the slot opening, h_{13} and h_{12} are dimensions according to Fig. 2.6. For the whole phase winding the length of the conductor per phase is

$$
\frac{z_1}{m_1}2\pi n\left(r+h_{wir}\frac{1+n}{2}\right)
$$

where z_1 is the number of the primary slots and $\frac{z_1}{m_1}$ is the number of cylindrical coils per phase in the case of an m_1 phase winding. The resistance of the primary winding per phase is

$$
R_1 = \frac{Z_1}{m_1}\pi\frac{N_{sl}}{a_p}\left[D_{1in} + 2(h_{14}+h_{13}+h_{12}) + h_{wir}\left(1+\frac{N_{sl}}{a_p}\right)\right]\times\frac{k_{1R}}{\sigma h_{wir}b_{wir}a_p a} \qquad (2.23)
$$

where h_{wir} is the height of the rectangular conductor, b_{wir} is the width of the conductor, σ is the electric conductivity of the conductor, N_{sl} is the number of conductors per slot, a_p is the number of parallel wires and $n = \frac{N_{sl}}{a_p}$ provided that parallel wires are located beside each other and a is the number of parallel current paths. It is recommended to multiply the cross section area of the conductor in the denominator by a factor 0.92 to 0.99 to take into account round corners of rectangular conductors. The bigger the cross section of the conductor, the bigger the factor including round corners. Eqn. (2.23) should always be adjusted to the arrangement of conductor wires in slots.

The armature leakage reactance is the sum of the slot leakage reactance X_{1s}, the end connection leakage reactance X_{1e}, and the differential leakage reactance X_{1d} (for higher space harmonics), i.e.,

$$
X_1 = X_{1s} + X_{1e} + X_{1d} = 4\pi f\mu_0\frac{L_i(N_1)^2}{pq_1}\left(\lambda_{1s}k_{1X} + \frac{l_{1e}}{L_i}\lambda_{1e} + \lambda_{1d}\right) \qquad (2.24)
$$

where N_1 is the number of turns per phase, k_{1X} is the skin-effect coefficient for leakage reactance, p is the number of pole pairs, $q_1 = z_1/(2pm_1)$ is the number of primary slots z_1 per pole per phase, l_{1e} is the length of the primary winding end connection, λ_{1s} is the coefficient of the slot leakage permeance (slot-specific permeance), λ_{1e} is the coefficient of the end connection leakage permeance, and λ_{1d} is the coefficient of the differential leakage. For a tubular LSM $\lambda_{1e} = 0$ and Li should be replaced by $L_i = \pi(D_{1in} + h_1)$ or $L_i = \pi(D_{1out} - h_1)$ There is no leakage flux about the end connections as they do not exist in tubular LIMs.

The coefficients of leakage permeances of the slots shown in Fig. 2.6 are:

©2002 CRC Press LLC

- for a semi-open slot (Fig. 26a):

$$\lambda_{1s} = \frac{h_{11}}{3b_{11}} + \frac{h_{12}}{b_{11}} + \frac{2h_{13}}{b_{11} + b_{14}} + \frac{h_{14}}{b_{14}} \tag{2.25}$$

- for an open slot (Fig. 2.6b) :

$$\lambda_{1s} \approx \frac{h_{11}}{3b_{11}} + \frac{h_{12} + h_{13} + h_{14}}{b_{11}} \tag{2.26}$$

The above specific-slot permeances are for single-layer windings. To obtain the specific permeances of slots containing double-layer windings, it is necessary to multiply eqns (2.25) and (2.26) by the factor

$$\frac{3w_c / \tau + 1}{4} \tag{2.27}$$

Such an approach is justified if $2/3 \leq w_c / \tau \leq 1.0$.

The specific permeance of the end connection (overhang) is estimated on the basis of experiments. For double-layer, low-voltage, small- and medium-power motors:

$$\lambda_{1e} \approx 0.34 q_1 \left(1 - \frac{2}{\pi}\frac{w_c}{l_{1e}}\right) \tag{2.28}$$

where l_{1e} is the length of a single end connection. Putting $\frac{w_c}{l_{1e}}$ = 0.64, eqn (2.28) also gives good results for single-layer windings, i.e.,

$$\lambda_{1e} \approx 0.2 q_1 \tag{2.29}$$

For double-layer, high-voltage windings,

$$\lambda_{1e} \approx 0.42 q_1 \left(1 - \frac{2}{\pi}\frac{w_c}{l_{1e}}\right) k^2{}_{w1} \tag{2.30}$$

where the armature winding factor for the fundamental space harmonic ν=1is

$$k_{w1} = k_{d1} k_{p1} \tag{2.31}$$

$$k_{d1} = \frac{\sin\left[\pi/(2m_1)\right]}{q_1 \sin\left[\pi/(2m_1 q_1)\right]} \tag{2.32}$$

$$k_{p1} = \sin\left(\frac{\pi}{2}\frac{w_c}{\tau}\right) \tag{2.33}$$

In general ,

$$\lambda_{1e} \approx 0.3 q_1 \tag{2.34}$$

for most of the windings.

The specific permeance of the differential leakage flux is

$$\lambda_{1d} = \frac{m_1 q_1 \tau k^2{}_{w1}}{\pi^2 g k_{c1} k_{sat}} \tau_{d1} \tag{2.35}$$

where the Carter's coefficient including the effect of slotting of the armature stack

$$k_{C1} = \frac{t_1}{t_1 - \gamma_1 g} \tag{2.36}$$

$$\gamma_1 = \frac{4}{\pi}\left[\frac{b_{14}}{2g}\arctan\frac{b_{14}}{2g} - \ln\sqrt{1+\left(\frac{b_{14}}{2g}\right)^2}\right] \tag{2.37}$$

and the differential leakage factor τ_{d1} is

$$\tau_{d1} = \frac{1}{k^2_{w1}}\sum_{v>1}\left(\frac{k_{w1v}}{v}\right)^2 \tag{2.38}$$

where k_{w1v} is the winding factor for $v > 1$. The curves of the differential leakage factor τ_{d1} are given in publications dealing with design of induction motors, e.g., [38, 40, 50, 70].

The specific permeance between the heads of teeth:

$$\lambda_{1t} \approx \frac{5g_t/b_{14}}{5 + 4g_t/b_{14}} \tag{2.39}$$

should be added to the differential specific permeance λ_{1d} .

Armature windings of long armature, large power LSMs can be made of a cable. For example, German *Transrapid* maglev guideway uses a multistrand very soft aluminum conductor of 300 mm^2 cross section. The insulation consists of a synthetic elastometer with small dielectric losses. Inner and outer conductive films limit the electric field to the space of the insulation. The cable has a conductive sheath, also consisting of an elastometer mixture, for an external protection and electric shielding.

2.8 Slotless Armature Systems

Slotless windings of LSMs for industrial applications can uniformly be distributed on the active surface of the armature core or designed as moving coils without any ferromagnetic stack (air-cored armature). In both cases the slotless coils can be wound using insulated conductors with round or rectangular cross section or insulated foil. Fig. 2.11 shows a double sided PM linear brush less motor with moving inner coil manufactured by *Trilogy Systems* , Webster, TX, U.S.A. [132]. A heavy duty conductor wire with high temperature insulation is used. To improve heat removal, *Trilogy Systems* forms the winding wire during fabrication into a planar surface at the interface with the aluminum attachment bar (U.S. Patent No. RE34674). The interface between the winding planar surface and the aluminum flat surface maximizes heat transfer. Once heat is transferred into the attachment bar, it is still important to provide adequate surface area in the carriage assembly to reject the heat. The use of thermal grease on the coil mounting surface is recommended.

A large power PM LSM with coreless armature and slotless winding has been proposed for a wheel-on-rail high speed train [90]. There is a long vertical armature system in the center of the track and train mounted double sided PM excitation system.

High speed maglev trains with superconducting electromagnets use ground coreless armature windings fixed to or integrated with concrete slabs. A coreless three phase slotless winding is designed as a double layer winding [126]. The U-shaped guideway of Yamanashi Maglev Test Line (Japan) has two three phase armature windings mounted on two opposite vertical walls of the guideway (Table 2.14). The on-board excitation system for both the LSM and electrodynamic levitation is provided by superconducting electromagnets located on both sides of the vehicle.

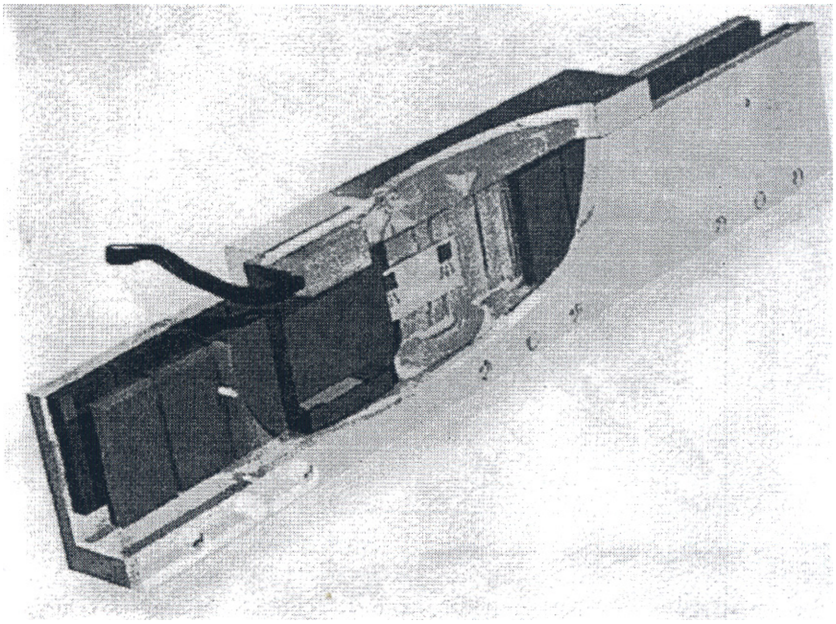

Figure 2.11 Flat double-sided PM LBM with inner moving coil. Photo courtesy of *Trilogy Systems Corporation*, Webster, TX, U.S.A.

Table 2.14 Specifications of three phase armature propulsion winding of superconducting LSM on Yamanashi Maglev Test Line.

Length × width of a coil, m	1.42 x 0.6
Coil pitch, m	0.9
Number of layers	2
Number of turns for the Northern Line	8 (front layer) 10 (back layer)
Number of turns for the Southern Line	7 (front layer) 8 (back layer)
Rated voltage, kV	22 Northern Line 11 Southern Line
Conductor	Al

©2002 CRC Press LLC

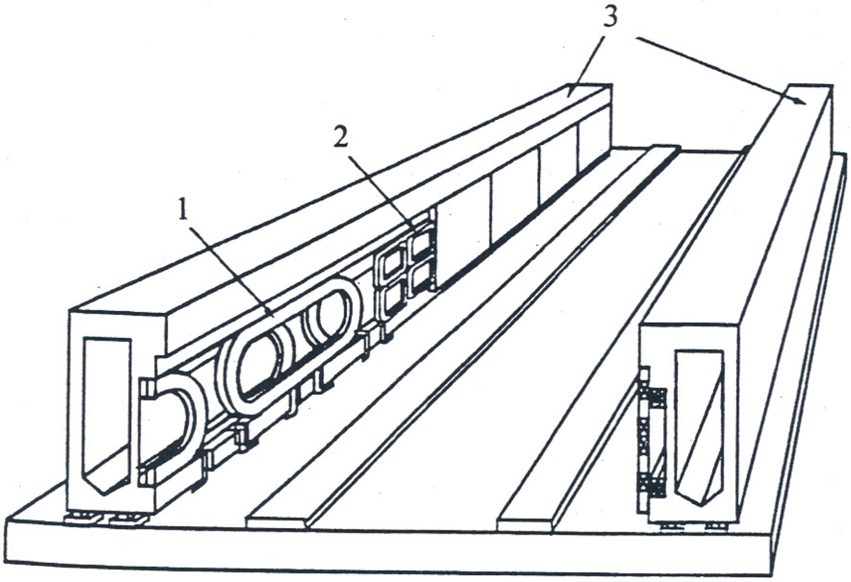

Figure 2.12 Side-wall beam type guideway of Yamansahi Maglev Test Line: 1 - armature (propulsion) winding, 2 - levitation and guidance coil, 3 - twin beams. Courtesy of *Central Japan Railway Company* and *Railway Technical Research Institute*, Tokyo, Japan.

Guideways of Yamanashi Maglev Test Line are classified according to the structure and characteristics of the side wall to which the winding is attached [145]:

(a) panel type;
(b) side-wall beam type (Fig. 2.12);
(c) direct attachment type.

Panel type windings are produced in the on-site manufacturing yards. Coils are attached to the side of the reinforced concrete panel. The panel is attached to the cast-in-place concrete side walls with the aid of bolts. This type is applied to the elevated bridges and high-speed sections.

A side-wall beam shown in Fig. 2.12 is a box type girder. Styrofoam is embedded in hollow box type beam to reduce the mass and facilitate the construction. Ground coils are attached to the beam in the manufacturing yard. The beam is then transported to the site and erected on the pre-produced support. This type is also applied to elevated bridges and high speed sections.

In the direct attachment type guideway the coils of the winding are attached direct to the side wall of a cast-in-place reinforced concrete

©2002 CRC Press LLC

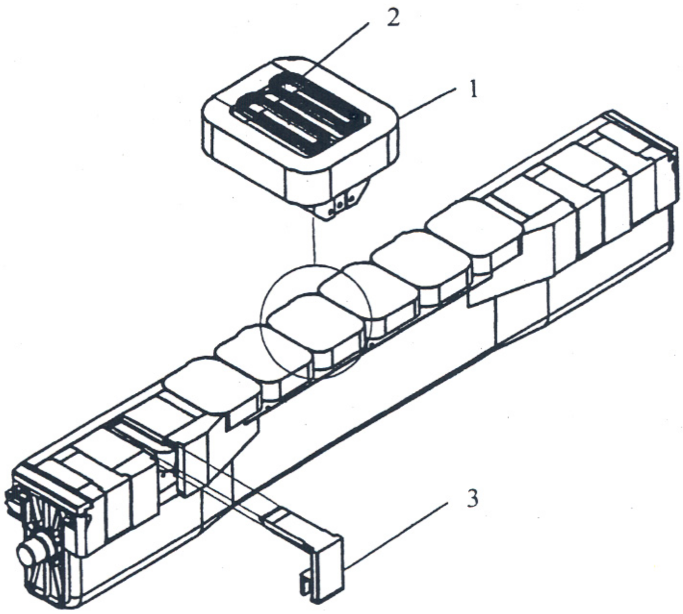

Figure 2.13 Electromagnetic excitation system with salient poles of *Transrapid* maglev vehicle: 1 - d.c. excitation winding, 2 - linear generator winding, 3 - airgap sensor. Courtesy of *Thyssen Transrapid System, GmbH*, München, Germany.

structure. This type, unlike the panel or side-wall beam type, cannot respond to structural displacements [145]. The direct attachment guidaway is applied mainly to tunnel sections situated on solid ground.

The resistance of the slotless armature winding can be calculated using eqn (2.21). It is recommended to use the finite element method (FEM) for calculating the inductance.

2.9 Electromagnetic Excitation Systems

Electromagnetic excitation systems, i.e., salient ferromagnetic poles with d .c. winding are used in large power LSMs. For example, German *Transrapid* system has on board mounted electromagnets (Fig. 2.13) which are used both for propulsion (excitation system of the LSM) and electromagnetic levitation (attraction forces). Electromagnet modules are approximately 3 m long [140]. There are twelve poles per one module. To deliver electric power to the vehicle, linear generator windings are integrated with each excitation pole. Electromagnet modules are fixed to the levitation frame with the aid of maintenance-free joints. The necessary freedom of movement is obtained by the use of vibration damping elastic bearings.

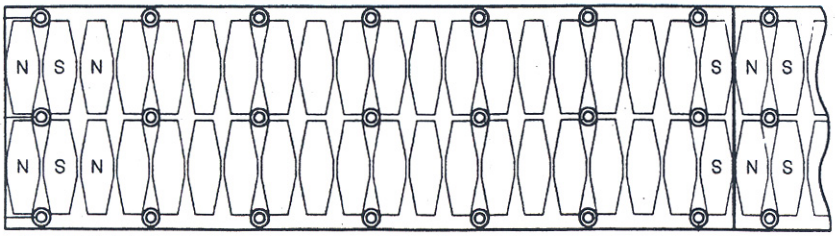

Figure 2.14 Hexagonal assembly of PMs of LBM. Courtesy of *Anorad Corporation*, Hauppauge, NY, U.S.A.

©2002 CRC Press LLC

Table 2.15 Specifications of superconducting electromagnet of MLX01 vehicle.

Length of four pole unit, m	5.32
Length of electromagnet, m	1.07
Height of electromagnet, m	0.5
Mass, kg	1500
Pole pitch, m	1.35
Number of coils	4
Magnetomotive force, kA	700
Maximum magnetic flux density, T	approx 4.23
Levitation force per electromagnet	115.5 k N
Refrigeration capacity	8 W at 4.3 K

2.10 Permanent Magnet Excitation Systems

To minimize the thrust ripple in LSMs or LBMs with slotted armature stack, PMs need to be skewed. The *skew* is approximately equal to one tooth pitch of the armature - eqn (2.20). Instead of skewed assembly (Fig. 1.7) of rectangular PMs, *Anorad Corporation* proposes to use hexagonal PMs, the symmetry axis of which is perpendicular to the direction of motion (Fig. 2.14) [8].

There are practically no power losses in PM excitation systems which do not require any forced cooling or heat exchangers.

2.11 Superconducting Excitation Systems

Superconducting excitation systems are recommended for high power LSMs which can be used in high speed electrodynamic levitation transport.

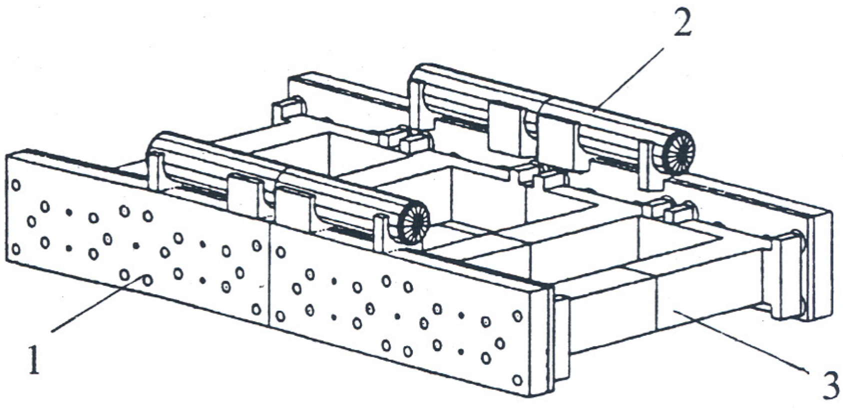

Figure 2.15 MLXO1 superconducting electromagnet and bogie frame. 1 – superconducting electromagnet, 2 - tank, 3 - bogie frame. Courtesy of *Central Japan Railway Company* and *Railway Technical Research Institute*, Tokyo, Japan.

©2002 CRC Press LLC

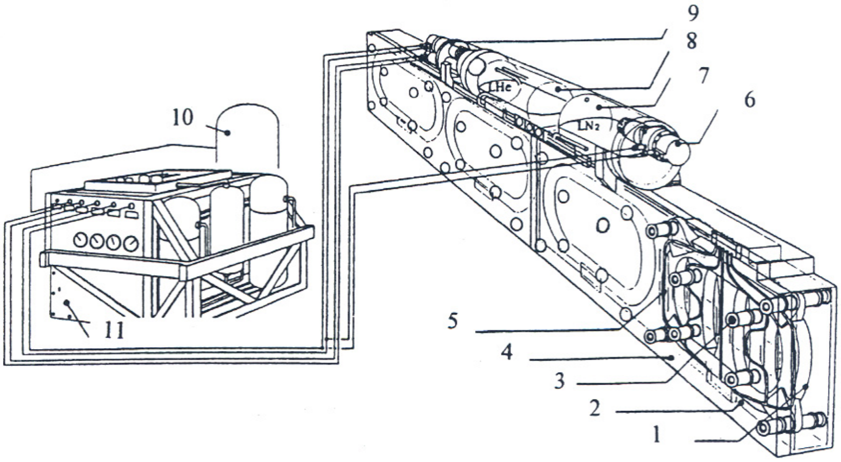

Figure 2.16 Structure of the MLXO1 superconducting electromagnet and on-board refrigeration system: 1 - superconducting winding (inner vessel), 2 - radiation shield plate, 3 - support, 4 - outer vessel, 5 - cooling pipe, 6 - 80 K refrigerator, 7 - liquid nitrogen reservoir, 8 - liquid helium reservoir, 9 - 4 K refrigerator, 10 - gaseous helium buffer tank, 11 – compressor unit. Courtesy of *Central Japan Railway Company* and *Railway Technical Research Institute*, Tokyo, Japan.

In 1972, an experimental superconducting maglev test vehicle ML100 was built in Japan. Since 1977, when Miyazaki Maglev Test Center on Kyushu Island opened, maglev vehicles ML and MLU with superconducting LSMs and electrodynamic suspension systems have been systematically tested. Air-cored armature winding has been installed in the form of a guideway on the ground. In 1990, a new 18.4 km Yamanashi Maglev Test Line (near Mount Fuji) for electrodynamic levitation vehicles with superconducting LSMs was constructed. In 1993, a test run of MLU002N (Miyazaki) started and since 1995 vehicles MLX01 (Yamanashi) have been tested.

Fig. 2.15 shows the bogie frame and Fig. 2.16 shows the structure of the superconducting electromagnet manufactured by *Toshiba, Hitachi* and *Mitsubishi* of the MLX01 vehicle. The bogie frame (*Sumitomo Heavy Industries*) is laid under the vehicle body. The superconducting electromagnet (Table 2.15) is wound with a superconducting wire and enclosed by and integrated with a stainless inner vessel (Fig. 2.16). The winding is made of *niobium-titanium alloy* wire which is embedded in a *copper matrix* in order to improve the stability of superconductivity. Permanent flow of current without losses is achieved by keeping the coils within a cryogenic temperature range using *liquid helium* (4.2 K or -269°C). The inner vessel is covered with a radiation shield plate on which a cooling pipe is crawled and liquid nitrogen is circulated inside the pipe to eliminate the radiation heat [133]. The shield plate is kept at liquid nitrogen temperature the boiling point of which is about 77 K.

These components are covered with an outer aluminum vacuum vessel (room temperature) and an insulating material which is packed in the space between the inner vessel and outer vessel [133]. The space is maintained in a high vacuum range to prolong the life of insulation. There are four sets of inner vessel (superconducting electromagnet) per one outer vessel. The on-board 4 K Gifford-McMahon/Joule-Thomson refrigerator for helium, 80 K Gifford-McMahon refrigerator for nitrogen, liquid helium reservoir and liquid nitrogen reservoir are incorporated inside the tank on the top of the outer vessel. This refrigerator re-liquefies the helium gas evaporated as a result of the heat generation inside the superconducting electromagnet. For commercial use, electro-magnets should be operated with no supply of both liquid

©2002 CRC Press LLC

helium and liquid nitrogen. The necessary equipment such as the compressor which supplies the compressed gas to the helium refrigerator and control units for operation of superconducting electromagnets are located inside the bogie.

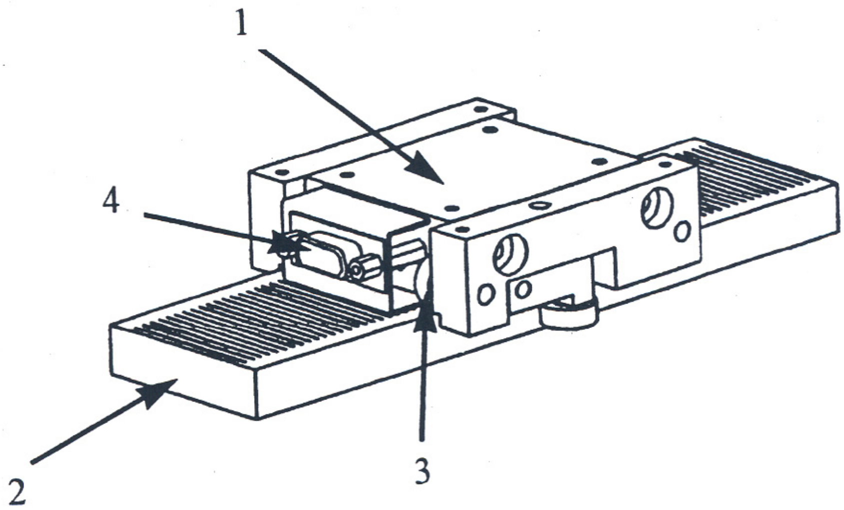

Figure 2.17 PM HLSM. 1 - forcer, 2 - platen, 3 - mechanical or air bearing, 4 - umbilical cable with power and air hose. Courtesy of *Normag Northern Magnetics Inc*., Santa Clarita, CA, U.S.A.

2.12 Hybrid Linear Stepping Motors

The PM HLSM manufactured by *Normag Northern Magnetics, Inc.,* Santa Clarita, CA, U.S.A. is shown in Fig. 2.17 [105].

Magnetic circuits of forcers of HLSMs are made of high permeable electrotechnical steels. The thickness of lamination is about 0.2 mm as the input frequency is high. Forcers are designed as symmetrical, i.e. with the PM joining the two stacks (Fig. 2.18a) or two PMs (Fig. 1.17) or asymmetrical, i.e., with PM located in one stack (Fig. 2.18b) designs. Asymmetrical design is easier for assembly.

©2002 CRC Press LLC

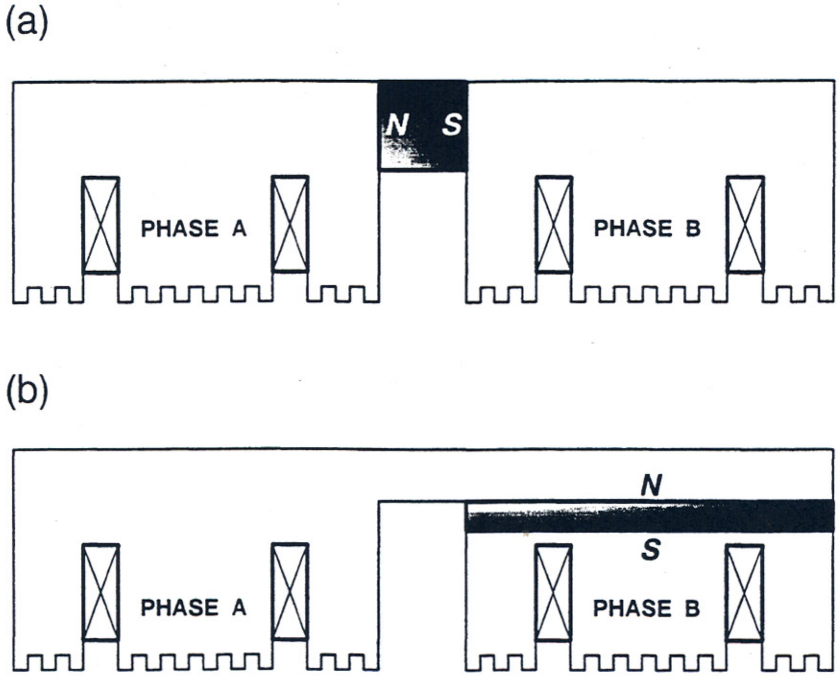

Figure 2.18 Longitudinal sections of forcers of HLSMs: (a) symmetrical forcer, (b) asymmetrical forcer.

©2002 CRC Press LLC

chapter 3

Theory of Linear Synchronous Motors

3.1 Permanent Magnet Synchronous Motors

3.1.1 Magnetic Field of the Armature Winding

The *time-space distribution of the MMF* of a symmetrical polyphase winding with distributed parameters fed with a balanced system of currents can be expressed as

$$\begin{aligned}F(x,t) &= \frac{N_1\sqrt{2}I_a}{\pi p}\sin\omega t\sum_{v=1}^{\infty}\frac{1}{v}k_{\omega 1v}\cos\left(v\frac{\pi}{\tau}x\right)\\&+\frac{N_1\sqrt{2}I_a}{\pi p}\sin\left(\omega t-\frac{1}{m_1}2\pi\right)\sum_{v=1}^{\infty}\frac{1}{v}k_{\omega 1v}\cos v\left(\frac{\pi}{\tau}x-\frac{1}{m_1}2\pi\right)+\ldots\\&+\frac{N_1\sqrt{2}I_a}{\pi p}\sin\left(\omega t-\frac{m_1-1}{m_1}2\pi\right)\sum_{v=1}^{\infty}\frac{1}{v}k_{w1v}\cos v\left(\frac{\pi}{\tau}x-\frac{m_1-1}{m_1}2\pi\right)\\&=\frac{1}{2}\sum_{v=1}^{\infty}F_{mv}\{\sin\left[\left(\omega t-v\frac{\pi}{\tau}x\right)+(v-1)\frac{2\pi}{m_1}\right]\\&+\sin\left[\left(\omega t+v\frac{\pi}{\tau}x\right)-(v-1)\frac{2\pi}{m_1}\right]\}\end{aligned}$$

where I_a is the armature phase current, m_1 is the number of phases, P is the number of pole pairs, N_1 is the number of series turns per phase, $k_{\omega 1v}$ is the winding factor, $\omega = 2\pi f$ is the angular frequency, τ is the pole pitch and

- for the forward-travelling field

$$v = 2m_1k + 1 \qquad k = 0,1,2,3,4,5,\ldots \tag{3.2}$$

- for the backward travelling field

$$v = 2m_1k - 1 \qquad k = 0,1,2,3,4,5,\ldots \tag{3.3}$$

The magnitude of the v harmonics of the primary MMF is

$$F_{mv} = \frac{2m_1\sqrt{2}}{\pi p}N_1 I_a\frac{1}{v}k_{w1v} = m_1\left[F_{mv}\right]m_1 = 1 \tag{3.4}$$

The winding factor for the v space harmonic is the product of the distribution factor, k_{d1v}, and pitch factor, k_{p1v}, i.e.,

©2000 CRC Press LLC

$$k_{w1v} = k_{d1v} k_{p1v} \tag{3.5}$$

$$k_{d1v} = \frac{\sin\left[v\pi/(2m_1)\right]}{q_1 \sin\left[v\pi/(2m_1 q_1)\right]} \tag{3.6}$$

$$k_{p1v} = \sin\left(v \frac{\pi}{\tau} \frac{\omega_c}{2}\right) \tag{3.7}$$

Assuming that $\omega t \mp v\pi x/\tau = 0$ the *linear synchronous speed* of the vth harmonic wave of the MMF is

$$v_{sv} = \mp 2 f \tau \frac{1}{v} \tag{3.8}$$

For a three-phase winding the time space distribution of the MMF is

$$F(x,t) = \frac{1}{2}\sum_{v=1}^{\infty} F_{mv} \{\sin\left[\left(\omega t - v\frac{\pi}{\tau}x\right) + (v-1)\frac{2\pi}{3}\right]$$

$$+ \sin\left[\left(\omega t + v\frac{\pi}{\tau}x\right) - (v+1)\frac{2\pi}{3}\right]\} \tag{3.9}$$

For a three-phase winding and the fundamental harmonic $v = 1$

$$F(x,t) = \frac{1}{2} F_m \sin\left(\omega t - \frac{\pi}{\tau}x\right) \tag{3.10}$$

$$F_m = \frac{2m_1\sqrt{2}}{\pi p} N_1 I_a k_{\omega 1} \approx 0.9 \frac{m_1 N_1 k_{\omega 1}}{p} I_a \tag{3.11}$$

the winding factor $k_{\omega 1} = k_{d1} k_{p1}$ is given by eqns (2.31), (2.32) and (2.33) and $v_s = v_{sv=1}$ is according to eqn (1.1).

The peak value of the armature line current density or *specific electric loading* is defined as the number of conductors in all phases $2m_1 N_1$ times the peak armature current $\sqrt{2} I_a$ divided by the armature stack length $2p\tau$, i.e.,

$$A_m = \frac{m_1 \sqrt{2} N_1 I_a}{p\tau} \tag{3.12}$$

3.1.2 Form Factors and Reaction Factors

The *form factor of the excitation field* is defined as the ratio of the *amplitude of the first harmonic-to-maximum value of the airgap magnetic flux density,* i.e.,

$$k_f = \frac{B_{mg1}}{B_{mg}} = \frac{4}{\pi} \sin\frac{\alpha_i \pi}{2} \tag{3.13}$$

where α_i is the *pole-shoe* b_p *-to-pole pitch* τ ratio, i.e.,

©2000 CRC Press LLC

$$\alpha_i = \frac{b_p}{\tau} \tag{3.14}$$

The *form factors of the armature reaction* are defined as the ratios of the *first harmonic amplitudes-to-maximum values of normal components of armature reaction magnetic flux densities* in the *d*-axis and *q*-axis, respectively, i.e.

$$k_{fd} = \frac{B_{ad1}}{B_{ad}} \qquad k_{fq} = \frac{B_{aq1}}{B_{aq}} \tag{3.15}$$

The peak values of the first harmonics B_{ad1} and B_{aq1} of the armature magnetic flux density can be calculated as coefficients of Fourier series for $\nu = 1$ i.e.,

$$B_{ad1} = \frac{4}{\pi}\int_0^{0.5\pi} B(x)\cos x dx \tag{3.16}$$

$$B_{aq1} = \frac{4}{\pi}\int_0^{0.5\pi} B(x)\sin x dx \tag{3.17}$$

For a salient-pole motor with electromagnetic excitation and the airgap $g \approx 0$ (fringing effects neglected), the *d*- and *q*-axis form factors of the armature reaction are

$$k_{fd} = \frac{\alpha_i\pi + \sin\alpha_i\pi}{\pi} \qquad k_{fq} = \frac{\alpha_i\pi - \sin\alpha_i\pi}{\pi} \tag{3.18}$$

For PM excitation systems the form factors of the armature reaction are [42]:

Table 3.1 Factors k_f, k_{fd}, k_{fq}, k_{ad} and k_{aq}, for salient-pole synchronous machines according to eqns (3.13), (3.18), and (3.21).

Factor	$\alpha_i = b_p/\tau$						
	0.4	0.5	0.6	2/π	0.7	0.8	1.0
k_f	0.748	0.900	1.030	1.071	1.134	1.211	1.273
k_{fd}	0.703	0.818	0.913	0.943	0.958	0.987	1.00
k_{fq}	0.097	0.182	0.287	0.391	0.442	0.613	1.00
k_{ad}	0.939	0.909	0.886	0.880	0.845	0.815	0.785
k_{aq}	0.129	0.202	0.279	0.365	0.389	0.505	0.785

- for surface PMs

$$k_{fd} = k_{fq} = 1 \tag{3.19}$$

- for buried magnets

$$k_{fd} = \frac{4}{\pi}\alpha_i^2 \frac{1}{\alpha_i^2 - 1}\cos\frac{\pi}{2\alpha_i} \qquad k_{fq} = \frac{1}{\pi}\left(\alpha_i\pi - \sin\alpha_i\pi\right) \tag{3.20}$$

©2000 CRC Press LLC

Formulae for k_{fd}, and k_{fq}, for inset type PMs and surface PMs with mild steel pole shoes are given in [42].

The *reaction factors* in the *d*- and *q*-axis are defined as

$$k_{ad} = \frac{k_{fd}}{k_f} \qquad k_{aq} = \frac{k_{fd}}{k_f} \tag{3.21}$$

The form factors k_f, k_{fd}, and k_{fq}, of the excitation field and armature reaction and reaction factors k_{ad} and k_{aq} for salient-pole synchronous machines according to eqns (3.13), (3.18), and (3.21) are given in Table 3.1.

Assuming $g = 0$, the *equivalent d-axis field MMF* (which produces the same fundamental wave flux as the armature-reaction MMF) is

$$F_{excd} = k_{ad} F_{ad} \frac{m_1 \sqrt{2}}{\pi} \frac{N_1 k_{\omega 1}}{p} k_{ad} I_a \sin \Psi \tag{3.22}$$

where I_a is the armature current and Ψ is the angle between the phasor of the armature current I_a and *q*-axis, i.e., $I_{ad} = I_a \sin \Psi$. Similarly, the *equivalent q-axis field MMF* is

$$F_{excq} = k_{aq} F_{aq} \frac{m_1 \sqrt{2}}{\pi} \frac{N_1 k_{\omega 1}}{p} k_{aq} I_a \cos \Psi \tag{3.23}$$

where $I_{aq} = I_a \cos \Psi$. In the theory of synchronous machines with electromagnetic excitation the MMFs F_{excd} and F_{excq} are defined as the *armature MMFs referred to the field excitation winding.*

3.1.3 Synchronous Reactance

For a salient pole synchronous machine the *d*-axis and *q*-axis *synchronous reactances* are

$$X_{sd} = X_1 + X_{ad} \qquad X_{sq} = X_1 + X_{aq} \tag{3.24}$$

where $X_1 = 2\pi f L_1$ is the armature *leakage reactance* according to eqn (2.24), X_{ad} is the *d-axis armature reaction reactance* also called *d*-axis *mutual reactance,* and X_{aq} is the *q*-axis armature reaction reactance also called *q*-axis mutual reactance. The reactance X_{ad} is sensitive to the saturation of the magnetic circuit whilst the influence of the magnetic saturation on the reactance X_{aq} depends on the excitation system design. In salient-pole synchronous machines with electromagnetic excitation X_{aq} is practically independent of the magnetic saturation. Usually, $X_{sd} > X_{sq}$ except for some PM synchronous machines.

The *d*-axis armature reaction reactance

$$X_{ad} = k_{fd} X_a = 4 m_1 \mu_O f \frac{(N_1 k_{\omega 1})^2}{\pi p} \frac{\tau L_i}{g'} k_{fd} \tag{3.25}$$

where μ_0 is the magnetic permeability of free space, L_i is the effective length of the stator core, $g^{/} \approx k_C k_{sat} g + h_M / \mu_{rrec}$ is the equivalent airgap in the *d*-axis, k_C is the Carter's coefficient for the airgap according to eqn (2.36), $k_{sat} > 1$ is the saturation factor of the magnetic circuit, and

©2000 CRC Press LLC

$$X_a = 4m_1\mu_O f \frac{(N_1 k_{\omega 1})^2}{\pi p} \frac{\tau L_i}{g'} \tag{3.26}$$

is the armature reaction reactance of a non-salient-pole (surface configuration of PMs) synchronous machine. Similarly, for the *q*-axis

$$X_{aq} = k_{fq} X_a = 4m_1\mu_O f \frac{(N_1 k_{\omega 1})^2}{\pi p} \frac{\tau L_i}{k_C k_{satq} g_q} k_{fq} \tag{3.27}$$

where g_q is the airgap in the *q*-axis. For salient pole excitation systems the saturation factor $k_{satq} \approx 1$ since the *q*-axis armature reaction fluxes, closing through the large air spaces between the poles, depend only slightly on the saturation.

The leakage reactance X_1 consists of the slot, end-connection differential and tooth-top leakage reactances - see eqn (2.24). Only the slot and differential leakage reactances depend on the magnetic saturation due to leakage fields.

3.1.4 Voltage Induced

The no-load *rms* voltage induced (EMF) in one phase of the armature winding by the d.c. or PM excitation flux Φ_f is

$$E_f = \pi\sqrt{2} f N_1 k_{w1} \Phi_f \tag{3.28}$$

where N_1 is the number of the armature turns per phase, k_{w1} is the armature winding coefficient and the fundamental harmonic Φ_{f1} of the excitation magnetic flux density Φ_f without armature reaction is

$$\Phi_{f1} = L_i \int_0^T B_{mg1} \sin\left(\frac{\pi}{T}x\right) dx = \frac{2}{\pi} \tau L_i B_{mg1} \tag{3.29}$$

Similarly, the voltage E_{ad} induced by the *d*-axis armature reaction flux Φ_{ad} and the voltage E_{aq} induced by the *q*-axis flux Φ_{aq} are, respectively:

$$E_{ad} = \pi\sqrt{2} f N_1 k_{w1} \Phi_{ad} \tag{3.30}$$

$$E_{aq} = \pi\sqrt{2} f N_1 k_{w1} \Phi_{aq} \tag{3.31}$$

The *direct* or *d*-axis is the center axis of the magnetic pole while the *quadrature* or *q*-axis is the axis parallel (90° electrical) to the *d*-axis. The EMFs E_f, E_{ad}, E_{aq} and magnetic fluxes Φ_f, Φ_{ad}, and Φ_{aq} are used in construction of phasor diagrams and equivalent circuits. The EMF E_i per phase with the armature reaction taken into account is

$$E_i = \pi\sqrt{2} f N_1 k_{w1} \Phi_g \tag{3.32}$$

where Φ_g is the airgap magnetic flux under load (excitation flux Φ_f reduced by the armature reaction flux). At no-load (very small armature current) $\Phi_g \approx \Phi_f$. Including the saturation of the magnetic circuit

$$E_i = 4\sigma_f f N_1 k_{w1} \Phi_g \tag{3.33}$$

The form factor σ_f of EMFs depends on the magnetic saturation of armature teeth, i.e., the sum of the airgap magnetic voltage drop (MVD) and the teeth MVD divided by the airgap MVD.

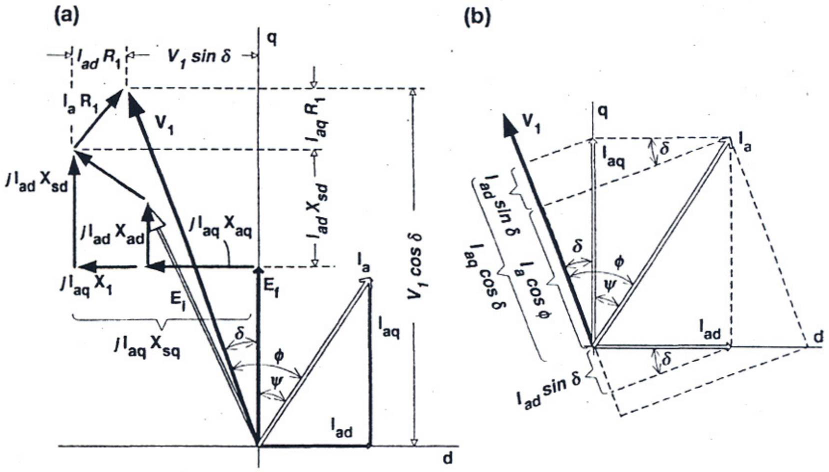

Figure 3.1 Phasor diagram of an underexcited salient pole synchronous motor.

3.1.5 Electromagnetic Power and Thrust

The following set of equations stems from the phasor diagram shown in Fig. 3.1:

$$V_1 \sin\delta = -I_{ad}R_1 + I_{aq}X_{sq}$$

$$V_1 \cos\delta = I_{aq}R_1 + I_{ad}X_{sd} + E_f \tag{3.34}$$

in which δ is the load angle between the terminal phase voltage $\mathbf{V}_1$ and $\mathbf{E}_f$ (q axis). The currents

$$I_{ad} = \frac{V_1\left(X_{sq}\cos\delta - R_1\sin\delta\right) - E_f X_{sq}}{X_{sd}X_{sq} + R_1^2} \tag{3.35}$$

$$I_{aq} = \frac{V_1\left(R_1\cos\delta - X_{sd}\sin\delta\right) - E_f R_1}{X_{sd}X_{sq} + R_1^2} \tag{3.36}$$

are obtained by solving the set of eqns (3.34). The *rms* armature current as a function of $V_1, E_f, X_{sd}, X_{sq}, \delta$, and R_1 is

$$I_a = \sqrt{I_{ad}^2 + I_{aq}^2} = \frac{V_1}{X_{sd}X_{sq} + R_1^2} \tag{3.37}$$

$$\times\sqrt{\left[\left(X_{sq}\cos\delta - R_1\sin\delta\right) - E_f X_{sq}\right]^2 + \left[\left(R_1\cos\delta + X_{sd}\sin\delta\right) - E_f R_1\right]^2}$$

The phasor diagram (Fig. 3.1) can also be used to find the input power [40], i.e.,

$$P_{in} = m_1 V_1 I_a \cos\phi = m_1 V_1\left(I_{aq}\cos\delta - I_{ad}\sin\delta\right) \tag{3.38}$$

©2000 CRC Press LLC

Putting eqns (3.34) into eqn (3.38)

$$P_{in} = m_1\left[I_{aq}E_f + I_{ad}I_{aq}X_{sd} + I_{aq}^2R_1 - I_{ad}I_{aq}X_{sq} + I_{ad}^2R_1\right]$$

$$= m_1\left[I_{aq}E_f + R_1I_a^2 - I_{ad}I_{aq}\left(X_{sd} - X_{sq}\right)\right] \tag{3.39}$$

Because the armature core loss has been neglected, the electromagnetic power is the motor input power minus the armature winding loss $\Delta P_{1w} = m_1I_a^2R_1 = m_1\left(I_{ad}^2 + I_{aq}^2\right)R_1$. Thus

$$P_{elm} = P_{in} - \Delta P_{1w} = m_1\left[I_{aq}E_f + I_{ad}I_{aq}\left(X_{sd} - X_{sq}\right)\right]$$

$$= \frac{m_1\left[V_1\left(R_1\cos\delta + X_{sd}\sin\delta\right) - E_fR_1\right]}{\left(X_{sd}X_{sq} + R_1^2\right)^2} \tag{3.40}$$

$$\times\left[V_1\left(X_{sq}\cos\delta - R_1\sin\delta\right)\left(X_{sd} - X_{sq}\right) + E_f\left(X_{sd}X_{sq} + R_1^2\right) - E_fX_{sq}\left(X_{sd} - X_{sq}\right)\right]$$

Putting $R_1 = 0$, eqn (3.40) takes the following simple form

$$P_{elm} = m_1\left[\frac{V_1E_f}{X_{sd}}\sin\delta + \frac{V_1^2}{2}\left(\frac{1}{X_{sq}} - \frac{1}{X_{sd}}\right)\sin 2\delta\right] \tag{3.41}$$

Small PM LSMs have a rather high armature winding resistance R_1 that is comparable with X_{sd} and X_{sq}. That is why eqn (3.40) instead of (3.41) is recommended for calculating the performance of small, low speed motors.

The electromagnetic thrust developed by a salient-pole LSM is:

$$F_{dx} = \frac{P_{elm}}{v_s} \quad \text{N} \tag{3.42}$$

Neglecting the armature winding resistance $(R_1 = 0)$

$$F_{dx} = \frac{m_1}{v_s}\left[\frac{V_1E_f}{X_{sd}}\sin\delta + \frac{V_1^2}{2}\left(\frac{1}{X_{sq}} - \frac{1}{X_{sd}}\right)\sin 2\delta\right] \tag{3.43}$$

In a salient pole-synchronous motor the electromagnetic thrust has two components (Fig.3.2)

$$F_{dx} = F_{dxsyn} + F_{dxrel} \tag{3.44}$$

©2000 CRC Press LLC

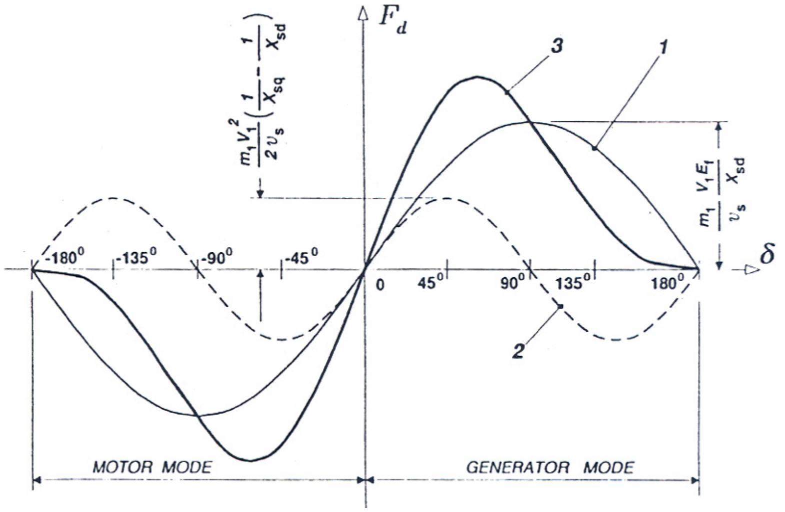

Figure 3.2 Thrust-angle characteristics of a salient-pole synchronous machine with $X_{sd} > X_{sq}$. 1 -synchronous thrust F_{dsyn}, 2 - reluctance thrust F_{dsyn}, 3 - resultant thrust F_d.

where the first term,

$$F_{dxsyn} = \frac{m_1}{v_s}\frac{V_1 E_f}{X_{sd}} \sin\delta \tag{3.45}$$

is a function of both the input voltage V_1 and the excitation EMF E_f.
The second term,

$$F_{dxrel} = \frac{m_1 V_1^2}{2 v_s}\left(\frac{1}{X_{sq}} - \frac{1}{X_{sd}}\right)\sin 2\delta \tag{3.46}$$

depends only on the voltage V_1 and also exists in an unexcited machine $\left(E_f = 0\right)$ provided that $X_{sd} \neq X_{sq}$. The thrust F_{dxsyn} is called the *synchronous thrust* and the thrust F_{dxrel} is called the *reluctance thrust.* The proportion between X_{sd} and X_{sq} strongly affects the shape of curves 2 and 3 in Fig. 3.2. For surface configurations of PMs $X_{sd} \approx X_{sq}$ (if the magnetic saturation is neglected) and

$$F_{dx} \approx F_{dxsyn} = \frac{m_1}{v_s}\frac{V_1 E_f}{X_{sd}} \sin\delta \tag{3.47}$$

3.1.6 Thrust Ripple

The *thrust ripple* can be expressed as the rms thrust ripple $\sqrt{\sum F_{dxv}^2}$ weighted to the mean value of the thrust, i.e.,

©2000 CRC Press LLC

$$f_r = \frac{1}{F_{dx}} \sqrt{\sum_{\nu} F_{dx\nu}^2} \tag{3.48}$$

The thrust ripple of a LSM consists of three components: (1) *cogging thrust,* i.e., interaction between the, excitation flux and variable permeance of the armature core due to slot openings, (2) distortion of sinusoidal or trapezoidal distribution of the magnetic flux density in the airgap and (3) phase current commutation and current ripple.

Case Study

A flat, short-armature, single-sided, three-phase LSM has a long reaction rail with surface configuration of PMs. High energy sintered NdFeB PMs with the remanent magnetic flux density B_r = 1.1 T and coercive force H_c = 800 kA/m have been used. The armature magnetic circuit has been made of cold-rolled steel laminations Dk-66 (Table 2.1) The following design data are available: armature phase windings are Y-connected, number of pole pairs p = 4, pole pitch τ = 56 mm, airgap in *d*-axis (mechanical clearance) g = 2.5 mm, airgap in *q*-axis g_q = 6.5 mm, effective width of the armature core L_i = 84 mm, width of the core (back iron) of the reaction rail w = 84 mm, height of the yoke of the armature core h_{1y} = 20 mm, length of the overhang (one side) l_e = 90 mm, number of armature turns per phase N_1 = 560, number of parallel wires a = 2, number of armature slots z_1 = 24, width of the armature tooth C_{t1} = 8.4 mm, height of the yoke of the reaction rail h_{2y} = 12 mm, dimensions of the armature open rectangular slot: h_{11} = 26.0 mm, h_{12} = 2.0 mm, h_{13} = 3.0 mm, h_{14} = 1.0 mm, b_{14} = 10.3 mm (see Fig. 2.6b), stacking coefficient of the armature core k_i = 0.96, conductivity of armature wire σ_{20} = 57 × 10^6 S/m at 20°C, diameter of armature wire d_{wir} = 1.02 mm, temperature of armature winding 75°C, height of the PM h_M = 4.0 mm, width of the PM w_M = 42.0 mm, length of the PM (in the direction of armature conductors) l_M = 84 mm, width of the pole shoe b_p = w_M = 42.0 mm, friction coefficient for rollers at constant speed μ = 0.01.

The coil pitch c_1 of the armature winding is equal to the pole pitch τ (full pitch winding).

The LSM is fed from a VVVF inverter and the ratio of the line voltage to input frequency V_{1L-L}/f = 10. The LSM has been designed for continuous duty cycle to operate with the load angle δ corresponding to the maximum efficiency. The current density in the armature winding normally does not exceeds 3.0 A/mm^2.

Calculate the steady-state performance characteristics for f = 20, 15, 10 and 5 Hz.

For V_{1L-L}/f = 10 the input line voltages are: 200 V for 20 Hz,150 V for 15 Hz, 100 V for 10 Hz and 50 V for 5 Hz. Steady state characteristics have been calculated using analytical equations given in Chapters 1, 2 and 3. The volume of the PM material is $p \times 2h_M \times w_M \times l_M = 4 \times 2 \times 4 \times 42 \times 84 =$ 112,896 mm^3.

Given below are parameters independent of the frequency, voltage and load angle δ :

- number of slots per pole per phase q_1 = 1
- winding factor k_{w1} = 1.0
- pole pitch in slots = 3
- pole shoe-to-pole pitch ratio α_i = 0.75

- coil pitch in slots = 3
- coil pitch in millimeters w_c = 56 mm
- armature slot pitch t_1 = 18.7 mm
- width of the armature slot $b_{11} = b_{12} = b_{14}$ = 10.3 mm
- number of conductors in each slot N_{sl} = 280
- conductors area-to-slot area k_{sl} = 0.2252
- Carter's coefficient k_C = 1.2
- form factor of the excitation field k_f = 1.176
- form factor of the *d*-axis armature reaction k_{fd} = 1.0
- form factor of the *q*-axis armature reaction k_{fd} = 1.0
- reaction factors $k_{ad} = k_{aq}$ = 0.85
- coefficient of leakage flux σ_1 = 1.156
- permeance of the airgap $G_g = 0.1370 \times 10^{-5}$ H
- permeance of the PM $G_M = 0.1213 \times 10^{-5}$ H
- permeance for leakage fluxes $G_{lM} = 0.2144 \times 10^{-6}$ H
- magnetic flux corresponding to the remanent magnetic flux density $\Phi_r = 0.3881 \times 10^{-2}$ Wb
- relative recoil magnetic permeability μ_{rrec} = 1.094
- PM edge line current density A_M = 800,000.00 A/m
- mass of the armature yoke m_{y1} = 5.56 kg
- mass of the armature teeth m_{t1} = 4.92 kg
- mass of the armature conductors m_{cu} = 15.55 kg
- friction force F_r = 1.542 N

Then, resistances and reactances independent of magnetic saturation have been calculated

- armature winding resistance $R_1 = 2.5643\ \Omega$ at 75°C
- armature winding leakage reactance $X_1 = 4.159\ \Omega$ at f = 20 Hz
- armature winding leakage reactance $X_1 = 1.0397\ \Omega$ at f = 5 Hz
- armature reaction reactance $X_{ad} = X_{aq} = 4.5293\ \Omega$ at f = 20 Hz

©2000 CRC Press LLC

- armature reaction reactance $X_{ad} = X_{aq} = 1.1323\ \Omega$ at $f = 5$ Hz
- specific slot leakage permeance $\lambda_{1s} = 1.3918$
- specific leakage permeance of end connections $\lambda_{1e} = 0.2192$
- specific tooth-top leakage permeance $\lambda_{1t} = 0.1786$
- specific differential leakage permeance $\lambda_{1d} = 0.21$
- coefficient of differential leakage $\tau_{d1} = 0.0965$

Note that for calculating X_{ad} of an LSM with surface PMs the non-ferromagnetic airgap is the gap between the ferromagnetic cores of the armature and reaction rail which is equal to the airgap g_q in the *q* axis. The relative magnetic permeability of NdFeB PMs is very close to unity.

Steady state performance characteristics have been calculated as functions of the load angle δ. The load angle of synchronous motors can be compared to slip of induction motors, which is also a measure how much the motor is loaded. Magnetic saturation due to main flux and leakage fluxes has been included. A LSM should operate with maximum efficiency. Maximum efficiency usually corresponds to the *d* axis current $I_{ad} \approx 0$. Table 3.2 shows fundamental steady state performance characteristics for f = 20, 15, 10 and 5 Hz. In practice, the maximum efficiency corresponds to small values (close to zero) of the angle Ψ, i.e., the angle between the phasor of the armature current $\mathbf{I}_a$ and *q*-axis which means

©2000 CRC Press LLC

Table 3.2 Steady state performance characteristics of a flat three phase four pole LSM with surface PMs and τ = 56 mm.

δ deg	Ψ deg	P_{out} W	F_x N	F_z N	I_a A	η –	$\cos\phi$ –
f = 20 Hz, V_{1L-L} = 200 V, υ_s = 2.24 m/s							
-20.0	58.69	-670.0	-300.4	992	5.91	0.5987	0.1960
-10.0	80.18	-178.0	-85.2	1004	5.01	0.0312	0.0032
1.0	70.51	308.7	145.3	1108	4.27	0.6582	0.3172
10.0	40.75	739.5	342.1	1273	4.10	0.8223	0.6326
12.0	33.77	839.1	387.7	1319	4.16	0.8351	0.6976
15.0	23.53	991.1	457.2	1393	4.32	0.8463	0.7823
20.0	7.20	1253.0	577.2	1544	4.78	**0.8515**	0.8894
22.4	0.11	1383.0	636.4	1628	5.09	0.8493	0.9238
30.0	-18.73	1803.0	829.1	1931	6.41	0.8287	0.9807
40.0	-36.89	2374.0	1091.0	2461	8.79	0.7805	0.9985
60.0	-72.75	3562.0	1644.0	5511	20.23	0.5212	0.9754
f =15 Hz, V_{1L-L} =150 V, υ_s =1.68 m/s							
-20.0	64.25	-406.1	-243.8	977	5.78	0.3703	0.1002
-10.0	84.85	-63.5	-44.1	1024	4.79	0.6035	0.0845
1.0	65.31	276.4	172.3	1160	3.94	0.6714	0.4018
10.0	33.47	576.8	355.3	1350	3.75	0.8146	0.7258
15.0	15.03	749.1	460.4	1487	4.00	**0.8332**	0.8658
19.4	0.21	903.4	554.6	1628	4.44	0.8320	0.9420
20.0	-1.64	924.6	567.6	1646	4.51	0.8309	0.9491
30.0	-27.01	1278.0	783.6	2055	6.24	0.7898	0.9986
40.0	-44.18	1616.0	990.7	2595	8.66	0.7203	0.9973
60.0	-75.94	1911.0	1179.0	5190	18.64	0.4104	0.9615
f = 10 Hz, V_{1L-L} = 100 V, υ_s = 1.12 m/s							
-20.0	72.91	-167.7	153.2	990	5.30	0.2779	0.0507
-10.0	87.43	15.5	17.8	1085	4.23	0.0974	0.2176
1.0	55.89	217.4	202.2	1265	3.30	0.6973	0.5462
10.0	20.14	380.5	351.4	1479	3.15	0.8068	0.8648
12.0	11.97	416.2	384.1	1535	3.24	**0.8118**	0.9138
15.0	0.36	469.0	432.5	1625	3.46	0.8108	0.9642
20.0	-16.30	554.5	510.9	1795	4.05	0.7920	0.9979
30.0	-39.74	708.8	652.5	2196	5.81	0.7140	0.9856
40.0	-55.12	822.6	757.8	2709	8.12	0.6060	0.9654
45.0	-61.75	851.9	785.4	3029	9.50	0.5404	0.9576
60.0	-80.56	634.9	592.4	4507	15.50	0.2525	0.9363
f = 5 Hz, V_{1L-L} =50 V, υ_s = 0.56 m/s							
-20	87.20	-8.2	-20.5	1149	3.70	0.0866	0.2957
-10	73.13	45.8	86.8	1278	2.75	0.4260	0.4520
1	35.88	102.2	190.0	1469	1.99	0.7424	0.7999
8.6	0.10	134.3	248.8	1630	2.00	**0.7859**	0.9885
10	-6.18	139.4	258.3	1661	2.06	0.7822	0.9978
15	-25.54	155.4	287.8	1781	2.44	0.7478	0.9831
20	-40.01	167.4	309.8	1911	2.99	0.6891	0.9397
30	-59.02	176.4	326.9	2201	4.36	0.5346	0.8745
40	-71.27	160.6	298.8	2521	5.94	0.3650	0.8547
60	-88.42	21.2	467.9	3254	9.53	0.0292	0.8795

©2000 CRC Press LLC

Table 3.3 Calculation results for maximum efficiency with magnetic saturation taken into account .

Quantity	$f = 20\ Hz$	$f = 5\ Hz$
Load angle δ	20^0	8.6^0
Angle between the armature current I_a and q axis Ψ	7.2^0	0.103^0
Output power P_{out}, W	1253	134.3
Output power-to-armature mass, W / Kg	48.16	5.16
Input power P_{in}, W	1472	170.9
Electromagnetic thrust F_{dx}, N	578.7	250.4
Thrust F_x, N	577.2	248.8
Normal force F_z, N	1544	1630
Electromagnetic power P_g, W	1296	140.2
Efficiency η	0.8515	0.7859
Power factor $\cos\phi$	0.8894	0.9885
Armature current I_a, A	4.78	2.0
d-axis armature current I_{ad}, A	0.6	0.0
q-axis armature current I_{aq}, A	4.74	2.0
Armature line current density, peak value, A_{m1}, A/m	50,670	21,170
Current density in the armature winding J_1, A/mm^2	2.946	1.231
Airgap magnetic flux density, maximum value B_{mg}, T	0.5244	0.5338
Per phase EMF excited by PMs E_f, V	91.22	23.42
Magnetic flux in the airgap Φ_g, Wb	0.1852×10^{-2}	0.1901×10^{-2}
Armature winding loss ΔP_{1w}, W	175.6	30.65
Armature core loss ΔP_{1Fe}, W	14.45	2.39
Mechanical losses ΔP_m, W	3.45	0.86
Additional losses ΔP_{ad}, W	25.1	2.7
Armature leakage reactance X_1, Ω	4.1286	1.0351
d-axis synchronous reactance X_{sd}, Ω	8.566	2.144
q-axis synchronous reactance X_{sq}, Ω	8.656	2.167
Magnetic flux density in the armature tooth, B_{1t}, T	1.2138	1.2471
Magnetic flux density in the armature yoke B_{1y}, T	0.574	0.5893
Saturation factor of the magnetic circuit k_{sat}	1.0203	1.0208

©2000 CRC Press LLC

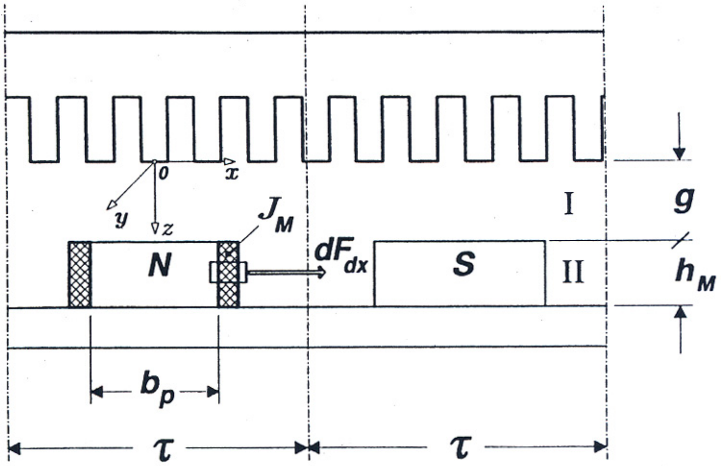

Figure 3.3 Model of a single-sided LSM with surface configuration of PMs for two dimensional electromagnetic field analysis.

that the *d*-axis armature current I_{ad} for maximum efficiency is very small or $I_{ad} = 0$ (Chapter 4).

Table 3.3 contains calculation results for maximum efficiency and two extreme frequencies $f = 20$ Hz and $f = 5$ Hz, including the magnetic saturation. The magnetic flux density in armature teeth for maximum efficiency is well below the saturation magnetic flux density (over 2.1 T for Dk-69 laminations). This value is close to the saturation value for higher load angles $\delta \geq 60°$. Also, the armature current I_a and consequently line current density A_{m1} and current density J_1 increase with the load angle δ.

3.1.7 Direct Calculation of Thrust

The thrust of a PM LSM can be calculated directly on the basis of the electromagnetic field distribution [98]. Fig. 3.3 shows a single-sided PM LSM in Cartesian coordinate system. The problem can be simplified to a two-dimensional field distribution where currents in the armature winding are perpendicular to the laminations (y direction) and magnetic flux density has only two components, i.e., tangential component B_x, and normal component B_z.

The two dimensional electromagnetic field distribution will be found on the basis of the following assumptions:

(a) the armature core is an isotropic and slotless cube with its magnetic permeability tending to infinity an electric conductivity tending to zero;
(b) the armature winding is represented by an infinitely thin current sheet distributed uniformly at the active surface of the armature core;
(c) the armature currents flow only in the direction perpendicular to the xz plane, i.e. in the y direction;
(d) the width of the PM is $b_p < \tau$;
(e) isotropic PMs are magnetized in the normal direction (z coordinate) and have zero electric conductivity;
(f) each PM is represented by an equivalent coil embracing the PM and carrying a fictitious surface current which produce an equivalent magnetic flux;
(g) the magnetic permeability of the space between PMs is equal to that of PMs;

©2000 CRC Press LLC

(h) the yoke of the reaction rail is an isotropic cube with its magnetic permeability tending to infinity an electric conductivity tending to zero.

Simplifications given by assumptions (a) and (b) can be corrected by replacing the airgap g between the armature core and PMs by an equivalent airgap $g' = k_C g$ where k_C is Carter's coefficient. The time-space distribution of the armature line current density for the fundamental space harmonic can be obtained by taking the first derivative of the primary MMF distribution with respect to the x coordinate. According to eqn (3.10)

$$a(x,t) = \frac{dF(x,t)}{dx} = -\frac{m_1\sqrt{2}}{p\tau} N_1 I_a k_{w1} \cos(\omega t - \beta x) \tag{3.49}$$

or

$$a(x,t) = -\mathrm{Re}\left[A_m e^{j\omega t - \beta x}\right] = -\mathrm{Re}\left[A_m e^{j\omega t} e^{-j\beta x}\right] \tag{3.50}$$

where

$$A_m = \frac{m_1\sqrt{2} N_1 k_{w1} I_a}{p\tau} \tag{3.51}$$

and

$$\beta = \frac{\pi}{\tau} \tag{3.52}$$

The line current density (3.51) obtained as $dF(x,t)/dx$ has in numerator the effective number of turns $N_1 k_{w1}$, instead of the number of turns N_1 - see eqn (3.12).

The space distribution of the armature line current density is simply

$$a(x) = -\mathrm{Re}\left[A_m e^{-j\beta x}\right] = -A_m \cos \beta x \tag{3.53}$$

According to the assumption (f) and for a two-dimensional problem, the equivalent edge line current density representing a PM is [98]:

$$J_M = \frac{B_r}{\mu_0 \mu_{rrec}} \qquad \text{A/m} \tag{3.54}$$

where B_r is the remanent magnetic flux density and μ_{rrec} is the relative recoil magnetic permeablity of a PM (Chapter 2 and Appendix A). If, say, B_r = 1.1 T and μ_{rrec} = 1.05 the equivalent line current density $J_M \approx 0.834 \times 10^6$ A/m.

Assumption (g) can be partially justified due to the fact that the relative magnetic permeability of the NdFeB PM is usually 1.0 to 1.1, i.e., close to the relative magnetic permeability of free space.

The two-dimensional electromagnetic field distribution excited by the armature winding in both regions I and II (Fig. 3.3) can be described by Laplace's equation

$$\frac{\partial^2 \vec{A}}{\partial x} + \frac{\partial^2 \vec{A}}{\partial z} = 0 \tag{3.55}$$

where $\vec{A}$ is the magnetic vector potential defined as $\vec{B} = curl \vec{A}$.

Using the method of separation of variables, the solution to eqn (3.55) for the fundamental space harmonic can have the following form

$$\mathrm{A}_y(x,z,t)=e^{j(\omega t-\beta x)}\left(Ae^{-\beta z}+Be^{\beta z}\right) \tag{3.56}$$

According to eqn (3.53) the space distribution of the primary line current density is according to cosinusoidal law. Hence, the line current density given by eqn (3.56) can be expressed as a real number, i.e.,

$$A_y(x,z)=\cos\beta x\left(Ae^{-\beta z}+Be^{\beta z}\right) \tag{3.57}$$

According to assumption (c) the magnetic vector potential can only have one component A_y in the y direction so that in Cartesian coordinate system

$$\mathrm{B}_x=-\frac{\partial \mathrm{A}_y}{\partial z} \qquad \mathrm{B}_z=\frac{\partial \mathrm{A}_y}{\partial x} \tag{3.58}$$

The components of the magnetic flux density in the region I and region II are

$$B_x(x,z)=-\frac{\partial A_y(x,z)}{\partial z}=\beta\cos\beta x\left(Ae^{-\beta z}-Be^{\beta z}\right) \tag{3.59}$$

$$B_z(x,z)=\frac{\partial A_y(x,z)}{\partial x}=-\beta\sin\beta x\left(Ae^{-\beta z}+Be^{\beta z}\right) \tag{3.60}$$

On the basis of assumption (a) the magnetic permeability of the primary stack tends to infinity. Thus, at z = 0

$$\frac{B_{xI}(x,z=0)}{\mu_0}=a(x)$$

or, on the basis of eqn (3.53)

$$\beta\left(A_I-B_I\right)=-\mu_0 A_m \tag{3.61}$$

where the amplitude of the line current density A_m is according to eqn (3.51).

At $z = g$

$$\frac{B_{xI}(x,z=g)}{\mu_0}=\frac{B_{xII}(x,z=g)}{\mu_0\mu_{rrec}} \qquad \text{and} \qquad B_{zI}(x,z=g)=B_{zII}(x,z=g)$$

or

$$\mu_{rrec}\left(A_Ie^{-\beta g}-B_Ie^{\beta g}\right)=A_{II}e^{-\beta g}-B_{II}e^{\beta g} \tag{3.62}$$

$$A_Ie^{-\beta g}+B_Ie^{\beta g}=A_{II}e^{-\beta g}+B_{II}e^{\beta g} \tag{3.63}$$

At $z = g + h_M$

$$B_x(x,z=g+h_M)=0$$

or

$$A_{II}e^{-B(g+h_M)}-B_{II}e^{\beta(g+h_M)}=0 \tag{3.64}$$

The above boundary conditions allow for finding all constants A_I , A_{II} , B_I and B_{II} (four equations). For example, the constants A_{II} and B_{II} are equal to

$$A_{II} = C'e^{\beta(g+h_M)} \quad B_{II} = C'e^{-\beta(g+h_M)}$$

where

$$C' = \frac{1}{\mu_{rrel}\cosh\beta h_M \sinh\beta g + \sinh\beta h_M \cosh\beta g}\frac{\mu_0\mu_{rrel}}{2\beta}A_m$$

Putting the constants A_{II} and B_{II} into eqns (3.60), the space distribution of the first harmonic of the normal component of the armature magnetic flux density is

$$B_{zII}(x,z) = -2\beta C' \sin\beta x \cosh\beta(g+h_M-z) \tag{3.65}$$

The thrust for the fundamental harmonic can be found on the basis of Lorentz equation. The force increment acting on an edge with the coordinate $x = b_p/2$ and current density J_m is $dF_{dx} = B_{zII}(x = 0.5b_{p,}z)J_M L_i dz$. For $2\times 2p$ edges and neglecting the '$-$' sign

$$F_{dx} = 8pL_iJ_M\beta C'\int_g^{g+h_M}\sin\alpha_i\frac{\pi}{2}\cosh\beta(g+h_M-z)dz \tag{3.66}$$

$$\int_g^{g+h_M}\cosh\beta(h_M+g-z)dz = \frac{1}{\beta}\sinh\beta h_M = \frac{\tau}{\pi}\sinh\beta h_M$$

Finally

$$F_{dx} = \frac{4}{\pi}p\tau L_iB_rA_m\sin\left(\frac{\alpha_i\pi}{2}\right)\frac{\tanh\beta h_M}{\mu_{rrel}\sinh\beta g + \tanh\beta h_M\cosh\beta g} \tag{3.67}$$

For example, for the LSM according to Tables 3.2 and 3.3, f = 5 Hz, V_{1L-L} = 50 V, υ_s = 0.56 m/s and δ = 8.6°, the relative permeability of the PM μ_{rrec} = 1.094, PM edge line current density J_M = 800,000 A/m eqn (3.67) gives F_{dx} = 278.0 N (for g' = gk_C). According to eqn (3.43) F_{dx} = 250.4 N.
The above eqn (3.67) has been derived and verified by H. Mosebach [98] and then developed further for armature line current waveforms other than sinusoidal [99].

3.2 Motors with Superconducting Excitation Coils

The model of a *coreless LSM with superconducting electromagnets* is shown in Fig. 3.4 [9, 37, 81,123]. The following assumptions have been made to find the two dimensional distribution of magnetic and electric field components:

(a) the armature winding is represented by an infinitely long (x direction) and infinitely thin (*z* direction) current sheet which is distributed uniformly at z = g (xy surface);

(b) the distribution of electromagnetic field in the x direction is periodical with the period equal to 2τ ;

(c) the armature currents flow only in the direction perpendicular to the xz plane, i.e., in the y direction;

©2000 CRC Press LLC

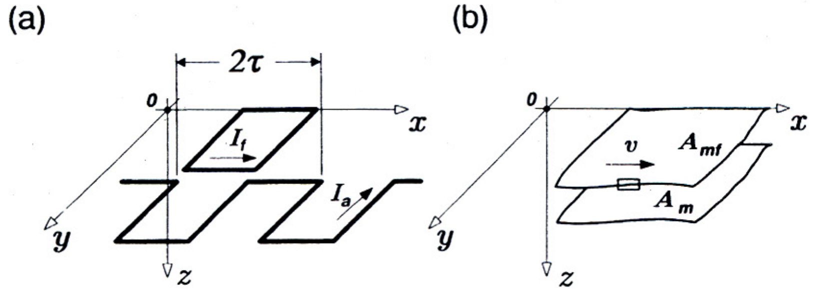

Figure 3.4 Model of an air-cored LSM with superconducting excitation system for the electromagnetic field analysis: (a) winding layout, (b) armature and field excitation current sheets.

(d) the aircored excitation winding is represented by an infinitely thin current sheet distributed uniformly at the $z = 0$ of the xy surface;
(e) the electromagnetic field does not change in the y direction;
(f) end effects due to the finite length of windings (x direction) are neglected;
(g) only the fundamental space harmonic $\nu = 1$ of the field distribution in the x direction is taken into account.

The armature winding can be represented by the following space-time distribution of the line current density (current sheet) expressed as a complex number

$$\mathrm{a}(x,t) = A_m e^{j(\omega t - \beta x)} \tag{3.68}$$

and the excitation winding can be described by the following space time distribution of the complex line current density

$$\mathrm{a}_f(x,t) = A_{mf} e^{j(\omega t - \beta x - \varepsilon)} \tag{3.69}$$

where the peak values of line current densities are:

- for the armature winding - see eqn (3.51)

$$A_m = \frac{m_1\sqrt{2}N_{1p}k_{w1}I_a}{p\tau} = \frac{2m_1\sqrt{2}N_{1p}k_{w1}I_a}{\tau} \tag{3.70}$$

- for the field excitation winding (d.c. current excitation)

$$A_{mf} = \frac{2N_f k_{wf} I_f}{p\tau} = \frac{4N_{fp}k_{wf}I_f}{\tau} \tag{3.71}$$

The number of series armature turns per phase is $N_1 = 2pN_{1p}$ where N_{1p} is the number of armature series turns per phase per pole and the number of field series turns $N_1 = 2pN_{fp}$ where N_{fp} is the number of field turns per pole.

The so called *force angle* $\varepsilon = 90^0 \mp \Psi$ is the angle between phasors of the excitation flux Φ_f in the *d*-axis and the armature current I_a.

©2000 CRC Press LLC

The two dimensional distribution of the magnetic vector potential of the field excitation winding is described by the Laplace's equation

$$\frac{\partial^2 \mathrm{A}_{fy}}{\partial x}+\frac{\partial^2 \mathrm{A}_{fy}}{\partial z}=0 \tag{3.72}$$

The general solution to eqn (3.72) for $0 \le z \le g$ is

$$\mathrm{A}_{fy}(x,z)=C_f e^{j(\omega t-\beta x-\varepsilon)}e^{-\beta z} \tag{3.73}$$

On the basis of the definition of the magnetic vector potential, there are only two components of the magnetic flux density of the field excitation winding, i.e.,

$$\mathrm{B}_{fx}=-\frac{\partial \mathrm{A}_{fy}}{\partial z}=\beta \mathrm{A}_{fy} \qquad \mathrm{B}_{fz}=\frac{\partial \mathrm{A}_{fy}}{\partial x}=-j\beta \mathrm{A}_{fy} \tag{3.74}$$

According to Ampere's circuital law applied to the field excitation current sheet (z = 0)

$$2\int \mathrm{H}_{fx}(x,z=0)\,dx=\int \mathrm{a}(x,t)\,dx$$

and using the first eqn (3.74)

$$\mathrm{H}_{fx}(x,z=0)=\frac{\mathrm{B}_{fx}(x,z=0)}{\mu_0}=-\frac{1}{\mu_0}\frac{\partial \mathrm{A}_{fy}(x,z=0)}{\partial z}=\frac{\beta}{\mu_0}\mathrm{A}_{fy}(x,z=0)$$

The constant C_f in eqn (3.73) is

$$C_f=\frac{\mu_0 A_{mf}}{2\beta}$$

and

$$\mathrm{A}_{fy}(x,z)=\frac{\mu_0}{2\beta}A_{mf}e^{j(\omega t-\beta x-\varepsilon)}e^{-\beta z} \tag{3.75}$$

The components B_{fx} and B_{fz} can be, found on the basis of eqns (3.74) and (3.75).

The magnetic vector potential of the armature winding has a similar form as eqn (3.75), i.e.,

$$\mathrm{A}_y(x,z)=\frac{\mu_0}{2\beta}\mathrm{A}_m e^{j(\omega t-\beta x)}e^{-\beta(g-z)} \tag{3.76}$$

The normal forces in the x and z direction per unit area can be found on the basis of Lorentz equations, i.e.,

$$f_{dx}=\frac{1}{2}Re\left[\mathrm{a}(x,t)\mathrm{B}^*_{fz}\right]=-\frac{1}{4}\mu_0 A_m A_{mf}e^{-\beta g}\sin\varepsilon \qquad \mathrm{N/m^2} \tag{3.77}$$

$$f_{dz}=-\frac{1}{2}Re\left[\mathrm{a}(x,t)\mathrm{B}^*_{fx}\right]=-\frac{1}{4}\mu_0 A_m A_{mf}e^{-\beta g}\cos\varepsilon \qquad \mathrm{N/m^2} \tag{3.78}$$

Multiplying by the area $2p\tau$ of the superconducting electromagnet

- the electromagnetic thrust

$$F_{dx} = -F_{\max} \sin\varepsilon \tag{3.79}$$

- the normal repulsive force

$$F_{dz} = -F_{\max} \cos\varepsilon \tag{3.80}$$

where the peak force

$$F_{\max} = 4\mu_0 m_1 p\sqrt{2} N_{1p} k_{w1} N_{fp} k_{wf} \frac{L_i}{\tau} I_a I_f e^{-\beta g} \tag{3.81}$$

Case Study

The following design data of a single-sided air-cored LSM with superconducting excitation winding are available: m_1 = 3, p = 2, $N_{fp} k_{wf} I_f$ = 700 × 10^3 A, k_{w1} = 1.0, I_a = 1000 A, g = 0.1 m, τ = 1.35 m and L_i = 1.07 m. Find the maximum force as a function of number of the armature turns $2 \le N_{1p} \le 20$ and the electromagnetic thrust F_{dx} and normal force F_{dz} as functions of the force angle ε.

The maximum force for N_{1p} = 2 is

$$F_{\max} = 4 \times 0.4\pi \times 10^{-6} \times 3 \times 2 \times \sqrt{2} \times 2 \times 1.0 \times 700 \times 10^3 \times 1000.0$$

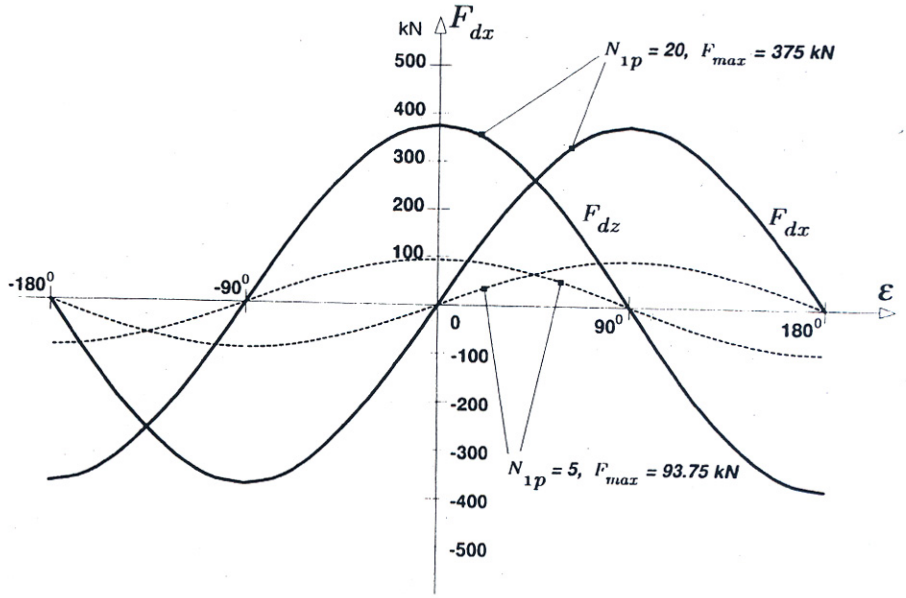

Figure 3.5 Electromagnetic thrust F_{dx} and normal force F_{dz} as functions of the force angle ε for typical parameters of an air-cored LSM.

$$\times \frac{1.07}{1.35} e^{-0.1\pi / 1.35} = 37{,}501.4 \text{ N} \approx 37.5 \text{ kN}$$

For N_{1p} = 5, $F_{\max}$ = 93.75 kN; for N_{1p} = 10, $F_{\max}$ = 187.5 kN; for N_{1p} = 15, $F_{\max}$ = 281.25 kN; and for N_{1p} = 20, $F_{\max}$ = 375.0 kN. The "$-$" sign has been neglected.

The forces $F_{dx} = F_{\max} \sin \varepsilon$ and $F_{dz} = F_{\max} \cos\varepsilon$ as functions of ε are plotted in Fig. 3.5.

3.3 Variable Reluctance Motors

Variable reluctance LSMs do not have any excitation system so that the EMF $E_f = 0$. The thrust is expressed by eqn (3.46) and is proportional the input voltage squared V_1^2, the difference $X_{sd} - X_{sq}$ between the *d* and *q*-axis synchronous reactances and sin 2δ where δ is the load angle (between the terminal voltage V_1 and *q*-axis. Including the stator winding resistance R_1, the thrust is

$$F_{dxrel} = \frac{P_{elm}}{\upsilon_s} = \frac{m_1 V_1^2}{2\upsilon_s} \frac{X_{sd} - X_{sq}}{\left(X_{sd} X_{sq} + R_1^2\right)^2} \left[\left(X_{sd} X_{sq} - R_1^2\right)\sin 2\delta + R_1\left(X_{sd} + X_{sq}\right)\cos 2\delta - R_1\left(X_{sd} - X_{sq}\right)\right] \tag{3.82}$$

where P_{elm} is according to eqn (3.40) for $E_f = 0$.

For the same load, the input current of a reluctance LSM is higher than that of a PM LSM since the EMF induced in the armature winding by the excitation system is zero - eqns (3.35) and (3.36). Correspondingly, it affects the efficiency because of higher power loss dissipated in the armature winding. The thrust can be increased by magnifying the ratio X_{sd} / X_{sq}. However, this in turn involves a heavier magnetizing current resulting in further increase in the input current due to a high reluctance of the magnetic circuit in the *q*-axis.

3.4 Permanent Magnet Hybrid Motors.

3.4.1 Finite Element Approach

The magnetic circuits of stepping motors are frequently highly saturated. Therefore, it is often difficult to calculate and analyze the motor performance with consistent accuracy by using the classical circuital or field approach. Using the finite element method (FEM) or other numerical methods, more accurate results can be obtained. Since the HLSM consists of two independent stacks, it is acceptable to model each stack separately. There is one potential difficulty in the modelling of the HLSM. This arises as a result of the tiny airgap, below 0.05 mm. For a better accuracy of the calculation, the airgap requires three or four layers of elements which in turn leads to high aspect ratios.

The fundamentmals of the FEM can be found in many monographs, e.g., [18, 127] and will not be presented here. In the FEM, both the *virtual work method* - eqn (1.10) and *Maxwell stress tensor* can be used for the thrust (tangential force) F_{dx} and normal force F_{dz} calculation. Forces calculated on the basis of Maxwell's stress tensor are

$$F_{dx} = \frac{L_i}{\mu_0} \int_l B_x B_z dl \qquad F_{dz} = \frac{L_i}{2\mu_0} \int_l \left(B_z^2 - B_x^2\right) dl \tag{3.83}$$

L_i is the width of the HLSM stack, B_x is the tangential component of the magnetic flux density, B_z is the normal component of the magnetic flux density and l is the integration path. In the method of virtual work x is the horizontal displacement between forcer and platen, z is the vertical displacement and W is the energy stored in the magnetic field – eqn (1.10).

The classical virtual work method needs two solutions, and the choice of suitable displacement has direct influence on the calculation accuracy. The following one solution approach based on Coulomb and Meunier's approach [25] has been used and implemented here for calculating the tangential force

$$F_{dx} = -\sum_{e} \left(\frac{\mathrm{B}^T}{\mu_0} \frac{\partial \mathrm{B}}{\partial x} + \frac{\mathrm{B}^T}{\mathrm{B}} 2\mu_0 \left|\mathrm{Q}\right|^{-1} \frac{\partial \left|\mathrm{Q}\right|}{\partial x} \right) V_e \tag{3.84}$$

where B is the matrix of magnetic flux density in the airgap region, B^{T} is the transpose matrix of B, |Q| is the determinant of Jacobian matrix and V_{e} is the volume of an element e. For linear triangular elements, the above equation can further be simplified to the following form

$$F_{dx} = -\sum_{e} \sum_{i} \frac{1}{4\mu_0} \left[(z_2 - z_3)\Delta_1^2 + 2(x_3 - x_2)\Delta_1\Delta_2 - (z_2 - z_3)\Delta_2^2 \right] \tag{3.85}$$

Similarly, the dual formulation for calculating normal force is obtained as

$$F_{dx} = -\sum_{e} \sum_{i} \frac{1}{4\mu_0} \left[(x_3 - x_2)\Delta_1^2 + 2(z_3 - z_2)\Delta_1\Delta_2 - (x_3 - x_2)\Delta_2^2 \right] \tag{3.86}$$

In eqns (3.85) and (3.86) x and z are rectangular coordinates of the 2D model, e and i are the numbers of virtually distorted elements and virtually moved nodes within an element, respectively, and subscripts 1, 2 and 3 correspond to the nodes of a triangular element. The parameters Δ_1 and Δ_2 are defined as

$$\Delta_1 = \frac{A_1(x_3 - x_2) + A_2(x_1 - x_3) + A_3(x_2 - x_1)}{Q} \tag{3.87}$$

$$\Delta_2 = \frac{A_1(z_3 - z_2) + A_2(z_1 - z_3) + A_3(z_2 - z_1)}{Q} \tag{3.88}$$

where A_1 to A_3 are magnitudes of the magnetic vector potential corresponding to each node of a triangular element. The Jacobian matrix becomes

$$Q = \begin{bmatrix} x_1 - x_3 & z_1 - z_3 \\ x_2 - x_3 & z_2 - z_3 \end{bmatrix} \tag{3.89}$$

3.4.2 Reluctance Network Approach

In the recent years, a lot of research has been done on the modelling of electrical devices by using the *reluctance network approach* (RNA). Part of this research relates to stepping motors [65, 66, 89, 111]. The RNA is simpler than the FEM and does not require a long computation time [134].

©2000 CRC Press LLC

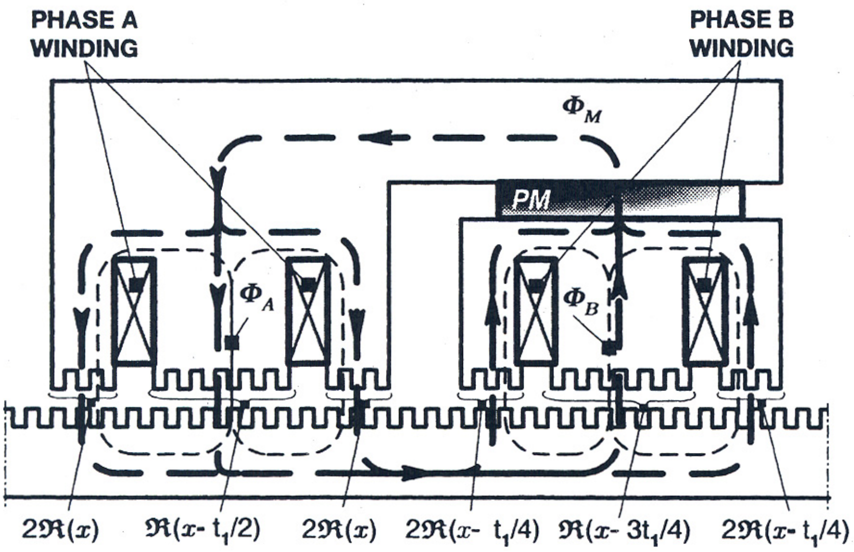

Figure 3.6 The outline of the magnetic circuit of a HLSM.

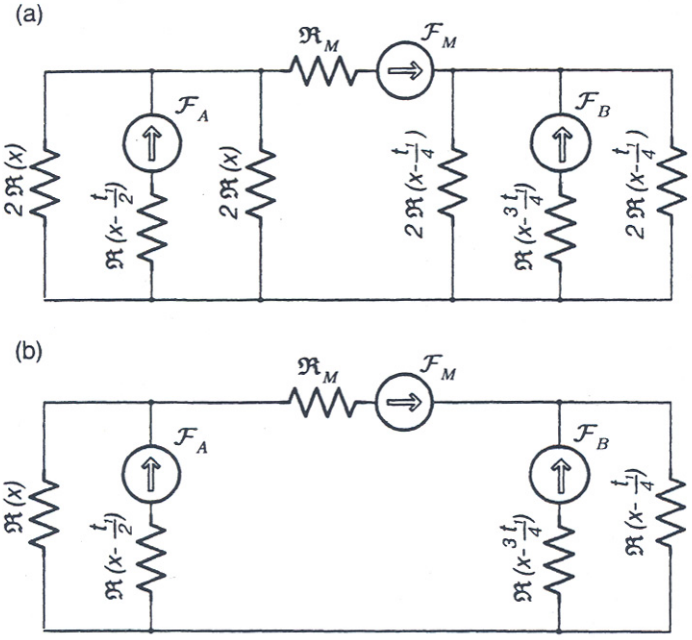

Figure 3.7 Equivalent magnetic circuit of a two-phase HLSM: (a) magnetic circuit corresponding to Fig. 3.6; (b) simplified magnetic circuit with equal numbers of teeth per pole.

As shown in Fig. 3.6, the fluxes of individual poles are dependent on the PM MMF, winding current and reluctances. The PM flux Φ_M circulates in the main loop while the winding excitation fluxes Φ_A and

Φ_B create local flux loops. Apart from these fluxes a leakage flux exists which, takes a path entirely or partially through the air or non-ferromagnetic parts of the forcer. The amount of such a flux is small as compared with the main flux and can, therefore, be neglected. The equivalent magnetic circuit is shown in Fig. 3.7a.

After further simplification, the magnetic circuit can be brought to that in Fig. 3.7b, in which the F_M, F_A and F_B are MMFs of the PM and phase windings A and B, respectively, $\Re(x)$, $\Re\left(x-\frac{1}{2}t_1\right)$, $\Re\left(x-\frac{3}{4}t_1\right)$ and $\Re\left(x-\frac{1}{4}t_1\right)$ are the reluctances of a single pole which vary with tooth alignments and t_1 is the tooth pitch.

Since a highly permeable steel is used in both the forcer and platen, only the airgap and PM reluctances are taken into account. For a pole consisting of n teeth, the reluctance of the airgap corresponding to one pole is

$$\Re = \frac{\Re_t}{n} = \frac{1}{nG_t} = \frac{1}{G} \tag{3.90}$$

where $\Re_t = 1/G_t$ stands for the reluctance of the airgap corresponding to one tooth pitch t_1. The calculated reluctance of the airgap over one tooth pitch is shown in Fig. 3.8. For unsaturated magnetic circuit ($\mu \to \infty$) as in Figs 3.9c and d all flux lines are perpendicular to ferromagnetic surfaces. As the teeth begin to saturate, the flux paths in the air change their shapes.

Toothed surface of the forcer and platen involves the permeance variation with respect to the linear displacement x according to a periodical function. The following cosinusoidal approximation can be used [20]:

$$G_t(x) = \frac{1}{2}\left[\left(G_{\max} + G_{\min}\right) + \left(G_{\max} - G_{\min}\right)\cos\frac{2\pi}{t_1}x\right] \tag{3.91}$$

where the maximum permeance $G_{\max}$ and minimum permeance $G_{\min}$ can be expressed as

$$G_{\max} = \mu_0 L_i\left[\frac{c}{g} + \frac{2}{\pi}\ln\left(1 + \frac{\pi b}{2g}\right)\right] \tag{3.92}$$

$$G_{\min} = \mu_0 L_i\left[\frac{b-c}{g + 0.25\pi(b-c)} + \frac{8}{\pi}\ln\frac{g + 0.25\pi b}{g + 0.25\pi(b-c)}\right] \tag{3.93}$$

and c and b are tooth and slot width, respectively. The approximation can further help finding the derivative of reluctance with regard to the displacement, i.e.,

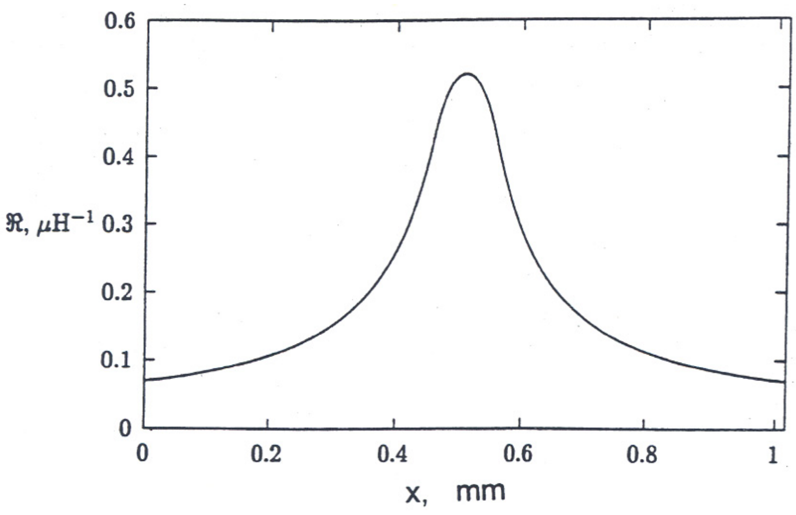

Figure 3.8 Airgap reluctance distribution over one tooth pitch.

$$\frac{\partial G_t}{\partial x} = -\frac{\pi}{t_1}(G_{\max} - G_{\min})\sin\frac{2\pi}{t_1}x \tag{3.94}$$

The calculated permeance of the airgap over one tooth pitch t_1 and its cosinusoidal approximation [20] are plotted in Fig. 3.10.

The PM can be modelled as an MMF source F_M in series with an internal reluctance $\Re_M$ of the PM

$$F_M = \frac{B_r h_M}{\mu_0 \mu_{rrec}}, \qquad \Re_M = \frac{2h_M}{\mu_0 \mu_{rrec} S_M} \tag{3.95}$$

where B_r is the remanent flux density, h_M is the length per pole of the PM in the polarization direction, μ_{rrec} is the relative recoil permeability equal to the relative permeability of the PM and S_M is the cross-section area of the PM.

The MMFs for phase A and B are simply expressed as

$$F_A = Ni_A, \qquad F_B = Ni_B \tag{3.96}$$

where *N* is the number of turns per phase (per coil). The windings are assumed to be identical.

For the micro-stepping mode (Chapter 4) the phase current waveform of the HLSM can be regarded as sinusoidal. A third harmonic of the amplitude I_{m3} has been added or subtracted in order to suppress detent effects. The phase current waveforms are given as follows [31]:

$$i_A = I_{m1}\cos\left(\frac{2\pi x}{t_1} - \phi\right) \pm I_{m3}\cos\left(\frac{6\pi}{t_1} - 3\phi\right) \tag{3.97}$$

©2000 CRC Press LLC

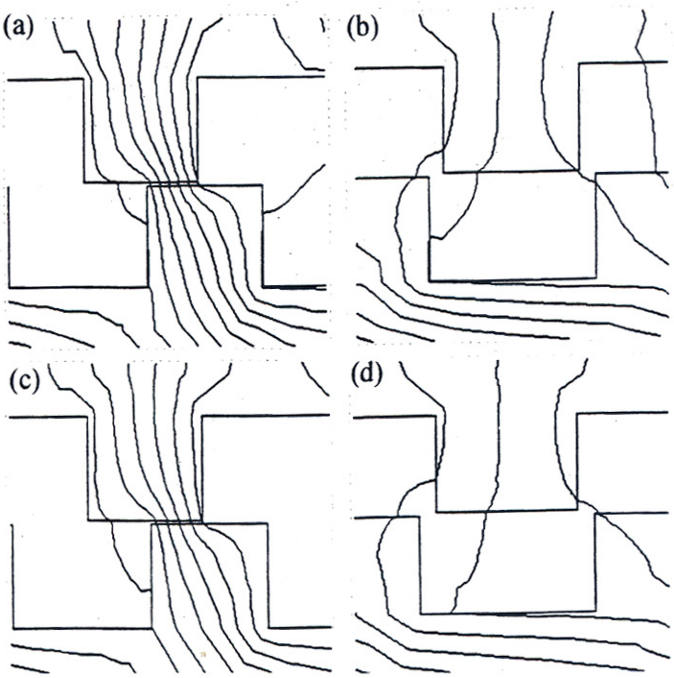

Figure 3.9 Flux patterns: (a) partially aligned teeth (saturated magnetic circuit), (b) complete misalignment of teeth (saturated magnetic circuit), (c) partially aligned teeth (unsaturated magnetic circuit), (d) complete misalignment of teeth (unsaturated magnetic circuit).

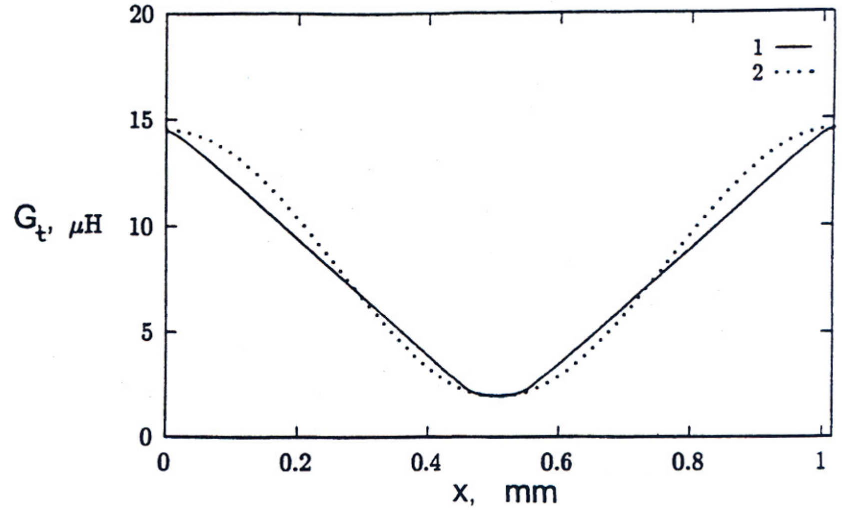

Figure 3.10 Comparison of calculated permeance (FEM) of the airgap over one tooth pitch t_i with its sinusoidal approximation. 1 - unsaturated permeance per pole, 2 - cosinusoidal approximation according to eqn (3.91).

©2000 CRC Press LLC

$$i_B = I_{m1}\sin\left(\frac{2\pi x}{t_1} - \phi\right) \pm I_{m3}\sin\left(\frac{6\pi}{t_1} - 3\phi\right) \qquad (3.98)$$

where ϕ is the phase angle which depends on the load.

The tangential force per pole is

$$F_{dxp} = \frac{1}{2}\Phi^2\frac{\partial\Re}{\partial x} = -\frac{1}{2n}\Phi^2\left[\frac{1}{G_t^2}\frac{\partial G_t}{\partial x}\right] \qquad (3.99)$$

where Φ is the magnetic flux through the pole and $\Re$ is the reluctance per pole according to eqn (3.90). Thus, for a $2p$ pole HLSM, the overall available tangential force is

$$F_{dx} = 2pF_{dxp} = -\frac{p}{n}\Phi^2\left[\frac{1}{G_t^2}\frac{\partial G_t}{\partial x}\right] \qquad (3.100)$$

The normal force can be written in the form of the derivative of co-energy W with respect to the airgap z = g i.e.,

$$F_{dz} = \frac{\partial W}{\partial z} = -\frac{p}{n}\Phi^2\left[\frac{1}{G_t^2}\frac{\partial G_t}{\partial z}\right] \qquad (3.101)$$

and the following simplification can be made [31]

$$\frac{\partial\Re}{\partial z} = \frac{1}{nG_t^2}\frac{\partial G}{\partial z} = \frac{\Re_{\max} - \Re_{\min}}{g_{\max} - g_{\min}} \qquad (3.102)$$

where $\Re_{\max} = 1/G_{\max}$ and $\Re_{\min} = 1/G_{\min}$.

To calculate either the tangential or normal force, it is always necessary to find the magnetic flux Φ on the basis of the equivalent magnetic circuit (Fig. 3.7).

3.4.3 Experimental Investigation

An experimental investigation into a small electrical machine requires a high accuracy of measurements. All the measured parameters need to be transformed into measurable electric signals. Considerable efforts need to be normally made to eliminate all sources of electromagnetic noise which would cause the electromagnetic interference (EMI) problem.

The fundamental steady state characteristics are: (1) the *force* versus *displacement* characteristic which gives the relationship between the tangential force and displacement from the equilibrium position; (2) the *force* versus *current* characteristic which shows how the maximum static force (holding force) increases with the peak excitation current. Unlike in a variable reluctance motor, the static force appears even at current free state (*detent force*).

Table 3.4 Design data of the tested L20 HLSM manufactured by *Parker Hannifin Corporation, Compumotor Division,* Rohnert Park, CA, U.S.A. [21].

Specification data	Value
Number of coils	4
Number of turns per coil	57
Wire diameter	0.452 mm
Tooth width	0.4572 mm
Slot width	0.5588 mm
Length of forcer	117.475 mm
Mass of forcer	0.8 kg
Material of forcer	laminated steel 0.35 mm thick
Platen width	49.53 mm
Platen tooth pitch	1.016 mm
Airgap (mechanical clearance)	0.0127 mm
Peak phase current	2.7 A
PM material	NdFeB (B_r = 1.23 T)
PM height	2.54 mm
PM face area	273.79 mm^2
Accuracy (worst case)	± 0.09 mm
Repeatability	± 0.0025 mm

The instantaneous force is recorded by measuring the output force when the motor is driven in two-phase on excitation scheme and reaches its steady state operation. It is recommended to apply different excitation current profiles at different resolution settings.

The stepping resolution of the HLSM has no significant influence on the amplitude of the both tangential and normal ripple forces. Both harmonic-added and harmonic-subtracted schemes work equally well in reducing the amplitude of force ripple. However, in the case of normal force, there is better improvement when subtracting the $3\,rd$ harmonic from the current profile than when adding it. It has also been found that the amplitude of tangential force ripple increases with the increase in phase current. The relation between them is not so linear as reported [89]. Higher order harmonics cannot be neglected when the magnetic circuit becomes highly saturated.

The transient performance measurements are focused on the acceleration (start-up) and deceleration (braking). The start-up tests can simply be done by supplying power to the HLSM and recording the motor's acceleration. The time interval from the instant at which the power is switched on to the instant at which the HLSM reaches steady state speed is called the *start-up setting* time. For a typical HLSM it is about 1 s to reach its steady state speed at no load. As expected, somewhat longer time will be needed when certain load is applied. The braking time is also inversely proportional to the attached mass.

©2000 CRC Press LLC

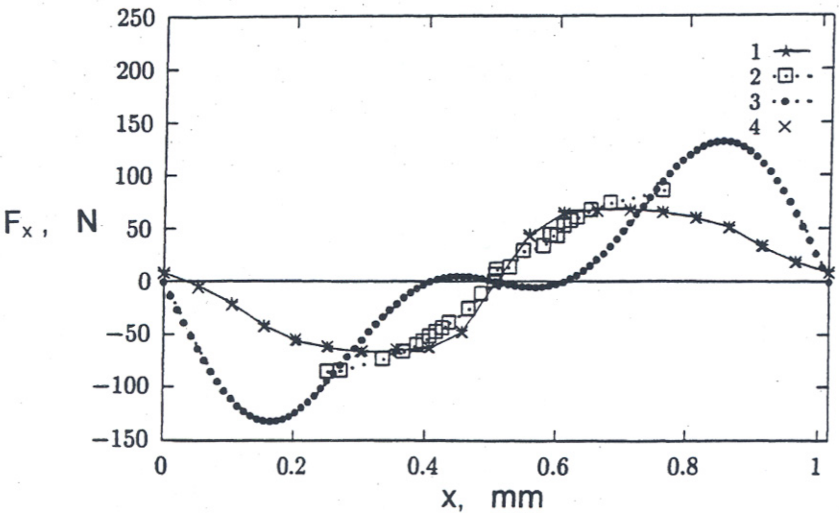

Figure 3.11 Tangential force versus displacement (when one phase of the motor is fed with 2.7 A current): 1- FEM, 2- measurements, 3- RNA, 4- Maxwell stress tensor.

Case Study

The L20 HLSM manufactured by *Parker Hannifin Corporation, Compumotor Division,* Rohnert Park, CA, U.S.A. [21] has been tested experimentally. The specification data of the L20 HLSM are given in Table 3.4. Then, its characteristics obtained from measurements have been compared with the FEM and RNA results.

The following static characteristics have been considered: (1) static force versus forcer position and (2) holding force versus peak phase current when only one phase of the HLSM is fed with peak phase current. The results obtained from the FEM, RNA and measurements are shown in Figs 3.11 and 3.12. It can be seen that the maximum holding force obtained from the FEM, measurements and RNA are 70 N, 85 N and 120 N, respectively (Fig. 3.11). The FEM (Coulomb's approach) results correlate well with the experimental results in the case of static characteristics. The RNA tends to overestimate the force since simplifications have been made to calculate the force.

The instantaneous characteristics of the HLSM refer to the output tangential force versus motor position when the HLSM has been powered up and reaching its steady state. A set of different excitation current waveforms have been used both in testing and computations. They are pure-sine waves and quasi-sinusoidal waves with 4% and 10% of the 3rd harmonics added, respectively.

©2000 CRC Press LLC

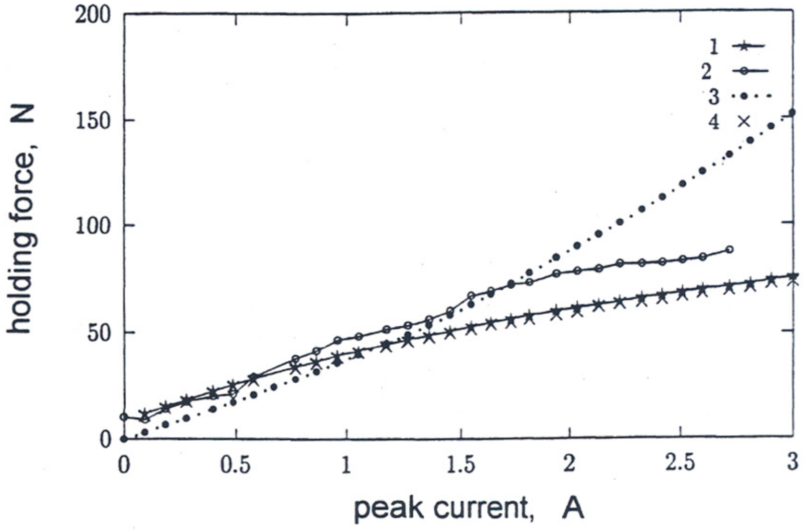

Figure 3.12 Holding force versus peak current when only one phase is fed. 1 - FEM (Coulomb's approach), 2 - measurements, 3 - RNA, 4 – FEM (Maxwell stress tensor).

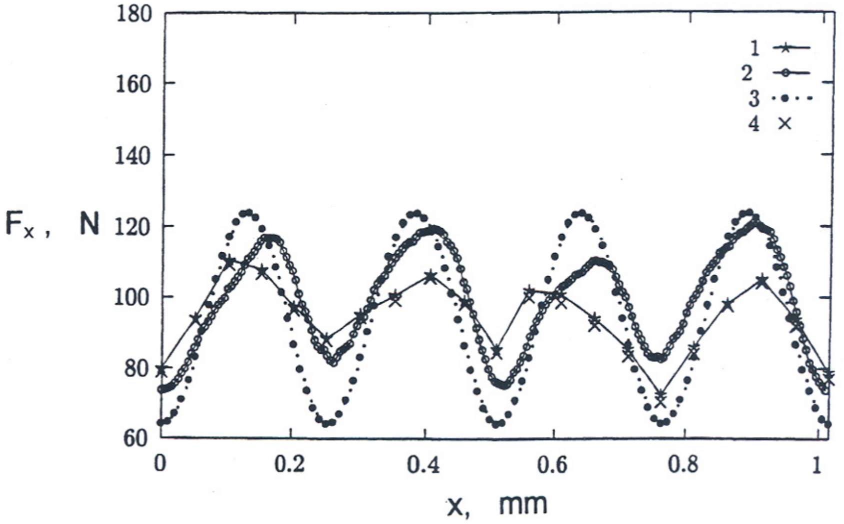

Figure 3.13 Instantaneous tangential forces versus displacement (when the phase A of the HLSM is driven with pure sine wave and phase B with pure cosine wave). 1 - FEM (Coulomb's approach), 2 - measurements, 3 - RNA, 4 - FEM (Maxwell stress tensor).

©2000 CRC Press LLC

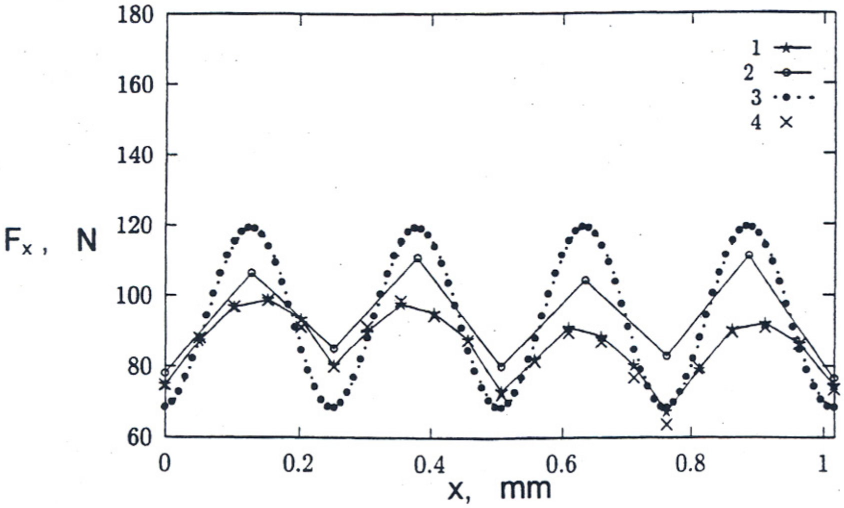

Figure 3.14 Instantaneous tangential force versus displacement (when 10% of the 3rd harmonic has been injected into the phase current). 1 – FEM (Coulomb's approach), 2 - measurements, 3 - RNA, 4 - FEM (Maxwell stress tensor).

The results obtained from both the FEM and RNA are then compared with measurements, as shown in Figs 3.13 and 3.14. Since the HLSM operated at a constant speed of 0.0508 m/s, the force-time curves could be easily transformed to force-displacement curves. In general, the RNA tends to overestimate the force versus displacement as compared with the measured values, while virtual work method gives more accurate (although underestimated) results. However, the RNA is a very efficient approach from the computation time point of view.

Fig. 3.15 shows the amplitude of tangential force ripple plotted against the peak current. This has been obtained by calculating the maximum force ripple for each peak value of the excitation current.

Owing to the existence of the PM, there is a strong normal force between the forcer and platen even when the HLSM is unenergized (Fig. 3.16). It can also be seen in Fig. 3.16 that the normal force is very sensitive to the small change in the airgap. The FEM results show that the normal force (Fig. 3.17) almost doubled when the HLSM is energized (peak phase current 2.7 A). In this case the RNA gives fairly close results to the FEM.

©2000 CRC Press LLC

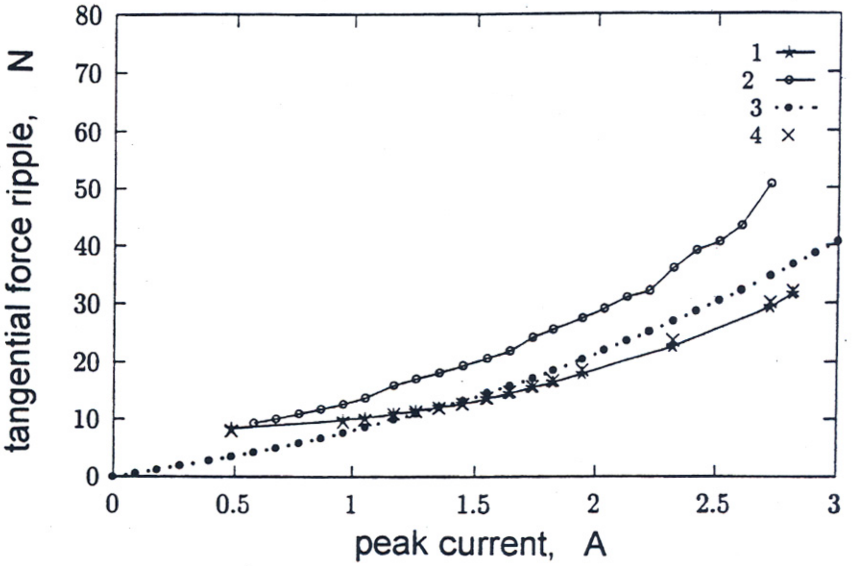

Figure 3.15 Tangential force ripple amplitude as a function of peak current: 1- FEM (Coulomb's approach), 2 - measurements, 3 - RNA, 4 – FEM (Maxwell stress tensor).

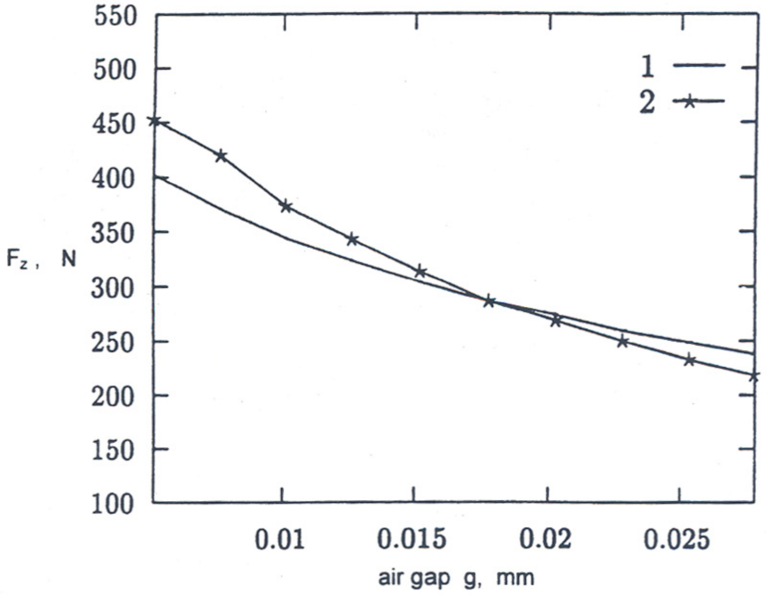

Figure 3.16 Calculated normal force between forcer and platen versus air-gap length at current free state: 1 - FEM (Coulomb's approach), 2 - RNA.

©2000 CRC Press LLC

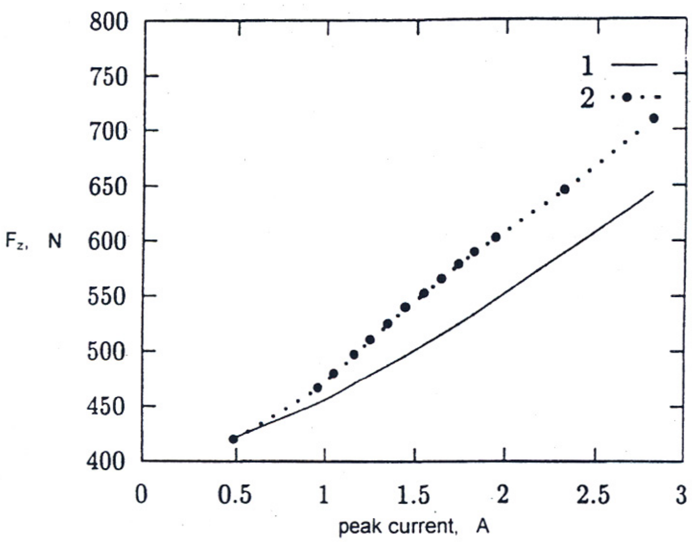

Figure 3.17 Normal force versus peak current: 1- FEM (Coulomb's approach), 2 - RNA.

An accurate prediction of forces is necessary not only for the motor design purposes but also for predicting the performance of a HLSM drive system. Both the FEM and RNA give the results very close to the test results. The accuracy of the FEM much depends on the discretization of the airgap region while the accuracy of the RNA depends on the evaluation of reluctances. The existence of PMs and toothed structure is the main factor for generating ripple forces. The reduction of ripple forces is necessary to obtain a smooth operation of the motor and minimize the audible noise. The force ripple can be suppressed by modifying the input current waveforms. HLSMs with adjustable current profiles offer new techniques of motion control.

3.5 Switched Reluctance Motors

The inductance of a *linear switched reluctance motor* (Fig. 1.19) can be approximated by the following function (see also eqn 3.91):

$$L(x) = \frac{1}{2}(L_{\max} + L_{\min}) - \frac{1}{2}(L_{\max} - L_{\min})\cos\frac{\pi}{T}x \ = L_O - \frac{1}{2}(k_L - 1)L_{\min}\cos\frac{\pi}{T}x \qquad (3.103)$$

where

$$L_O = \frac{1}{2}(L_{\max} + L_{\min}) \qquad (3.104)$$

$$k_L = \frac{L_{\max}}{L_{\min}} \qquad (3.105)$$

$L_{\max}$ is the maximum inductance (armature and platen poles are aligned) and $L_{\min}$ is the minimum inductance (complete misalignment of armature and platen poles).

©2000 CRC Press LLC

If the magnetic saturation is negligible, the electromagnetic thrust (in the *x*-direction) according to eqns (1.8) and (1.10) is

$$F_{dx} = \frac{dW}{dx} = \frac{1}{2} I_a^{\,2} \frac{dL(x)}{dx} = F_{\max} I_a^{\,2} \sin \frac{\pi}{T} x \tag{3.106}$$

where

$$F_{\max} = \frac{1}{4} \frac{\pi}{\tau} (k_L - 1) L_{\min} \tag{3.107}$$

The electromagnetic thrust of a 1inear switched reluctance motor is directly proportional to the armature current squared $I_a^{\,2}$ and the ratio k_L of maximum to minimum inductance and it is inversely proportional to the pole pitch τ. Eqns (3.106) and (3.107) do not take into account the current waveform shape (current turn-on and turn-off instants).

©2000 CRC Press LLC

chapter 4

Motion Control

4.1 Control of a.c. Motors

Control variables are classified into input variables (input voltage, input frequency), output variables (speed, angular displacement, torque) and internal variables (armature current, magnetic flux). The mathematical model of an a.c. motor is nonlinear which for small variations of the input voltage, input frequency and output speed can be linearized.

Scalar control methods are based on changing only the amplitudes of controlled variables. A typical example is to maintain constant torque (magnetic flux) of a.c. motors by keeping constant V / f ratio. The scalar control can be implemented both in the *open loop* (most of industrial applications) and *closed loop* control system with the speed feedback.

In the *vector oriented control* method (Fig. 4.1) both the amplitudes and phases of the space vectors of variables are changed. The vector control based upon the *field orientation* principle uses the analogy between the a.c. (induction or synchronous) motor and d.c. commutator motor. The active and reactive currents are decoupled, which in turn, determine the thrust and magnetic flux, respectively.

Standard controllers have a fixed structure and constant parameters. However, the parameters of electric motors are variable, e.g., winding resistances are temperature dependent and winding inductances are magnetic saturation dependent. Consequently, the deterioration of the dynamic behavior of the drive can even lead to its unstability. In *adaptive controllers* variable parameters or structure are adjusted to the change in parameters of the drive system.

In *a self-tuning adaptive control* the controller parameters are tuned to adapt to the drive parameter variation. In a *model reference adaptive control* the drive response is forced to track the response of a reference model irrespective of the drive parameter variation. This can be achieved by storing the fixed parameter reference model in the computer memory. Some model reference control methods are based on *search strategy*.

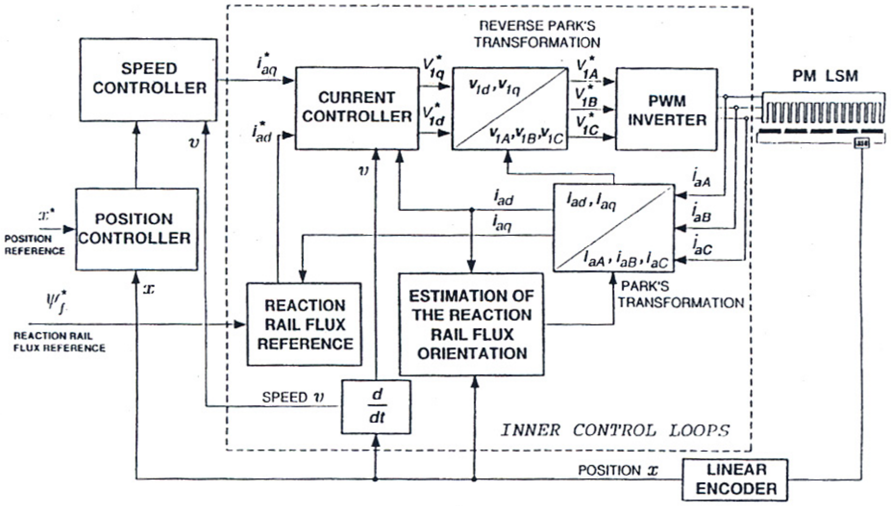

Figure 4.1 Vector oriented control of an a.c. motor.

©2000 CRC Press LLC

The *sliding mode control* is a variable structure control technique, similar to the adaptive model reference control. In a sliding mode control the response of the drive system is insensitive to the parameter and load variations. Thus, this method is suitable for servo drives, e.g., machine tools, robots, factory automation systems, etc. The drive system is forced to 'slide' along the so called *predefined trajectory* in the *state space* by a switching control algorithm independently of change in its parameters and load.

The above classical control methods use a mathematical model of the controlled system, either in the form of a transfer function or in the form of state space equations. Neural and fuzzy logic control are based on *artificial intelligence* and do not need any mathematical models.

The *neural control* applies an *artificial neural network* as a controller or emulator of the dynamic system. The artificial neural network is a network of artificial neurons which simulate the nervous system of the human brain. Each neuron in a single layer is connected with all neurons of the neighboring layers with the aid of so-called *synapses*[1] The neural controller with its associative property memory can create a nonlinear relationship between its input and output values. Since there is no flux estimator, the input-output relationship has to be trained on a sufficient number of samples. The training can be performed either on-line or off-line.

A controller that is based on *fuzzy logic* uses the experience and intuition of a human plant operator. The memory of a fuzzy controller creates fuzzy logic rules, e.g., if the speed of a LSM is *slow* and the reference speed is *fast,* then set the input signal (frequency) *high.* The main advantage of fuzzy control is that a strictly nonlinear or unknown system can be controlled by linguistic variables. Plants which are difficult to model using conventional parameter identification techniques can be controllable by implementing the *human expert knowledge.*

4.2 EMF and Thrust of PM Synchronous and Brush-less Motors

4.2.1 Sine-Wave Motors

A three-phase (multi-phase) armature winding with distributed parameters produces sinusoidal or quasi-sinusoidal distribution of the MMF. For a sinusoidal distribution of the airgap magnetic flux density, the first harmonic of the excitation flux can be found on the basis of eqn (3.29). The excitation magnetic flux calculated on the basis of the maximum airgap magnetic flux density B_{mg} is then $\Phi_f \approx \Phi_{f^1} =$ (2/π) $L_{iTk_f B_{mg}}$ where the *form factor of the excitation field* $k_f = B_{mg1}/B_{mg}$ is according to eqn (3.13). Assuming that the instantaneous value of EMF induced in a single stator conductor by the first harmonic of the magnetic flux density is $e_{f1} = E_{mf1}\sin(\omega t) = B_{mg1}L_i\upsilon_s\sin(\omega t) = 2\,fB_{mg1}L_{i\tau}\sin(\omega t)$, the *rms* EMF is $E_{mf1}/\sqrt{2} = \sqrt{2}\,fB_{mg1}L_{i\tau} = (1/2)\pi\sqrt{2}\,f(2/\pi)B_{mg1}L_{i\tau}$. For two conductors or one turn $E_{mf1}/\sqrt{2} = \pi\sqrt{2}\,f(2/\pi)B_{mg1}L_{iT}$. For N_1k_{w1} turns, where k_{w1} is the winding factor, the *rms* EMF is

$$E_f \approx E_{f1} = \pi\sqrt{2}\,fN_1k_{w1}\alpha_i k_f B_{mg}L_i\tau$$
$$= \frac{\pi}{\tau}\frac{1}{\sqrt{2}}N_1k_{w1}\Phi_f\upsilon_s = c_E\Phi_f\upsilon_s \qquad (4.1)$$

where 2/π is replaced by α_i and the armature constant is

$$C_E = \frac{\pi}{\tau}\frac{1}{\sqrt{2}}N_1k_{w1} \qquad (4.2)$$

---

[1] In medicine, a synapse is a point at which a nerve charge passes from one basic reaction unit cell to another.

Assuming a negligible difference between d- and q-axis synchronous reactances, i.e., $X_{Sd} \approx X_{Sq}$, the electromagnetic (airgap) power $P_{elm} \approx m_1 E_f I_{aq} = m_1 E_f I_a \cos\Psi$. Note that in academic textbooks the electro-magnetic power is usually calculated neglecting the armature winding

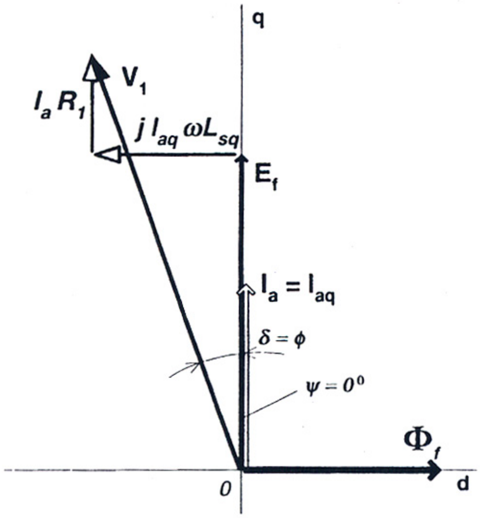

Figure 4.2 Phasor diagram at I_{ad} =0

resistance R_1 as $P_{elm} \approx P_{in} = m_1 V_1 I_a \cos\varphi = m_1 V_1 I_a \cos(\delta + \Psi)$ where $\cos((\delta + \Psi) = E_f \sin\delta / (I_a X_{sd})$ Putting E_f according to eqn (4.1) and $\upsilon_s = 2 f \tau$ the electromagnetic thrust developed by the LSM is:

$$F_{dx} = \frac{P_{elm}}{\upsilon_s} = \frac{m_1 E_f I_a}{\upsilon_s} \cos\Psi$$
$$= m_1 \frac{\pi}{T} \frac{1}{\sqrt{2}} N_1 k_{w1} \Phi_f I_a \cos\Psi = \frac{m_1}{2} C_F \Phi_f I_a \cos\Psi \tag{4.3}$$

where the *thrust constant* is

$$c_F = 2c_E = \frac{\pi\sqrt{2}}{\tau} N_1 k_{w1}$$

The maximum thrust

$$F_{dx\max} = \frac{m_1}{2} c_F \Phi_f I_a \tag{4.4}$$

©2000 CRC Press LLC

is for the angle Ψ = 0° which means that $\delta = \phi$ (Fig. 4.2). In such a case there is no demagnetizing component Φ_{ad} of the armature reaction flux and the airgap magnetic flux density takes its maximum value. The EMF F_f is high so it can better balance the input voltage V_1 thus minimizing the armature current I_a. When $\Psi \approx$ 0°, the low armature current $I_a \approx I_{aq}$ is mainly torque producing. An angle Ψ = 0° results in a decoupling of the rotor flux Φ_f and the armature flux Φ_a.

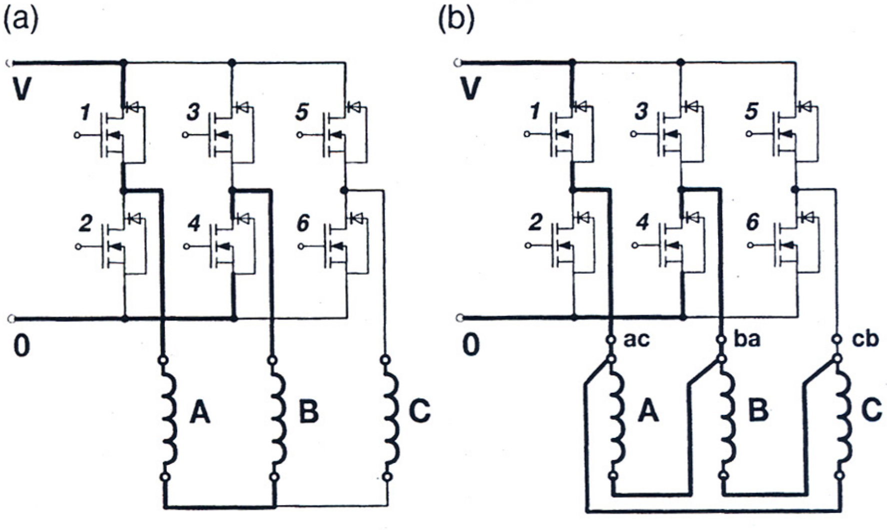

Figure 4.3 IGBT inverter-fed armature circuits of PM LBMs: (a) Y-connected phase windings, (b) Δ-connected armature windings.

4.2.2 Square Wave (Trapezoidal) Motors

PM LBMs predominantly have the reaction rail designed with surface PMs and large effective pole-arc coefficient $\alpha_i^{(sq)} = b_p / \tau$. The three phase armature winding with distributed parameters can be Y or Δ connected. For the Y -connected winding, as in Fig. 4.3, two phases conduct the armature current at the same time.

For a.c. synchronous motors [40]

$$\mathrm{V}_1 = \mathrm{E}_f + \mathrm{I}_{ad}(R_1 + jX_{sd}) + \mathrm{I}_{aq}(R_1 + jX_{sq}) \tag{4.5}$$

Rectangular (trapezoidal) waveforms in the armature winding of an inverter-fed LBM correspond to the operation of a d.c. commutator motor. For a d.c. motor $\omega \to 0$, then eqn (4.5) becomes

$$V = E_f + RI_a^{(sq)} \tag{4.6}$$

where R is the sum of two-phase resistances in series (for Y –connected phase windings), and E_f is the sum of two phase EMFs in series, V is the d.c. input voltage supplying the inverter and $I_a^{(sq)}$ is the flat-top value of the square-wave current equal to the inverter input current.

©2000 CRC Press LLC

For an ideal rectangular distribution of B_{mg} = *const* in the interval of $0 \le x \le \tau$ or from 0 to 180 electrical degrees

$$\Phi_f^{(sq)} = L_i \int_0^\tau B_{mg} dx = \tau L_i B_{mg}$$

Including the pole shoe width $b_p < \tau$ and a fringing flux, the excitation flux is somewhat smaller

$$\Phi_f^{(sq)} = b_p L_i B_{mg} = \alpha_i^{(sq)} \tau L_i B_{mg} \tag{4.7}$$

For a rectangular (trapezoidal) wave excitation, the EMF induced in a single turn (two conductors) is $2B_{mg} L_i \upsilon = 4 f B_{mg} L_i \tau$. Including b_p and fringing flux the EMF for $N_1 k_{w1}$ turns $e_f = 4 f N_1 k_{w1} \alpha_i^{(sq)} \tau L_i B_{mg} = 4 f N_1 k_{w1} \Phi_f^{(sq)}$. For the Y-connection of the armature windings, as in Fig. 4.3a, two phases are conducting at the same time. The EMF contributing to the electromagnetic power is

$$E_f = 2e_f = 8 f N_1 k_{w1} \alpha_i^{(sq)} \tau L_i B_{mg} = \frac{4}{\tau} N_1 k_{w1} \Phi_f^{(sq)} \upsilon = c_{Edc} \Phi_f^{(sq)} \upsilon \tag{4.8}$$

where the armature constant is

$$c_{Edc} = \frac{4}{\tau} N_1 k_{w1}$$

The electromagnetic thrust developed by the LSM is

$$F_{dx} = \frac{p_g}{\upsilon} = \frac{E_f I_a^{(sq)}}{\upsilon} = \frac{4}{\tau} N_1 k_{w1} \Phi_f^{(sq)} I_a^{(sq)} = c_{Fdc} \Phi_f^{(sq)} I_a^{(sq)} \tag{4.9}$$

where $c_{Fdc} = c_{Edc}$ and $I_a^{(sq)}$ is the flat-top value of the phase current. Eqn (4.9) indicates that thrust developed by the PM LBM can be controlled directly by varying the current.
For $\upsilon = \upsilon_s$ and $\Psi = 0^0$ the ratio F_{dx} of a *square-wave motor-to-* F_{dx} of a sinewave motor is

$$\frac{F_{dx}^{(sq)}}{F_{dx}} = \frac{4\sqrt{2}}{\pi m_1} \frac{\Phi_f^{(sq)}}{\Phi_f} \frac{I_a^{(sq)}}{I_a} \tag{4.10}$$

For three-phase motors

$$\frac{F_{dx}^{(sq)}}{F_{dx}} \approx 0.6 \frac{\Phi_f^{(sq)}}{\Phi_f} \frac{I_a^{(sq)}}{I_a} \tag{4.11}$$

4.3 Dynamic Model of a PM Motor

Control algorithms of sinusoidally excited synchronous motors frequently use the *d-q* model of synchronous machines. The *d-q* dynamic model is expressed in a *rotating reference frame* that moves at synchronous speed ω. The time varying parameters are eliminated and all variables are expressed in *orthogonal or mutually decoupled d* and *q* axes.

A synchronous machine is described by the following set of general equations:

$$\upsilon_{1d} = R_1 i_{ad} + \frac{d\psi_d}{dt} - \omega \psi_q \tag{4.12}$$

©2000 CRC Press LLC

$$\upsilon_{1q} = R_1 i_{aq} + \frac{d\psi_q}{dt} + \omega\psi_d \tag{4.13}$$

$$\upsilon_f = R_f I_f + \frac{d\psi_f}{dt} \tag{4.14}$$

$$0 = R_D i_D + \frac{d\psi_D}{dt} \tag{4.15}$$

$$0 = R_Q i_Q + \frac{d\psi_Q}{dt} \tag{4.16}$$

The linkage fluxes in the above equations are defined as

$$\psi_d = (L_{ad} + L_1) i_{ad} + L_{ad} i_D + \psi_f = L_{sd} i_{ad} + L_{ad} i_D + \psi_f \tag{4.17}$$

$$\psi_q = (L_{aq} + L_1) i_{aq} + L_{aq} i_Q = L_{sq} i_{aq} + L_{aq} i_Q \tag{4.18}$$

$$\psi_f = L_{fd} I_f \tag{4.19}$$

$$\psi_D = L_{ad} i_{ad} + (L_{ad} + L_D) i_D + \psi_f \tag{4.20}$$

$$\psi_Q = L_{aq} i_{aq} + (L_{aq} + L_Q) i_Q \tag{4.21}$$

where υ_{1d} and υ_{1q} are d- and q-axis components of terminal voltage, ψ_f is the maximum flux linkage per phase produced by the excitation system, R_1 is the armature winding resistance, L_{ad}, L_{aq} are d- and q-axis components of the armature self-inductance, $\omega = \pi\upsilon_s / \tau$ is the angular frequency of the armature current, τ is the pole pitch, υ_s is the linear synchronous velocity, i_{ad}, i_{aq} are d- and q-axes components of the armature current, i_D, i_Q are d- and q-axes components of the damper current. The field winding resistance which exists only in the case of electromagnetic excitation is R_f, the field excitation current is I_f and the excitation linkage flux is ψ_f The damper resistance and inductance in the d axis R_D and L_D, respectively. The damper resistance and inductance in the q axis is R_Q and L_Q, respectively. The resultant armature inductances are

$$L_{sd} = L_{ad} + L_1, \qquad L_{sq} = L_{aq} + L_1 \tag{4.22}$$

where L_{ad} and L_{aq} are self-inductances in *d* and *q* axis, respectively, and L_1 is the leakage inductance of the armature winding per phase. In a three-phase machine L_{ad} = (3/2) L'_{ad} and L_{aq} = (3/2) L'_{aq} where L'_{ad} and L'_{aq} are self-inductances of a single phase machine.

The excitation linkage flux ψ_f = $L_{fd} I_f$ where L_{fd} is the maximum value of the mutual inductance between the armature and field winding. In the case of a PM excitation, the ficticious current is $I_f = H_c h_M$

For no damper winding, i.e., $i_D = i_Q = 0$, the voltage equations in the d and q-axis are

$$\upsilon_{1d} = R_1 i_{ad} + \frac{d\psi_d}{dt} - \omega\psi_q = (R_1 + \frac{dL_{sd}}{dt})i_{ad} - \omega L_{sq} i_{aq} \tag{4.23}$$

$$\upsilon_{1q} = R_1 i_{aq} + \frac{d\psi_q}{dt} + \omega\psi_d = (R_1 + \frac{dL_{sq}}{dt})i_{aq} + \omega L_{sd} i_{ad} + \omega\psi_f \tag{4.24}$$

The matrix form of voltage equations in terms of inductances L_{sd} and L_{sq} is

$$\begin{bmatrix} \upsilon_{1d} \\ \upsilon_{1q} \end{bmatrix} = \begin{pmatrix} R_1 + \frac{d}{dt}L_{sd} & -\omega L_{sq} \\ \omega L_{sd} & R_1 + \frac{d}{dt}L_{sq} \end{pmatrix} \begin{pmatrix} i_{ad} \\ i_{aq} \end{pmatrix} + \begin{bmatrix} 0 \\ \omega\psi_f \end{bmatrix} \tag{4.25}$$

For the steady state response $(d/dt)L_{sd}i_{ad} = (d/dt)L_{sq}i_{aq} = 0,$ $\mathrm{I}_a = I_{ad} + jI_{aq},$ $\mathrm{V}_1 = V_{1d} + jV_{1q},$ $i_{ad} = \sqrt{2}I_{ad},$ $\upsilon_{1d} = \sqrt{2}V_{1d},$ $E_f = \omega L_{fd} I_f / \sqrt{2} = \omega\psi_f / \sqrt{2}$[34] The quantities wL_{sd} and wL_{sq} are known as the d- and q-axis synchronous reactances, respectively. Eqn (4.25) can be brought to the form (3.34).

The instantaneous power input to the three phase armature is

$$p_{in} = \upsilon_{1A}i_{aA} + \upsilon_{1B}i_{aB} + \upsilon_{1C}i_{aC} = \frac{3}{2}(\upsilon_{1d}i_{ad} + \upsilon_{1q}i_{aq}) \tag{4.26}$$

The power balance equations is obtained from eqns (4.23) and (4.24),i.e.

$$\upsilon_{1d}i_{ad} + \upsilon_{1q}i_{aq} = R_1 i_{ad}^2 + \frac{d\psi_d}{dt}i_{ad} + R_1 i_{aq}^2 + \frac{d\psi_q}{dt}i_{aq} + \omega(\psi_d i_{aq} - \psi_q i_{ad}) \tag{4.27}$$

The last term $\omega(\psi_d i_{aq} + \psi_q i_{ad})$ accounts for the electromagnetic power of a single phase, two pole synchronous machine. For a three phase machine

$$\begin{aligned} p_{elm} &= \frac{3}{2}\omega(\psi_d i_{aq} - \psi_q i_{ad}) = \frac{3}{2}\omega\left[(L_{sd}i_{ad} + \psi_f)i_{aq} - L_{sq}i_{ad}i_{aq}\right] \\ &= \frac{3}{2}\omega\left[\psi_f + (L_{sd} - L_{sq})i_{ad}\right]i_{aq} \end{aligned} \tag{4.28}$$

The electromagnetic thrust of a three phase LSM with P pole pairs is

$$F_{dx} = p\frac{p_{elm}}{\upsilon_s} = \frac{3}{2}p\frac{\pi}{\tau}\left[\psi_f + (L_{sd} - L_{sq})i_{ad}\right]i_{aq} \quad \mathrm{N} \tag{4.29}$$

Compare eqn (4.29) with eqn (3.43).

The relationships between i_{ad}, i_{aq} and phase currents i_{aA}, i_{aB}, and i_{aC} are

$$i_{ad} = \frac{2}{3}\left[i_{aA}\cos\omega t + i_{aB}\cos(\omega t - \frac{2\pi}{3}) + i_{aC}\cos(\omega t + \frac{2\pi}{3})\right] \tag{4.30}$$

$$i_{aq} = -\frac{2}{3}\left[i_{aA} \sin \omega t + i_{aB} \sin(\omega t - \frac{2\pi}{3}) + i_{aC} \sin(\omega t + \frac{2\pi}{3}) \right] \tag{4.31}$$

The reverse relations, obtained by simultaneous solution of eqns (4.30) and (4.31) in conjunction with $i_{aA} + i_{aB} + i_{aC} = 0,$ are

$$\begin{aligned} i_{aA} &= i_{ad} \cos \omega t - i_{aq} \sin \omega t \\ i_{aB} &= i_{ad} \cos(\omega t - \frac{2\pi}{3}) - i_{aq} \sin(\omega t - \frac{2\pi}{3}) \\ i_{aC} &= i_{ad} \cos(\omega t + \frac{2\pi}{3}) - i_{aq} \sin(\omega t + \frac{2\pi}{3}) \end{aligned} \tag{4.32}$$

4.4 Thrust and Speed Control of PM Motors

Thrust-speed envelopes of PM LSMs are classified into two categories: constant thrust (Fig. 4.4a) and constant power (Fig. 4.4b).

For *constant thrust* requirements, the thrust-speed envelope is of a rectangular shape. The maximum thrust $F_{x\max}$ should be obtained at all linear speeds up to the speed V_b. Such envelope is required for linear servo drives and actuators.

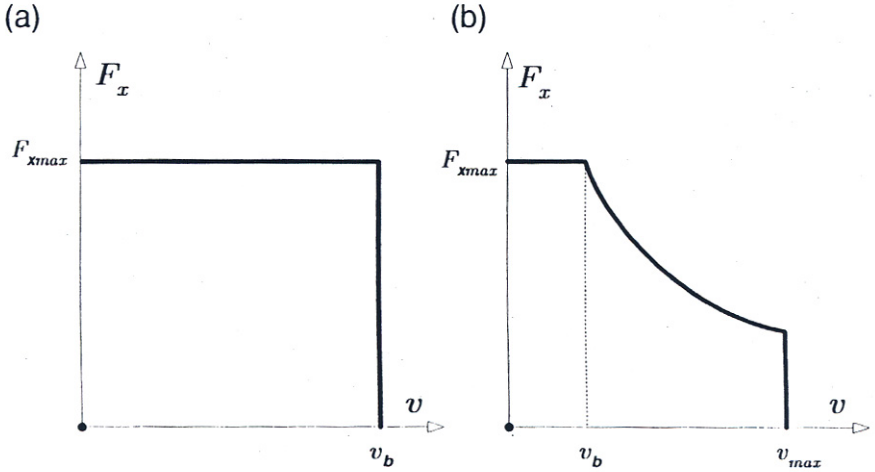

Figure 4.4 Thrust-speed envelopes of LSMs: (a) constant thrust, (b) constant power.

For *constant power* requirements, the thrust-speed envelope is of a hyperbolic shape because $F_x \upsilon = p_{out}$ = *const.* The constant power trajectory is maintained over a wide speed range from the base speed υ_b to the maximum speed $\upsilon_{\max}$ .Such envelope is required for traction linear motors which are used in, e.g., linear motor driven vehicles. A constant power operation is implemented by weakening the excitation flux. Since PM motors do not have field excitation windings, the magnetic flux is weakened by applying appropriate control techniques. It can also be done by hardware, i.e., using a hybrid excitation system which consists of PMs and additional excitation coils placed around PMs.

©2000 CRC Press LLC

Control algorithms are, in principle, similar for both sine-wave and square-wave PM motors. Fig. 4.5 shows how control loops can be developed to achieve thrust, speed and position control in motion control systems with PM LSMs. These cascaded control structures (Fig. 4.5) for LSMs have been based on control structures for rotary PM synchronous motors [60].

Given below are some examples of control of PM LSMs and LBMs.

4.4.1 Open Loop Control

Aluminum shields or mild steel pole shoes of surface PM LSMs are equivalent to damper cage windings. Solid steel poles of buried PMs behave also as dampers. A damper adds a component of asynchronous thrust

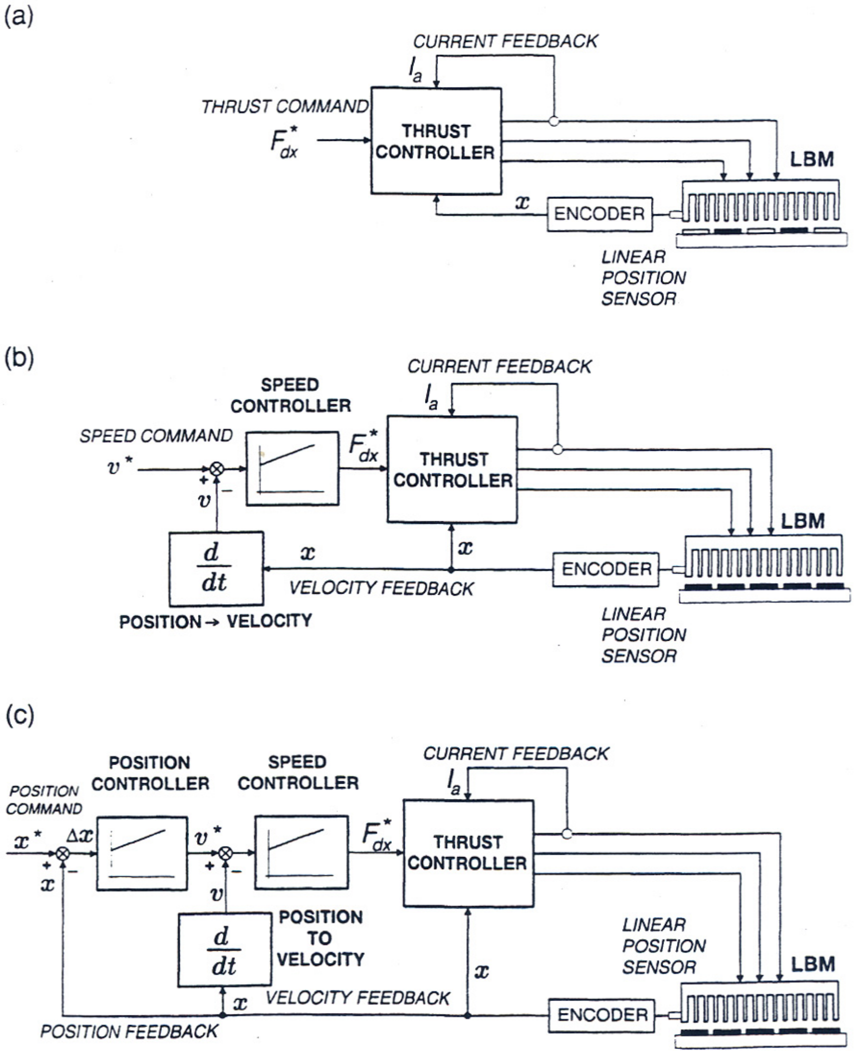

Figure 4.5 Cascaded control loops for PM LSMs: (a) current-regulated thrust control, (b) velocity and thrust control, (c) position, velocity and current control.

©2000 CRC Press LLC

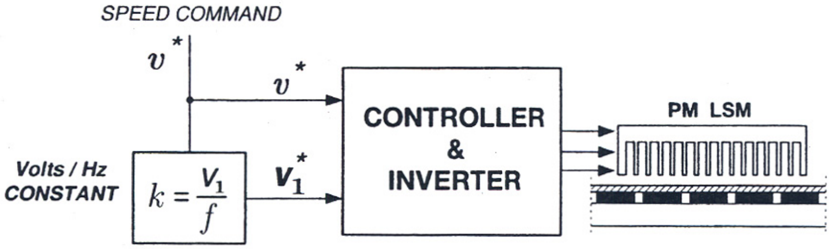

Figure 4.6 Simplified block diagram of open loop *voltage-to-frequency* control of a PM LSM with damper.

production so that the PM LSM can be operated stably from an inverter without position sensors. As a result, a simple *constant voltage-to-frequency* control algorithm (Fig. 4.6) can provide speed control for applications which do not require fast dynamic response. Thus, PM LSM motors can replace LIMs in some variable-speed drives to improve the drive efficiency with minimal changes to the control electronics.

4.4.2 Closed Loop Control

To achieve *high performance motion control* with a PM LSM, a position sensor is typically required. The rotor position feedback needed to continuously perform the self-synchronization function for a sinusoidal PM motor is significantly more demanding than for a square-wave motor. An absolute encoder or resolver is typically required. The second condition for achieving high-performance motion control is high-quality phase current control.

One of the possible approaches is the *vector control* shown in Fig. 4.7.The incoming thrust command F_{dx}^* is mapped into commands for i_{ad}^* and i_{aq}^* current components according to eqn (4.29).

The current commands in the moving reaction rail d-q reference frame (seen as d.c. quantities for a constant thrust command) are then transformed into the instantaneous sinusoidal current commands for the individual armature phases i_{aA}^*, i_{aB}^* and i_{aC}^* using the reaction rail or armature position feedback and reverse Park's transformation equations [34, 58]. Current regulators for each of the three armature current phases then operate to excite the phase windings with the desired current amplitudes. The most common means of mapping the thrust command F_{dx}^* into values for i_{ad}^* and i_{aq}^* is to set a constraint of maximum *thrust-to-current* operation which is nearly equivalent to maximizing operating efficiency [59].

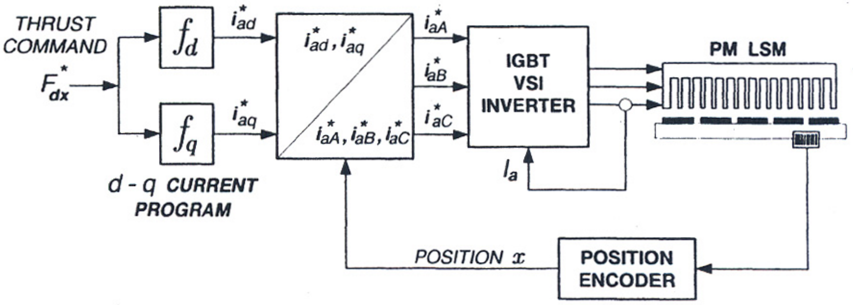

Figure 4.7 Block diagram of high-performance thrust control scheme for PM LSM using vector control concept.

©2000 CRC Press LLC

4.4.3 Zero Direct Axis Current Control

To obtain the thrust proportional to the armature current $i_a = i_{aq}$ and free from the demagnetization of PMs, the PM LSM is driven by the direct axis current $i_{ad} = 0$ control, i.e.,

$$F_{dx} = \frac{3}{2} p \frac{\pi}{\tau} \psi_f i_{aq} \qquad \text{N} \tag{4.33}$$

This means that the angle Ψ between the armature current and q-axis always remains 0° (see the phasor diagram in Fig. 4.2). Eqn (4.33) can also be simply derived assuming sinusoidal space distribution of the excitation magnetic flux density and sinusoidal time varying armature currents including appropriate phase shifts.

4.4.4 Flux-Weakening Control

High coerceivity rare-earth PMs are not affected by the armature reaction flux and they cannot be permanently demagnetized by the armature flux. The d-axis reaction flux can be used for weakening the flux Φ_f produced by PMs. The *flux-weakening control* is similar to the field weakening control of d.c. commutator motors. In PM LSMs the angle Ψ between the armature current and q axis is controlled. The drawback of this control technique is a decrease in the motor efficiency.

The armature current i_a is limited by the maximum current $i_{a\max}$, i.e.,

$$i_a = \sqrt{i_{ad}^2 + i_{aq}^2} \le i_{a\max} \tag{4.34}$$

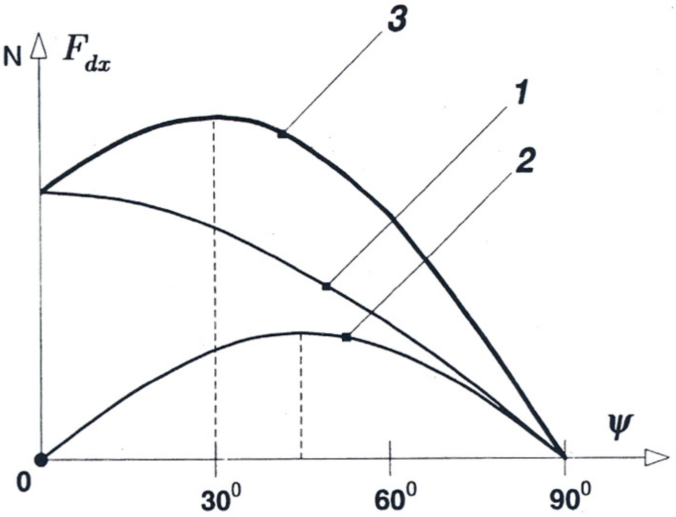

Figure 4.8 Thrust plotted against the angle Ψ : 1 - synchronous thrust, 2 - reluctance thrust, 3 - total thrust.

The maximum current $i_{a\max}$ is a continuous rated armature current for continuous duty cycle or a maximum available current of the inverter during short time duty cycle [116].

The terminal voltage V_1 is limited by the maximum voltage $V_{1\max}$, i.e.,

©2000 CRC Press LLC

$$\upsilon_1 = \sqrt{\upsilon_{1d}^2 + \upsilon_{1q}^2} \leq \upsilon_{1\max} \tag{4.35}$$

The maximum voltage $V_{1\max}$ is the maximum available output voltage of the inverter which depends on the d.c. link voltage [116].

According to eqns (3.43) and (4.29), the thrust has two components: synchronous and reluctance thrust. Fig. 4.8 shows the thrust components of the LSM versus angle Ψ for the flux weakening control. The synchronous thrust is proportional to cos Ψ with maximum at $\Psi = 0°$. The reluctance thrust takes its maximum value at $\Psi = 45°$. There is a critical angle Ψ_{cr} which corresponds to the maximum total thrust. The critical angle $\Psi > 0$ only if the reluctance thrust is produced. In a LSM with $X_{sd} \neq X_{sq}$ the maximum thrust for $\Psi_{cr} > 0$ is greater than the thrust for $i_{ad} = 0$ ($\Psi = 0°$) control.

The thrust-speed characteristics of a LSM for $i_{ad} = 0$ control and flux weakening control are shown in Fig. 4.9.

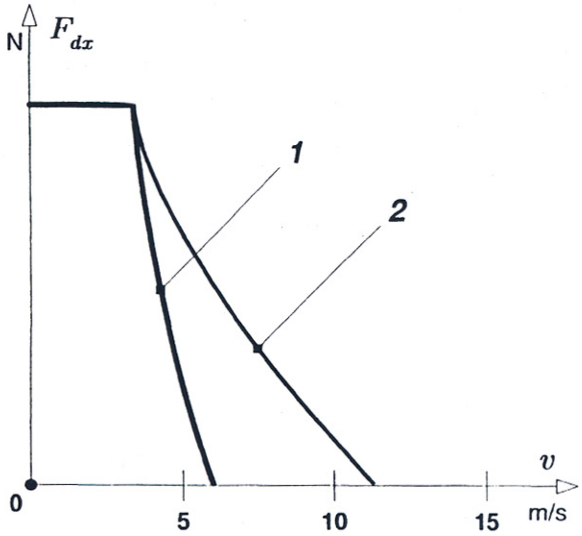

Figure 4.9 Thrust-speed characteristics: 1 - $i_{ad} = 0$ control, 2 – flux weakening control.

4.4.5 Direct Thrust Control

The basic idea of the *direct thrust control* (DTC) is to calculate the armature linkage flux directly from the electromagnetic induction law. The *space phasor* form of the armature voltage equation in the stationary reference frame is

$$\mathrm{v}_1 = R_1 \mathrm{i}_a + \frac{d\psi}{dt} \tag{4.36}$$

The armature linkage flux can be found as [73, 151]

$$\psi = \psi_0 + \int_{t_0}^{t_1} (\mathrm{v}_1 - R_1 \mathrm{i}_a)\, dt \tag{4.37}$$

Since the armature linkage flux is calculated as an integral, an initial value of the armature linkage flux ψ_0 is required. The initial value is

$$\psi_0 = \psi_f \exp\left[j\left(90^0 \pm \Psi\right)\right]$$

where ψ_f is the PM flux to be estimated and ($90^0 \pm \Psi$) is the angle between the armature and excitation linkage fluxes.

Only the armature resistance R_1 space phasor of the armature voltage vector V_1 and space phasor of the armature current i_a is needed to find the armature linkage flux. This on-line integration (4.37) can be made with the aid of a high speed DSP.

Eqn (4.37) shows that the variation of flux ψ depends on the voltage phasor V_1. Thus, the flux can be controlled using the voltage phasor. In DTC, an optimum voltage phasor which makes the flux to rotate and produce the desired thrust needs to be chosen.

Each voltage phasor is constant during each switching interval and eqn (4.36) can be written as

$$\psi = \psi_0 + V_1 t - R_1 \int_{t_0}^{t} i_a dt \tag{4.38}$$

If R_1 is negligible, the armature linkage flux ψ will be following the voltage phasor V_1.

In induction motors, when V_1 = 0, the armature linkage flux ψ is in a stationary position. In PM LSMs at V_1 = 0, the armature flux ψ is not stationary, because there is a relative motion between the armature and excitation system. Zero voltage phasors cannot be used to control the rotation of ψ of PM LSMs.

The thrust of PM LSMs can be controlled by controlling the angle ($90° \pm \Psi$) between the armature and excitation linkage fluxes [73].

Depending on whether the actual thrust is smaller or larger than the reference thrust, the voltage phasors turn the linkage flux in the appropriate direction to increase or decrease the angle ($90° \pm \Psi$) and the thrust. The armature linkage flux always rotates in the direction determined by the output of the hysteresis controller of the thrust [73].

The linkage fluxes ψ_d (k) and ψ_q (k) at the *k*th sampling instant are

$$\psi_{dk} = \psi_{dk-1} + \left(\upsilon_{1dk-1} - R_1 i_{ad}\right) t_s \tag{4.39}$$

$$\psi_{qk} = \psi_{qk-1} + \left(\upsilon_{1qk-1} - R_1 i_{aq}\right) t_s \tag{4.40}$$

$$\psi_k = \sqrt{\psi_{dk}^2 + \psi_{qk}^2} \tag{4.41}$$

where the subscript k-l denotes previous samples and t_s is the sampling period.

The electromagnetic thrust of a LSM is expressed by eqn (4.29). The end effect can be included by multiplying the thrust by a coefficient k_{end} < 1 which takes into account the thrust reduction due to the end effect. Thus

$$F_{dx} = \frac{3}{2} p k_{end} \frac{\pi}{\tau} \left(\psi_d i_{aq} - \psi_q i_{ad}\right) \tag{4.42}$$

The i_{ad} and i_{aq} currents are obtained from the measured three-phase currents i_{aA}, i_{aB}, i_{aC} and the V_{1d} and V_{1q} voltages are calculated on the basis of the d.c. link voltage. The block diagram of the DTC control is shown in Fig. 4.10 [73].

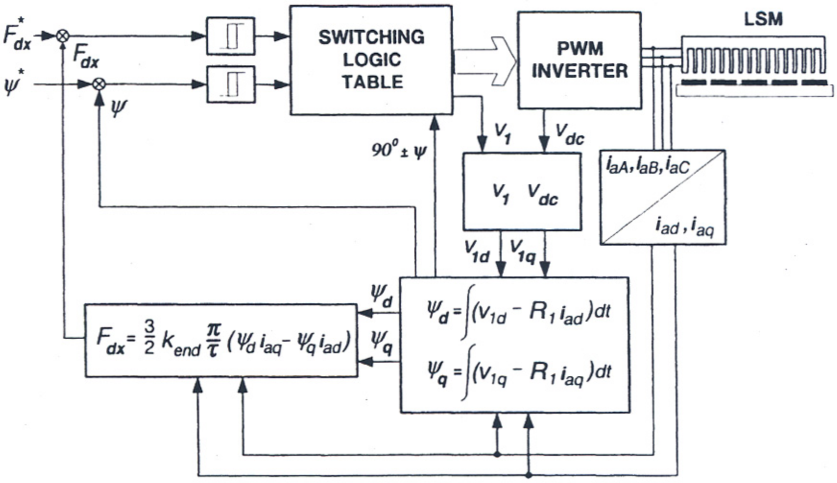

Figure 4.10 Block diagram of direct thrust control of a PM LSM.

4.4.6 Fuzzy Control

Fuzzy control of a PM LSM or LBM can be implemented according to the block diagram shown in Fig. 4.11. Two fuzzy controllers have been applied: for position and for speed control. A vector control is used in the power circuit with a current controlled VSI.

4.5 Control of Hybrid Stepping Motors

4.5.1 Microstepping

When a stepping motor is driven in its *full-stepping* mode and two phases are energized simultaneously (Fig. 4.12a), the thrust available on each step is approximately the same. In the *half-stepping mode,* two phases and then only one are energized (Fig. 4.12b). If there is the same current in full-stepping and half-stepping modes, in each case a greater thrust is produced where two phases are energized simultaneously. This means that stronger thrust an weaker thrust are produced in each alternate step. The useful thrust is limited by the weaker step, however, there will be a reduction of low speed pulsations over the full step mode.

Approximately equal thrust in every step can be obtained by supplying a higher current when only one phase is energized (Fig. 4.13). The motor will not get overheated because it is designed to operate with two phases to be energized simultaneously. Since the winding losses are

©2000 CRC Press LLC

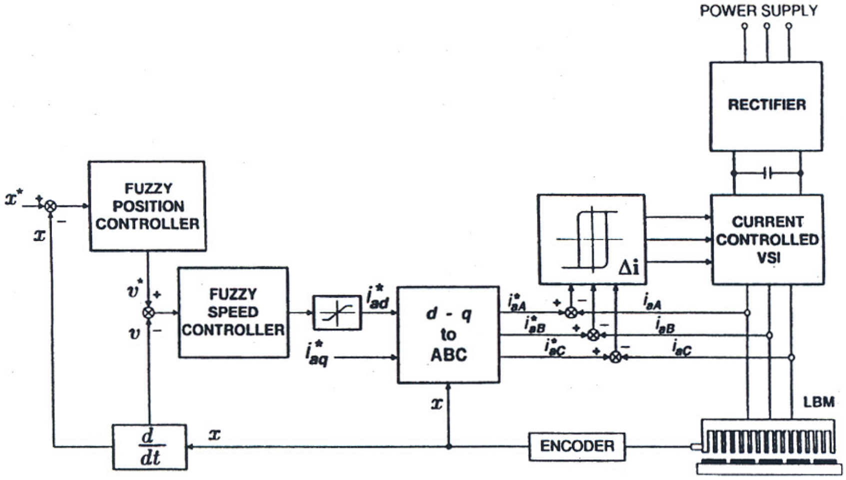

Figure 4.11 Fuzzy control of a PM LSM or LBM.

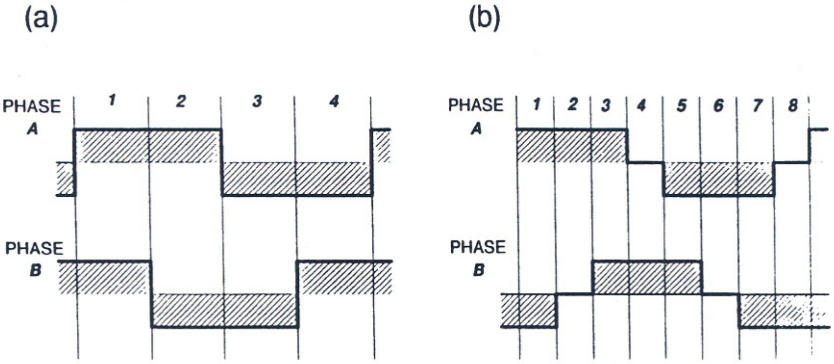

Figure 4.12 Phase current waveforms: (a) full-stepping, two phases on, (b) half-stepping.

©2000 CRC Press LLC

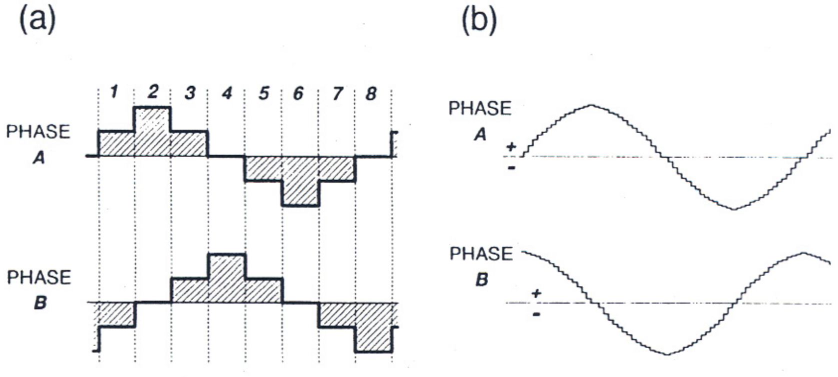

Figure 4.13 Phase current waveforms to produce approximately equal thrust: (a) half-step current, profiled, (b) microstepping mode.

proportional to the current squared, approximately the same winding losses are dissipated if two phases are fed at the same time or if only one phase is fed with current increased by $\sqrt{2}$.

The same currents in both two phases produce an intermediate step equal to half of that for only one phase being energized. With unequal two phase currents, the position of platen will be shifted towards the stronger pole. This effect is utilized in the *microstepping* controller which subdivides the basic motor step by proportioning the current in the two phase winding (Fig. 4.13b). Thus, the step size is reduced and the operation at low speeds is very smooth. The motor in its microstepping mode operates similar to a two-phase synchronous motor and can even be driven directly from 50 or 60 Hz sinusoidal power supply, provided that a capacitor is connected in series with one phase.

The advantages of microstepping a linear stepping motor include [21]:

- higher resolution for positioning accuracy,
- smoothness at low speeds,
- wide speed range,
- minimal force loss at resonant frequencies.

4.5.2 Electronic Controllers

To obtain the best performance at minimum settling time (Fig. 4.14) an *accelerometer feedback* is added which provides electronic damping to the motor [21]. Accelerometer damping is recommended for HLSM applications which require:

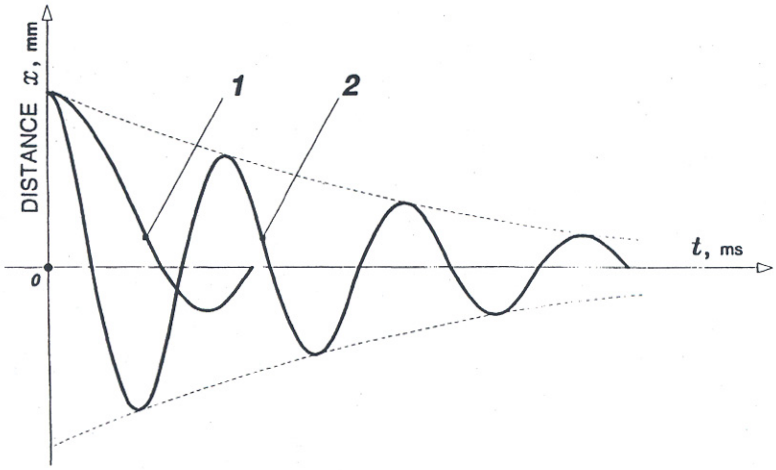

Figure 4.14 HLSM settling time. 1 - with accelerometer, 2 – without accelerometer.

- very short settling time (Fig. 4.14),
- repetitive moves or periodic acceleration transients,
- maximum force utilization.

The block diagram of an HLSM controller is shown in Fig. 4.15. Power amplifiers of bipolar type are current controlled and use about 20 kHz fixed frequency and PWM. The resolution is from 50 to 125 microsteps per full step [21].

4.6 Precision Linear Positioning

Linear motors are now playing a key role in *advanced precision linear positioning* [14]. Linear *precision positioning systems* can be classified into open loop systems with HLSMs and closed loop servo systems with LSMs, LBMs or LIMs (Fig. 4.16).

A PM LBM (or LSM) driven *positioning stage* is shown in Fig. 4.17 [105]. A stationary base is made of aluminum, steel, ceramic or granite plate. It provides a stable, precise and flat platform to which all stationary positioning components are attached. The base of the stage is attached to the host system with the aid of mounting screws.

The *moving table* accommodates all moving positioning components. To achieve maximum acceleration, the mass of the moving table should be as small as possible and usually aluminum is used as a lightweight material. A number of mounting holes on the moving table is necessary to fix the payload to the mounting table.

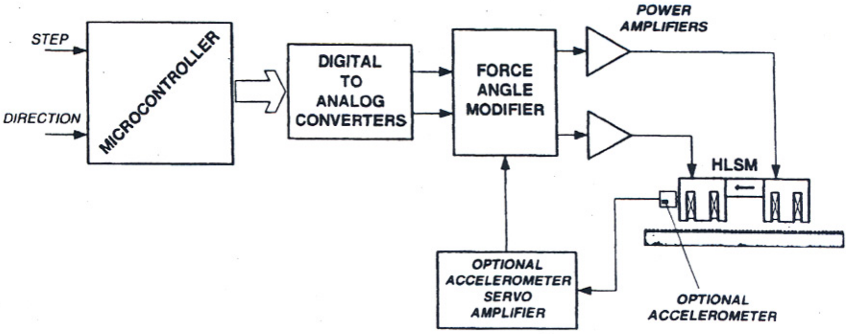

Figure 4.15 Block diagram of a HLSM controller.

Linear bearing rails provide a precise guidance to the moving table. Minimum one bearing rail is required. Linear ball bearing or air bearings are attached to each rail.

The armature of a linear motor is fastened to the moving table and reaction rail (PM excitation system) is built in the base between rails (Fig. 4.17).

A linear encoder is needed to obtain precise control of position of the table, velocity and acceleration. The readhead of encoder is attached to the moving table.

Non-contact limit switches fixed to the base provide an over-travel protection and initial homing. A cable carrier accommodates and routes electrical cables between the moving table and stationary connector box fixed to the base.

An HLSM driven linear precision stage is of similar construction. Instead of PMs between bearing rails it has a variable reluctance platen. HLSMs usually need air bearings and, in addition to the electrical cables, an air hose between air bearings and compressor is required. Comparison between a HLSM and LSM of similar size with air bearings is given in [61].

An *enclosed linear positioning stage* shown in Fig. 4.18 is equipped with bellows covers (protection against dust and debris), in addition to components sketched in Fig. 4.17 [105].

Linear positioning stages with moving *coreless armature windings* arranged vertically are shown in Fig. 4.19. Fig. 4.19a shows a stage with one moving armature [132], while Fig. 4.19b shows a *twin armature stage*

©2000 CRC Press LLC

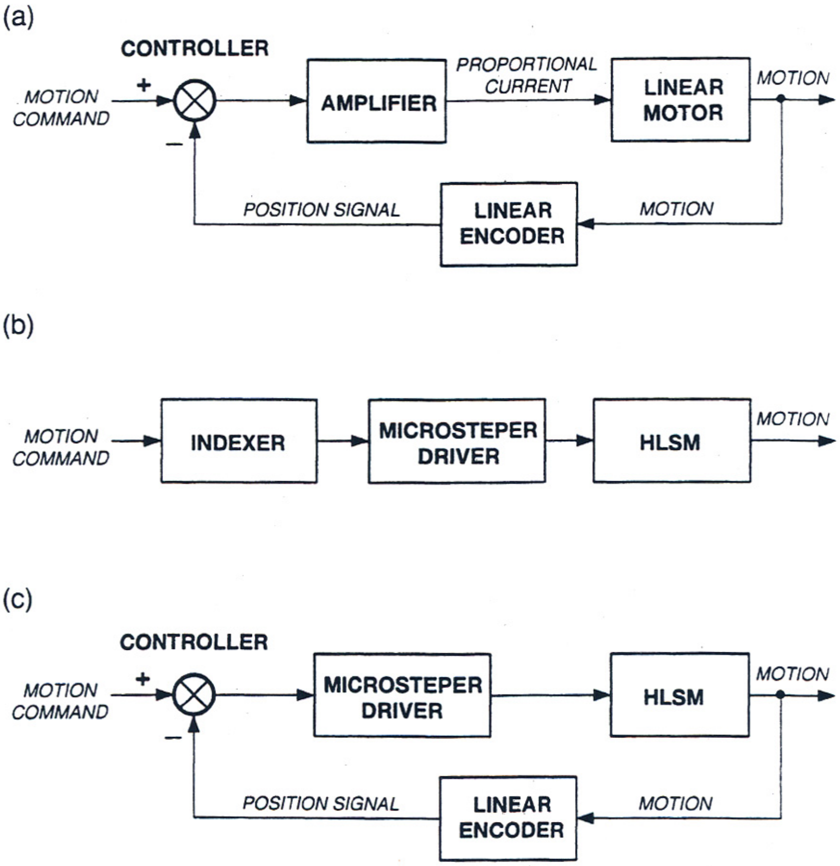

Figure 4.16 Typical linear positioning systems: (a) closed loop servo system with a.c. or d.c. linear motors, (b) open loop positioning system with HLSMs, (c) closed loop positioning system with HLSMs.

©2000 CRC Press LLC

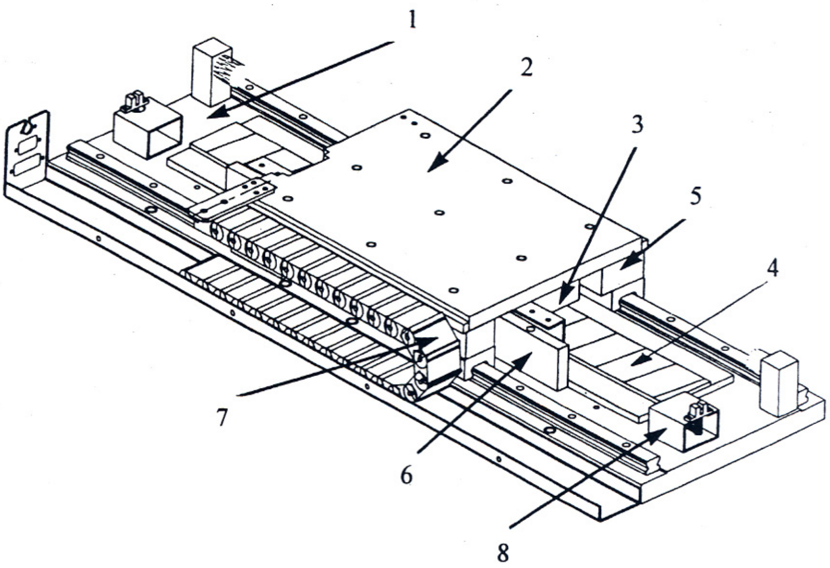

Figure 4.17 Linear positioning stage driven by PM LBM: 1 – base , 2 –moving table, 3 - armature of LBM, 4 – PMs , 5- linear bearing , 6- encoder , 7 - cable carrier, 8 - limit switch. Courtesy of *Normag,* Santa Clarita, CA, U.S.A.

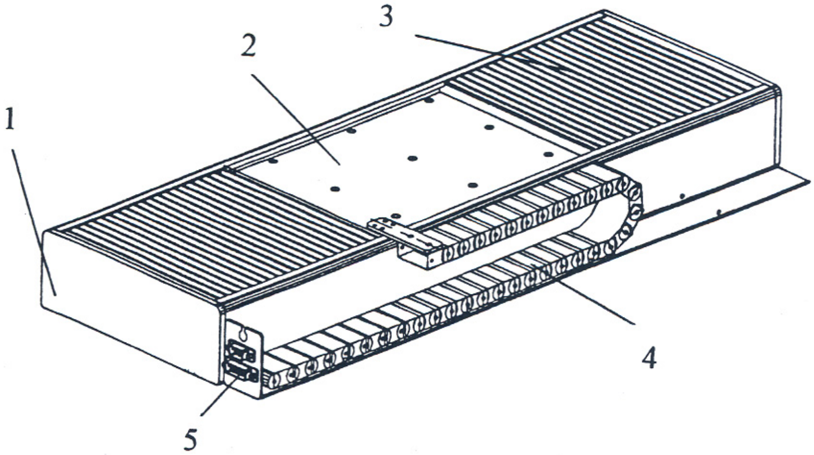

Figure 4.18 Enclosed linear positioning stage. 1 – base, 2 - moving table, 3 - bellows cover, 4 - cable carrier, 4 - input/output terminals. Courtesy of *Normag,* Santa Clarita, CA, U.S.A.

©2000 CRC Press LLC

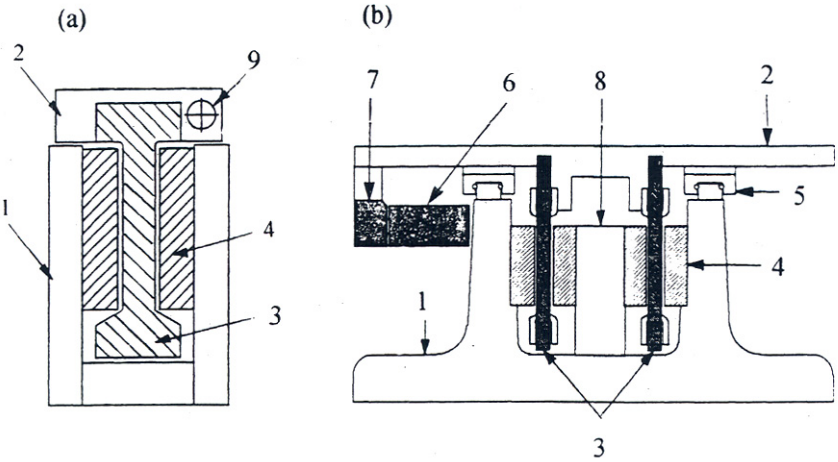

Figure 4.19 Linear positioning stages with moving coreless armature windings: (a) single armature, (b) twin armature. 1 – base , 2 - moving table, 3 - armature of LBM, 4 - PMs, 5 - linear bearing, 6 - linear scale of encoder, 7 - readhead of encoder, 8 - yoke, 9 - cable.

[11] A coreless moving armature does not have any ferromagnetic materials so that the positioning stage does not produce any cogging thrust. Moreover, a lightweight moving armature provides high speed response and high acceleration.

It is possible to employ more than two linear motors in parallel Fig. 4.20a shows a linear positioning stage with three moving coreless armature windings while Fig. 4.20b shows a similar construction with four stationary armature windings and three moving PM excitation systems [3]. Fig. 4.21 shows *a multilayer positioning stage* with five moving PM excitation systems [3].

The FEM modeling indicates that the magnetic flux density distribution along the airgap of multilayer LSMs is nonuniform [3]. Any nonuniformity in the magnetic field distribution causes different values of EMFs induced in coils which are distributed along the armature. Consequently, the current density distribution in the armature winding is also nonuniform which can cause local overheating of the armature system.

Linear positioning stages are used in semiconductor technology, electronic assembly, quality assurance, laser cutting, optical scanning, water jet cutting, gantry systems (x, y, z stages), color printers, plotters and Cartesian coordinate robotics [132].

Fig. 4.22 shows an application of a linear positioning stage according to Fig. 4.19b to a recorder [11]. The table driven by a twin armature LSM or LBM moves along the rotating drum. The optical recording head fixed to the moving table writes data on the track of the recording film.

©2000 CRC Press LLC

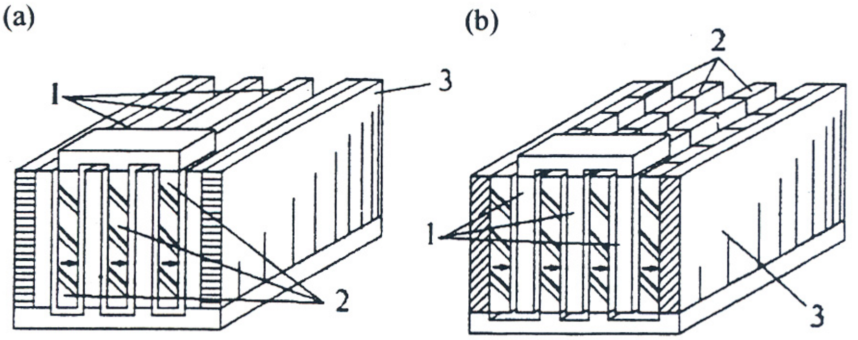

Figure 4.20 Triple linear positioning stages with moving: (a) PMs, (b) coreless armature windings. 1 - coreless armature winding, 2 - PMs, 3 – base. Courtesy of *Technical University of Szczecin*, Poland and *Institute of Electrodynamics of UNAS*, Kiev, Ukraine.

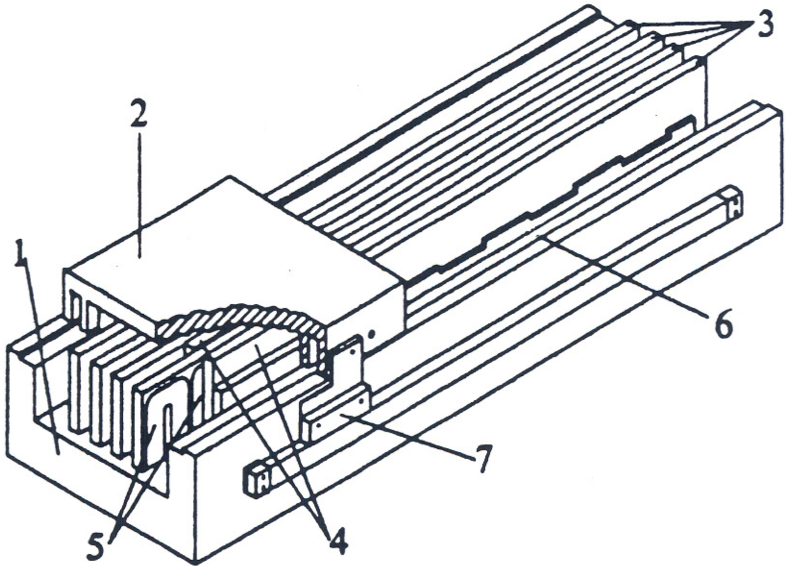

Figure 4.21 Multilayer linear positioning stage. 1 - base, 2 – moving table, 3 - armature, 4 - PMs, 5 - armature coils, 6 - linear bearing, 7 - readhead of linear encoder. Courtesy of *Technical University of Szczecin*, Poland and *Institute of Electrodynamics of UNAS*, Kiev, Ukraine.

©2000 CRC Press LLC

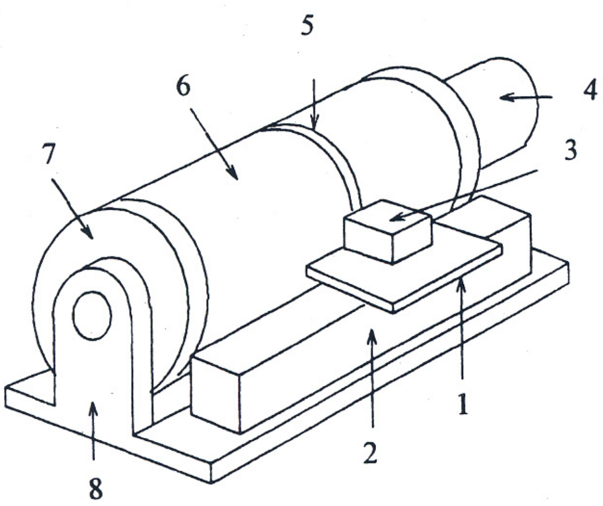

Figure 4.22 Recorder with a linear positioning stage. 1 - moving table, 2 - base of positioning stage, 3 - recording head, 4 - rotary motor, 5- recording track, 6 - recording film, 7 - rotary drum, 8 - pedestal. Courtesy of *Hitachi Metals Ltd*, Saitama, Japan.

The mass of recording head is 2 kg and the width of track is 1.4 mm. The recording head while writing data must keep constant position with high accuracy $\pm 1\mu m$. After writing, the head needs to move quickly to the next track and settle down within 20 ms. The maximum speed and maximum acceleration are 0.22 m/s and 44 m/s^2, respectively [11].

©2000 CRC Press LLC

chapter 5

Sensors

5.1 Linear Optical Sensors

The encoder functioning as a feedback device is one of the basic components of motion control systems. There are three different sensor technologies used in linear servo applications, i.e., inductive, magnetic and optical. The earliest linear encoders utilized in high precision machines, e.g., in metal-cutting industry, were optical. Although other techniques are now also available, optical encoders are still predominant in industrial applications. In linear motor drives, where precision actuation and measurement is involved, most designers employ an incremental optical encoder as a well-accepted part of the electromechanical drive system. The typical optical encoder makes use of a graduated *scale* which is scanned by a movable optical *readhead* . The most important advantage of optical encoders is their easily achievable non-contact operation which eliminates friction and wear and permits reliable high speed performance in workshop environments. Linear optical encoders are capable of achieving very *high resolution* , in some cases comparable to the *laser interferometer technology* . Their accuracy is a few orders of magnitude higher than that of similar magnetic or inductive linear encoders. This is possibly due to the superior precision of *interpolation* performed on much smaller scale grating periods. The interpolation is a self-subdivision process of the signal representing the scale period.

5.1.1 Incremental Encoders

There are two basic methods of generating optical encoder signals. In the first method the *transmitted light* is processed (Fig. 5.1a), while the second method employs the *reflected light* (Fig. 5.1b).

The simplest configuration of an optical encoder is described below. The light emitted by an LED either travels through, or reflects off the scale. It is then directed through an identical index grating and onto photo detectors, which generate electrical currents. Twin signals s_1 and

©2000 CRC Press LLC

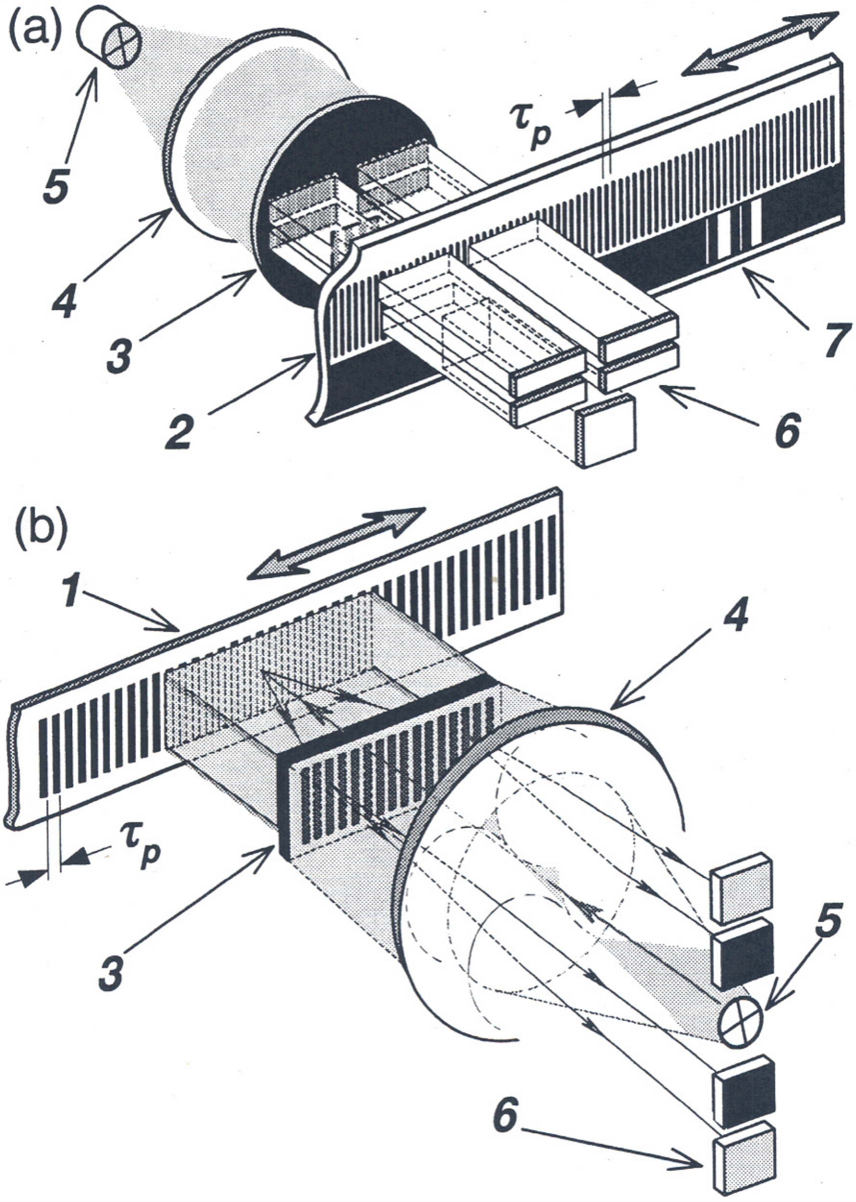

Figure 5.1 Typical scanning methods: (a) transmitted light method, (b) reflected light method. 1 -scale reflective tape, 2 - scale transparent glass,3 - scanning reticle, 4 - condenser lens, 5 - light source (LED), 6 -photodetectors,7 - reference mark.

©2000 CRC Press LLC

s_2, 90° out of phase representing sine and cosine waveforms are generated. These operation principles of the optical incremental encoder are illustrated in Fig. 5.2. The photo detector reads the maximum luminous intensity when transparent slots of the scale fully align with transparent slots of the scanning reticle. The light source and the photo detectors move along the glass scale grating. In consequence, the transparent slots of the scanning reticle change periodically their position relative to the stationary slots of the scale. Therefore, the light intensity detected by the photo sensors (photo elements) changes its value from maximum to zero according to a sinusoidal function (Fig. 5.2). Because the photo elements are displaced at the distance of one quarter of the grating period τ_p of the scale, when one photo element detects maximum, the other one reads only half of that. This displacement effectively shifts the two signals s_1 and s_2 by 90° apart in the time domain. The 90° electrical separation or one quarter of the period between the two signals is referred to as the *quadrature* . Signals in the quadrature permit determination of the motion direction and speed at the same time allowing additional resolution through the *edge counting* .

Linear motors employed in the x-y positioning stages and used in harsh factory or workshop environments require precise resolution with high reliability. The combination of a reflective, flexible scale tape placed along the track, and the read head moving over the tape offers many unique features.

The scale is made out of the steel ribbon 5 to 10 mm wide and 0.2 mm thick, which has relatively low stiffness. Other materials, such as glass, mylar, or non-ferrous metal tapes can also be used. The scale is grated with alternating reflective strips (often made out of gold) and light absorbing spaces. The grating period ranges from 100 to less than 20 μ_m, and after interpolation, resolution up to 0.1 μ_m is possible. The scale can be secured to the most commonly used materials (metals, composites and ceramics) by means of a double-sided, elastic adhesive tape to accommodate the thermal expansion of the base. However, the mounting surface should be relatively smooth, clean and parallel to the axis of motion with the scale ends rigidly fixed to the axis of substrate. The location of stationary scale and moving read head mounted on a positioning stage is shown in Fig. 5.3. The differential movement between the scale and the substrate should be close to zero, even in the presence of large temperature gradients. Usually, the scale tape is protected by varnish coating to facilitate easy cleaning. Scale tapes are generally supplied on a reel for 'cut-to-suit' convenience. For comparison, glass scales reach maximum length of 3 m in a single piece. Usually, the incremental tapes are installed together with the reference marks. Limit switches are separately installed next to the scale itself. These home position and/or zero point indicators for the end of travel are also sensed by the

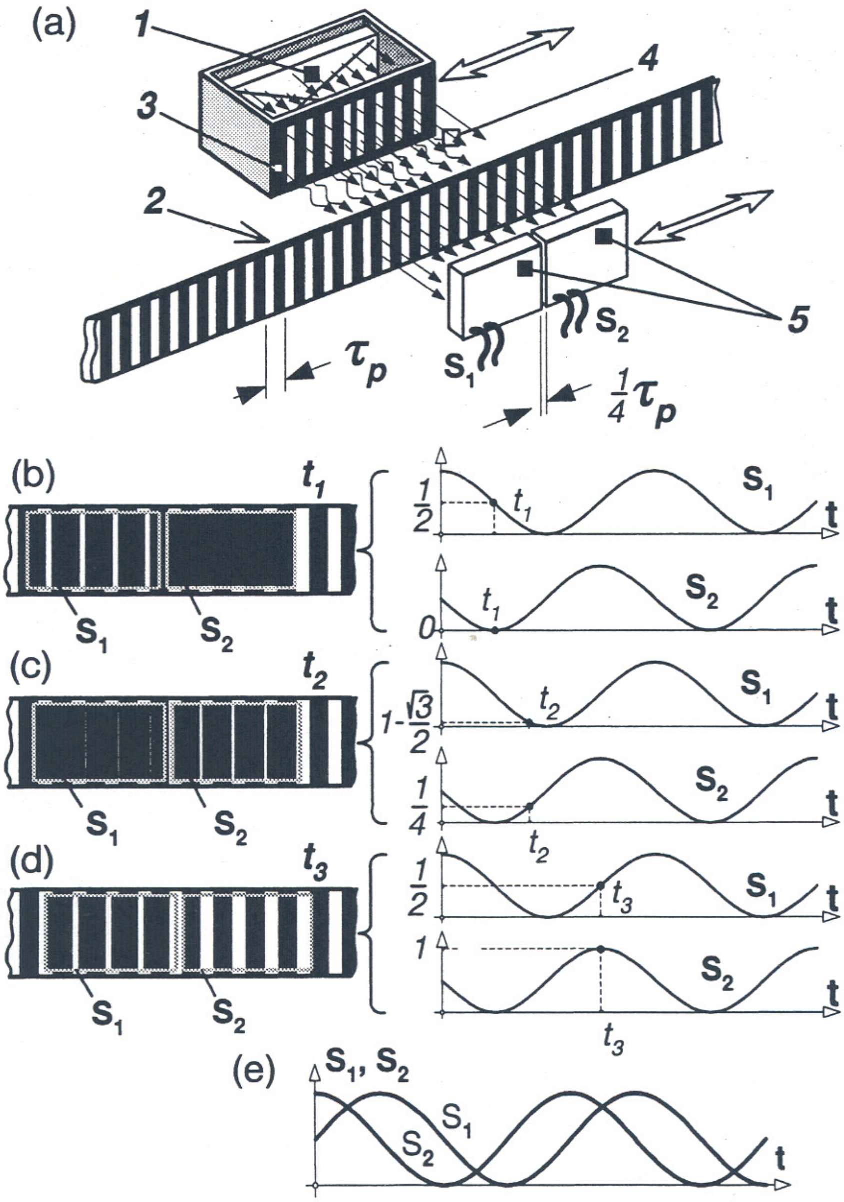

Figure 5.2 Generation of photo detector signals: (a) photoelectric scanning principles; (b),(c), (d) instants of relative position of scale gratings and scanning reticle; (e) variation of signals. 1 - light source (LED), 2 - glass scale grating, 3 - scanning reticle, 4 - light rays, 5 – photo detectors.

©2000 CRC Press LLC

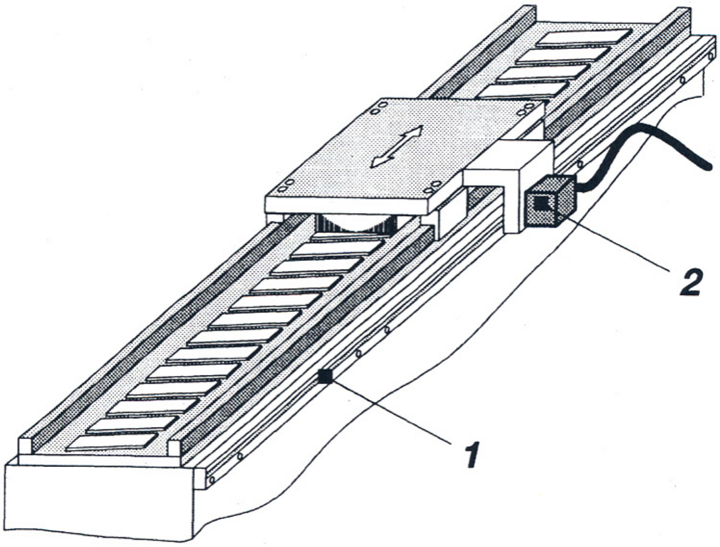

Figure 5.3 Typical location of the linear encoder installed in the positioning stage driven by a linear motor. 1 - scale, 2 – read head.

scanning read head. The signals are synchronized with the incremental channels to guarantee repeatability.

The principle of scanning process can be exemplified by the LIDA linear encoder which was introduced to the market in 1977 by *Heidenhain GmbH* , Traunreut, Germany [49]. The operation of LIDA encoder is explained in Fig. 5.1b. The redhead travels along the scale, while a light beam emitted by an LED source is directed onto the incremental scale grating through a condenser lens and four scanning reticles. Then, it is reflected, and after passing back through the reticles, it is focused onto the photoelectric cells. Photo sensors detect changes in the light intensity caused by the interaction between the scale and reticle gratings. The four sinusoidal scanning signals, corresponding to the changes in the light intensity, are produced by the sensors. These waveforms with 90° phase shift enable formulation of symmetrical encoder zero output signals.

To improve the accuracy, especially in the high precision positioning applications within microelectronics industry, encoders frequently use the interferential scanning principles. The diffracted (interferential) light method is required in the optical encoders with grating periods $\tau_p < 8\,\mu\text{m}$. These devices employ a reflection-type diffraction grating fixed the carrier (Fig. 5.4). An infrared LED emits light onto angular scale facets where it is scattered back into the read head through the transparent grating. The periodic pattern on the scale and the periodic indexing of the grating produce sinusoidal interference fringes at the photo detector plane. The fringes move across the detector plane as read head moves along the scale. The arrangement of interlaced groups of photo detectors positioned in repeating patterns generates electric signals related to the fringe movement. The read head electronics processes these signals and generates two sinusoidal waveforms of equal amplitude with the phase shift of 90°. In RGH encoders manufactured by *Renishaw plc* the signal is averaged from over 80 facets in the detector plane. Therefore, the loss of a number of scale facets has only a marginal effect on the signal's amplitude and does not affect the counting process. Furthermore, because the signal is often subjected to disturbing effects (contamination or minor damage to the scale), the filtering and averaging process ensures its stability. In essence, the electronics within the read head eliminates signals which do not match the scale period of $20\,\mu\text{m}$.

The electronics embedded in the read head converts scanned incremental signals into analog or digital sinusoidal waveforms in the quadrature (Fig. 5.5a). The signal period is equal to the scale pitch. The wave formats follow industry standard outputs: micro current (in μ A) or voltage (1 V peak-to-peak). The read head generates incremental square pulse trains in the quadrature which conform to the standard EIA/RS422 differential line drive output (Fig. 5.5b). These fine resolution digital waveforms are obtained by the subdivision of the analog signal passed from the read head optics. In this context, the resolution is defined as the distance between consecutive edges of the digitized pulse trains. Commercially available read heads typically achieve the resolution of 5.0, 1.0, 0.5 or 0.1 μ m. The read head interpolation is ratio metric, i.e., it is independent of the signal amplitude.

For digital output read heads, the recommended counter clock frequency for a given traversing speed is:

$$f = \frac{v_{tr}}{\tau_p} k_{sf} \tag{5.1}$$

where v_{tr} is the traversing speed, τ_p is the read head resolution, f is the counter clock frequency of interpolation electronics, and k_{sf} , is the safety factor, typically k_{sf} = 4. If v_{tr} is in m/s and τ_p is in μ m, the counter clock frequency f is in MHz.

Specification of incremental self-adhesive scale RGS-S produced by *Renishaw plc* , Gloucestershire, U.K., is shown in Table 5.1 and Fig. 5.6. Specifications of analog and digital read heads RGH series used in conjunction with RGS-S tape are presented in Table 5.2 and Table 5.3. The edge separation characteristics typical for digital read heads are shown in Fig. 5.7.

©2000 CRC Press LLC

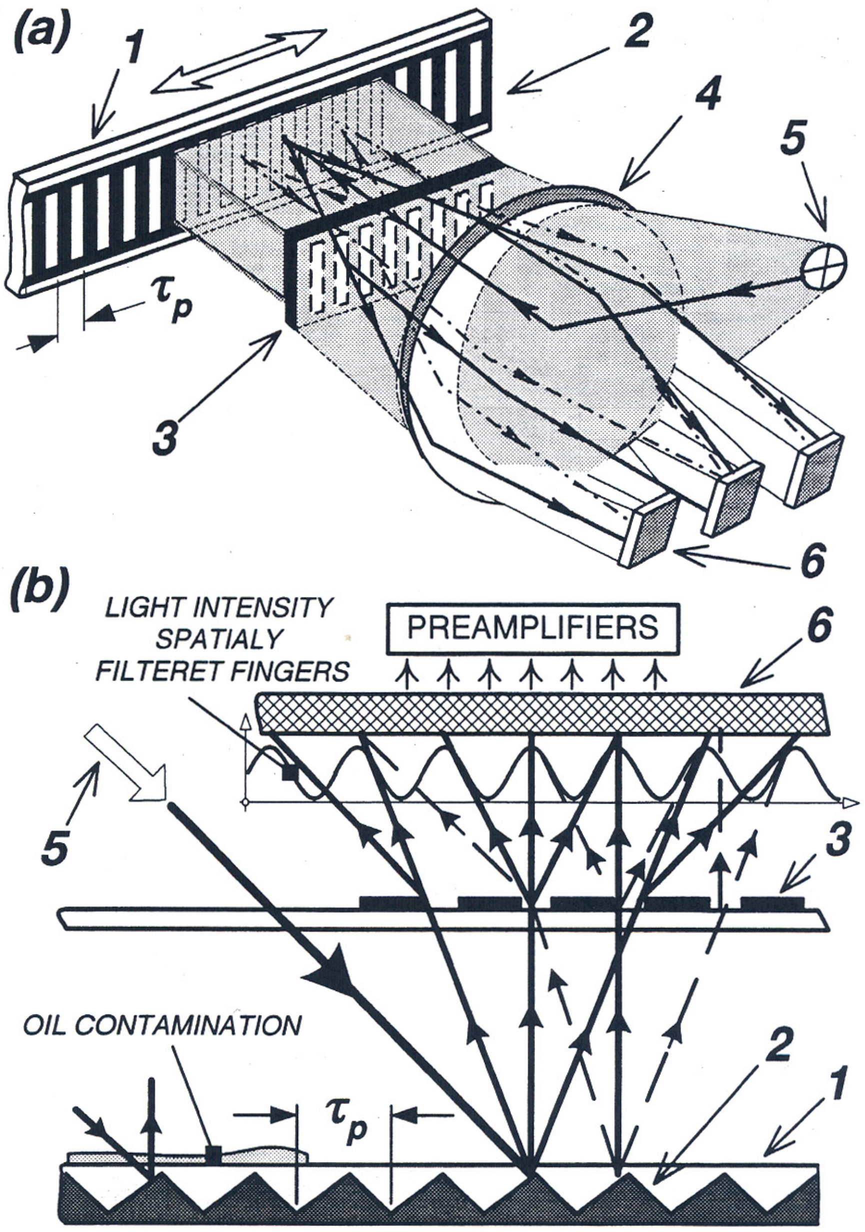

Figure 5.4 Interferential measuring: (a) photo electronic scanning, (b) optical filtering principle. 1 - scale, 2 - scale facets, 3 - phase gratings (read head window), 4 - condenser lens, 5 - oblique illumination from LED, 6 – photo detectors.

©2000 CRC Press LLC

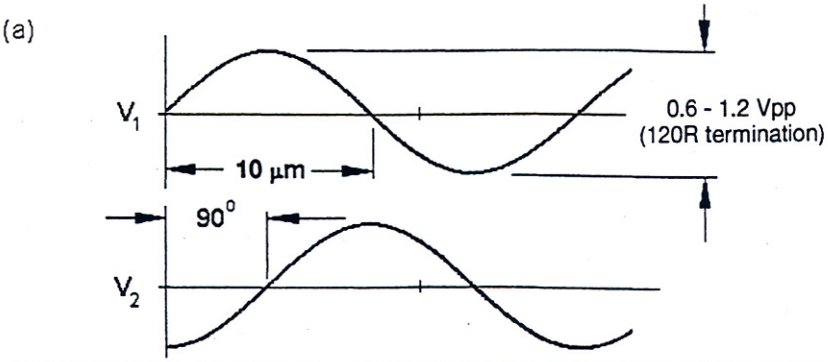

INCREMENTAL 2 CHANNELS V_1 and V_2 DIFFERENTIAL SINUSOIDS in QUADRATURE

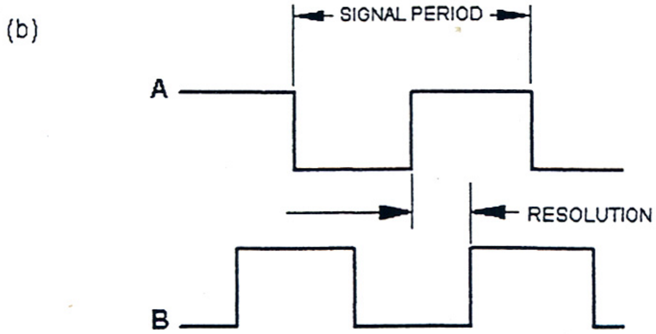

INCREMENTAL 2 CHANNELS A and B in QUADRATURE

READHEAD MODEL	PERIOD (µm)	RESOLUTION (µm)
RGH22 D	20	5
RGH22 X	4	1
RGH22 Z	2	0.5
RGH22 Y	0.4	0.1

Figure 5.5 Incremental signals readheads manufactured by Renishaw: (a) analog readhead, (b) digital readhead. Courtesy of *Renishaw plc*, Gloucestershire, U.K.

©2000 CRC Press LLC

Table 5.1 Self-adhesive scale RGS-S for RG2 encoder system manufactured by *Renishaw plc*, Gloucestershire, U.K.

Parameter	Specification
Scale type	Reflective gold plated steel tape with lacquer coating and self-adhesive backing
Scale pitch	20 μ m
Available lengths	Continuous length up to 50 m Longer than 50 m by special order
Measuring lengths	User selectable 'cut-to-requirements' at the place of installation
Accuracy	Typical 15 μ m/m without compensation
Linearity	±3 μ m/m, ±1 μ m/60mm
Substrate materials	Metals, ceramics and composites with expansion coefficient less than 22 μ m/m/°C
Reference mark	Magnetic actuator RGM22S epoxy mounted. One or more at user selected locations. Repeatability of position within: • temperature range ±10°C from installation • speed < 250 mm/s Screw mounted option RGM22SB available

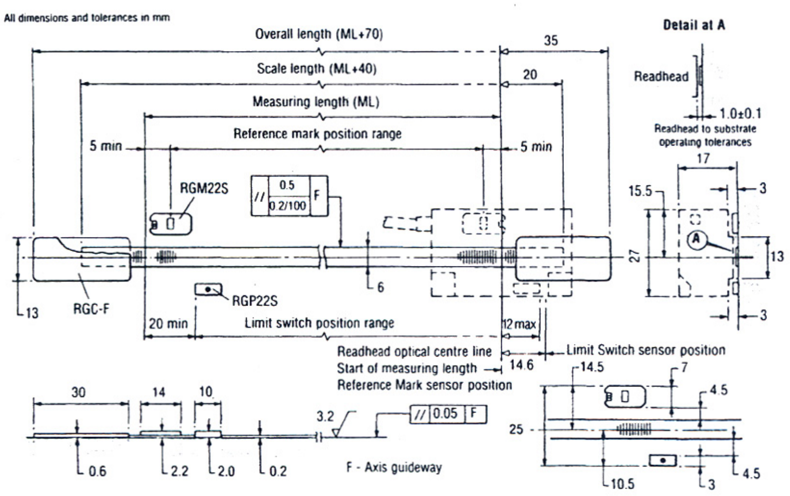

Figure 5.6 Dimensions of RGS-S scale and associated components. Courtesy of *Renishaw plc*, Gloucestershire, U.K.

©2000 CRC Press LLC

Table 5.2 Analog read heads manufactured by *Renishaw plc*, Gloucestershire, U.K.

Parameter	Specifications	
Type	RGH22C 12 μ A differential.	RGH22B 1 V (peak-to-peak) differential
Signals	Incremental 2 channels I_1 and I_2 differential sinusoids in quadrature (90° phase shift). Signal period 20 μ m.	Incremental 2 channels V_1 and V_2 differential sinusoids in quadrature (90° phase shift). Signal period 20 μ m.
Output	7 to 16 μ A	0.6 to 1.2 V (peak-to-peak)
Reference	Differential pulse 10 μ A duration 126°	Differential pulse Duration 126°
Power supply	5v ±5%, 120 mA (typical)	
Speed	1 m/s at 50 kHz maximum	5 m/s at 250 kHz maximum
Temperature	-20 to +70°c storage 0 to +55°c operating	
Humidity	10 to 90% RH non-condensing	
Sealing	IP54	
Operating acceleration	30g	
Shock acceleration	100g (11 ms , one half of sinusoid)	
Vibration Under operation	10g at 55 to 2000Hz	
Mass	Read head: 45g, cable: 32g/m	
Cable	Available lengths 0.5,1.0,1.5,3.0 and 5.0 m Flexible life> 10^7 cycles at 50 mm bend radius for integral cable and> 10^6cycles at 75 mm bend radius for extension cable14 core, double shield, outer diameter 7.2 mm	

©2000 CRC Press LLC

Table 5.3 Specifications of digital readhead manufactured by *Renishaw plc*, Gloucestershire, U.K.

Parameter	Specifications
Output signal	Square differential line driver to EIA RS422 Incremental channels A and B in quadrature (90° phase shift)
Signal period	20 μm for D type 4 μm for X type 2 μm for Z type 0.4 μm for Y type Resolution for all models 0.25xperiod
Alarm period	Separate alarm channel or three state alarm Incremental channels force an open circuit for reliable operation when signal is too low
Power supply	5v ±5%, 120 mA (typical) 150 ma for Y type only
Operating acceleration	30g
Shock acceleration	100g (11 ms , 1/2 sine)
Vibration Under operation	10g at 55 to 2000Hz(ICE 68-2-6)
Temperature	-20 to +70°c storage 0 to +55°c operating
Humidity	10 to 90% RH non-condensing
Mass	Read head: 45g, cable: 32g/m
Signal terminations	Standard RS422A line receiver circuitry RC filter is recommended Resistance 120 Ω Capacitor 4.7 nF for cable length < 25 m and 10 nF for cable length> 25 m
Cable	Available lengths 0.5,1.0,1.5,3.0 and 5.0 m Flexible life> 10^7 cycles at 50 mm bend radius for integral cable and> 10^6cycles at 75 mm bend radius for extension cable 14 core, double shield, outer diameter 7.2 mm

©2000 CRC Press LLC

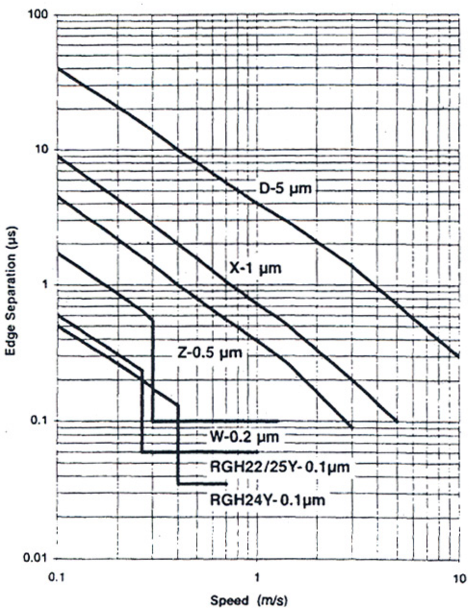

Figure 5.7 Edge separation for RGH readheads. Courtesy of *Renishaw plc*, Gloucestershire, U.K.

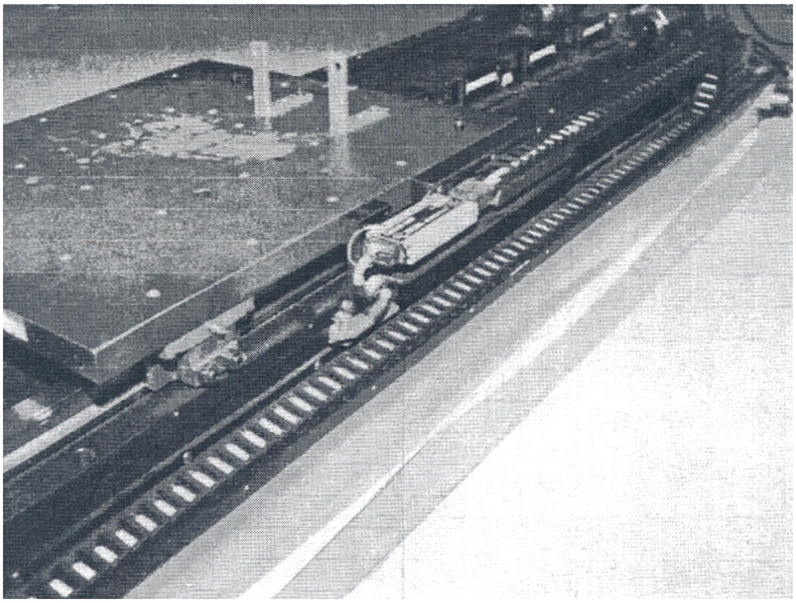

Figure 5.8 Readhead and reflective scale arrangement on the positioning stage with a linear motor. Photo courtesy of *United Technologies Research Center*, East Hartford, CT, U.S.A.

©2000 CRC Press LLC

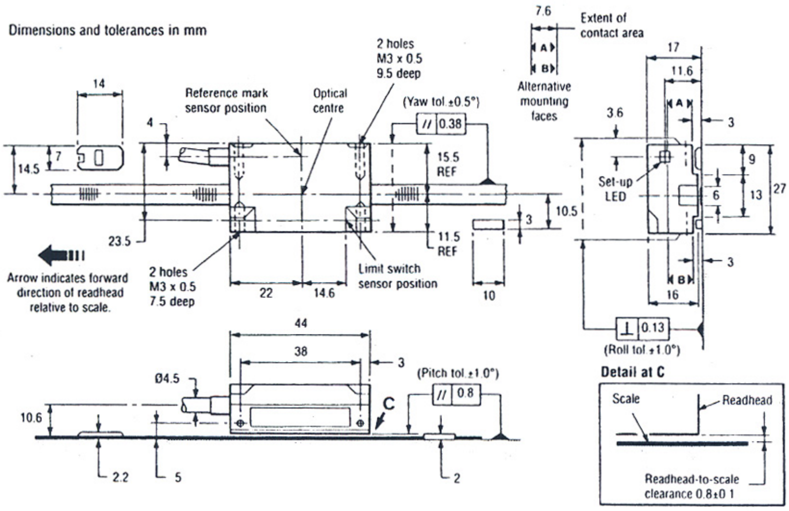

Figure 5.9 Dimensions of the analog readhead RGH. Courtesy of *Renishaw plc*, Gloucestershire, U.K.

The optical readhead working with reflective scale is shown in Fig. 5.8.

The commonly used scale RGS-S and one of the RGH22 series read-heads comprise the RG2 system, i.e., non-contact, optical encoder designed for position feedback solutions (*Renishaw*). The readhead can be chosen with either sinusoidal or square wave output. The selected type depends on the application, electrical interfacing, and required resolution. Typically, the RG2 encoders are employed in linear motor-driven machines such as tool presetters, measuring and layout equipment and other high speed systems in which interpolation is provided by subsequent electronics. In the environments subjected to severe radio frequency interference (RFI), the RGH22B readhead with analog differential output voltage is preferred to the RGH22C model having the output current signal.

Specifications of the two-coordinate PP 281 R encoder manufactured by *Heidenhain, GmbH* , Traunreut, Germany, are listed in Table 5.4.

The *x-y* motion stages applied in clean-room environments, e.g., semiconductor industry or ultra-precision machine tools, such as grinders for ferrite components and diamond lathes for optics are equipped with integrated two-coordinate encoders. The incremental *x-y* encoder contains a two-dimensional phase grating structure on a glass substrate (Fig. 5.10).

©2000 CRC Press LLC

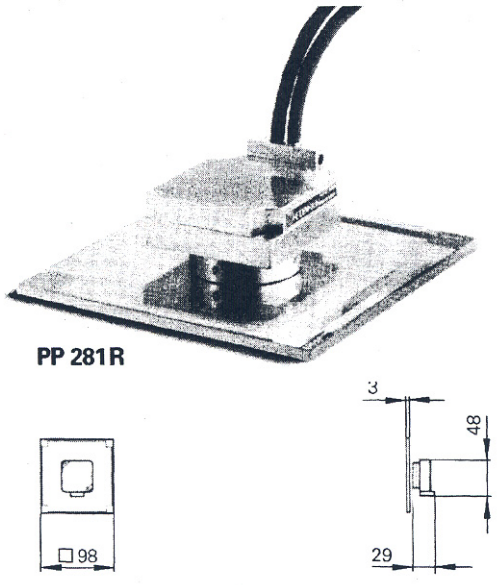

Figure 5.10 Two-coordinate incremental encoder PP281R. Photo courtesy of *Heidenhain, GmbH*, Traunreut, Germany.

Table 5.4 Specifications of PP 281 R two-coordinate incremental encoder manufactured by *Heidenhain, GmbH*, Traunreut, Germany.

Parameter	Specification
Grating period	τ_p = 8 μm
Coefficient of thermal expansion	8 pikomillimeter /K
Accuracy	±1 μm
Measuring range	68 mm X 68 mm other ranges also available
Vibration	less than 80 m/s^2 at 55 to 2000 Hz
Shock vibration	less than 100 m/s^2(11 mS)
Operating temperature	0 to +50°C
Mass of grid plate	75g
Mass of APE and cable	120g
Mass of scanning head	170g
Power supply	5 V ±10%, 100 mA (without load)
Output signal	1 v (peak-to-peak)
Signal period	4 μm

The measurement in a plane is possible through an interferential scanning method. Two reference marks, one in each measurement direction, serve to define accurately zero positions. The 8 μm grating period with fine interpolation and high uniformity of scanning is capable of 10 nm resolution.

©2000 CRC Press LLC

5.1.2 Absolute Encoders.

Typically, *absolute encoders* are utilized in the devices inactive for long periods of time or moving at low speeds. They are also applied to the systems where linear position must be maintained regardless of power interruptions, or where safe and failure-free operation is required. Primarily, machine tools and robotics applications make use of the absolute position encoders. These devices supply a whole output word with unique binary code pattern representing each position. This code is derived from independent tracks on the linear scale detected by individual photo detectors. The output from these detectors would then be *high* or *low* depending on the code pattern read off the linear scale for the particular position. Absolute encoders are similar to incremental devices; however, they contain more sensors. The overall complexity depends on the generated size of the word. The longer the *logic* word, the more complex and expensive the system. For each *bit* in the output signal the encoder uses one track of the code scale. Therefore, a 10 bit encoder has 10 tracks to detect the light passing through them. For higher number of tracks it may be necessary to use multiple sources of light to assure an adequate illumination. The principle of operation of the linear absolute encoder is illustrated in Fig. 5.11. Although the information read from data tracks can be converted into position signals using many different codes, natural binary code (NBC), gray, gray excess, and binary coded decimal (BCD) codes are most common.

The NBC derives the numerical value from exponents with base 2. For example, the number 179 is expressed as $1 \times 2^7 + 0 \times 2^6 + 1 \times 2^5 + 1 \times 2^4 + 0 \times 2^3 + 0 \times 2^2 + 1 \times 2^1 + 1 \times 2^0$. In other words, the NBC value for 179 is 10110011.

The binary code is a *polystrophic code* characterized by multiple bit changes [121]. It requires many bit transitions simultaneously, e.g., counting from 127 to 128 in NBC requires simultaneous transition of 8 bits from 01111111 binary to 10000000 binary. In a practical electronic circuitry, all of these bits cannot be changed at precisely the same time. There is some delay within individual bit transitions. Ambiguity in the simultaneous bit changes, imperfection in the readhead mechanical installation, hysteresis and noise comprise only a few factors which affect the accuracy of the position detection. The potential error in the reading of the most significant bit can result in 180° feedback signal error.

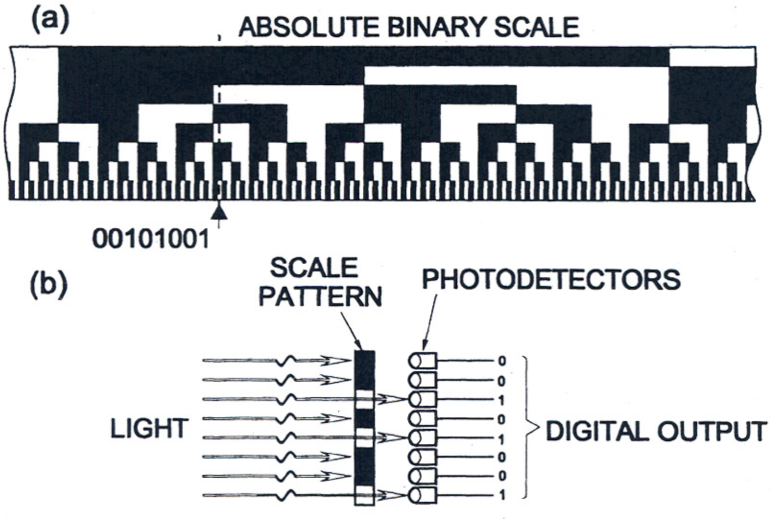

Figure 5.11 Principle of operation of an absolute encoder: (a) absolute linear scale, (b) detection of bits.

©2000 CRC Press LLC

More sophisticated scanning methods are used in modern absolute position encoders. Two of them, the V-scan and the U-scan allow for reliable simultaneous bit transitions. In the V-scan method, the sensors are positioned in the V-shape arrangement in two sensor banks (Fig. 5.12). Such a distribution makes room for error tolerances in the encoder system. The less significant bit is used to define in which direction the scale is moving, i.e., what kind of transition is performed (high-low or low-high).

Another non-ambiguous method is the gray code, particularly well suited to optical encoders. In this *monostropic code* , only two neighboring position values differ in exactly one binary digit, i.e. only one track changes at a time. This limits any decision during edge transition to plus or minus one count. Therefore, the maximum error when moving from one position to the next is 1/4 of the grating period of the finest track.

The gray excess code consists of a section from the middle of the gray code pattern. This permits a position value other than 2 and yet remains a unit-distance code (monostropic). An example of the gray excess code is: 4-bits of gray code provide 16 absolute position values, and to solve 10 positions, the first and last 3 values are omitted from the graduation pattern to produce the *10-excess-3 gray code*. In the end, these codes (gray code, gray excess code, or any other appropriate code) are converted by the subsequent electronics (microprocessor) into the NBC. Differences between the binary and gray codes are shown in Table 5.5.

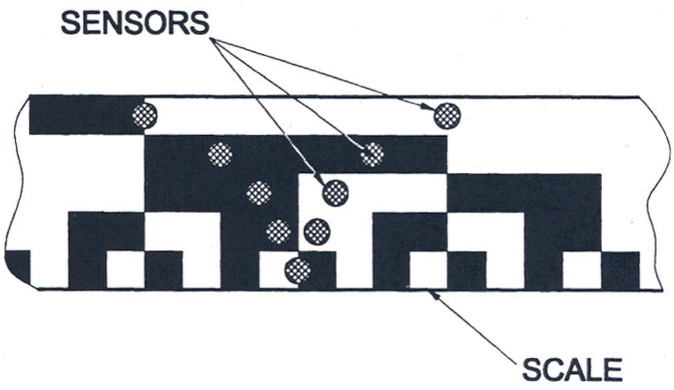

Figure 5.12 Arrangement of sensors in V-scan method.

Table 5.5 Decimal, binary, gray and gray excess codes

Decimal code	0	1	2	3	4	5	6	7
Binary code	0000	0001	0010	0011	0100	0101	0110	0111
Gray code	0000	0001	0011	0010	0110	0111	0101	0100
Gray excess	0010	0110	0111	0101	0100	1100	1101	1111

In linear motion systems with single axes and travel distances over several meters, the application of absolute encoder scales has serious limitations in insufficient step resolution. For example, the scale with 12 tracks can generate 12-bit position information. This translates to 4096 unique encodings per scale length, providing approximately 250 μ m resolution for 1 m of travel distance. In some cases it may be insufficient. An increase in the number of tracks can overcome this problem, but it results in higher complexity and costs of the encoder system. In practice, the total travel distance is subdivided into sections

©2000 CRC Press LLC

instead. Each section has the same absolute linear scale. To detect which section is actually scanned, the encoders use *distance-code* reference marks. The span between every second reference mark is constant, but it varies by a resolution step between two consecutive marks. The information as to which section is sampled comes from these reference mark signals. This method can reduce the search interval to 100 mm or less, instead of the entire scale length. In motion systems where the safety and failure free operation is not a priority, incremental instead of the absolute optical scales can be employed for sections working with distance-code reference marks. Absolute position is determined by counting the number of steps from the reference marks; however, the information can be lost in the case of power interruption.

Linear encoders used in the metal cutting industry, i.e. LBM drives for machine tool tables, must meet the following requirements [49]:

- high counting accuracy at high speeds, e.g. from 0.1 to 0.25 m/s in milling of gray-cast iron and aluminum (this translates into wide frequency range of position loop-control and therefore, fast feed- forward control);
- high acceleration capability, typically from 10 to 40 m/s^2 and even higher;
- high maximum rapid-travel speeds, typically from 1 to 1.5 m/s, sometimes even 2 m/s.

Manufacturers have developed two types of constructions which can meet these requirements: (a) exposed and (b) sealed encoders. Exposed encoders are recommended in clean environments without a danger to contaminate the optics. However, in machines either completely encapsulated or using coolant and/or lubricant, sealed encoders are preferred. The advantage of the sealed system lies in the reduction of requirements for finishing the mounting surface. Furthermore, sealed linear encoders are characterized by simple mounting and higher protection rating. On the other hand, the advantages of exposed encoders include higher traversing speed, no friction and better accuracy. Therefore, exposed encoders most often find applications in precision machines, measuring systems, and production equipment for the semiconductor industry. On the other hand, the sealed linear encoders are widely utilized in the metal cutting machines.

The *Heidenhain* LC 181 sealed absolute position encoder data is shown in Table 5.6. The LC 181 absolute encoder generates the absolute position value from seven incremental tracks. The grating periods of the tracks differ in a manner that makes it possible to evaluate the measuring signals of all seven tracks. This allows identification of any location on the scale within the measuring length of 3 m. In addition to the absolute position information, the LC 181 encoder provides sinusoidal incremental signal with its period of 16 μm at 1 V (peak-to-peak).

Table 5.6 Sealed absolute linear encoder LC 181 manufactured by *Heidenhain, GmbH*, Traunreut, Germany.

Parameter	Specifications
Measuring standard	DIADUR glass scale with 7 tracks with different grating periods
Data interface	Synchronous serial (EnDat)
Incremental signal	1 V (peak-to-peak) signal period 16 μm
Accuracy grades	±5 μm, ±3 μm
Measuring steps	1 μm, 0.1 μm
Measuring length	240 to 3040 mm
Length of sealed scale	Measuring length + 119 mm
Width of sealed scale	40 mm
Height of sealed scale	62.5 mm
Height of sealed scale and read head	85 mm

©2000 CRC Press LLC

5.2 Linear Magnetic Encoders

5.2.1 Construction

As compared with optical sensors, their magnetic counterparts are characterized by simplicity, reduced sensitivity to contamination, robustness and low cost. Magnetic sensors can work in the presence of heavy liquid and chip build up. Made out of metal, they can withstand more severe vibrations, and are perceived to be more reliable. In addition, these devices have lower power requirements, good performance characteristics and are well suited for large volume manufacturing technology.

Magnetic encoders utilize *magneto-resistive* (MR) sensing elements and *magnetically salient targets* . The magnetically salient target is a long, alternatively magnetized ruler. The MR elements (sensors) change their resistance under the influence of the magnetic flux density and can sense flux densities above 0.005 T [121]. The principle of operation of the magnetic linear encoder with the MR sensors is explained in Fig. 5.13. The MR sensor resistance changes approximately ±1.6% as the magnetic field excited by the passing salient target changes its polarity. Four sensors are electrically connected to a resistive bridge polarized by 5 V d.c. source. The bridge output voltage varies sinusoidally within the amplitude of 0.08 V (peak-to-peak) reflecting changes of sensor resistances. The two magnetic poles affect the sensors in the same way but with opposite polarity. Therefore, when the alternatively magnetized ruler moves one pole pitch τ , the output signal will complete one cycle.

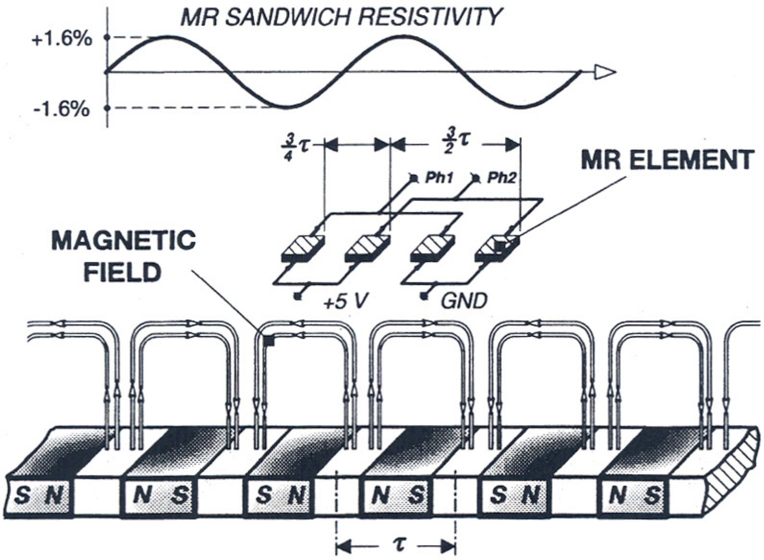

Figure 5.13 Magnetic encoder with magneto-resistive sensors.

Magnetic encoders employing MR sensors are capable of producing output signals with frequencies up to 200 kHz. High frequency response requires very high resolution, which is a function of the air gap size. The smaller the gap, the higher the resolution. This gap size should be approximately 80% of the pole pitch. For example, if a motion system requires the resolution of 0.05 mm (20 kHz frequency with 1 m/s linear speed), the encoder with 4x interpolation should contain the magnetic target with 0.2 mm pole pitch. The air gap in such a system is about 0.15 mm.

Sensing elements and magnetically salient targets can be supplied to the end user as separate components. Sometimes, the adaptation of motion system hardware to serve as a long salient target is possible. In such a system adapted by the user, air gaps between sensors and the target are usually of the order of a few millimeters.

©2000 CRC Press LLC

In magnetic encoders with large air gaps the *Hall elements* are more suitable than MR sensors. These are true solid state devices with good operating temperature limits, typically from -40 to 150 °C, long life expectation (20 billion operations), and can work at zero speeds. The linear (analog) Hall element has a wide range of output signal (from 1.5 to 4.5 V) and a reasonable frequency response (100 kHz). Its output voltage is

Table 5.7 Specifications of the IHRM 12P15001 sensor employing magnetically biased Hall element manufactured by *BEl Corporation, Industrial Encoder Division*, Tustin, CA, U.S.A.

Parameter	Specifications
Voltage supply range	8 to 28 V d.c.
Supply current	20 mA
Max. switching current	100 mA
Max. switching frequency	20 kHz
Voltage drop	< 3 V d.c.
Air gap	2.5mm
Temperature range	-40 to 120°C
Temperature coefficient	-3%/K
Short circuit protection	Yes
Reverse polarity protection	Yes
Housing	Stainless steel
External dimensions	M12xl (thread) X 60 mm length

$$V_H = k_H \frac{1}{\delta} I_c B \sin\theta \tag{5.2}$$

where I_c is the applied current, $B\sin\theta$ represents the component of the magnetic flux density vector perpendicular to the current path, θ is the angle between the magnetic flux density vector and Hall element surface, δ is the thickness of Hall element and k_H is Hall constant (m^3/C).

Specifications of a typical Hall effect sensor are listed in Table 5.7. This sensor is used to scan moving electromagnetic objects, preferably toothed ferromagnetic racks [15].

Encoder systems with Hall effect devices are arranged differently than those comprising MR elements. Hall sensors are typically placed between a moving, magnetically salient target, e.g., ferromagnetic ruler with teeth, and a bias PM which excites the magnetic field. In the case of low resolution of positioning systems a long *flexible magnetic strip* distributed along the motion track serves as the magnetically salient target. This strip is made out of ferrite material or low energy NdFeB PMs mixed with rubber, and is usually alternatively magnetized, i.e., N, S,...N, S with pole pitch of a few millimeters. The alternatively magnetized flexible strip permits achieving the repeatability up to ±5 μm (1.22 μm resolution) with 4096 x multiplier (electronic circuit). The relative position is-determined by counting the number of poles or target saliencies (steel teeth) moving through the sensor, while the speed is obtained from the frequency at which they pass. Meanwhile, the movement

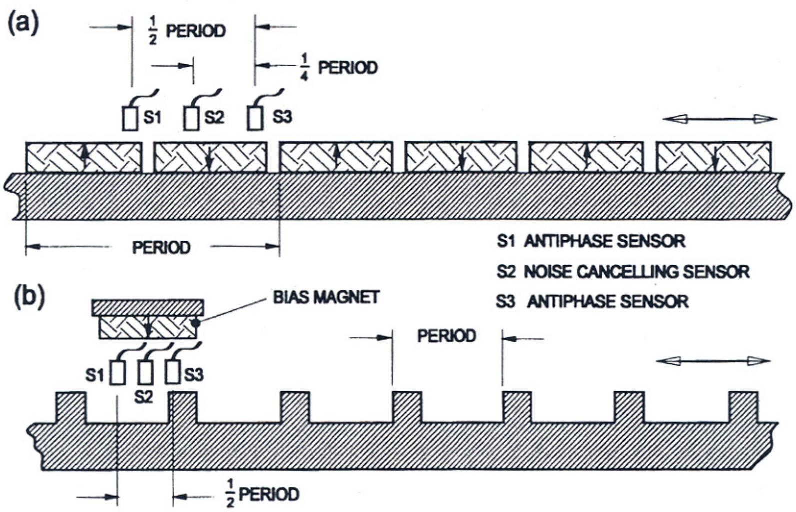

Figure 5.14 Noise canceling magnetic sensor array.

direction is obtained from the relative timing of two sensors in the quadrature with the target saliency. This flexible-strip-based linear encoder is used in LBMs with inner air-cored armature winding and moving PMs (Lighting Series) manufactured by *Anorad* [8].

In linear motors utilized for propulsion with an array of magnetic poles N, S,...N, S and short pole pitch, the installation of an additional magnetic strip for the encoder is not necessary. Encoder sensors are located near the surface of the guide away and the field produced by PMs is used as the magnetic target.

5.2.2 Noise Cancellation

One of disadvantages of linear magnetic encoders is their sensitivity to external magnetic fields and temperature changes. Sometimes, the *magnetic noise* can exceed the sensor generated signal up to one order of magnitude. Therefore, noise cancellation techniques aimed at suppression of unwanted disturbance signals are required.

One of simple noise cancellation methods is based on an array of three magnetic sensors [110]. Two of them are situated half of the magnetic period apart (in anti-phase relationship, i.e., 180° out-of-phase), while the third sensor is placed between the two remaining. The three-sensor array is shown in Fig. 5.14.

The individual sensor output signal is a function of the magnetic flux density created by passing magnetic targets and the ambient noise of magnetic origin. For magnetic poles of alternative polarity (Fig. 5.14), the three sensor output signals can be expressed as

$$s_1 = \sin\frac{\pi}{\tau}x + N \tag{5.3}$$

$$s_2 = \sin\left(\frac{\pi}{\tau}x + \frac{1}{2}\pi\right) + N \tag{5.4}$$

$$s_3 = \sin\left(\frac{\pi}{\tau}x + \pi\right) + N \tag{5.5}$$

where x is the pole or saliency position in the direction of motion and N is the noise signal. Quadrature positions s_{1c} and s_{2c} are derived from the three sensor signals s_1, s_2 and s_3 as follows

$$s_1 = s_1 - s_2 = \sqrt{2}\cos\left(\frac{\pi}{\tau}x + \frac{1}{4}\pi\right) \tag{5.6}$$

©2000 CRC Press LLC

and

$$s_{2c} = s_3 - s_2 = \sqrt{2}\cos\left(\frac{\pi}{\tau}x + \frac{3}{4}\pi\right) \qquad (5.7)$$

The sensor output quadrature signals s_{1c} and s_{2c} are digitized for the complete noise cancellation enhancement. In some applications, the noise N depends on the position of the magnetic pole within the strip along the reaction rail. This results in an incomplete noise cancellation. However, the digitization with zero-crossing detection occurring at points of geometrical symmetry will fully cancel the noise signals. Fig. 5.15 depicts the sensor output signal with resulting zero-crossing digitization.

5.2.3 Signal Interpolation Process

The interpolation is a process of an encoder signal subdivision into phase shifted copies. It can be applied to sinusoidal outputs in the quadrature only. For example, the TTL signals cannot be interpolated. To enhance the resolution effectiveness, i.e., the overall accuracy, the interpolated signals are recombinated in electronic circuitry.

The sinusoidal signals formed by the incremental encoders are processed by the digitizing electronic units. These are often incorporated into a numerical motion controller and enclosed in a separate housing. Three of the commonly used interpolation methods, i.e. (a) analog digital interpolation using a resistor networks, (b) digital interpolation with look-up and tracking counter, and (c) digital interpolation with, arc-tangent calculator, have successfully been applied to the *Heidenhain, GmbH* encoders.

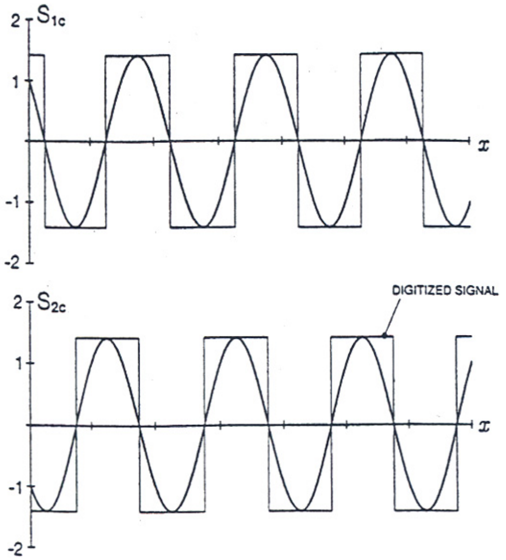

Figure 5.15 Quadrature sensor output signals S_{1c} and S_{2c} digitized by sensing zero-crossings.

The first method makes use of the trigonometric identity $\sin(\alpha+\beta) = \sin\alpha\cos\beta + \cos\alpha\sin\beta$ to develop the phase-shifted copies of the original signals.

The encoder LS 774/LS 774C manufactured by *Heidenhain, GmbH* is based on the analog-digital conversion with 5-fold interpolation (the so called $5\times$ interpolator). The scanning signals s_{1c} and s_{2c} are amplified and interpolated in the resistor network that generates collateral phase-shifted signals by using vector algebra. The 5-fold interpolation process is shown in Fig. 5.16. Ten signals are produced with a phase shift ranging from 0 to 162° electrical. After conversion to the quadrature, these signals are combined into two square-wave trains by exclusive-OR (XOR) gates. The trains of impulses have the frequency five times greater than that of the scanning input signals and are phase-shifted by the quarter of period. Each edge of the signals S_1 and S_2 can be used as a counting pulse within one period. The reference pulse S_0 is gated between the two successive edges of S_1 and S_2. The 20 μm grating period of the encoder, which combines 5-fold interpolation with 4-fold electronic evaluation is capable of achieving 1 μm measuring step. A similar process can be used for 10 or 25-fold interpolation that results in 1/40 or 1/100 measuring step of the grating period.

In interpolation processes utilizing higher subdivisions (50-fold and above), digital methods are required. Two scanning signals are first

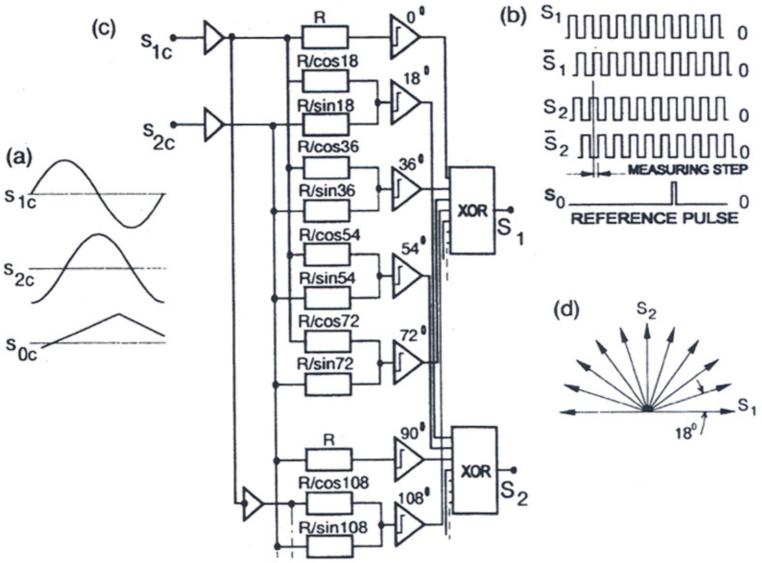

Figure 5.16 Interpolation process with resistor network: (a) scanning signals, (b) measuring signals after 5-fold interpolation and digitization, (c) electronic circuit, (d) phasor diagram.

amplified, then quantified in the sample-and-hold circuitry and finally digitized into regular intervals in the A/D converter. These digitized voltages define a single address (row and column) in a look-up table describing an instantaneous position (Fig. 5.l7a). The actual position is compared with the value determined in the previous cycle which is stored in a tracking counter. The tracking counter produces incremental square-wave signals (0° and 90°) from the differences between previous and current positions. The look-up table interpolation method is used in the EXE 650 (50-fold interpolation) and EXE 660 (100-fold interpolation) encoders manufactured by *Heidenhain, GmbH.*

The most advanced interpolators use microprocessor technology. Fig. 5.l7b illustrates the digital interpolation process employing an *arc-tangent* calculator. The microprocessor calculates the tangent S_1 / S_2 from two digitized input voltages. The corresponding angle value (*arc-tangent*) which indicates the position within one signal period is derived from the table stored in EPROM. The analog input signals s_{1c} and s_{2c} are simultaneously converted into quadrature waveforms and signal periods are determined. The actual position is derived from the evaluated period and the calculated angle. Finally, to compensate for the system errors, appropriate correction values are read from the table stored in the RAM. After the error correction, the digital signal is transmitted to the motion control unit.

©2000 CRC Press LLC

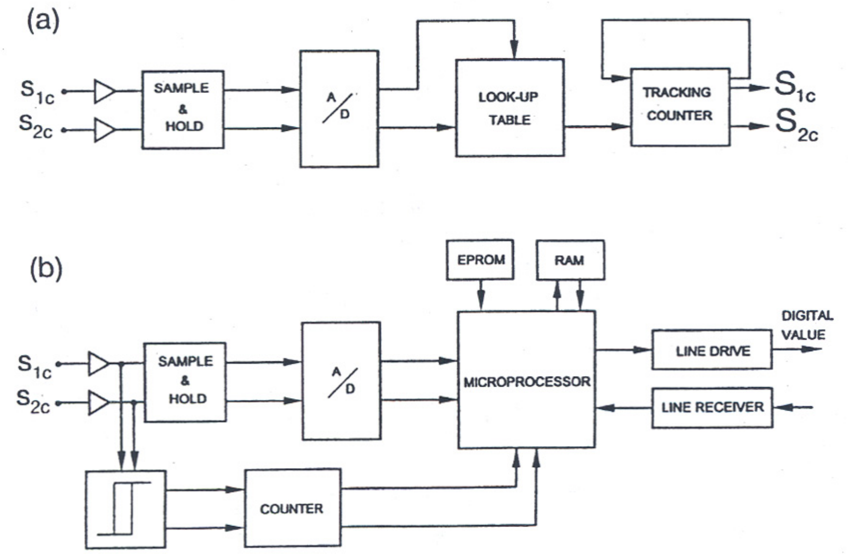

Figure 5.17 Digital interpolation methods: (a) using look-up table and tracking counter, (b) using microprocessor to compute arctan.

5.2.4 Transmission of Speed and Position Signals

The speed and position control systems are limited by the *pulse per meter* counts and the maximum linear *speed/frequency* response rate which depends on

- mechanically permissible traversing speed,
- minimum possible edge separation of the square-wave output signals S_1 and S_2,
- maximum input frequency of the interpolating and the digitizing electronics.

The maximum traversing speed

$$v_{tr} = \tau_p f \tag{5.8}$$

depends on the maximum input frequency f of the interpolation and digitizing electronics and the scale grating period τ_p .If f is in kHz, and τ_p is in μm, the speed v_{tr} is in mm/s. An example of the relationship between maximum traversing speed and the grating period at various maximum permissible input frequencies is illustrated in Fig. 5.18.

The encoder signal is subdivided in the subsequent electronics. The subdivision factor should remain in the reasonable proportion to the

©2000 CRC Press LLC

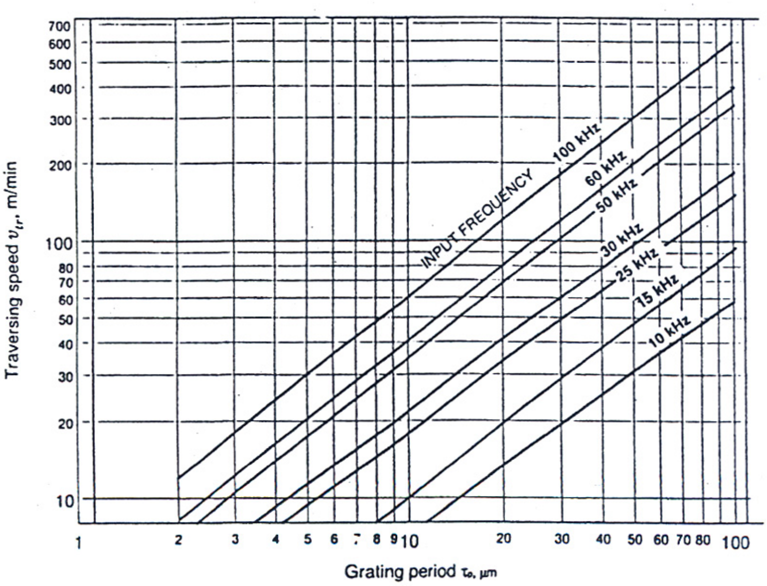

Figure 5.18 Maximum permissible input frequencies for EXE interpolation unit. Courtesy of *Heidenhain, GmbH*, Traunreut, Germany.

accuracy of the encoder. For example, the subdivision factor of 1024 applied to the 10 μm or 40 μm signal period gives the resolution of approximately 10 nm and 40 nm, respectively.

Feed drives of machine tools can reach linear speeds over 2 m/s, while the handling equipment - over 5 m/s. It can be calculated that the velocity of 1 m/s and measuring step of 0.1 μm (after a 4-fold evaluation) result in the input frequency of 2.5 MHz. Owing to large distances separating the encoder and the processing electronics (up to 50 m), the interpolating and digitizing circuit is often connected as a separate unit between them. For signals with frequencies above 1 MHz, short cables need to be employed, in order to preserve good transmission quality. Therefore, high speed motion systems utilize encoders containing interpolation and digitizing circuits. If the high frequency transmission signal is unavoidable, e.g., in the system with high traversing speed and small measuring steps, a linear encoder with sinusoidal output signals should be used. This sinusoidal signal should be 1 V (peak-to-peak) at the cutoff frequency of 200 kHz with amplitude of -3 dB. In this case, the cable length can reach 150 m.

Low traversing speed with high uniformity of motion requirement sets another limit for the measurement system. To maintain adequately uniform speed a resolution of 0.1 μm and higher may be required.

©2000 CRC Press LLC

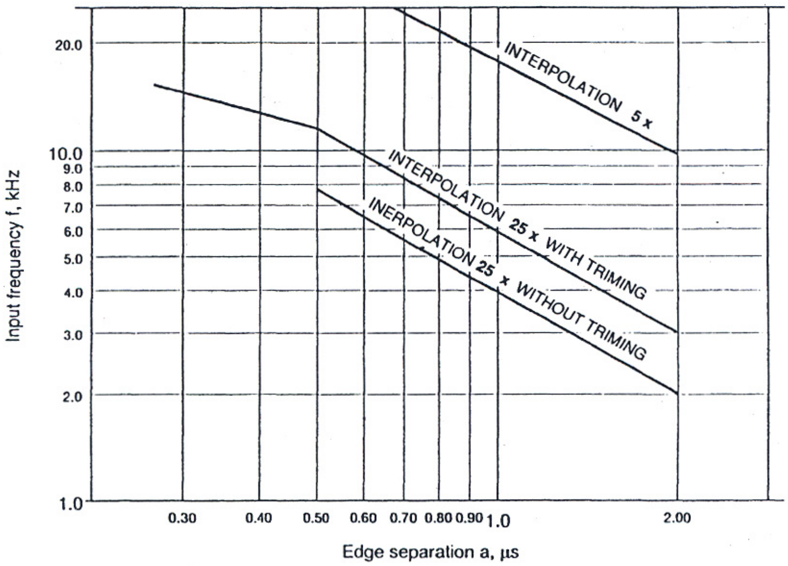

Figure 5.19 Edge separation diagram applied to non-clock EXE interpolation unit. Courtesy of *Heidenhain, GmbH,* Traunreut, Germany.

In general, the control electronics limits the minimum edge separation for square wave output signals. The relationship between input frequency f and the edge separation a for a given interpolation factor, is shown in Fig. 5.19. The input frequency f can be found from eqn (5.8).

]

chapter 6

High Speed Maglev Transport

6.1 Electromagnetic and Electrodynamic Levitation

Magnetic levitation (maglev) can provide a super high-speed ground transport with a non-adhesive drive system that is independent of frictional forces between the guideway (track) and vehicle bogies. Maglev trains, a combination of contactless magnetic suspension and linear motor technology, realizes super high-speed running, safety, reliability, low environmental impact and minimum maintenance. Two maglev transportation technologies emerged in the early 1970s: *electromagnetic* (ELM) levitation which utilizes attractive forces of electromagnets with controlled airgap and *electrodynamic* (ELD) levitation which utilizes repulsive forces and superconductivity.

Nowadays, the target speed of ground transport of economic superpowers is minimum 400 km/h. Research done in Germany and Japan shows that vehicles suspended magnetically and propelled by linear motors are the optimum solution to modern transport problems. Magnetic levitation trains can run at speeds up to 550 km/h consuming less energy than aircrafts and road vehicles. Speed above 500 km/h can also be achieved by wheel-on-rail trains (TGV *Atlantique* set the word speed record of 515.3 km/h in 1990), but this kind of propulsion is not adhesion free and emits a high level acoustic noise.

In ELM levitation systems (Fig. 6.1) the attraction force between the steel yoke (guidance) and electromagnet poles lift the vehicle. The electromagnet is fixed to the undercarriage. The current of the electromagnet is automatically controlled in proportion to the airgap. Assuming that the magnetic permeability of steel tends to infinity, there is no fringing effect and no leakage fluxes the inductance of the electromagnet

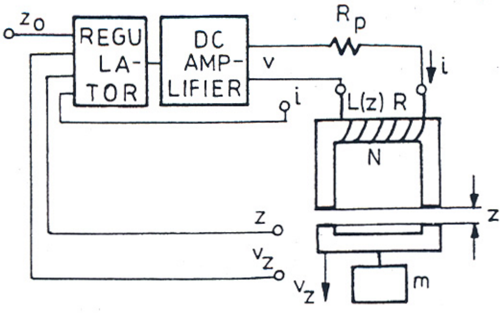

Figure 6.1 Electromagnetic levitation system: z_o - required airgap, z - actual airgap, v_z - speed of the electromagnet in the z-direction, m - mass of yoke (part being suspended).

©2000 CRC Press LLC

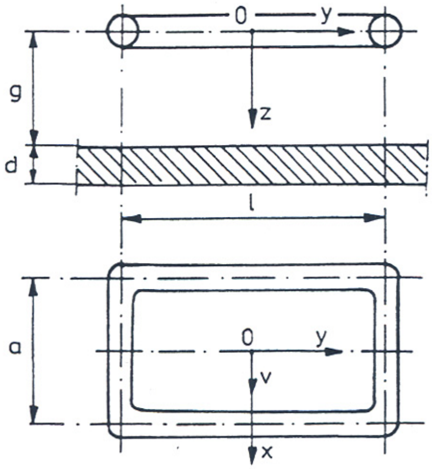

Figure 6.2 Electrodynamic levitation system: a - coil width, l - coil length, d - aluminum plate thickness, g - airgap.

winding as a function of the airgap is simply

$$L(z) = L_g \frac{g}{z} \tag{6.1}$$

where the inductance at nominal airgap is

$$L_g = \frac{1}{2}\mu_0 \frac{N^2}{g} A \tag{6.2}$$

In the above eqns (6.1) and (6.2) μ_0 is the magnetic permeability of free space, A is the area of the airgap under a single pole of the electromagnet, N is the number of turns of the coil, z is the axis perpendicular to the electromagnet pole shoes and g is the nominal airgap. The *attraction force* can be found using eqn (1.12), Chapter 1.

An ELM levitation system needs a control system. When the airgap between the pole and the yoke increases, the current in the coil of the electromagnet must increase. When the airgap decreases, the current must decrease. In practice, to keep the required airgap $z = g =$ *constant* (about 10 mm), a control system with three feedback signals is used: displacement z, linear velocity v_z in the z direction, and current i.

In ELD levitation systems (Fig. 6.2) the repulsive forces between the superconductive electromagnet mounted on the undercarriage and aluminum plates or short circuited coils (guidance) fixed to the guideway are used. The airgap (100 to 300 mm) is much higher than that in ELM levitation systems. Owing to the large airgap, the electrodynamically levitated trains can operate in severe climates with heavy snowfalls, ice formations, and white frost formations. The *repulsive force* between the d.c. fed coil moving with velocity v and a nonferromagnetic conductive plate placed below the coil can be calculated using Hannakam's [47] formula, which has been modified by Guderjahn *et al*., [43] i.e.,

©2000 CRC Press LLC

$$
\begin{aligned}
F_z = \frac{\mu_0 (Ni)^2}{\pi g} \Bigg\{ & \sqrt{\left(\frac{l}{2}\right)^2 + g^2} + \sqrt{\left(\frac{a}{2}\right)^2 + g^2} - 2g \\
& - \left[\sqrt{\left(\frac{l}{2}\right)^2 + \left(\frac{a}{2}\right)^2 + g^2} - \sqrt{\left(\frac{a}{2}\right)^2 + g^2} \right] \frac{g^2}{(a/2)^2 + g^2} \\
& - \left[\sqrt{\left(\frac{l}{2}\right)^2 + \left(\frac{a}{2}\right)^2 + g^2} - \sqrt{\left(\frac{l}{2}\right)^2 + g^2} \right] \frac{g^2}{(l/2)^2 + g^2} \Bigg\} \frac{1}{1+k^2}
\end{aligned}
\tag{6.3}
$$

where $k = 2/(\mu_o \upsilon \sigma d)$ if the plate thickness $d < \delta$ and $k = 2/(\mu_o \upsilon \sigma \delta)$ if $d < \delta$. The parameter $\delta = 1/\sqrt{\pi f \mu_o \sigma} = \sqrt{\lambda/(\pi \upsilon \mu_0 \sigma)} \approx \sqrt{a/(\pi \upsilon \mu_0 \sigma)}$ is the equivalent depth of penetration of electromagnetic field into the nonferromagnetic conductor with electric conductivity σ. The length of electromagnetic wave is $\lambda = v/f \approx a$ [43]. The coefficient 1/ (1 + k^2) in eqn (6.2) can also be replaced by $\exp\left\{-\xi/[1+2(g/l)^{3/2}]\right\}$, where $\xi = \left[4\pi/(\mu_o v \sigma g)\right]^{1/2}$. The coil moving with velocity v is subject to the braking force $F_x = kF_z$. More detailed discussions of eqn (6.3) are given in [17, 43].

6.2 Transrapid System (Germany)

6.2.1 Background

Research in transportation engineering carried out in Germany in the 1960s and early 1970s was focused on the energy consumption, costs, safety and impact on environment by trains, road cars, aircraft, and maglev vehicles [91]. Fig. 6.3a shows energy consumption per passenger per 1 km against speed of trains, cars, aircraft, and magnetic levitation trains [91]. The speed of magnetic levitation trains is less than that of airplanes but the energy consumption is much lower. Maglev trains can enter city centers and no time is wasted to travel from home to the airport and vice versa. Other advantages include low level of noise (Fig.6.3b), high level of safety of riding (Fig. 6.3c), high comfort of riding, easy maintenance, low land absorbtion, adaptability to the landscape due to the high gradability of 10% and the small curvature radii of 2.25 km at 300 km/h, and no pollution to natural environment.

6.2.2 Propulsion, Support and Guidance

The *Transrapid* maglev system (Fig. 6.4) uses attractive forces produced by U-shaped electromagnets (ELM levitation system) with current control and long armature three phase LSMs. The levitation electromagnets attached to the vehicle bogie are also the excitation electromagnets for LSMs. Another set of on board electromagnets, i.e. guidance electromagnets provides lateral stabilization. No superconducting coils are used. The support and guidance electromagnets and vehicle electric system are supplied by contactless linear generators.

Long armature cores of LSMs are placed in two parallel rows at both sides of the guidaway. Each armature has a laminated core with slots as in a typical a.c. linear motor. Laminations are stamped from an adhesive coated steel tape. For the manufacturing of the armature windings, not only electrical and geometrical conditions, but also efficient large-scale production and assembly, have been taken into account. The three phase winding is made of a cable with synthetic elastometer insulation pre-shaped with small radii. Typical cable construction used in the South

©2000 CRC Press LLC

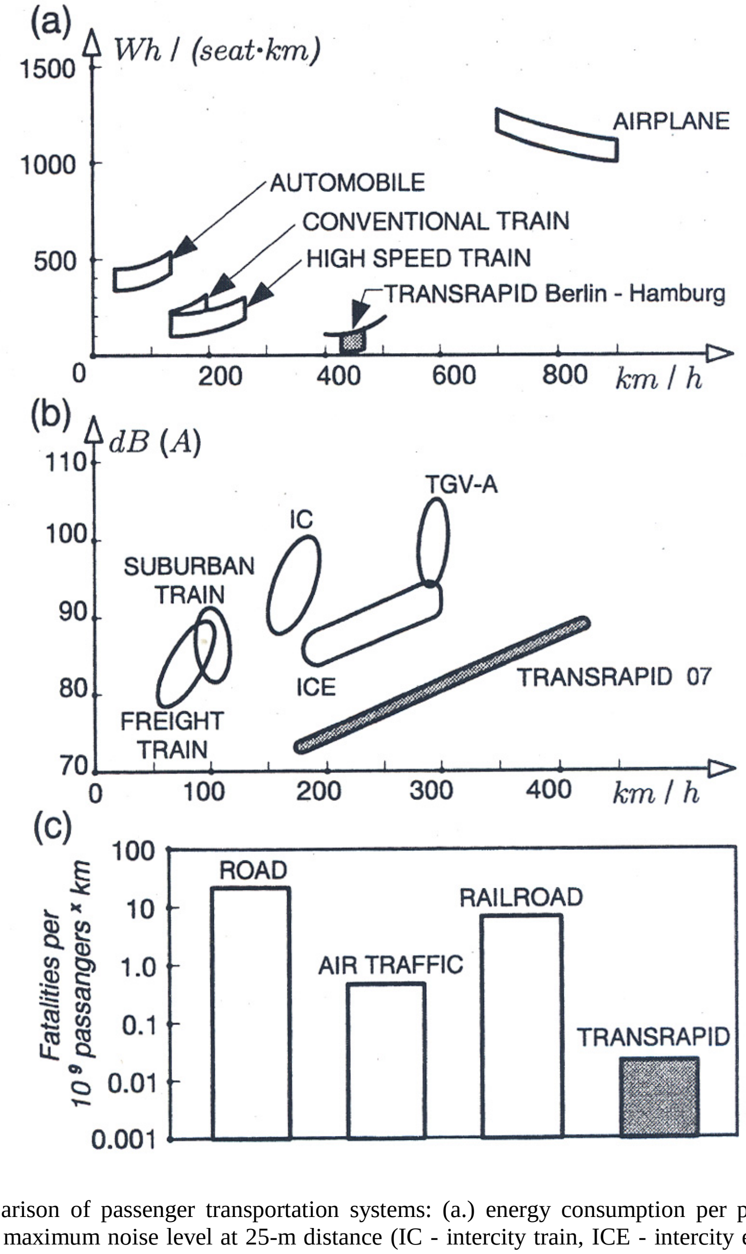

Figure 6.3 Comparison of passenger transportation systems: (a.) energy consumption per passenger per kilometer against speed, (b) maximum noise level at 25-m distance (IC - intercity train, ICE - intercity express, TGV-A - TGV Atlantique), (c) safety analysis - transportation system risk. Courtesy of *Thyssen Transrapid System, GmbH,* München, Germany.

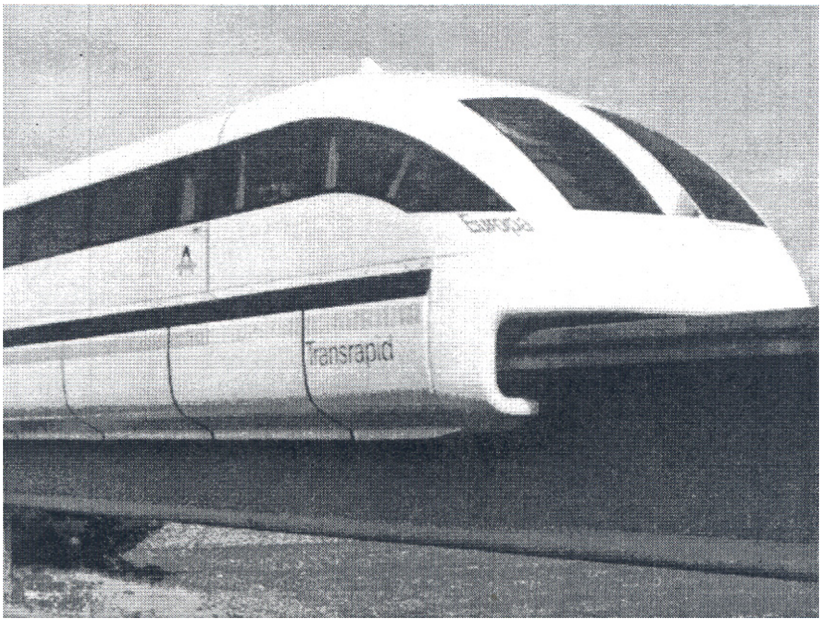

Figure 6.4 *Transrapid 07 Europa* (Emsland Transrapid Test Facility). Photo courtesy of *Thyssen Transrapid System, GmbH*, München, Germany.

Loop of Emsland Transrapid Test Facility is a multistrand aluminum conductor of 300 mm^2 cross section. The cable winding is fixed in the armature stack slots with the aid of winding casings (snap locks).

The excitation system of LSMs and ELM suspension of vehicles is integrated and consists of vehicle-mounted U-shaped electromagnets. Interaction of electromagnet poles and laminated cores of LSMs produce attractive forces which lift the vehicle. An electronic control system ensures a constant uniform airgap of about 10 mm (see also Fig. 6.1). Other sets of E-shape electromagnets, so called guide electromagnets, face the side steel rails and provide lateral guidance (stabilization). Every section of the vehicle is equipped with 15 autonomous support and 13 autonomous guidance electromagnets. The cross section of the support, guidance and propulsion system is shown in Fig. 6.5. There is a large clearance between the top of the guideway and bottom of the vehicle, so that the maglev train can also levitate over obstacles or a snow cover on the guideway.

The *attractive and lateral forces are controlled by currents of support and guide electromagnets,* respectively. The *thrust can be varied only by the magnitude and phase angle of the armature current.* By reversing the phase sequence, LSMs become synchronous generators which then provide electrodynamic braking forces without any contact. The

©2000 CRC Press LLC

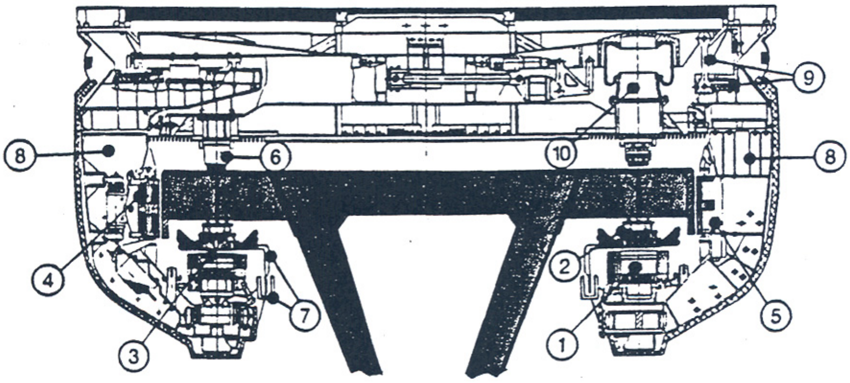

Figure 6.5 Cross section of the support, guidance and propulsion system: 1 - support electromagnet, 2 - LSM armature stack with windings, 3 –linear generator windings, 4 - guidance magnet, 5 - eddy-current brake electromagnet, 6 - support skids,7 - *Inkrefa sensor* (vehicle location), 8 –levitation bogies, 9 - cabin suspension, 10 - pneumatic spring. Courtesy of *Thyssen Transrapid System, GmbH,* München, Germany.

braking energy is fed back to the network. The long-armature LSM is characterized by the following features [131]:

- as a result of the combination of the suspension and drive systems the mass of the vehicle determines the excitation of the LSM,
- the three phase armature winding is fed from VVVF solid state converters installed in substations which are distributed along the line,
- control of the tractive effort keeps the airgap flux constant,
- leakage reactance of the armature winding and of the feeder cable primarily determines the LSM characteristics since the individual sections of the armature windings are longer than the vehicle.

To reduce the energy consumption, the long-armature LSM of the guideway is divided into sections. Only that section in which the vehicle is running is switched on.

6.2.3 Guideway

The T-shaped elevated guideway has two rows of long stator (armature) LSMs with laminated cores on its bottom and lateral steel rails for guidance. The LSM armature core serves also as a suspension rail. Because

©2000 CRC Press LLC

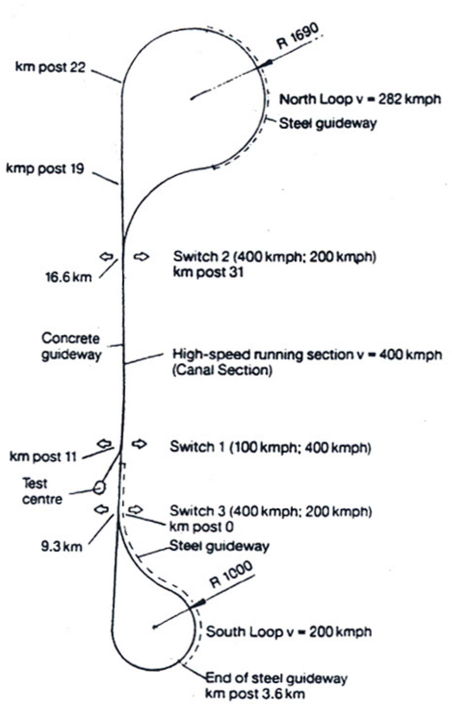

Figure 6.6 The Emsland test line. Courtesy of *Thyssen Transrapid System, GmbH,* München, Germany.

the vehicle clasps its guideway, derailment is impossible. The construction of the *Transrapid* guideway and any other maglev train guideways demands:

- minimum restrictions on the use of the existing terrain,
- good visual blending into the landscape,
- low noise level,
- low maintenance requirements and long life,
- protection against effects of the environment and vandalism.

The 31.5 km long *Transrapid* test line with two loops is located in Emsland region (Fig. 6.6). The first 20.5 km section began operating in 1985. The Emsland *Transrapid* Test Facility (TVE) was completed in 1987. About 20 km of TVE was erected as an elevated concrete guideway, about 5 km as an elevated steel guideway and the rest as a ground level guideway.

©2000 CRC Press LLC

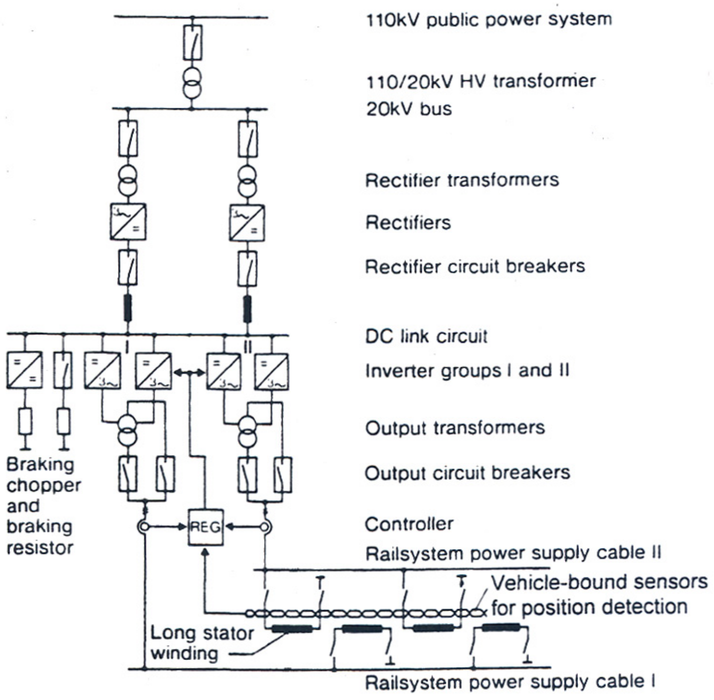

Figure 6.7 Basic circuit of LSMs power supply of the Emsland *Transrapid* Test Facility. Courtesy of *Thyssen Tansrapid System, GmbH*, München, Germany.

6.2.4 Power Supply

The Emsland *Transrapid* Test Facility is supplied with power from the 110 kV public system (Fig. 6.7). The d.c. link circuit is supplied with 2.6 kV, 2×33 kA through a 110/20 kV transformer and two 20/1.2 kV rectifier transformers connected in parallel. The rectifier transformers each supply two connected in series fully controlled rectifier bridges to obtain a twelve phase group. Smoothing reactors and protective d.c. high-speed circuit breakers are arranged at the input of the d.c. link circuit. The d.c. link voltage is converted by two PWM inverters into a three-phase VVVF changing from 0 to 2027 V and 0 to 215 Hz. The maximum LSM current is 1.2 kA. The energy consumption from the substation for the prototype vehicle is about 60 Wh/(seat×km) at constant speed of 400 km/h.

6.2.5 Vehicle

Specification data of the ELM levitation vehicle *Transrapid 07* introduced by *Thyssen Henschel* in 1988 at the International Traffic Fair

©2000 CRC Press LLC

Table 6.1 Technical data of *Transrapid 07*. Courtesy of *Thyssen Transrapid System, GmbH*, München, Germany.

Length	26.99 m (end car), 24.77 m (intermediate car)
Width	3.7 m
Height	4.16 m
Mass	50.0 t (end car), 49.1 t (intermediate car)
Speed	300...500 km/h
Acceleration	up to 1.5 m/ S^2
Braking ability	up to 1.5 m/ S^2
Rated airgap	8 mm

IVA '88 in Hamburg are presented in Table 6.1. A two-section train with passenger capacity 136 to 298 persons is formed only with two end cars. The measured aerodynamic drag for two-section vehicle at 400 km/h was originally 35.5 kN and then reduced to 33 kN.

The *support and guidance system* of the *Transrapid 07* is characterized by a chain-like arrangement of electromagnets attached to the hinge points and adjustable in two degrees of freedom with a secondary suspension system between the levitating bogie and car body [131]. To minimize the unsprung masses the support electromagnets are suspended horizontally and the guiding electromagnets are suspended vertically through linear guides and rubber spring elements.

The electromagnet windings are fed with variable current commanded by the airgap control system by separate choppers for the support and guidance. The power for the electromagnets and auxiliary equipment of the vehicle is produced by *linear generators*. Each support electromagnet is fitted with two five-phase symmetrical linear generators (Fig. 6.8). The on-board boost converters adjust the voltage according to the frequency which increase in proportion to the speed [131].

The speed record of 450 km/h was achieved by *Transrapid 07* in June 1993.

Further optimization of the *Transrapid 07* was carried out to lower the manufacturing cost and to improve the ride comfort and safety. The new vehicle *Transrapid 08* shown in Fig. 6.9 [140] is a prototype of the fleet for the Berlin-Hamburg route (Table 6.2).

6.2.6 Control System of Electromagnets

The mechanical clearance between suspension electromagnets and guideway rails is kept constant by means of the *electromagnet current control* system (Fig. 6.10). The contactless *gap sensor* integrated in the pole

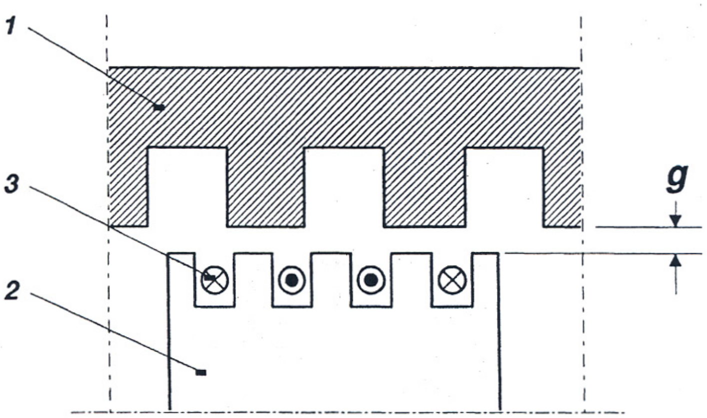

Figure 6.8 Linear generator of *Transrapid vehicles*. 1 - armature (guideway), 2 - pole of a suspension electromagnet (vehicle), 3 - winding of the linear generator.

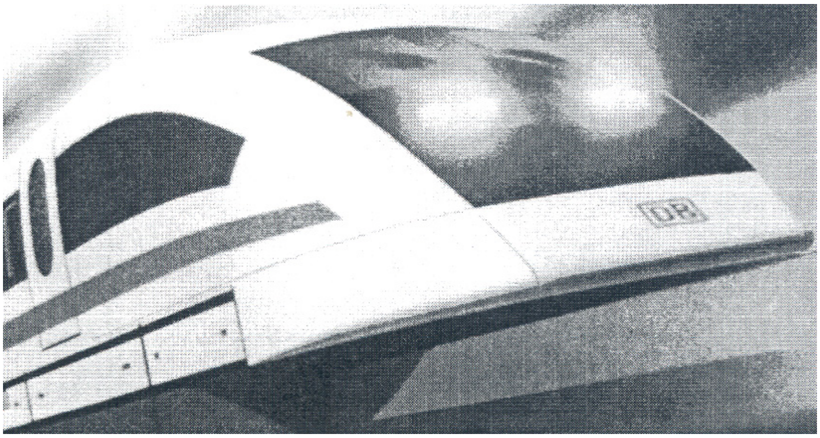

Figure 6.9 *Transrapid* 08- Photo Courtesy of *Thyssen Transrapid System, GmbH*, München, Germany.

Table 6.2 Technical data of *Transrapid 08*. Courtesy of *Thyssen Transrapid System, GmbH*, München, Germany.

Specifications	Transrapid 08	Berlin-Hamburg line	
		4-section train	5-section train
Length, m	79.7	103.5	128.3
Mass of empty train, t	149.5	198.2	247.8
Payload, t	39.0	54.8	70.2
Total mass, t	188.5	253.0	318.0
Number of seats	245	336	444

©2000 CRC Press LLC

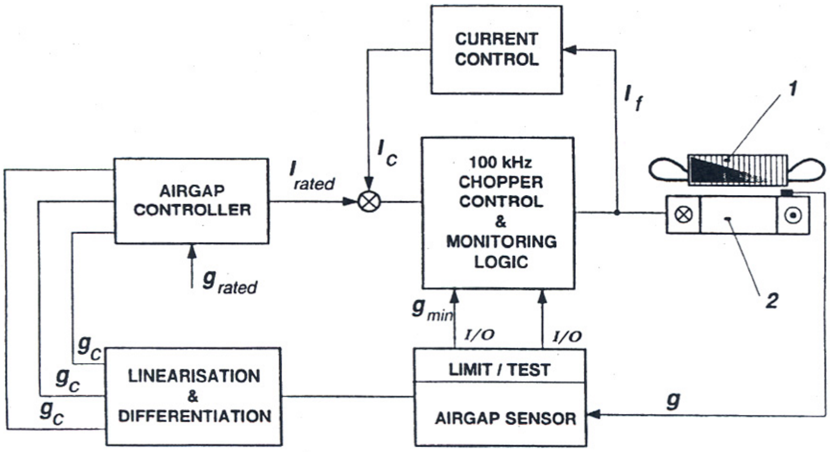

Figure 6.10 Airgap control system of *Transrapid vehicles*. 1 – armature (guideway), 2 - suspension electromagnet (vehicle).

face of the support electromagnet determines an electrical signal proportional to the distance between the electromagnet and steel rail. From the measured signals proportional to the electromagnet current, acceleration and airgap, the rated electromagnet current is adjusted in the control loop and transmitted to the chopper as input signal.

6.2.7 The Future of Transrapid System

In March 1994 the plan of construction of 292 km maglev line from Berlin via Schwerin (main control center) to Hamburg (Table 6.3) was approved by German federal government. Five stations have been planned, i.e., Berlin Lehrter Bahnhof, Berlin Spandau, Schwerin, Hamburg Moorfleet and Hamburg Hauptbahnhof. This decision was made due to plans to transfer the lower house of parliament (Deutsche Bundestag) and part of German government to Berlin. The route Bonn - Berlin had also been investigated but it was deferred due to unacceptable high costs [142].

For a five-section train, the energy consumption has been foreseen as follows [94]:

- 33...38 Wh/ (seat×km) at constant speed 300 km/h;
- 57...65 Wh/ (seat×km) at constant speed 430 km/h;
- 158...182 Wh/ (seat×km) at acceleration from 0 to 430 km/h in 3.7 min (distance 16.5 km);

©2000 CRC Press LLC

Table 6.3 Berlin-Hamburg Maglev line.

Route Length	292 km 131 km elevated guidaway 161 km ground level guidaway
Span length of guideway girders	3 to 30 m
Maximum gradient	10%
Height of gradient	1.25 to 20.0 m
Maximum superelevation	12^0 (special applications 16^0)
Curve radii at superelevation 16^0 and lateral acceleration 1.5 m/s^2	705 m at 200 km/h 4415 m at 500 km/h
Number of stations	5
Main control center	Schwerin, 100 km from Hamburg
Main maintenance center	Perleberg, 268 km from Hamburg
Revenue speed	430 km/h
Maximum speed	500 km/h
Acceleration	$\leq$ 1.0(1.5) m/s^2
Deceleration (braking)	$\leq$ 1.0(1.5) m/s^2
Travelling time between Berlin Lehrter and Hamburg Hauptbahnhof	53 min
Train configuration	4 to 5 sections per trainset 336 to 444 seats per trainset
Trains fleet	20
Interval between trains	20 min
Number of passengers per year (2010)	11.4 to 15.2 million
Traffic density (passengers × km/year)	2.6 to 3.5 billion
Total investment (DM 1.7 = $ 1.0 at prices in 1996)	DM 9.8 billion
Operation cost per year	DM 250 million
Revenue per year	DM 700...950 million

- 219...252 Wh/(seat×km) at acceleration from 0 to 300 km/h in 1.9 min (distance 4.8 km).

For comparison, IC trains consume 56 Wh/ (seat×km), TGV superexpress train consumes 108 Wh/ (seat×km) at constant speed.

The financial concept is based on the separation of the guideway and operator companies. The federal government (*Deutsche Bahn AG*) is responsible for the financing and construction of the guideway (DM 6.1 billion in 1996). The operator companies, i.e., *Adtranz (ABB Daimler Benz), Siemens* and *Thyssen Transrapid System, GmbH* will finance and construct the operating system (DM 3.7 billion in 1996). The total investment will be of DM 9.8 billion as calculated in 1996. It has been, assumed that Berlin-Hamburg maglev line will be completed by 2005.

6.2.8 History of Transrapid Maglev System in Germany

- 1922 - First consideration of ELM levitation train by H. Kemper.
- 1939-43 - Basic work on ELM levitation train with jet engine at the Aerodynamic Test Establishment in Goettingen.
- 1969 - Construction of the first practical ELM levitation model vehicle *Transrapid 01* (TR 01) by *Krauss-Maffei*, Munich. Support and guidance according to H. Kemper. Propulsion by a short armature linear motor.
- 1971 - First passenger-carrying ELM levitation prototype vehicle built by *Messerschmitt-Boelkow-Blohm* (MBB) tested on a 660 m long track at Ottobrun. Propulsion by a short-

©2000 CRC Press LLC

primary LIM. Maximum speed 90 km/h. *Transrapid 02* operated by *Krauss-Maffei* on 0.93 km track with ELM levitation support and maximum speed 164 km/h.

- 1972 - *Transrapid 03* operated by *Krauss-Maffei* on 0.93 km track with ELM levitation support and short-primary LIM at maximum speed 140 km/h. Start of the development of ELD levitation system with superconducting coils by *AEG- Telefunken, Brown Boverie & Cie AG* (BBC) and *Siemens*. Construction of a 0.9 km circular track and EET 01 test vehicle at Enlargen.
- 1973 - *Transrapid 04* operated by *Krauss Maffei* on 2.4 km track with ELM levitation support.
- 1974 - Merger of *Krauss-Maffei* and *MBB*, forming *Transrapid EMS*. Construction of *Komet* vehicle with ELM support, rocket engines and maximum speed 401.3 km/h by MBB.
- 1975 - First practical vehicle HMB 1 with long armature LSM and ELM levitation support introduced by *Thyssen Henschel*, Kassel.
- 1976 - First passenger-carrying vehicle HMB 2 with long armature LSM and ELM levitation support introduced by *Thyssen Henschel*, Kassel.
- 1977 - Federal Ministry of Research and Technology decides to develop ELM levitation systems and abandon ELD systems.
- 1978 - Foundation of the *Magnetbahn Transrapid* consortium by *AEG-Telefunken, Brown Boveri & Cie AG, Dyckerhoff & Widmann, Krauss-Maffei, MBB, Siemens AG* and *Thyssen Industrie AG Henschel.*
- 1979 - Emsland *Transrapid* Test Facility (TVE) construction work starts. International Traffic Fair (IVA '79) in Hamburg with first in the world operation of *Transrapid 05* vehicle (ELM and LSM) authorized to carry passengers at speed 75 km/h.
- 1980 - Construction of *Transrapid 06*. Emsland *Transrapid* Test Facility starts.
- 1981 - Foundation of *Gesellschaft für Magnetbahnsysteme Transrapid*
- International with Krauss-Maffei, Messerschmitt Boelkow Blohm and Thyssen Industrie AG Henschel as partners.
- 1983 - First operation of *Transrapid 06* (EML and LSM).
- 1984 - Opening of the first 21.5 km section of Emsland *Transrapid* Test Facility (North Loop). *Transrapid 06* achieves the speed of 302 km/h.
- 1987- Completion of the Emsland *Transrapid* Test Facility (South Loop). *Transrapid 06* achieves the speed of 406 km/h.
- 1988 - *Transrapid 06* achieves the speed of 412.6 km/h. *Transrapid 07* at the International Traffic Fair (IVA '88) in Hamburg.
- 1992 - Maglev link between Berlin and Hamburg in unified Germany indentified.
- 1993 - *Transrapid 07* achieves the speed record of 450 km/h.
- 1994 - Maglev link between Berlin and Hamburg approved by parliamentary bodies.
- 1995 - Public demonstration of *Transrapid 07* in Emsland starts.
- 1999 - Construction of Berlin-Hamburg line starts. First tests of *Transrapid 08.*

©2000 CRC Press LLC

6.3 Yamanashi Maglev Test Line in Japan

6.3.1 Background

The population of greater Tokyo including Chiba, Kanagawa and Saitama prefectures is now about 40 million inhabitants or almost one third of the total population of Japan (126 million). Most of the governmental, administrative, business, financial and cultural institutions are located in Tokyo. To correct the imbalance created by the overcentralisation of people, power and resources, it is essential that the political, economic, and social functions served by the greater Tokyo metropolitan area are partially relocated and distributed through the nation.

At present time, Tokyo and Osaka are connected by the *Tokaido Shinkansen* superexpress trains with the maximum speed of 270 km/h, carrying about 368,000 passengers in 283 trains a day, which is nearly the limit of this line [104]. There is a strong demand on another environmental friendly transportation system with higher speed. The *Chuo Shinkansen*, a new transportation artery between Tokyo and Osaka using superconducting technology, is expected to be implemented at the beginning of the 21st century. New *Chuo Shinkansen* trains achieving the speed over 500 km/h are necessary to unload the limited capacity of the *Tokaido Shinkansen* line, preserve the natural environment and limit the risks from natural disasters.

6.3.2 Location of Yamanashi Maglev Test Line

The Yamanashi Maglev Test Line is a part of the future *Chuo Shinkansen* line between Tokyo and Osaka. It is a joint project of the *Central Japan Railway Company* (JR Central), *Railway Technical Research Institute* (RTRI) and *Japan Railway Construction Public Corporation* which was approved by the Ministry of Transport in 1990. The 42.8-km test line will be constructed between Sakaigawa village, Higashi-Yatsushiro district and Akiyama village, Minami-Tsuru district in Yamanashi Prefucture, west from Tokyo. At present, an 18.4-km Katsunuma-budokyo – Ohtsuki section has been completed (Figs 6.11 and 6.12). The maximum planned speed is 550 km/h (operation speed 500 km/h), minimum curve radius is 8 km, maximum gradient is 4% and distance between the centers of adjacent parallel guideways is 5.8 m. A 12.8-km section is a double track line where the dynamics of two trains passing each other at a relative speed of about 1000 km/h will be studied. Other specifications are given in Table 6.4. The cost of 18.4 km test line, power conversion substation, control center, train and train depot is about 230 billion yen (1996).

©2000 CRC Press LLC

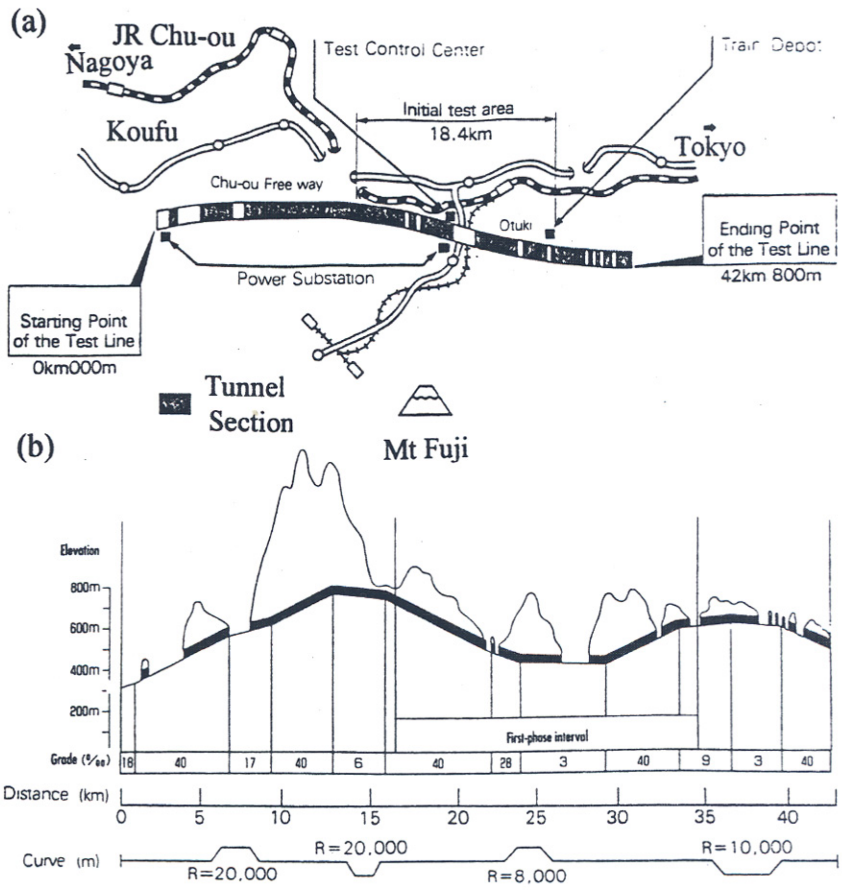

Figure 6.11 Yamanashi Maglev Test Line: (a) outline, (b) profile. Courtesy of *Central Japan Railway Company* and *Railway Technical Research Institute*, Tokyo, Japan.

©2000 CRC Press LLC

Figure 6.12 Yamanashi Maglev Test Line: Ogatayama Bridge over the Chuo Expressway. Courtesy of *Central Japan Railway Company* and *Railway Technical Research Institute,* Tokyo, Japan.

Table 6.4 Yamanashi Maglev Test Line: data of experimental track. Courtesy of *Central Japan Railway Company* and *Railway Technical Research Institute,* Tokyo, Japan.

Specifications	Total	Priority section
Length, km	42.8	18.4 (12.8 km double track)
Length of tunnel section, km	34.6	16.0
Elevated section, km	8.2	2.4
Curve radius, km	8 to 20	
Maximum gradient	4%	
Number of control centers	1	1
Number of substations	2	1
Number of train depots	1	1

©2000 CRC Press LLC

6.3.3 Principle of Operation

The experimental maglev train MLX01 for Yamanashi Maglev Test Line is suspended on the principle of ELD levitation where the repulsive forces are produced between stationary short-circuited coils and moving superconducting electromagnets. The track is U-shaped and embraces the bottom of the vehicle. At each side of the track non-powered short-circuited coils serving both as levitation and lateral guideway coils are mounted in vertical position. The vehicle is equipped with superconducting electromagnets. In addition, a three-phase propulsion vertical winding fed with three-phase current is installed at each side of the track which, together with the train electromagnets, forms an air-cored LSM. The three-phase stationary winding produces a travelling magnetic field and corresponds to the armature winding of a conventional synchronous motor. The vehicle superconducting electromagnets correspond to the excitation system of a synchronous machine. When the train propelled by the LSM passes short-circuited coils at high speed, currents induced in these coils together with magnetic field excited by superconding electromagnets produce strong repulsive and lateral stabilization forces on the vehicle. The same superconducting electromagnets are used both for levitation, lateral guidance and propulsion.

6.3.4 Guideway

The arrangement of ground and vehicle windings is shown in Fig. 6.13. Both propulsion coils and levitation-guidance coils are attached to concrete side walls of the guideway (Fig. 2.12).

All ground coils are made of aluminium conductors insulated with polyester (epoxy) resin. *Propulsion coils* have dimensions approximately 1.42 × 0.6 m. The 8-shaped *levitation* and *guidance coils* have dimensions approximately 0.9 × 0.9 m and are attached to the surface of the three-phase two-layer propulsion winding. The levitation and guidance coils consist of two sections: for levitation and for lateral stabilization (guidance) of the vehicle (Fig. 6.14). The guidance sections facing each other at two opposite sides are electrically connected under the track constituting a *null flux connection* (Fig. 6.15). If the train deviates from the center of the guideway, the deviation is reversed by the attractive forces of the superconducting electromagnet on the distant side of the guideway and repulsive forces on the opposite (near) side.

In order to achieve passenger comfort when travelling at very high speeds, the ground coils must be installed more precisely than *Shinkansen* rails. The accurate attachment, easy construction and simple maintenance require three types of guideways: (a) panel type, (b) side-wall beam type and (c) direct attachment type (Chapter 2).

©2000 CRC Press LLC

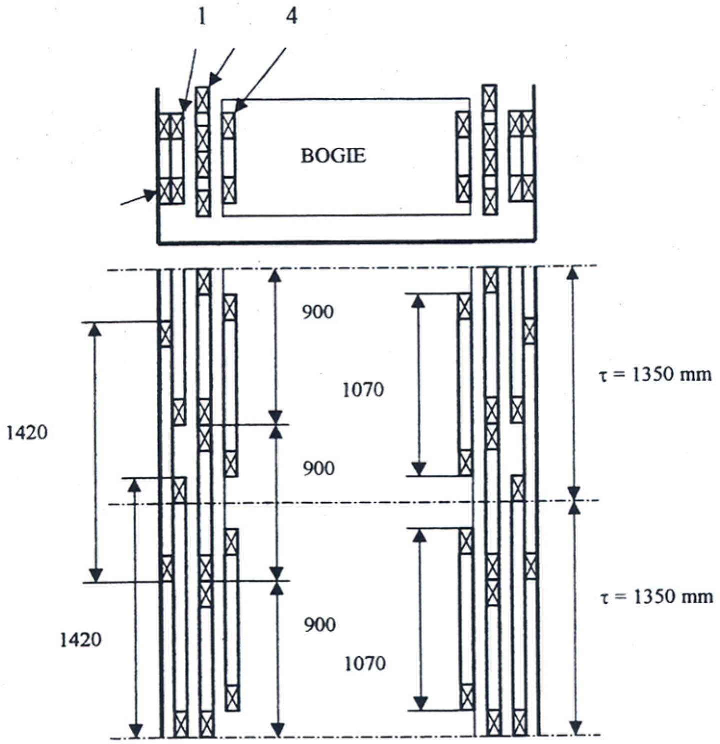

Figure 6.13 Arrangement of propulsion, levitation-guidance and excitation coils: 1 - propulsion, front side, 2 - propulsion, reverse side, 3 - 8-shaped levitation and guidance coils, 4 - excitation coil (on board superconducting electromagnet) [143].

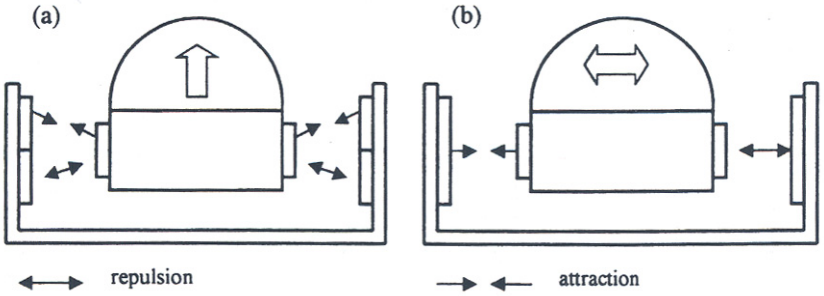

Figure 6.14 Operation of 8-shaped coils: (a) levitation, (b) lateral stabilization (guidance) of the vehicle [143].

©2000 CRC Press LLC

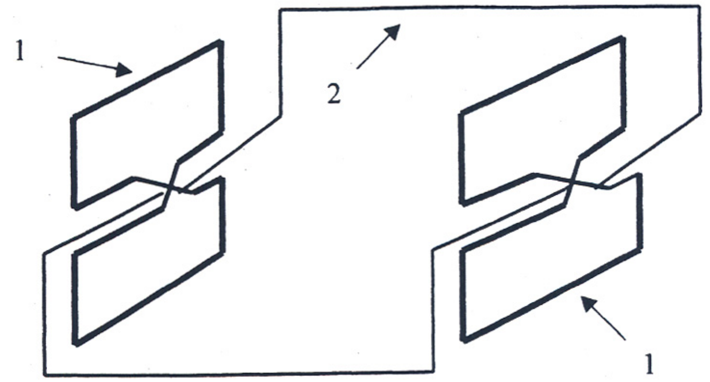

Figure 6.15 Null-flux connection of levitation and guidance coils. 1 - coils, 2 - null-flux cable [143].

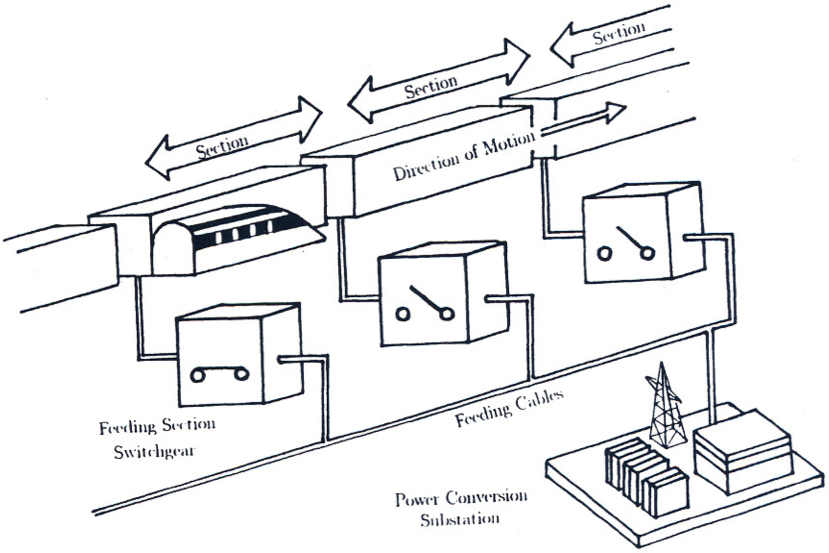

Figure 6.16 Feeding system of propulsion winding sections. Courtesy of *Central Japan Railway Company* and *Railway Technical Research Institute*, Tokyo, Japan.

©2000 CRC Press LLC

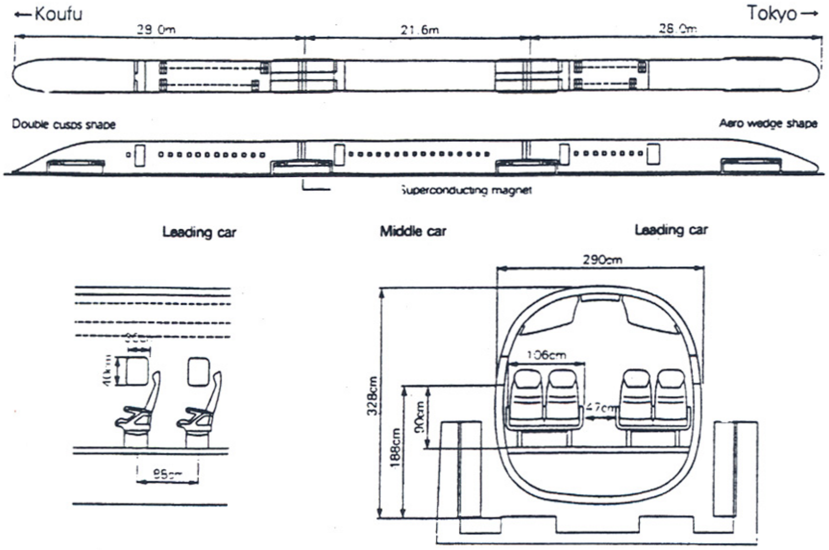

Figure 6.17 Outline of the MLX01 Maglev Train. Courtesy of *Central Japan Railway Company* and *Railway Technical Research Institute*, Tokyo, Japan.

To save energy, a group of propulsion coils are connected in series and create a winding section. Only those sections carrying the train are powered through the feeding *section switchgears* (Fig. 6.16).

6.3.5 Vehicle

The MLX01 test vehicle (Table 6.5) consisting of two end cars and one intermediate car is shown in Fig. 6.17 and Fig. 6.18 [143]. The car body has been designed to obtain a mass reduction and provide a comfortable interior. Both the mass and cross section of the car is smaller than those of existing *Shinkansen* trains to reduce the air drag and improve dynamic performance. The structure of the body using the aircraft and rolling stock technologies has a light weight and enough strength to endure the repeat of large pressure fluctuations when passing through tunnels. Two types of nose shapes, i.e., *double cusp* and *aerowedge* were developed which considerably reduce air drag and aerodynamic noise.

The bogie, on which the superconducting magnets are mounted, serves to transmit the propulsion and levitation forces to the vehicles (Fig. 6.19). A refrigeration system for freezing the helium is also mounted on the bogie. To improve the travelling comfort, pneumatic springs for car body suspension and vibration control devices are incorporated in some bogies.

©2000 CRC Press LLC

Table 6.5 Specification data of MLX01 Maglev Trains. Courtesy of *Central Japan Railway Company* and *Railway Technical Research Institute*, Tokyo, Japan.

Specifications	MLX01 (first train)	MLX01 (second train)
Maximum speed	550 km/h	
Number of cars	3	4
Pole pitch of electromagnets	1.35 m	
Vehicle configuration	Articulated bogie system with superconducting electromagnets	
Car body structure	Semi-monocoque structure using aluminium alloy	
Levitation height	0.1 m at 500 km/h	
Width of car	2.9 m car body, 3.22 bogie	
Height of car	3.28 m while levitating 3.22 m on-gear running	
Length of end cars	28.0 m	
Length of intermediate car	21.6 m	24.3 m and 21.6 m
Cross section area of the car	8.9 m^2	
Maximum mass of fully loaded car	32 t end car 20 t intermediate car	33 t end car 22 t intermediate cars
Length of the train	77.6 m	101.9 m

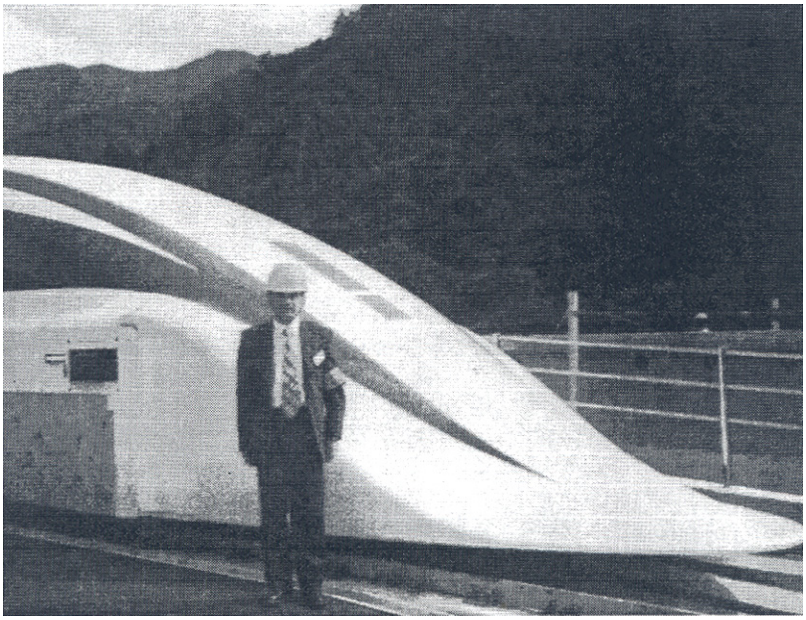

Figure 6.18 Double-cusp shaped head car (facing Koufu) of the MLX01 Maglev Train. Courtesy of *Central Japan Railway Company* and *Railway Technical Research Institute,* Tokyo, Japan.

The bogie is fitted with landing and guide gear wheels which are necessary when travelling at low speeds. Hydraulic apparatus are used for raising and lowering these wheels.

Landing gears have been developed taking durability and mass reduction into consideration. Disk brakes and rubber tires are now capable of use at speeds over 500 km/h. To follow the track center at low speeds, the train is equipped with side guide gear wheels of smaller diameter than landing gear wheels.

6.3.6 Superconducting Electromagnet

Light and strong superconducting electromagnets are carried on bogies of the MLX01 maglev trains (Fig. 6.19). There are eight superconducting coils per experimental vehicle, four at each side. The structure of superconducting electromagnet (Chapter 2) prevents the so-called *quench* effect (superconducting-to-normal transition) and reduces internal excess heat. Supercomputer simulations of electromagnetic disturbances and mechanical vibration have been made to understand better these parasitic phenomena. The heat generation within the cryostat housing the superconducting coils has been quantified to establish countermeasures.

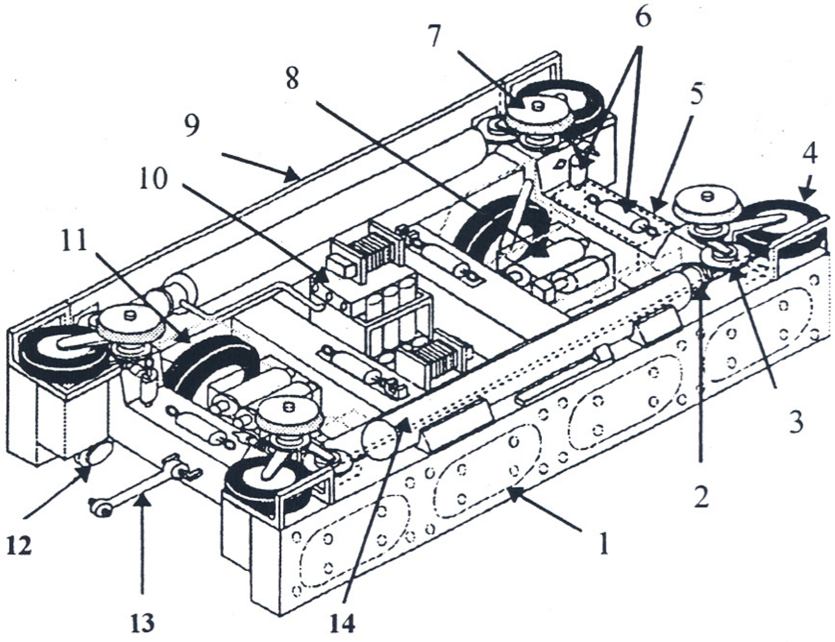

Figure 6.19 Bogie of Yamanashi Maglev Test Line Vehicle: 1 - super-conducting magnet, 2 - helium refrigerator, 3 - guiding stopper wheel,4 - guiding gear, 5 - oil reservoir tank, 6 - dampers, 7 - air spring, 8 - hydraulic pressure unit, 9 - side cover, 10 - helium compressor, 11 –landing gear, 12 - emergency landing wheel, 13 - longitudinal anchor (to car body), 14 -liquid helium and nitrogen tanks. Courtesy of *Central Japan Railway Company and Railway Technical Research Institute*, Tokyo, Japan.

©2000 CRC Press LLC

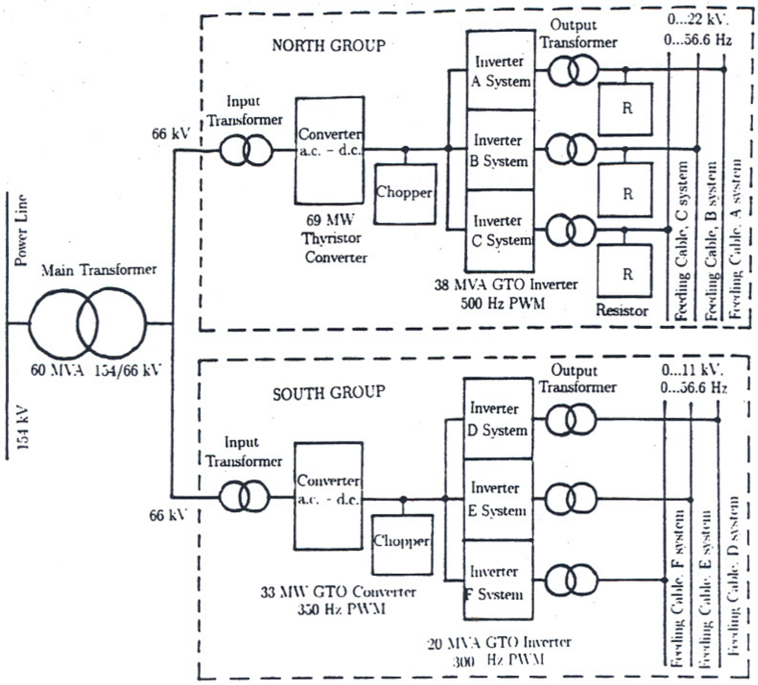

Figure 6.20 Block diagram of power conversion substation [143].

Both the cryostat and on-board refrigeration system to re-liquefy the helium gas vaporized within the cryostat are light and robust.

6.3.7 Power Conversion Substation

There are two groups of converters identified according to location on the substation yard and lines to be fed: North Line Group and South Line Group (Table 6.6). The power conversion substation (Fig. 6.20) converts electric power from 154 kV into 0 to 22 kV, 0 to 56.6 Hz (North Line Group) and 0 to 11 kV, 0 to 46.3 Hz (South Line Group) suitable for the velocity and acceleration or deceleration of the maglev train. At the frequency f = 56.6 Hz and pole pitch τ = 1.35 m (Tables 6.5 and 6.6) the maximum train velocity is $\upsilon_{\max} = 2f\tau$ = 2 x 56.6 x 1.35 = 152.82 m/s ≈ 550 km/h. At f = 46.3 Hz, the maximum velocity is 450 km/h.

The main step down transformer is rated at 60 MVA, 154/66 kV. The North Line Group consists of a 69 MW thyristor converter and 38 MVA GTO inverter with 500 Hz PWM. The South Line Group consists of 33 MW GTO converter with 350 Hz PWM and 20 MVA GTO inverter with 300 Hz PWM. High power 4.5 kV, 4 kA GTO devices have been used [88].

©2000 CRC Press LLC

Table 6.6 Specifications of power converters. Courtesy of *Central Japan Railway Company* and *Railway Technical Research Institute*, Tokyo, Japan.

Parameter	North Line North Group	South Line South Group
<u>Converter</u>		
• Rated power	69 MW	33 MW
• Input voltage	66 Kv	66 Kv
• Input frequency	50 Hz	50 Hz
• Output voltage	± 3450 V d.c.	± 2625 V d.c.
<u>Inverter</u>		
• Number of phases	3	3
• Rated power	38 MVA	20 MVA
• Output voltage	0...12.7 kV	0...6.35 kV
• Output voltage behind output transformer	0...22 kV	0...11 kV
• Output current	0...960 A	0...1015 A
• Output frequency	0 to 56.6 Hz	0 to 46.3 Hz
<u>d.c. chopper</u>		
• Rated power	19 MW	4.09 MW
• Input voltage	±3. 55kV	±2.625 kV
• Chopping frequency	300 Hz	350 Hz
• Control	PWM	PWM

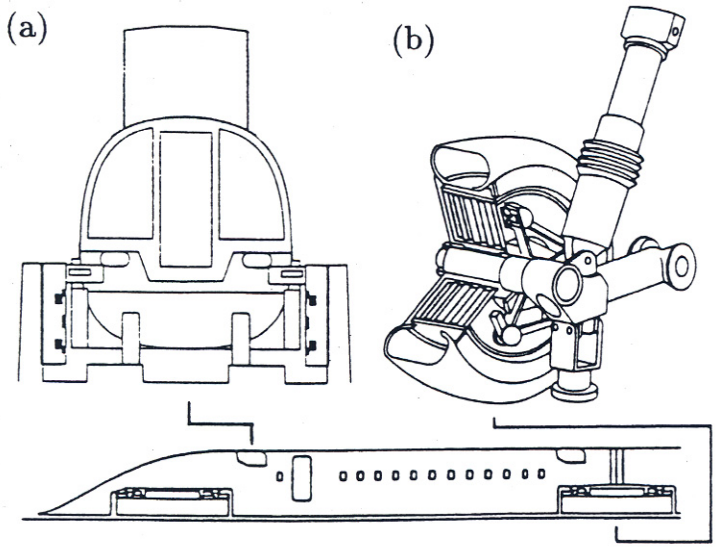

Figure 6.21 On-board brakes: (a) aerodynamic brake, (b) disc brake. Courtesy of *Central Japan Railway Company and Railway Technical Research Institute*, Tokyo, Japan.

©2000 CRC Press LLC

Thus, the Yamanashi Maglev Test Line uses the largest inverters in the world. The inverter output current must be high (about 1 kA) because the insulation system of ground coils can withstand only limited voltage level. To reduce the input harmonic current at low speed operation and improve the power factor, converters are of multi-bridge structure.

Each group of three-phase inverters feeds three sections of the North Line and three sections of the South Line. The North Line with maximum speed of 550 km/h is fed with 22 kV. The South Line with maximum speed of 450 km/h is fed with 11 kV. The feeding section switchgears turn on and off each time the train passes by. Vacuum switches have been developed for endurance through over one million test operations.

6.3.8 Brakes

The braking system of the prototype maglev train consists of ground-based brakes and on-board brakes.

The *ground-based brakes* incorporate the regenerative braking and rheostatic braking. During the regenerative braking, the current is reversed and returned to the power system. In the rheostatic braking the LSM operates as a generator and the kinetic energy of the train is converted into electric energy dissipated in the braking resistor.

The *on-board brakes* constitute a backup. To achieve a stable braking force from very high speed to standstill, two kinds of on-board brakes are installed. In high-speed range *aerodynamic brakes* are effective, while in middle to low-speed range the train is brought to a halt by built-in-wheel *disk brakes* (Fig. 6.21).

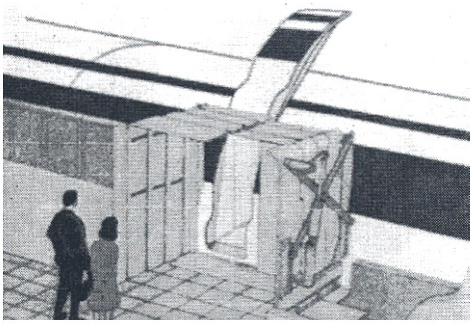

Figure 6.22 Passenger boarding system. Courtesy of *Central Japan Railway Company and Railway Technical Research Institute,* Tokyo, Japan.

6.3.9 Boarding System

An *indoor type passenger platform* has been designed (Fig. 6.22). The boarding system aligns with the passenger door in order to guide the passengers during boarding and provides a *magnetic shielding.* A narrow section of the guideway wall (where guide tyres have a contact) facing the train door can fold down to allow passengers to board.

In order to make the interior of the passenger cabin more spacious while providing extra smoothness on the exterior of the cars and make them more airtight, special *upward-sliding doors* have been designed. Doors have been equipped both with infrared and contact sensors which sense passengers getting on and off the train thus eliminating the danger of doors accidentally closing.

©2000 CRC Press LLC

6.3.10 Control System

The experimental maglev train is operated automatically by the ground based control equipment. The whole control system (Fig. 6.23) consists of the three following systems: (a) traffic control, (b) safety control and (3) drive control system. The train operation control center is located in the station building.

Traffic control system

The traffic control system comprises the central traffic control system, the regional traffic control system and the train operation control system. The central traffic control system generates a *schedule of all trains*, and the regional traffic control system regionally details it. The train operation system controls each train according to the direction of the regional traffic control system. The traffic control system also monitors all trains on the whole line.

©2000 CRC Press LLC

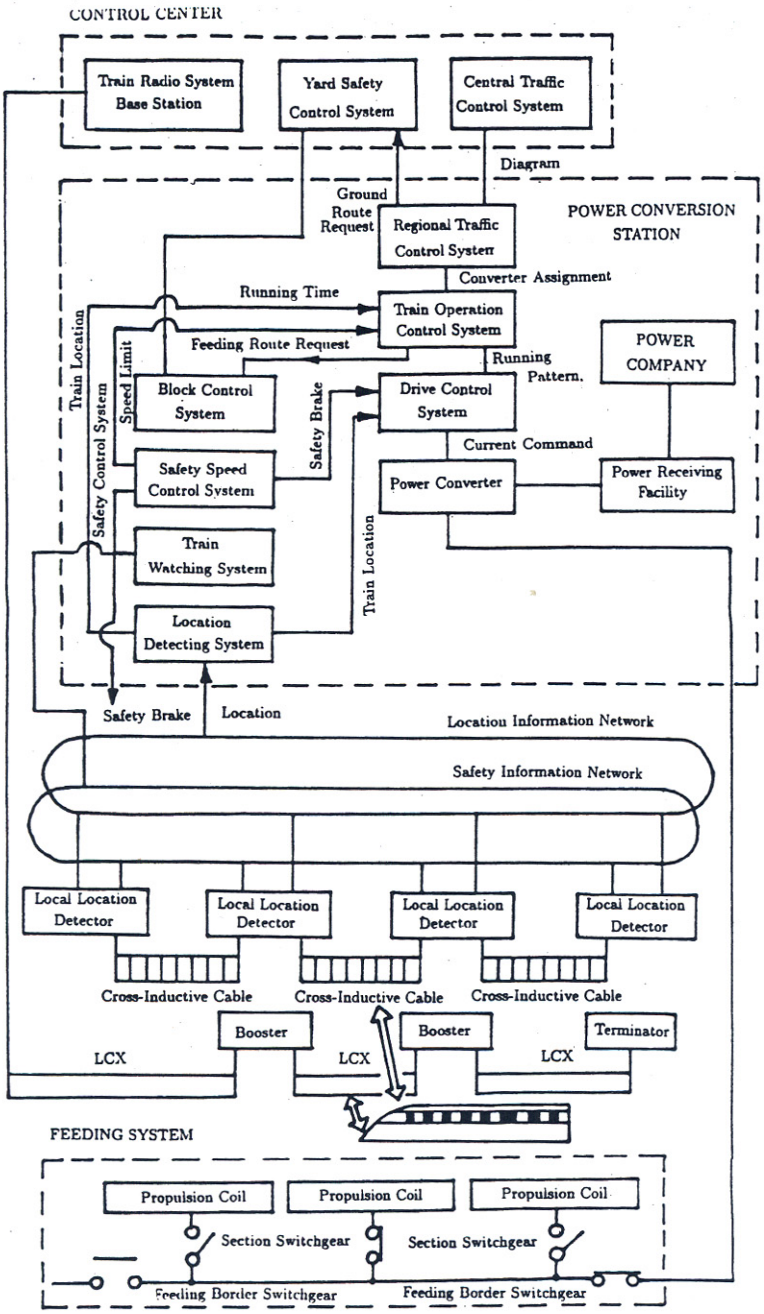

Figure 6.23 Operation system of the experimental Yamanashi Maglev Test Line. Courtesy of *Central Japan Railway Company and Railway Technical Research Institute*, Tokyo, Japan.

Safety control system

The *safety control* system monitors the location and the velocity of trains at all times and generates an acceptable speed limit for each train. Only within this limit, the traffic control system and the drive control system are allowed to work. If the train runs out of this acceptable limit, the safety control system outputs the command of the safety brake and stops the train safely.

©2000 CRC Press LLC

Since the maglev train is controlled on the ground, the safety control system uses cross-inductive cable installed along the whole line to detect the position of the train with high precision within several centimeters.

Drive control system

The *drive control* system corresponds to the driver in the conventional railway system. This system takes the running (rolling, gradient, acceleration, curve and air) resistance and riding comfort into account and enforces the running pattern generated by the train operation system with the power electronics converters. It also switches on and off the section switchgears according to the position of the train.

6.3.11 Communication System

One leaky coaxial cable (LCX) per each track has been installed for the train radio communication system. The train radio system uses: millimetric waves from 30 to 300 GHz.

6.3.12 Experiments

The following experiments are carried out on Yamanashi Maglev Test Line:

- basic running tests, i.e., levitation running tests, wheel running tests, speed increasing tests, maximum speed (approximately 550 km/h) verification tests;
- general functional tests, i.e., high speed passing tests, tunnel entering tests, substation cross-over tests, multiple train control tests, emergency tests, etc.;
- reliability verification tests, i.e., high speed continuous running tests, transportation capability verification tests, etc.;
- other verification tests as passenger physiology confirmation tests, station facilities verification tests, environmental impact verification tests, economy verification tests, maintenance standards verification tests, etc.

Experiments begun in April 1997. Intensive experiments with two trains were carried out in 1998. High speed running tests were performed in 1999.

The main goal of the tests is (a) confirmation for possibilities of safe, comfortable, and stable run at 500 km/h, (b) confirmation of reliability and durability of the vehicle, wayside facilities, and equipment as well as superconducting magnets, (c) confirmation of structural standards including the minimum radius of curvature and the steepest gradient, (d) confirmation of center-to-center track distance for safety of trains passing each other, (e) confirmation of vehicle performance in relation to tunnel cross-section and pressure fluctuations in tunnels, (f) confirmation of performance of the turnout facilities, (g) confirmation of environmental impact, (h) establishment of multiple-train operation control systems, (i) confirmation of operation and safety systems and track maintenance criteria, (j) establishment of inter-substation control systems and (k) pursuit of economic issues, construction and operation costs.

After three years of testing, at the beginning of the next century, the prospect of application of the superconducting maglev transport technology to a revenue service will be evaluated.

6.3.13 History of Superconducting Maglev Transportation Technology in Japan

- 1962 - Research in linear motor propulsion and non-contact suspension started.
- 1972 - Experimental superconducting maglev test vehicle ML-100 succeeded in 10 cm levitation on the yard of the Railway Technical Research Institute (RTRI) in Kokubunji, Tokyo.
- 1977 - Test run of ML 500 vehicle on inverse T -shaped guideway started.
- 1979 -Unmanned test vehicle ML 500 achieves the world speed record of 517 km/h at the 7-km Miyazaki Maglev Test Track, Kyushu island.
- 1980- Test run of MLU001 vehicle on U-shaped guideway started.

©2000 CRC Press LLC

- 1987 - The speed of 400.8 km/h achieved by 2-car manned unit. RTRI reorganized. Test run of MLU001 started.
- 1990 - The Yamanashi Maglev Test Line construction plan approved by the Ministry of Transport.
- 1991 - Test run on sidewall levitation system started (Miyazaki, Maglev Test Track). MLU002 was destroyed by a fire during a test run
- 1994 - The speed of 431 km/h attained on Miyazaki Maglev Test Track by unmanned MLU002N vehicle.
- 1995 - The speed of 411 km/h attained on Miyazaki Maglev Test Track by manned MLU002N vehicle.
- 1996 - The 18.4 km section of Yamanashi Maglev Test Line completed. First train MLX01 (3 cars) delivered.
- 1997 - Running tests with MLX01 train commenced. Speed records on Yamanashi Maglev Test Line: 531 km/h on December 12 (manned train), 550.0 km/h on December 24 (unmanned train). Second train MLX01 delivered.
- 1998 - Maglev trains MLX01 passed each other at a relative speed of 966 km/h on Yamanashi Maglev Test Line.
- 1999 - Speed record of 552 km/h (manned train) on Yamanashi Maglev Test Line.

6.4 Swissmetro

Switzerland is a small country (41,293 km^2) with a mountainous landscape and moderate density of population, i.e., 172 inhabitants per km^2 (compare with 234.5 inhabitants per km^2 in Germany and 333.3 inhabitants per km^2 in Japan). The highest population density spread over a distance of 300 km is in the Swiss central plateau with major cities Geneva Lausanne, Bern, Luzern, Zürich, St Gallen (West to East) and Basel and Bellinzona (North to South). The distance between each of the neighboring major cities is from 40 to 100 km. There is a high saturation of main transport routes in Switzerland. To solve the transportation problems and protect the natural environment, a high speed *underground transportation network* seems to be the only solution (Fig.6.24).

6.4.1 Assumptions

The *Swissmetro* network project assumes speeds around 400 km/h, about 12 min travel time between stations, 3 min stops at stations, 4 to 8 trains per hour and trains with minimum passenger capacity of 200 persons. The travel time from Zürich to Geneva will take less than 1 h as compared with 3 h by surface trains.

The *Swissmetro* project is based on four complementary modern technologies:

- an underground infrastructure with two parallel tunnels of 5 m in diameter in each direction and stations linked to the existing public means of transportation (railways, roads, airports);
- a partial vacuum with the air pressure reduced to 8 to 10 k Pa (0.08 to 0.1 atm) in tunnels to minimize the air resistance and thus to reduce the energy consumption;
- a propulsion system by using linear motors with guidaway mounted armatures;
- support and guidance system by using the ELM levitation technology.

©2000 CRC Press LLC

6.4.2 Pilot Project

The line Geneva-Lausanne, about 60 km long, has been selected as the *pilot project.* The cross section of the tunnel and the vehicle is shown in Fig. 6.25. Specifications of the pilot vehicle are given in Table 6.7. To control the airgap of levitation and guidance electromagnets, airgap estimators based on determination of inductance will be used rather than position sensors.

Swissmetro vehicles require electric power for propulsion, guidance and auxiliary equipment such as lights, airconditioning, communication and safety equipment which is estimated as 500 kW (peak demand). The power will be transferred to the vehicle with the aid of high frequency linear transformers. The long primary (about 1 km) of the linear transformer is fixed to the guidaway and the secondary winding is fixed to the vehicle. At the frequency 2 kHz and airgap 20 mm the predicted efficiency of the linear transformer is about 80%.

Two configurations of iron cored LSMs have been investigated [115]:

- guideway mounted long armature with three phase winding and on board excitation system;
- guideway mounted short three-phase armature integrated with excitation system and vehicle mounted passive reaction rail.

Both two configurations use two LSMs with pole pitch $\tau \approx 0.323$ m located in parallel at both sides of the guideway. LSMs are rated at 4.5

©2000 CRC Press LLC

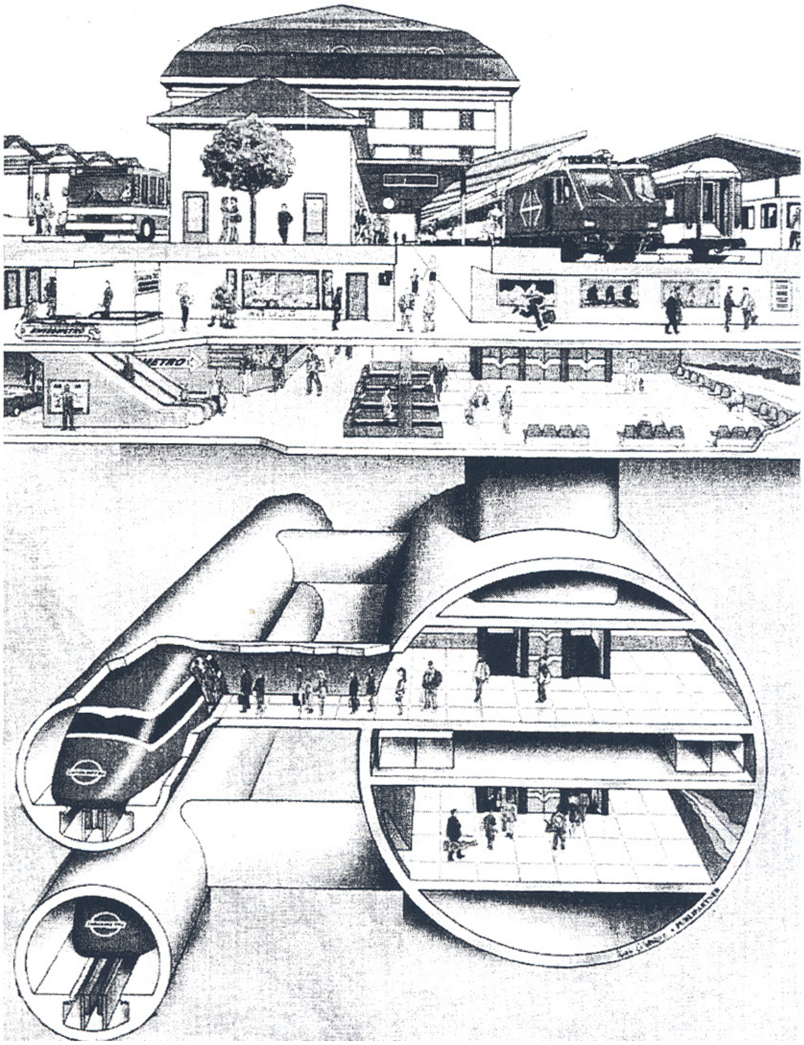

Figure 6.24 Cross section through the station of *Swissmetro*. Courtesy of *Swissmetro*, Geneva, Switzerland.

©2000 CRC Press LLC

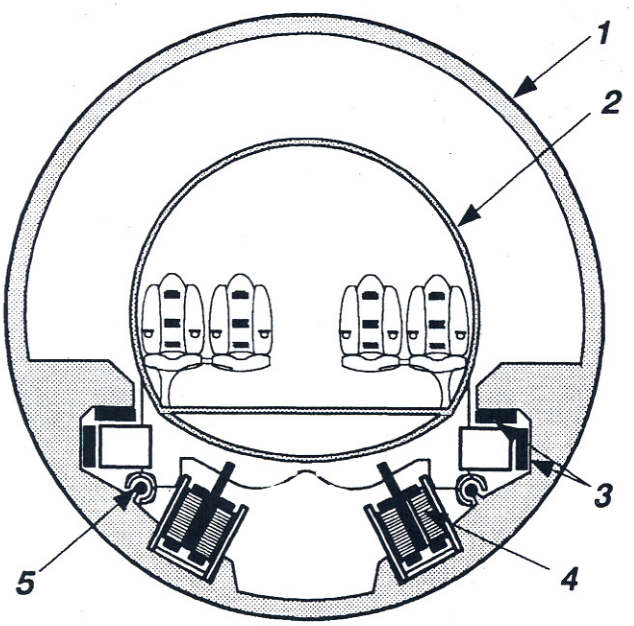

Figure 6.25 Cross section of the tunnel and vehicle of Swissmetro pilot project: 1 - inner concrete tunnel ring (5 m diameter), 2 - passenger car body, 3 - ELM levitation support and guidance system, 4 - LSM, 5 –linear transformer. Courtesy of Swissmetro, Geneva, Switzerland.

Table 6.7 Specification data of *Swissmetro* pilot vehicle. Courtesy of *Swissmetro,* Geneva, Switzerland.

Maximum speed	500 km/h
Mechanical power demand	6 MW
Power supplied to the vehicle (levitation, guidance and auxiliary equipment	500 kW
Diameter of vehicle	3.2 m
Length of vehicle	80 m
Number of passengers per vehicle	200
Total mass of vehicle	50 t
Initial acceleration from standstill to 290 km/h	1.3 m/s^2
Airgap for propulsion, levitation, guidance and linear transformer	20 mm

©2000 CRC Press LLC

kV /1.4 kA or 6.4 kV /0.9 kA. The second configuration, i.e., double sided homopolar LSM (Fig. 1.12, Chapter 1) seems to have more economical advantages. No electrical propulsion energy has to be delivered to the vehicle as three phase armature windings are stationary and the vehicle mounted passive reaction rail needs neither windings nor PMs. The short armature sections about 10 m long are distributed along the tunnel in approximately 50 m intervals, equal to the length of the on-board passive reaction rail. The distance between armature sections should be shorter near and at the stations where trains require higher power for acceleration. Even if the armature sections are oversized due to the presence of the excitation system as compared with typical LSMs, there is a substantial saving on ferromagnetic materials and conductors. Both electromagnetic and PM excitation of homopolar LSMs have been considered.

The power supply system distributing the electrical energy along the tunnel consists of 125/6.1 kV, 50 Hz transformers and voltage source PWM converters with the output frequency 0 to 215 Hz. The following requirements are to be met by converters [115]:

- maximum apparent power of8.5 MVA at power factor cost$\phi = 0.85$ (active power 7.225 MW);
- power factor on the line side cost$\phi = 1.0$;
- operation in propulsion and regenerative braking mode with any desired power factor on the LSM side;
- from 290 km/h up to maximum speed 500 km/h the acceleration at constant electric power of 7 MW with efficiency exceeding 85%.

The maximum d.c. link voltage between rectifier and inverter has been assumed 10 kV.

The predicted energy consumption at constant speed of 400km/h of the *Swissmetro* system, taking into account the maintenance of vacuum, is 43 Wh/(seat×km). At the same speed the *Transrapid 07* consumes 50.4 Wh/seat ×km. The revenue service can be realistic after 2010.

History of *Swissmetro*

- 1974 - Swiss engineer R. Nieth develops the concept of *Swissmetro* to provide high-speed transport between principal urban and rural areas.
- 1985 - Interest in the project is shown at a political level.
- 1989 - The Federal Department of Transport, Communication and Energy (EVED) grants the Swiss Federal Institute of Technology (EPFL), Lausanne, a subsidy to conduct the preliminary study.
- 1992 - Foundation of *Swissmetro,* S.A. as a joint stock corporation.
- 1993 - The results of the preliminary study confirm the desirability, feasibility and viability of the project. Inauguration of the first *Swissmetro* exhibition at Swiss Transport Museum in Lucerne.
- 1994 - Launch of the main study supported financially by major Swiss companies.
- 1998 - Main study of the system and components.
- 1999 - Swiss Government supports the project.

6.5 Marine Express

A reliable and weather independent, short distance inter-island or island-mainland link is still a difficult transportation and civil engineering task. Ferry connections are subject to the weather and world statistics show numerous ferry sinkings with many casualties. Undersea tunnels are extremely expensive and demand expensive maintenance, e.g. to pump in fresh air and pump out the excessive water coming in all the time. For example, the world's longest 53.85-km Seikan Tunnel between Honshu and Hokkaido islands (Japan) took over 40 years to be completed since its idea was conceived and geological survey began.

©2000 CRC Press LLC

To combat noise, save land and protect the natural environment, it is wise, where possible, to locate future airports on the sea, minimum 10 km away from the mainland. This can be done by building artificial islands. Such an airport requires reliable and convenient 24-hour passenger transportation between the mainland and artificial island. A similar problem arises in the case of future undersea cities accommodating hundreds thousands of inhabitants.

Amphibious trains travelling both under the water and on the dry land would be an ideal solution [147]. Such an underwater train, also called *marine express* is proposed to be levitated on an elevated guidaway and propelled by linear motors [147]. The elevated guidaway can be laid on the sea bottom or on the land. To overcome the buoyancy of the train under the water, the bogie needs to be electromagnetically attracted to the guidaway. On the land, the train needs to be levitated by repulsive forces. In both cases a constant airgap is to be maintained by controlling the input electrical variables. A LSM with superconducting excitation system has been identified as the best candidate due to its high thrust, large airgap, low excitation power and controllability of the vehicle buoyancy under the water [147]

The water density is much higher than that of the air and consequently the water resistance force is much higher than the air resistance force see eqn (1.37). It has been found that in order to keep the same thrust, a 100-m long marine express travelling on the land with the speed of 420, km/h will have to reduce its speed to 61 km/h under the water [147] .On the other hand, the power required to run on the land is 9.3 MW at 420 km/h in comparison with only 1.4 MW at 62 km/h under the water (the power is approximately proportional to υ^3) [148].

A research team lead by K. Yoshida and T. Ota at Kyushu University, Fukuoka, Japan, has successfully tested small scale models of underwater train cars to prove the feasibility of the idea. A superconducting LSM has been replaced by a PM LSM [148]. When the buoyancy of the water is larger than the weight of the vehicle, attractive-mode levitation and propulsion is realized by controlling the armature current and load angle.

A *pitching-damping control* method has been proposed to obtain the stable levitation and propulsion. It is impossible to control the pitching angle completely together with the control of levitation and propulsion by controlling only the thrust F_x and normal force F_z [148]. On the other hand, by controlling the thrust F_x of a LSM, the pitching motion can be easily and effectively damped. The *decoupled control* of levitation and propulsion with pitching motion control is effective and it has enabled a small scale prototype vehicle to run successfully under water in a repulsive mode [148].

©2000 CRC Press LLC

chapter 7

Building and Factory Transportation Systems

7.1 Elevator Hoisting Machines

Hoisting technology started when Archimedes constructed his first winch in 236 B.C. However, early primitive elevators did not guarantee any safety for passengers. The situation changed with Elisha Otis' invention of a reliable *safety gear* in 1853 [107]. In the first elevators the *drum* was used to collect the *rope*. The major disadvantage was the necessity to lift the load together with the supporting structure. The next type, referred to as a *rope traction elevator*, has been constructed in such a way as to obtain the load balanced by the *counterweight*. This latter construction is widely used today.

Elevators can be classified into three major categories based on their size:

- High-rise elevators used in the tallest buildings in major cities and manufactured at a volume of about 2,000 units annually. These elevators add image and prestige to the company manufacturing them.
- Mid-rise elevators installed in office buildings, hotels, and other similar structures (annual market size of approximately 20,000 units). The appearance, comfort and ride quality become most important for these installations.
- Low-rise elevators mostly installed in residential buildings (total annual sales of about 200,000 units world-wide).

There is an increasing demand to reduce both the space needed for *hoistways* in buildings and the size of elevator electrical supplies. These requirements have a strong influence on the selection of the hoisting machine, which can be remarkably improved by utilizing a linear motor [44]. Because the linear motor produces straightforward movement without mechanical transformations thus improving the efficiency due to a smaller number of components, the usage of linear motors appears highly attractive. This technology matured in 1991 when *Nippon Otis* introduced the first commercial application of the *linear motor elevator* onto the Japanese market [130]. Since then, the intensive research in this field was aimed at surpassing conventional technology in performance and cost. The type of electric motor, i.e., induction, switched reluctance, or synchronous is important in the linear motor elevator technology. However, the elevator structure is even more important because requirements for the hoisting system vary with the arrangements of the elevator components. Sometimes the hoisting machinery must lift all travelling masses, whereas in other cases the counterweight does part of the work. Moreover, in some elevators, the weight of the motor can be utilized as the part of the mass balance.

7.1.1 Linear Motor Driven Elevator Cars

The earliest patent concerning a linear motor in elevators was granted to K. Kudermann in 1970[71]. The principle of that patent is illustrated in Fig. 7.1. The proposed system consists of a counterweight and two *linear motor armatures on both sides of the car*. The disadvantage of this set-up is that the motor must also lift its own weight thus increasing the demand for power supply during acceleration.

The best linear motor drive is a combination of the double-sided motor with the guide rail, which provides an advantage in balancing the attractive forces. The linear motor must be distributed on both sides of the car to obtain a symmetrical hoisting. The analysis of a few types of motors indicates that the LSM with ferrite PMs can offer the smallest cost-related mass, as shown in Table 7.1 [44]. The relative power used in Table 7.1 is defined as:

©2000 CRC Press LLC

$$p = \frac{P_{inm} + \Delta P}{P_{hoist}} \tag{7.1}$$

where $P_{hoist} = m_l g \upsilon$ is the hoisting power, υ is the rated speed at rated load of the elevator, P_{inm} is the power supplied by the hoisting machinery and ΔP is power dissipated in hoisting system. The relative power loss is the ratio of losses to the hoisting power

$$\Delta p = \frac{\Delta P}{P_{hoist}} \tag{7.2}$$

The P_{hoist} is not a theoretical minimum for the power of the hoisting machine because the counterweight does a part of the hoisting work, and the rest must by supplied by the hoisting machinery.

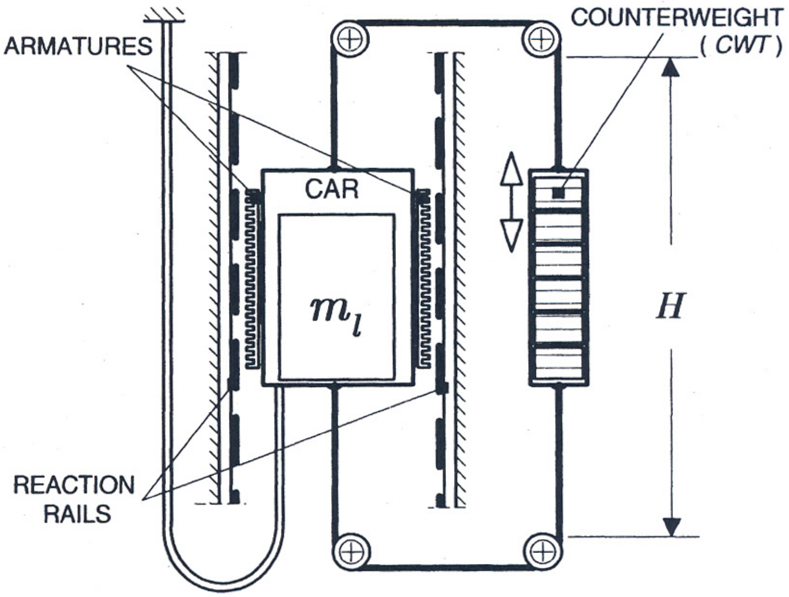

Figure 7.1 Armature of a linear motor installed in the elevator car.

The relative masses are moving masses or stationary masses related to the mass of the rated load of the elevator m_l .

The relative drive size is defined as the ratio of the maximum electrical current demand $I_{\max}$ to the current corresponding to the hoisting power I_{hoist} .

The relative cost represents the weighted prices of the active material used for the elevator excluding all the supportive structures and scaled to the mass of the whole hoisting system. The cost weighting coefficients have been assumed as follows: 1 for steel, 4 for aluminum, 6 for copper, 4 for ferrite PMs and 200 for NdFeB PMs.

Coefficients listed in Table 7.1 lead to the conclusion that the PM LSM can offer the smallest cost-related mass being thus the most promising alternative. On the other hand, it still remains uncertain whether the benefit of eliminating the rotary machine can be favorably compared to the increased cost of the linear motor.

7.1.2 Elevator with Linear Motor in the Pit

The alternative for a hydraulic elevator can be a linear motor with moving reaction rail as shown in Fig. 7.2.

The idea is to replace the piston of hydraulic machinery with the reaction rail and the cylinder with the armature of the linear motor.

Table 7.1 Comparison of different linear motors applied in 1000 kg car travelling at 2 m/s for mid-rise elevator.

Parameter	Motor		
	Reluctance	LSM, ferrite PMs	LSM, NdFeB PMs
Relative power, p	1.51	0.84	0.81
Relative power loss, Δp	0.57	0.15	0.14
Relative travelling mass	7.46	5.47	5.25
Relative moving mass of motor	1.29	0.36	0.26
Relative stationary mass of motor	0.66	0.90	0.30
Cost related mass	3.55	2.59	6.85
Relative drive size	9.68	1.63	1.52

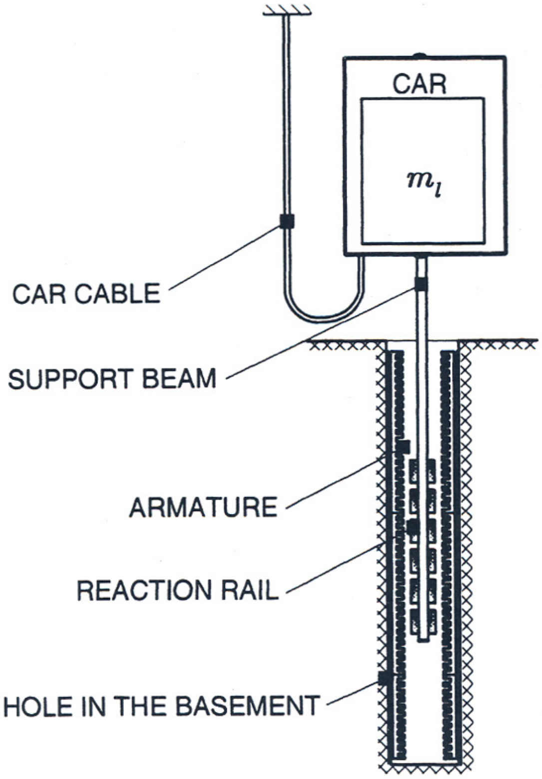

Figure 7.2 Linear motor driven elevator with moving reaction rail.

©2000 CRC Press LLC

Table 7.2 Comparison of different linear motors installed in the pit for low-rise ropeless elevator (1600 kg car, 4 m/s) [44].

Parameter	Motor		
	Reluctance	LSM, ferrite PMs	LSM, NdFeB PMs
Relative power, p	17.75	7.96	7.01
Relative power loss, Δp	8.05	1.90	1.60
Relative travelling mass	3.58	3.70	3.40
Relative moving mass of motor	0.33	0.45	0.15
Relative stationary mass of motor	4.98	1.66	1.11
Cost related mass	11.54	4.64	5.64
Relative drive size	111.6	10.37	12.40

The power can be supplied to the stationary winding. However, either a pit in the basement or the 1:2 roping ratio is required to obtain the required doubled force. Furthermore, the car travel distance is limited to maximum 20 m. Comparison of different linear motors installed in the pit for low-rise elevators is given in Table 7.2.

The structure has the same features as the hydraulic set-up but with a few additional advantages, i.e.,

- no oil and oil tank,
- all machinery is located in the shaft, so that a separate room is not needed,
- the regenerative braking can be applied for the car going down-ward, so that the lack of counterweight can be partially compensated.

The performance of this elevator with PM LSM compares well with the conventional hydraulic system, but the amount of magnetic material required makes this structure commercially unattainable.

7.1.3 Linear Motor in Counterweight

The *counterweight* is the most natural place for the linear motor in a traction type elevator. In this way, the mass of the motor can be utilized as a part of the balance. However, the energy must be supplied to the motor through a cable, the length of which on the balance side varies with the counterweight position. Proper measures should then be taken to compensate for this variation of the balance weight. This counterbalance motor placement has been well known for some time and even commercially explored [33, 35, 130]. Although, similar to the motor installation in the car, when the motor is installed in the counterbalance, the difference in the mass of the supply cable must be taken into account (Fig.7.3a).

Table 7.3 Comparison of different linear motors mounted in the counterweight of a low-rise elevator (630 kg car, 1 m/s) [44].

Parameter	Motor		
	Reluctance	LSM, ferrite PMs	LSM, NdFeB PMs
Relative power, p	2.48	1.07	1.03
Relative power loss, Δp	1.13	0.26	0.24
Relative travelling mass	5.48	5.48	5.48
Relative moving mass of motor	1.13	0.36	0.27
Relative stationary mass of motor	0.33	0.45	0.15
Cost related mass	2.87	3.73	1.71
Relative drive size	25.59	2.75	2.5

The mass of the counterweight for optimum balancing should be:

$$m_c = m + \frac{1}{2} m_l + \frac{H}{4}\left(m_{ec} - m_e\right) \tag{7.3}$$

and the mass of balancing ropes (per unit length)

$$m_{brp} = m_{rope} - \frac{m_e}{4} \tag{7.4}$$

where m_c is the mass of the counterweight, m is the mass of the car, m_l is the mass of the rated load, m_{ec} is the mass per unit length (kg/m) of the travelling electric cable on the counterweight side, m_e is the mass per unit (kg/m) of the travelling electric cable on the car side, m_{rope} is the mass of rope per unit length (kg/m) and H is the total hoisting height. The possible linear motor placement in the counterweight is shown in Fig. 7.3b. The system can be designed with the armature in the counterweight and reaction rail on the wall, as well as with reaction rail in the moving counterweight and armature on the wall.

Table 7.3 shows a comparison of different linear motors mounted in the counterweight of a low rise elevator. PM LSMs require less power than conventional hoisting motors. Further analysis shows that the performance of a reluctance motor improves at higher speeds.

Table 7.4 Rotary motors versus linear motors for mid-rise elevators (1000 kg car, 2 m/s).

Parameter	Direct hoisting (rotary motor)	Geared hoisting (rotary motor)	Linear reluctance motor in the car	Linear motor in the counterweight
Relative supply power, p	1.03	1.12	1.98	1.98
Relative power loss, Δp	0.31	0.28	0.92	0.86
Relative travelling mass	4.82	4.81	6.59	5.53
Relative moving mass of motor	0.18	0.02	0.49	0.44
Relative stationary mass of motor	0.23	0.05	1.32	1.32
Cost related mass	0.91	0.14	3.40	3.31
Relative drive size	2.21	1.97	7.44	6.84

©2000 CRC Press LLC

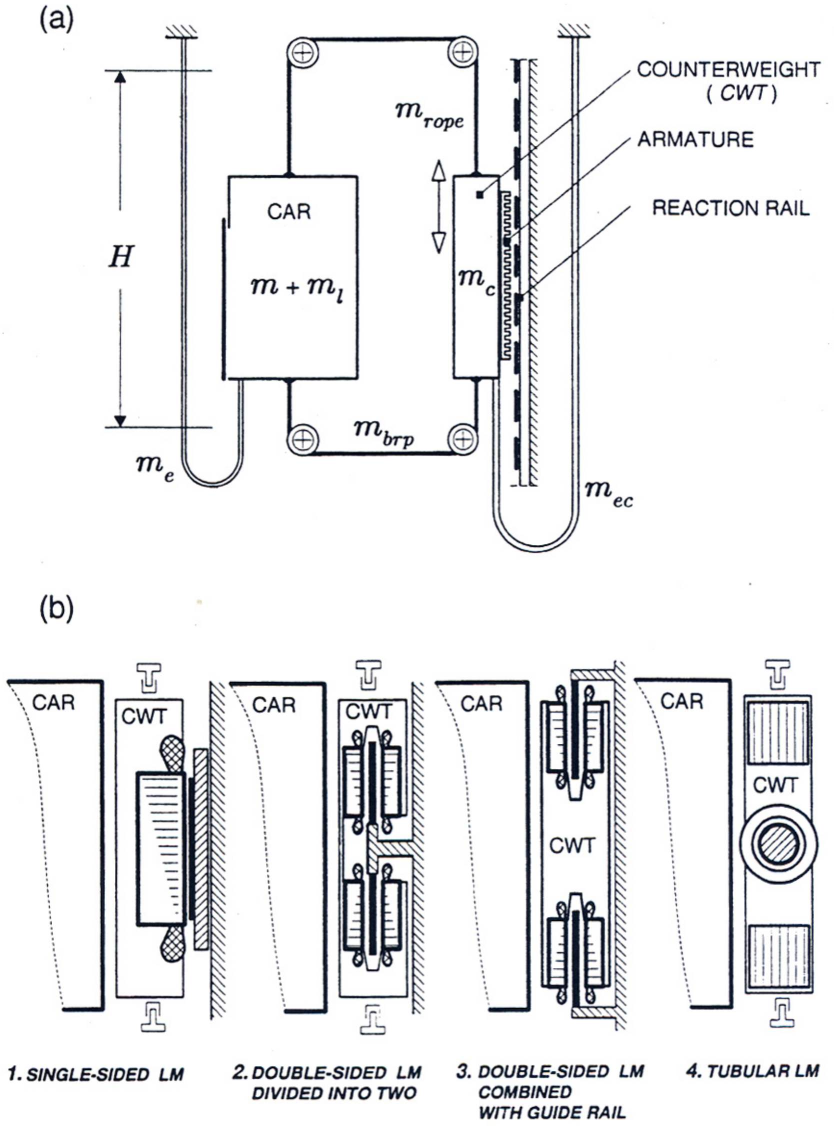

Figure 7.3 Elevator system with the linear motor in the counterweight: (a) construction, (b) possible location of the linear motor.

7.1.4 Conventional versus Linear Motor Driven Elevator

Table 7.4 illustrates the major parameters of a mid-rise elevator system with different motor types [44]. Both the conventional traction motor and linear motor placed either in the car or in the counterweight offer approximately the same sizing of hoisting machinery and the drive.

©2000 CRC Press LLC

7.2 Ropeless Elevators

7.2.1 Vertical transport in Ultra-High Buildings

Land in the world's biggest cities, e.g., New York or Tokyo, is extremely expensive, which drives the expansion of rentable spaces into higher and higher buildings and underground areas. However, the larger and taller the buildings, the more elevators are required to keep acceptable waiting time for dispatching. The increasing interest in *ultra-high buildings* also called (*hyperbuildings* or *vertical cities*) that could possibly exceed 600 m in their height inspires elevator companies to intensify their research effort in alternative technologies for vertical transportation. This becomes apparent in Japan where building contractors, elevator companies, and other institutions are spending a lot of effort to develop transportation concepts for these hyperbuildings. Vertical transportation systems in ultra-high buildings must address many technical issues, amongst others:

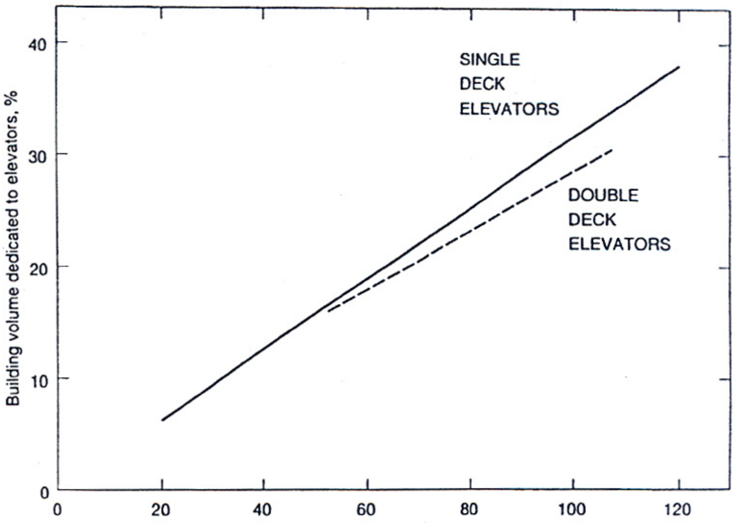

Figure 7.4 Elevator system space occupancy ratio in a tall building.

- transport configuration with traffic flow within and between buildings ;
- diverse building capacity incorporating residential, commercial and service functions;
- use of alternative building transportation systems (roped elevators, ropeless elevators, escalators, people movers) ;
- the highest levels of reliability, safety and passenger rescue;
- comfort of travel (air pressure changes, vibration, vertical and horizontal motions, travel time);
- elevator propulsion, guidance, brakes, power consumption, control, and communication.

Ultra-high buildings pose new problems in construction of high speed elevator systems, i.e., vertical oscillations, horizontal swing, car noise and cable length limitations. Because the ropes (steel cables supporting the car) are very long and usually have a low dumping coefficient, even small disturbances, e.g., traction machine torque ripple can cause car oscillations. This vibration can further be amplified when the disturbance

©2000 CRC Press LLC

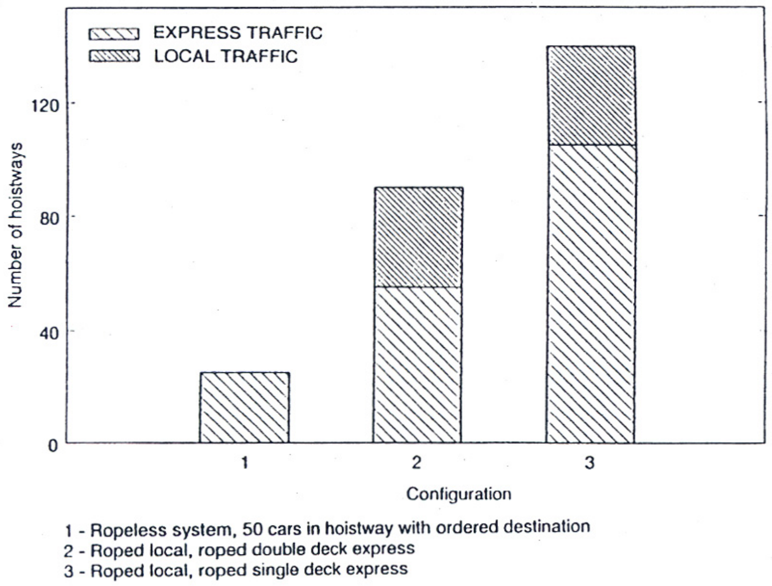

Figure 7.5 Required number of hoistways in roped and ropeless elevator system capable to dispatch 2000 passengers per minute. Study for 250 floor building 1000 m tall with 100,000 population.

frequency coincides with the car's natural frequency. In some instances this bounce may destabilize the system that controls the elevator speed. The horizontal swing of the elevator car can be caused by curvatures of the guiding rails or by imperfect rail segment junctions. Car noise is due to the guide-shoes tracking the rails and by the wind noise (air passing through the travelling car).

The car rise limit is imposed by the cable weight and strength and can be considered as a function of five variables: (a) safety factor, (b) rope strength, (c) rope mass per unit length, (d) number of ropes and (e) mass of the car. Under the most favorable conditions, a cable-based elevator can achieve a rise of approximately 1200 m, based on 10 commonly used steel cables with 320 kN strength, mass per unit length of 2.14 kg/m and safety factor of 10 [28].

Ropeless elevators with multiple cars in one shaft may be perceived as practical solution for ultra-tall buildings above 1000 m. The primary concern is that the roping technology may not be extensible to hoistways of that height, both from a rope strength standpoint as well as from safety margin considerations. Another problem is that roped elevator systems, understood to be based on the sky lobbies, would consume too much space to make such a building financially viable. An analysis conducted by *Mitsubishi Corporation* [28] found that almost 30% of the total space in a 100-floor skyscraper must be devoted to elevators, including their hoistways, halls, and machine rooms, Fig. 7.4. Recently, the peak rents for Tokyo skyscrapers were estimated about \$1000/m^2/year. Clearly, the elevator space occupancy ratio has a significant financial impact on the building utilization.

The one shaft, multi-car, ropeless elevator system is considered to be the most promising answer to these problems. It eliminates the suspension cables and with them the rope-strength and vertical-oscillation problems. Usage of multiple cars in a single hoistway improves the space occupancy factor even when compared with roped double-deck elevators. For example, the required number of hoistways can be reduced by 65 to 80% when using a ropeless elevator with multiple cars versus traditional roped system, Fig. 7.5.

The mining industry is also interested in alternative vertical transportation systems with ropeless elevators [22]. South African ultra-deep gold mines (exceeding 3500 m) are considering the implementation of PM LSM driven hoisting systems because the maximum depth achievable by a roped hoist system is approximately 2800 m. After this depth, the hoisting rope can no1onger support its own weight and the payload. To overcome this problem, at present time, sub-vertical shafts are sunk, i.e., additional roped hoist system are installed underground at a depth of about 2000 m [22].

7.3 Assessment of Hoist Performance

The *hoist efficiency* without the rope is independent of the height (in a mine - independent of the depth) and therefore the operation of the lifting machinery is not limited by the rope mass.

The successful implementation of the linear motor hoist depends on two main factors: (a) the ratio of the *motor weight-to-thrust* that it can produce and (b) the motor size (cost).

One of the main criterion for assessing the performance of the hoist is the efficiency of the overall system [23]:

$$\eta = \frac{P_{outm}}{P_{inm}} = \frac{m_l g \upsilon}{\left(m_l + m + m_{rope}\right) g \upsilon} \tag{7.5}$$

where P_{outm} is the mechanical power required to lift the payload, P_{inm} is the total mechanical power required to operate the system, m_l is the mass of the payload, m is the mass of the car, m_{rope} is the mass of ropes, g is the acceleration of gravity and υ is the linear speed.

Assuming a constant speed of operation and neglecting the friction, the efficiency of the hoist system without a counterweight can be expressed as follows [23]:

- for a conventional roped hoist

$$\eta = \frac{m_l}{m_l + m + m_{rope}} \tag{7.6}$$

- for a ropeless hoist

$$\eta = \frac{m_l}{m_l + m} \tag{7.7}$$

Assuming that the mass of the car and payload are the same in both cases, the system efficiency becomes entirely dependent on the mass of ropes.

The taller (deeper) the hoist shaft, the longer and therefore the heavier the rope since m_{rope} = $0.25\pi\rho n_{rope} d_{rope}^2 l_{rope}$ where ρ is the specific mass density of steel and n_{rope}, d_{rope} and l_{rope} are the number of ropes, diameter and length of the rope, respectively. Heavier ropes have larger diameter to withstand the increased tensile stresses. As a result, the increased cross-sectional area of ropes contributes further to their mass, affecting the overall system efficiency (Fig. 7.6a) [22].

The efficiency of roped hoist without counterweight tends to zero as the height (or depth) approaches the operating limit, (about 2800 m for steel ropes).

Technologies crucial to the successful development of ropeless elevators can be divided into four major categories:

- system configuration and energy management,
- propulsion and guidance,
- safety and brakes,
- control and communication.

7.3.1 Construction of Ropeless Elevators

The unique features of the ropeless elevator include:

- unlimited rise,
- vertical and horizontal motion,
- multiple cars in the same hoistway,
- no travelling cable,
- high traffic handling capacity with minimum core space.

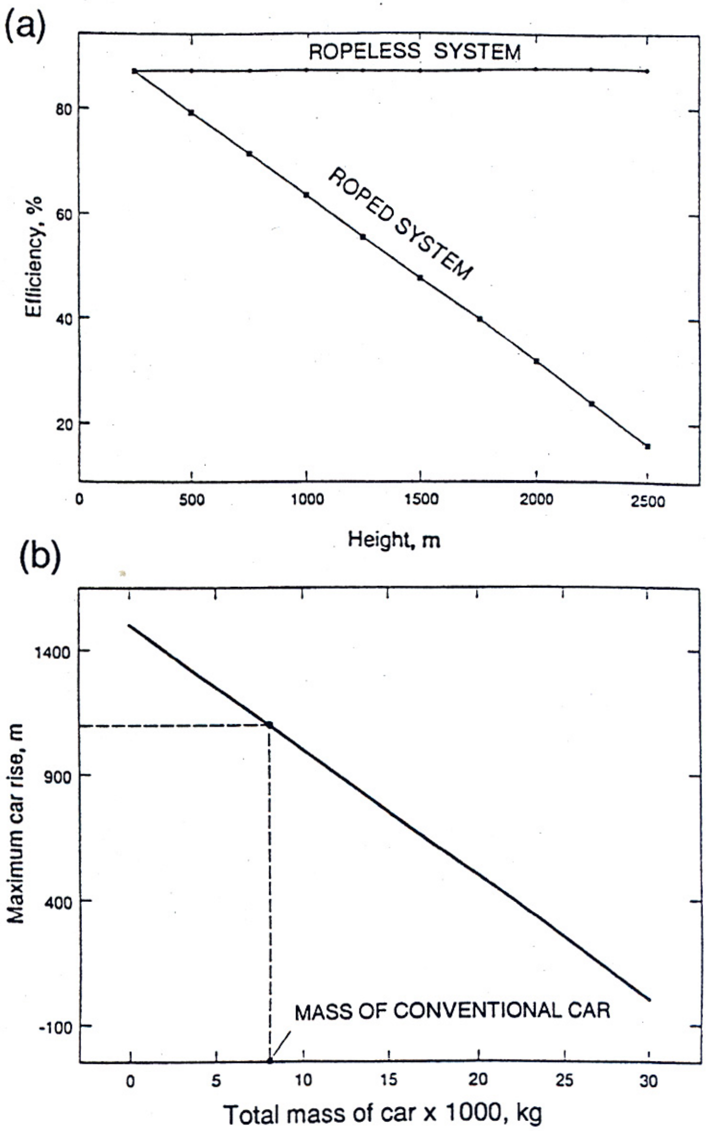

Figure.7.6 Limits of rope lift system imposed by cable mass, (a) comparison of hoisting system efficiencies, (b) rope ability to support its own weight.

©2000 CRC Press LLC

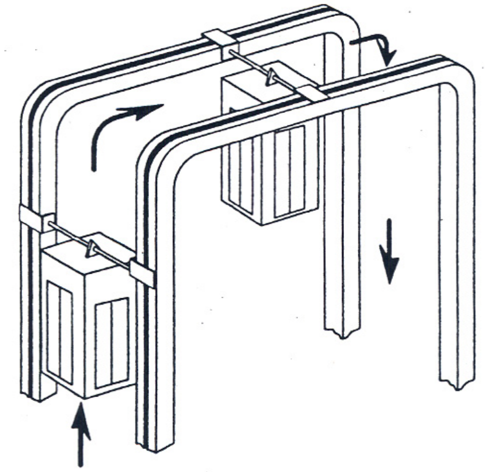

Figure 7.7 One shaft, multi-car, ropeless elevator with two long armature LSMs.

The ropeless elevator with multiple cars in one shaft can be built by hanging each cab from a bar fixed to the movers of a pair of LSMs (Fig. 7.7). Long armature windings are stationary and PMs are integrated with movers. Each car hangs from a shaft fixed to the PM movers. The mover is a steel rail with PMs which is installed between two parallel stationary armature systems. Armature units are segmented into blocks (Fig. 7.8). The guidance system maintains a small and constant airgap between the armature cores and PMs. When the armature windings are excited, the interaction between the excitation flux and the flux of PMs produces linear thrust moving the car up or down. The long stationary armature is divided into sections the minimum number of which is equal to the number of cars. Only one car can be permitted in each section at a time so that each car may be controlled independently of the others. The more sections there are, the more precisely the system can be controlled; however, the construction cost is higher since each section requires its own high power converters.

7.3.2 Operation

The LSM powered ropeless elevator consumes significantly more energy than an equivalent roped elevator to move a given number of passengers at a given distance. The reason for this is that a typical counterweighted elevator with ropes needs to drive only the offset load (typically only 12 to 14% of the total moving mass), while the ropeless elevator must lift the entire combined mass of the car, the frame, passengers and the

©2000 CRC Press LLC

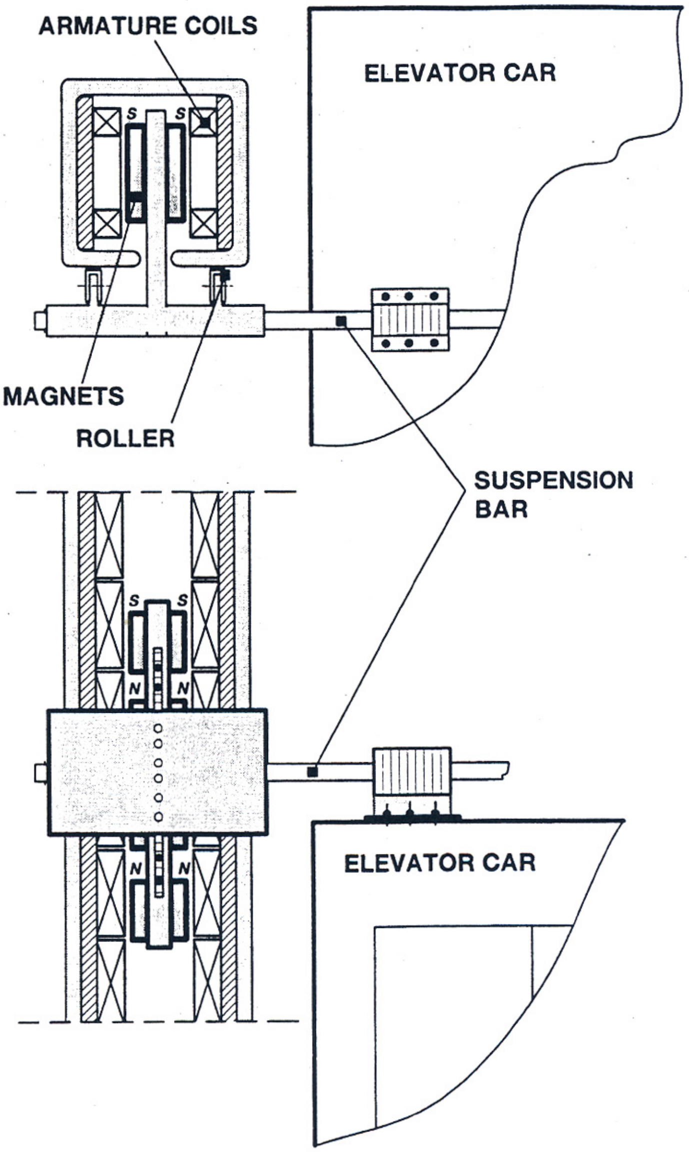

Figure 7.8 Ropeless elevator with double-sided PM LSM.

©2000 CRC Press LLC

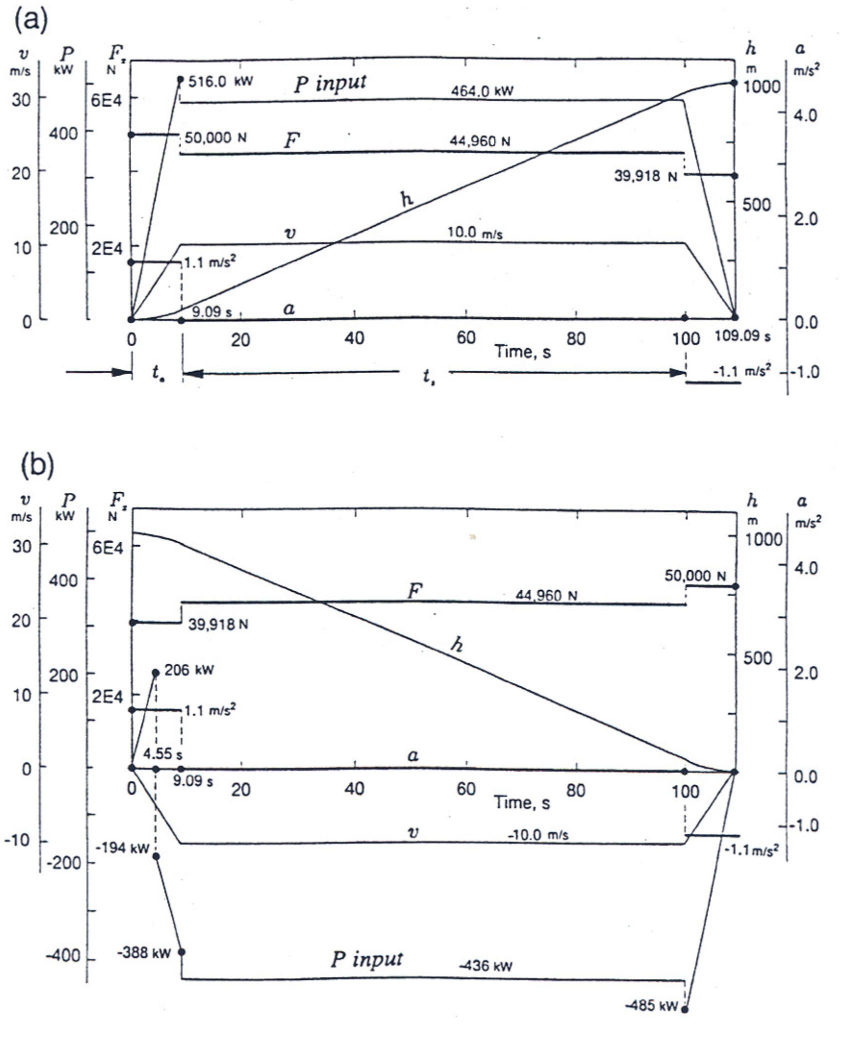

Figure 7.9 Computed motion profile for a ropeless elevator: (a) for car going up, (b) for car going down.

©2000 CRC Press LLC

PM movers. Assuming motors and converters of similar efficiency, the ropeless elevator requires power supply 7 to 8 times that of its roped counterpart.

An ascending ropeless elevator requires almost constant power for a given load as it rises in the hoistway. When moving at constant speed, the power is consumed to overcome the force of gravity. Peak acceleration or deceleration, when limited to 0.1g increases or decreases the power required by only about 10%. During the descent, some energy is recovered as the LSM is able to regenerate it from the passage of PM excitation system through the armature windings. However, the recovered energy is always smaller than the propulsion energy because the regeneration occurs only when the car travels with full speed during its descent. Fig: 7.9b shows that the car absorbs the power taken from the electric supply system as it starts travelling downward. A freely falling car would develop the acceleration equal to 1.0g that is too high for the passengers riding inside. To limit the acceleration to 0.1g the LSMs must develop the thrust directed upward slightly smaller than the gravitational force, When the car decelerates before stopping; the LSM also develops the braking force (thrust in opposite direction). Therefore, during the acceleration and deceleration, the LSM is taking energy from the power supply for electrical braking, which is commonly known as the plugging mode. No regeneration occurs during the inter-floor travel due to the limited speed attained between adjacent floors.

Case Study

Consider a ropeless elevator introduced in *Example 1.6* (Chapter 1). The mass of fully loaded car is m = 4583 kg (with 16 passengers), acceleration/deceleration a = 1.1 m/s^2, speed υ = 10.0 m/s and LSM efficiency η = 0.97. It is assumed that the hoistway efficiency is 100%. Analyze the motion, thrust, power and energy profiles in the time t domain for a car ascending and descending the hoistway 1000 m high.

Solution

Car going upward - Acceleration

The time to reach the full speed υ = 10.0 m/s, i.e., acceleration time

$$t_a = t_1 = \frac{\upsilon}{a} = \frac{10.0}{1.1} \approx 9.09 \text{ s}$$

The travel distance (height) as a function of time

$$h(t) = \frac{1}{2}at^2$$

The travel distance at the end of the acceleration phase

$$h_a = h_1 = \frac{1}{2}at_1^2 = \frac{1}{2}\times 1.1 \times 9.09^2 = 45.45 \quad m$$

The thrust required to accelerate the mass m = 4583 kg upward with acceleration a

$$F_{xa} = m(g+a) = 4583\times(9.81+1.1) \approx 50,000 \quad N$$

The input power as a function of time

$$P_{in}(t) = \frac{1}{\eta}F_{xa}at$$

The peak input power at the end of the acceleration phase ($t = t_1$)

$$P_{ina} = \frac{1}{\eta}F_{xa}at_1 = \frac{1}{0.97}\times 50,000\times 1.1\times 9.09 \approx 516.0 \text{ kW}$$

©2000 CRC Press LLC

Energy delivered to the LSM during the up acceleration phase

$$E_a = \frac{1}{\eta} F_{xa} h_1 = \frac{1}{0.97} \times 50,000 \times 45.45 \approx 2,343 \ \text{kJ}$$

Car going upward - Steady State

The elevator car is cruising up with constant speed υ = 10.0 m/s and acceleration is equal to zero, (a = 0.0). The duration time of the steady state phase is calculated on the assumption that the car accelerates and decelerates with the same rate $|a|$ = 1.1 m/s^2. Then, the deceleration time t_d as well as the corresponding distance h_d is the same as the acceleration time t_a = t_1 and acceleration distance h_a, i.e.,

$$t_d = t_3 - t_1 - t_s \approx 9.09 \ s$$

where t_3 is the total time of travelling from start to stop.

Then, the travel distance during the steady state is

$$h_s = h - 2h_a = 1000 - 2 \times 45.45 = 909.1 \ m$$

The duration of the steady state

$$t_s = \frac{h_s}{\upsilon} = \frac{909.08}{10.0} \approx 90.91 \ s$$

The steady state thrust

$$F_{xs} = mg = 4583 \times 9.81 = 44,960 \ N$$

The LSM steady state input power is independent of time, i.e.

$$P_{ins} = \frac{1}{\eta} F_{ds} \upsilon = \frac{1}{0.97} \times 44,960 \times 10.0 \approx 464.0 \ kW$$

Energy delivered to the LSM

$$E_s = P_{ins} t_s = 464,000 \times 90.91 \approx 42,182 \ kJ$$

Car going upward – Deceleration

The time instant when the car starts to decelerate $t_2 = t_1 + t_s = 9.09 + 90.91 = 100.0 \ s$.

The speed as a function of time is

$$\upsilon(t) = \upsilon - a(t - t_2)$$

The travel distance is

$$h(t) = h_a + \upsilon(t - t_2) - a(t - t_2)^2$$

The thrust directed upward which is required to maintain the deceleration of 1.1 m/s^2

$$F_{xd} = m(g - a) 4583 \times (9.81 - 1.1) = 39,918 \ N$$

The LSM input power at deceleration as a function of time

©2000 CRC Press LLC

$$P_{ind}\left(t\right)=\frac{1}{\eta}F_{xd}\left[\upsilon-a\left(t_2-t\right)\right]$$

The peak input power at $t=t_2+t_d$

$$P_{ind}=\frac{1}{\eta}F_{xd}\left(\upsilon+at_d\right)=\frac{1}{0.97}\times39{,}918\left(10.0+1.1\times9.09\right)=822.99 \text{ kW}$$

Energy delivered to the LSM during the up deceleration phase

$$E_d=\frac{1}{\eta}F_{xd}h_d=\frac{1}{0.97}\times39{,}918\times45.45\approx1{,}870 \text{ kJ}$$

The total energy consumed by the LSM during the travel up

$$E_{up}=E_a+E_s+E_d=2{,}343.0+42{,}182.0.0+1{,}870\approx46{,}395.0 \text{ kJ}$$

Car going downward

To keep the acceleration and speed at acceptable levels the LSM operates as a brake (plugging) during the entire period of downward travel. The LSM produces the force directed upwards limiting the acceleration to 0.1 g . In this mode, the car runs in the opposite direction to the travelling electromagnetic field produced by the armature winding. The power is delivered from the inverter to the LSM armature. Let us assume that the control changes the braking mode from plugging to regenerative braking at half of the final speed υ_{ch} = -0.5υ = -5.0 m/s. After switching on, the LSM starts to supply power to the electrical system. The regenerative braking is effective only at reasonable speeds of the car because the EMF excited in the armature winding the PM excitation system must be high enough to obtain the current flow from the inverter to the power system.

Car going downward – Acceleration

The time to reach the full speed υ = 10.0 m/s is the same as the acceleration time t_a for car going up, i.e., t_a = 9.09 s.

The car position in the hoistway as a function of time

$$h\left(t\right)=H-\frac{1}{2}at^2$$

where H is the hoistway height.

The position of the car at the end of the acceleration phase

$$h\left(t_1\right)=H-\frac{1}{2}at_a^2=1000-\frac{1}{2}\times1.1\times9.09^2\approx954.55 \;\; m$$

The distance travelled by the car during the acceleration downward

$$h_a=\frac{1}{2}at_a^2=\frac{1}{2}\times1.1\times9.09^2\approx45.45 \;\; m$$

The thrust required to limit the acceleration of the mass m downward to the rate of a = 1.1 m/s^2

$$F_{xa}=m\left(g-a\right)=4583\times\left(9.81-1.1\right)\approx39{,}918 \;\; N$$

The motor input power as a function of time

$$P_{in}(t) = \frac{1}{\eta} F_{xa} a t$$

The time of changing the braking mode from plugging to regeneration t_{ch} = υ_{ch} / a = 5.0/1.1 = 4.55 s. The power generated by the LSM as a function of time

$$P_g(t) = -\eta F_{xa} a t$$

The peak input power at the end of plugging

$$P_{ina}(t_{ch}) = \frac{1}{\eta} F_{xa} a t_{ch} = \frac{1}{0.97} \times 39,918 \times 1.1 \times 4.55 \approx 206.0 \text{ kW}$$

The generated power after changing the braking mode

$$P_{ga}(t_{ch}) = -\eta F_{xa} a t_{ch} = -0.97 \times 39,918 \times 1.1 \times 4.55 \approx -194.0 \text{ kW}$$

The travel distance of the car corresponding to the time at which the braking switch is on $\Delta h_{ch} = 1/2 a t_{ch}{}^2 = 1/2 \times 1.1 \times 4.55^2 = 11.39$ m Energy needed for the downward acceleration phase

$$E_a = \frac{1}{\eta} F_{xa} \Delta h_{ch} - \eta F_{xa} \frac{1}{2} a (t_1^2 - t_{ch}^2)$$

$$= \frac{1}{0.97} \times 39,918 \times 11.39 - 0.97 \times 39,918 \times \frac{1}{2} \times 1.1 \times (9.09^2 - 4.55^2) \approx -850.0 \text{ kJ}$$

Car going downward - Steady State

The elevator car is cruising down with constant speed υ = 10.0 m/s and the acceleration is equal to zero (a = 0.0). The duration time of the steady state phase is the same as in the case of travelling upward, i.e., t_s = 90.91 s. Similarly, the travelled distances are the same in the two cases, i.e., h_s = 909.1 m.

The car position at the steady state as a function of time

$$h(t) = h_a - \upsilon_s (t - t_a)$$

The braking force at the steady state

$$F_{xs} = mg = 4583 \times 9.81 = 44,960 \text{ N}$$

The power generated by the LSM at steady speed is independent of time

$$P_{gs} = -\eta F_{xs} \upsilon = -0.97 \times 44,960 \times 10.0 \approx -436.0 \text{ kW}$$

The generated energy

$$E_s = -P_{gs} t_s = -436.0 \times 90.91 \approx -39,637 \text{ kJ}$$

Car going downward - Deceleration

The speed as a function of time

$$\upsilon(t) = -\upsilon + a(t - t_2)$$

The position of the car as a function of time

©2000 CRC Press LLC

$$h(t) = H - (h_a + h_s) + \frac{1}{2}a(t - t_2)^2$$

The upward thrust which is required to maintain the deceleration of -1.1 m/s^2

$$F_{xd} = m(g + a) = 4583 \times (9.81 + 1.1) = 50,000 \text{ N}$$

The generated power as a function of time

$$P(t) = -\eta F_{xd}\left[-\upsilon_s + a(t - t_2)\right]$$

The time of changing the braking mode is $t_{chd} = t_2 + \upsilon_{chd} / a = 100 + 5.0/1.1 = 104.55s$ where $\upsilon_{chd} = \upsilon_{ch} = -5m/s$

The generated power at the beginning of the deceleration

$$P_{gd}(t_2) = -\eta F_{xd}\upsilon = -0.97 \times 50,000 \times 10.0 \approx -485.0kW$$

The generated power at t_{chd}

$$P_{gd}(t_{chd}) = \eta F_{xd}\left[-\upsilon + a(t_{chd} - t_2)\right] = 0.97 \times 50,000 \times \left[-10.0 + 1.1 \times (104.55 - 100)\right] \approx -242.0 \text{ kW}$$

The input power of the LSM as a function of time after switching to plugging mode

$$P_{in}(t) = -\frac{1}{\eta}F_{xd}\left[\left|-\upsilon_{chd}\right| - a(t - t_{chd})\right]$$

The input power after switching to plugging mode at $t = t_{chd}$

$$P_{ind}(t_{chd}) = \frac{1}{\eta}F_{xd}\upsilon_{ch}\frac{1}{0.97} \times 50,000 \times 5.0 \approx 258.0 \text{ kW}$$

The travel distance Δh_{chd} of the car from the beginning of braking to the activation of the braking switch is equal to $\Delta h_{chd} = h_a - \Delta h_{ch} = 45.45 - 11.39 \approx 34.06m$

The energy recovered during the deceleration

$$E_d = -\eta F_{xd}\Delta h_{chd} + \frac{1}{\eta}F_{xa}(H - h_a - h_S - \Delta h_{chd})$$

$$= -0.97 \times 50,000 \times 34.06 + \frac{1}{0.97} \times 50,000 \times (1000 - 45.46 - 909.08 - 34.06) \approx -1.064.0 \text{ KJ}$$

The total energy recovered when travelling downward

$$E_{dn} = E_a + E_s + E_d = -850.0 - 39,637.0 - 1,064.0 \approx -41,551.0 \text{ KJ}$$

One fully loaded car descending down generates 41,544 kJ energy, which is returned to the power system. The energy balance for one fully loaded car for a round trip is

$$\Delta E = E_{up} + E_{dn} = 46,395.0 - 41,551.0 \approx 4,844.0 \text{ KJ}$$

It means that the fully loaded car (with 16 passengers) during one round trip consumes only 4,778.0 kJ energy.

The hoistway *cycling energy efficiency*, defined as the ratio of *energy recovered* during the descent of fully loaded car to the *energy consumed* by this car during the ascend, is

©2000 CRC Press LLC

$$\eta_{cy} = \left| \frac{E_{dn}}{E_{up}} \right| = \frac{41,551.0}{46,395.0} = 0.8956$$

For comparison, Fig. 7.10 shows the speed, power and energy versus time curves measured for the roped elevator with propulsion system based on the tandem of LIMs. This experimental system was built and tested by *Otis Elevator Company* in the early 1990s. The elevator was driven by two flat linear induction motors installed in the counterweight running over long stationary reaction rails consisting of copper backed by a steel plate. The elevator was capable of carrying 16 passengers between 7 floors with 2.5 m/s rated speed. The peak 20,000 N thrust has been developed by the tandem of flat LIMs during the acceleration phase. The energy curve (Fig. 7.10) b shows that even for a fully loaded car going downward, the total energy on the end of the cycle is positive. This means that the energy supplied by the power system exceeds that generated during the regenerative braking. This is due to the relatively low efficiency of LIMs. In the considered example the peak LIM efficiency is 43 %.

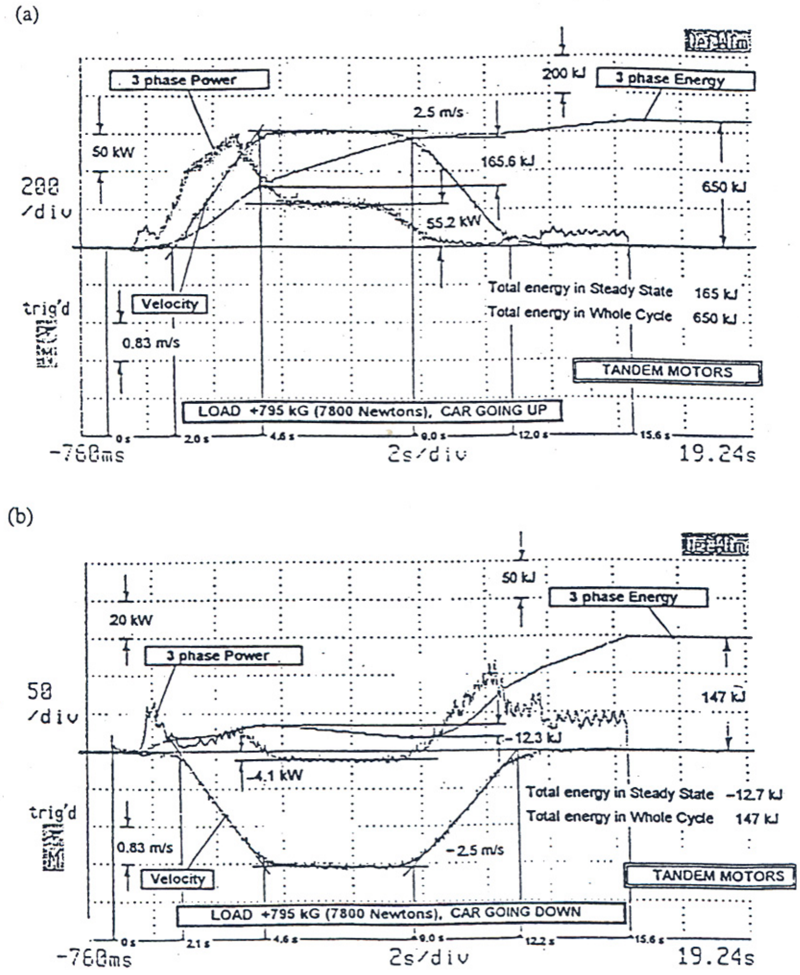

Figure 7.10 Velocity, power and energy for flat linear motor elevator system, (a) ascending car, (b) descending car. Courtesy of *Otis Elevator Company*, Farmington, CT, U.S.A.

©2000 CRC Press LLC

Case Study

Consider a 250 story, 1,000 m high hyperbuilding, with population of 100,000 people. The elevator system consists of 17 ropeless hoistways with fifty 16-passenger cars each,. plus two additional ropeless hoistways, containing 20 cars each and serving 13 floor zones for interfloor traffic. Analyze the energy usage by the system for 24 hours a day.

Traffic scenario:

- up peak (morning)and down peak (evening) periods: 10,000 passengers/5 min, duration 1.0 h at peak load and 1.0 h at 50% load both in the morning and evening;
- peak period inter-floor counterflow: 1% of up peak during peak periods, e.g., in the morning nearly all passengers travel up; however, about 1% go down - in counterflow direction;
- mid-day peak period: 50% nominal off peak period, duration 2.0 h at lunch time.

Traffic configuration:

- 50 cars/hoistway, each car with destination to 5 floor group - stops at each floor of the group;
- nominal round trip time = 400 s;
- car size: 4583 kg, 16 passengers, (3483 kg empty car + 11 00 kg duty load);
- motor efficiency η = 97% (propulsion and regeneration);
- time for car to reach top floor = 110 s;
- time to service next 4 floors = 18 s per floor (4 s floor-to-floor run,4 s door time, 10 second enter-exit).

Assumptions:

(a) There are no friction losses (due to the non-contact guidance system), and no windage losses are taken into account. The power requirement for guidance, control, lighting and ventilation is neglected. Similarly the power to move in transverse direction in the loading areas is not considered.

(b) All cars in 17 fast traffic hoistways are assumed to be full when leaving the lobby and empty upon return. The up peak energy analysis is based on fully loaded car operating at full propulsion power (calculated in the previous *Case Study* - car running to the highest floor) for the entire run time to the first stop at the lowest floor serviced by each car. The regenerated energy for the down run has been calculated on the basis of previous *Case Study* with the mass of empty car (3483. kg) used in all equations.

(c) Energy usage by the two interfloor hoistways is calculated on the basis of the following: the average load of a car is 50%; cars never reach regenerative speeds; the extra acceleration power is offset by the reduced deceleration power; cars are making an average of four 3-floor runs up plus another four 3-floor runs down in each round trip with three 7.0 s inter-floor stops. The two inter-floor hoistways together can carry 733 passengers up and another 733 passengers down in each 5 min period, at 50% capacity. If required, the nominal 50% capacity can be upgraded to the full capacity with higher number of passengers.

Solution

The ropeless elevators are estimated to consume approximately 255,000 kWh (255 MWh) of energy during a 24 h day. This number has been obtained from computer simulation using dedicated software. The highest power is necessary for the 1 h up-peak period. During that time, the elevator system, i.e., all elevators require approximately 49,500 kW power for the peak load.

It is interesting that this peak power consumption considered together with typical linear motor efficiency yields a thermal dissipation of approximately 11,500 kW (power losses in all LSMs) during that one peak hour. It should be mentioned that the thermal dissipation is consider ably less at all other times of the day. Most of the heat is generated in the armature windings of LSMs, since PM excitation systems do not generate power losses. The estimated heat dissipation leads to the conclusion that an effective cooling system must be applied directly to the armature windings. Preferably, the cooling system should use a chilled liquid rather than the air flowing directly through cooling ducts in the armature. It is interesting to note that one person can generate during 1 h approximately 0.117 kWh of thermal energy in an office environment. The 100,000 occupants in the hyperbuilding collectively generate about 11,700 k Wh, or roughly the same amount as that of ropeless elevators during the 1 h peak period. Thus, the energy usage by the airconditioning system is comparable with elevator energy converted into heat losses.

7.3.3 First Prototypes

Completing a study on very large drives in the early 1990s, the Underground Development Utilization Research Center of the Engineering Advancement Association of Japan (ENNA) is seriously considering the application of linear motors to ropeless elevators. This demonstrative research was conducted by a group of five companies: *Fuji Electric*, *Ishikawajima-Harima Heavy Industries*, *Kawasaki Heavy Industries*, *Simizu Corporation* and *Fujitec*. ENNA has already built a working model of a horizontal and vertical ropeless transport system [76]. This scaled installation serves as a model for future hyperbuilding transportation systems. Specifications are the following:

- Maximum thrust 3,000 N
- Vertical travel distance 8 m .
- Horizontal travel distance 1 m
- Velocity from 0 to 1 m/s
- Acceleration 1 m/s^2
- Moving mass 270 kg (including payload)
- Car dimensions: 1.0 W × 0.9 D × l.8 H m
- Power and control: IGBT inverter
- Position encoder: optical pulse generator

The overall view of the test system is shown in Fig. 7.11. The car is suspended as a pendulum from the travelling carriage. To prevent the car from swaying at the time of acceleration or when passing through a curved rail, a friction plate has been set between the carriage structure and the car. The car is guided by two rails: (a) a rigid H-shaped beam, which supports and guides the car (travel rail) and (b) a motor guidance maintaining a constant linear motor airgap. The system is capable of moving the car both along the straight and curved path. Such a transition takes approximately 10 s.

To meet the most important propulsion system requirements, i.e. lightweight and large motive force, a LSM with PM mover installed on the car and the armature on the track has been adopted. The mover is placed between two sets of stationary armature systems. High energy

©2000 CRC Press LLC

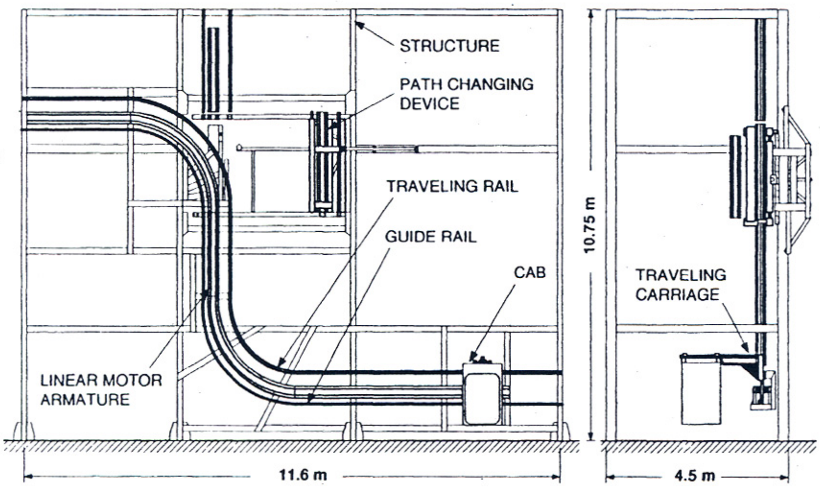

Figure 7.11 Linear motor driven vertical-horizontal transportation system, built by Japanese ENNA consortium.

NdFeB 32 PMs (energy product 255 kJ/m^3) have been used. PMs are fixed to both sides of 10 mm thick steel rails and skewed by one slot pitch of armature core to reduce the thrust ripple (Fig. 7.12a). To minimize the attractive forces between PMs and armature cores, double sided armature configuration has been chosen (Fig. 7.12). This motor topology is referred to as a U-type LSM with short PM reaction rail and two long armature systems.

The armature of LSM is divided into ten straight and curved sections, each about 2 m long. The segments are powered from sinusoidal IGBT inverters with low noise emission levels arranged in a tandem. The power from inverters is distributed by means of switches connecting individual armature sections in a sequence (Fig. 7.13). When mover travels between the segments, both inverters operate; otherwise, only one is used .The presented system is able to fully control the movement of a single carriage. For higher number of cars, a more complicated power distribution scheme is needed. The speed and position is detected by a slotted plate on the car and photo detectors mounted on the track.

The safety of the system is guaranteed by a braking device activated by a hydraulic system which is mounted at each end of the trace ends to hold the travelling carriage in position. Oil buffers are mounted to minimize a sudden impact in the case of improperly decelerating carriage. An electrical dynamic braking is applied in the case of power failure to prevent a free fall of the car. The armature windings are automatically connected (shunted) to the external resistors. The power dissipated in

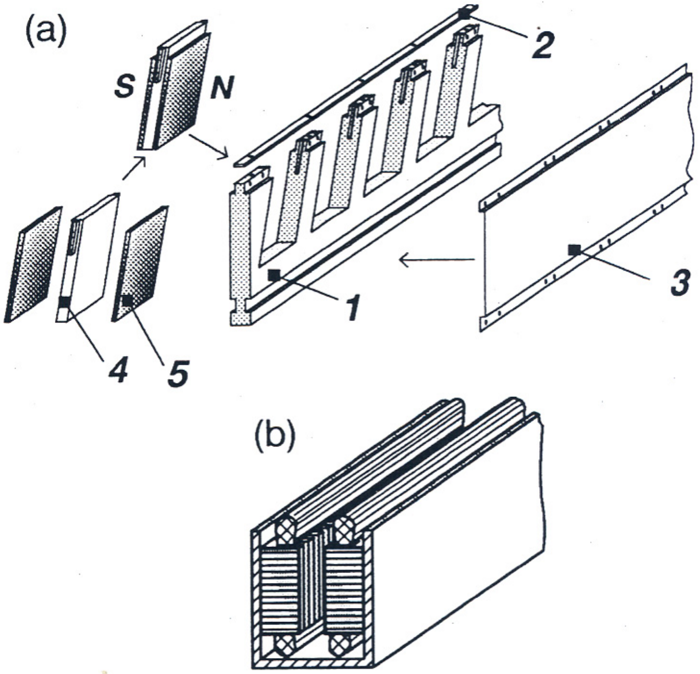

Figure 7.12 Construction of PM LSM for ENNA ropeless elevator system, (8,) PM mover, (b) double-sided armature. 1- PM mounting aluminum plate, 2 - locking bar, 3 - protective cover made of non-ferromagnetic stainless steel, 4 - steel plate, 5 - PM.

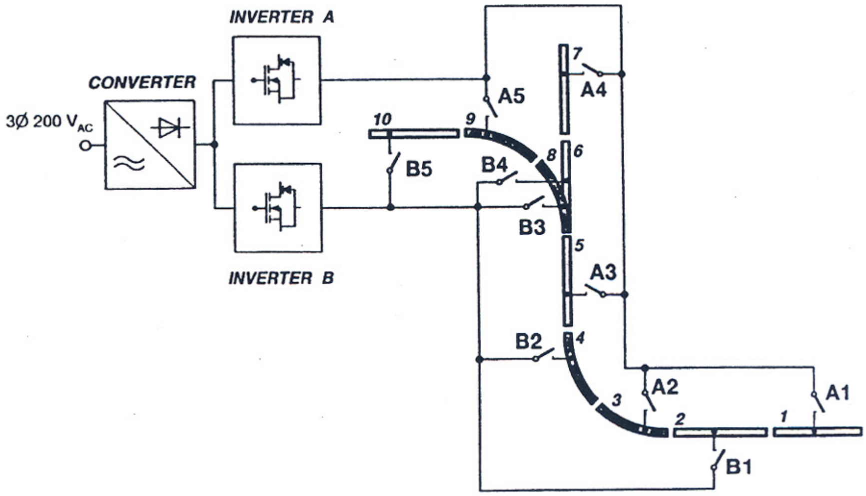

Figure 7.13 Power distribution system.

©2000 CRC Press LLC

the braking resistor provides smooth, controllable braking force, allowing the car to descend at stable crawl speed even when all safety monitoring equipment fails.

The ENNA project completed in 1995 shows that in the near future the vertical transportation system would evolve into arteries in which cars could move three-dimensionally. Travel will not be limited to enclosed spaces, like conventional elevator systems in use today, but multiple passenger cars will be moving freely between floors, buildings, underground or in any subterranean space.

7.3.4 Brakes

One of the most important elevator subcomponents is a *braking system.* The brake must:

- maintain the car in a fixed vertical and horizontal (side-to-side and front-to-back) position while passengers are boarding and exiting;
- operate to stop the vertical motion of the car under complete power failure;
- have the capability of producing at least 1.0 m/s^2 deceleration for periods above 10 s when the car is travelling downward;
- supply auxiliary guidance to the car in the case of a complete power failure. This requirement is important for elevators with active magnetic guidance (AMG) [101].

The primary function of a brake is to hold the car in a fixed position when passengers are entering and exiting. While this function could be accomplished using an electric motor, it is more efficient to use a friction brake to hold the car in position. In a roped elevator, this brake generally acts on a drum attached to the sheave. Therefore, a relevelling process is required as the car load changes and the cable length between the brake and the car stretches or contracts. For the brake mounted directly on the car (ropeless design), the need for relevelling is eliminated as there is no cable located between the brake and car stretch. The second function of the brake is to provide stopping power for the car in case of a power failure. The braking force in a conventional elevator is generally applied by a spring pressure and released using an electrical actuator (solenoid). In the case of an electrical outage, the braking force is automatically produced by the spring pressure. Usually, elevator brakes are either fully applied or fully disengaged. Normally they would not be modulated or applied gently to generate for example 50% of possible braking force.

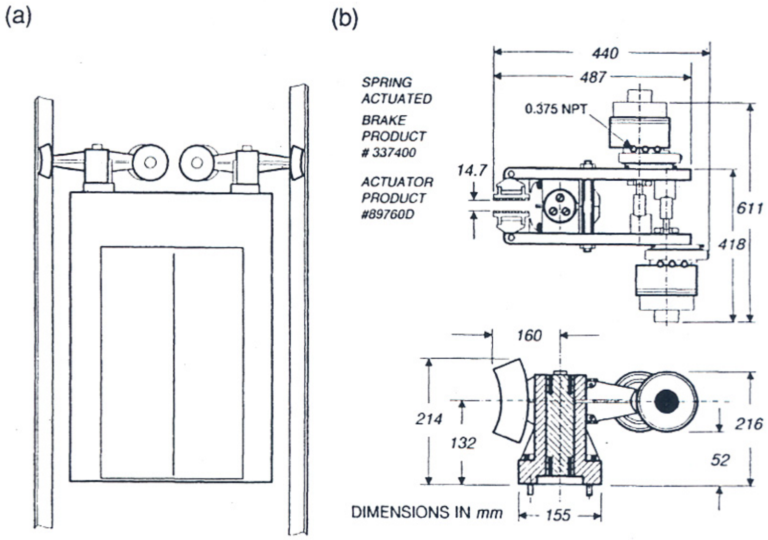

Figure 7.14 Ropeless elevator brakes: (a) installation, (b) commercial brake caliper type from *Nexen*, Vadnais Heights, MN, U.S.A. (formerly *Horton Industrial Products*).

©2000 CRC Press LLC

The brake in a standard roped elevator is used under the steady state conditions. It is applied after the car has completely stopped, and released only after the motor has been torqued to support the car. This is done to prevent the car from lurching either up or down at the brake release. Conventional elevator brakes may also operate in a dynamic mode if power is lost to the hoistway or safety limits are exceeded. In this mode the brake is required to stop the car safely while it is moving up to 120% of the contract speed, i.e., speed negotiated between the manufacturer and customer.

Brakes for ropeless elevators will have to meet more severe requirements. With ropeless elevators, it is possible to use a *caliper friction brake,* similar to the standard elevator brake. The caliper and brake assemblies should be attached to and move with the car. These brakes can be actuated by a spring and retracted by an electromagnetic actuator. There should be one brake assembly on each side of the car, acting against the same rails (T - rails) as safety devices. Under normal operation, the car comes to a stop being driven by the LSM, and the brake is only deployed after car has stopped. In the case of emergency, the brake needs to be capable of stopping the moving car. An example of caliper brake installation on the ropeless elevator car is shown in Fig.7.14.

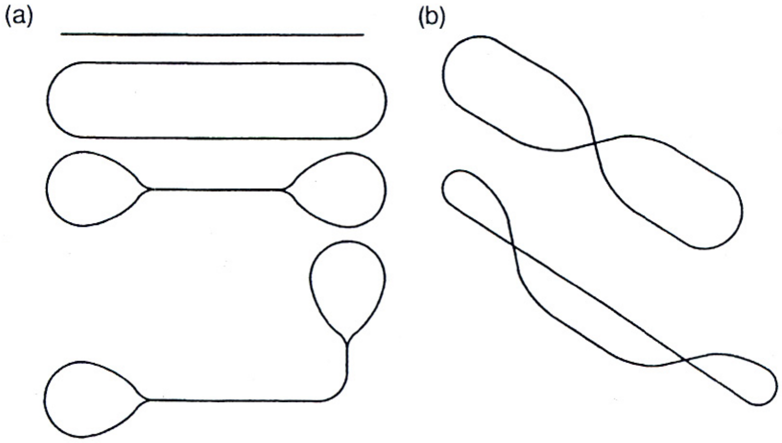

Figure 7.15 Arrangement of linear motor transportation lines: (a) on one level, (b) on two levels.

©2000 CRC Press LLC

7.4 Horizontal Transportation Systems.

7.4.1 Guidelines for Installation

Linear motors can simplify the transfer bulk and loose materials, small containers, pallets, bottled liquids, parts, hand tools, documents, hand tools, documents, etc. in building and factory transportation systems. It is easy to adopt the linear motor system to the allowable space as linear motors are compact machines, do not have rotating parts, do not need maintenance and allow design of a transfer system that is in harmony with surrounding equipment. Linear motors are silent and the noise emitted does not exceed 65 dB. Magnetic fields emitted by armature windings and PM excitation system are not dangerous to human organisms and well designed transportation systems emit very low level of RFI. High intensity magnetic fields exist only in the airgap between the armature and reaction rail.

It is possible to design both on-floor and overhead transportation system. Moreover, the linear motor transportation line can be sloped to create a link between two or more floors. Parallel transportation lines or line for double deck carriages can also be designed. The rule is that transportation lines must never cross. If, say, a loop like ’8’ shaped line is needed, the crossing must be designed on two different levels. The possible designs are shown in Fig. 7.15 [64].

Stations for loading and unloading materials must be carefully planned and additional space must be reserved. Linear motors cannot be installed near inlets and exhausts of airconditioning systems because airborne dirty particles could deteriorate sensors performance and some times contaminate the airgap between the armature and reaction rail. In the case of PM excitation the space around the reaction rail must be free of any ferromagnetic particles.

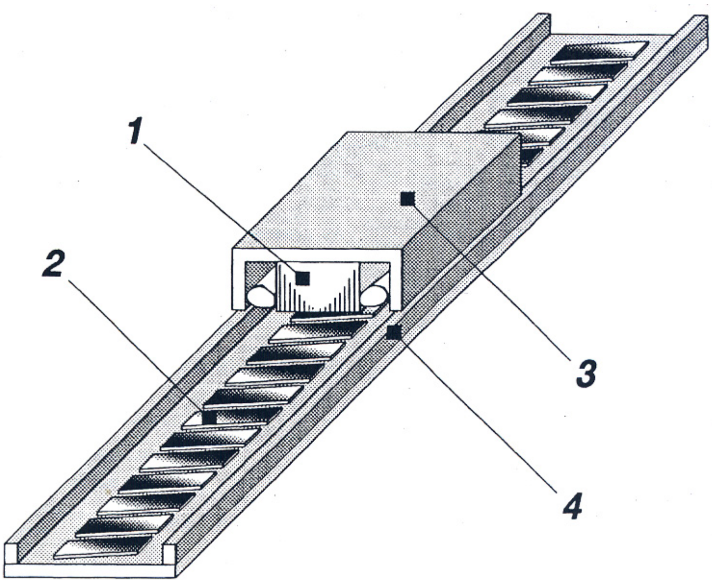

Figure 7.16 Horizontal factory transportation system with moving short armature LSM and long PM reaction rail. 1 - armature, 2 - PMs, 3 -carrier, 4 - guiderail.

7.4.2 Construction

There are two basic constructions of building or factory horizontal transportation systems with LSMs or LBMs:

- long stationary reaction rail with PMs and moving short armature (Fig. 7.16);
- stationary armature or armatures and moving reaction rail with PMs (Fig. 7.17) [118, 119].

The stationary long reaction rail is expensive and moving armature winding needs a contactless energy transfer [137]. It is more economical to use stationary short armature units distributed along the track. The mover is accelerated by the short armature unit and then is driven by its own inertia. Since the speed decreases, a next unit must be installed at

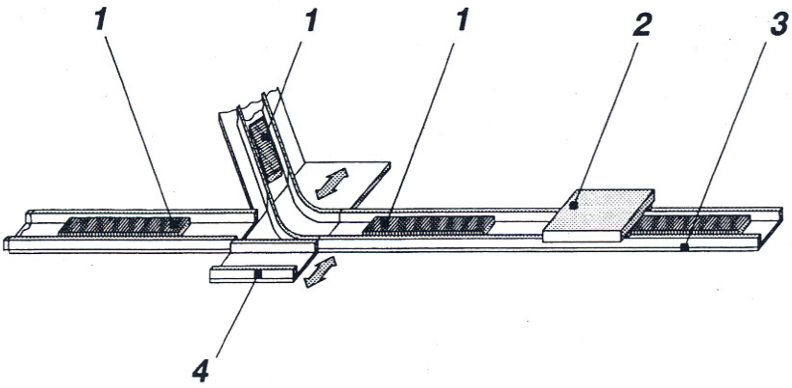

Figure 7.17 LSM horizontal transportation system with stationary discontinuous armature and short moving PM reaction rail. 1 - armature unit, 2- carrier with PM excitation system, 3 - guiderail, 4 - switch.

©2000 CRC Press LLC

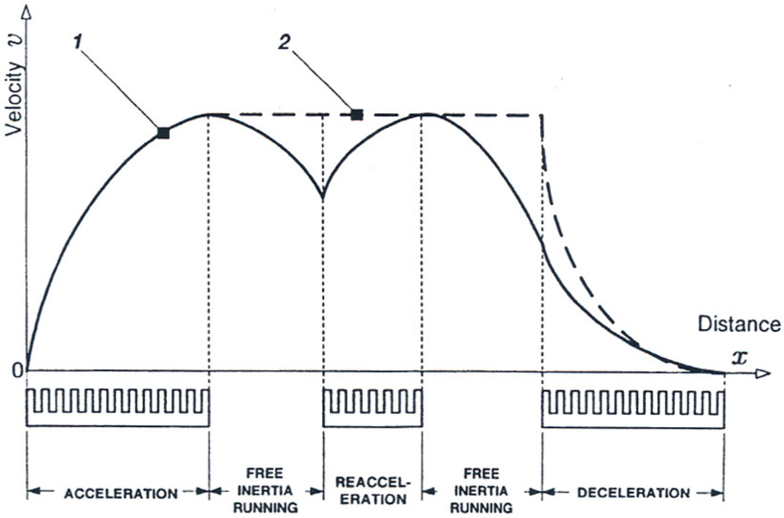

Figure 7.18 Speed profiles of LSM horizontal transportation systems. 1 – discontinuous arrangement of armature units, 2 - continuous arrangement of armature units.

a certain distance to re-accelerate the mover (Fig. 7.18). The longer the travel distance, the more armature units need to be used. Such discontinuous arrangement of LSMs requires synchronization of the speed of the mover (PM reaction rail) and travelling magnetic field. The method of synchronization can use either feedback signals from position sensors or open loop control of synchronization [118, 119]. The first methods are very reliable; however, they are costly. Open loop methods are more economical (lower cost of sensors).

7.4.3 Applications

The horizontal transportation system with stationary short armature units can be used, for *transfer 0f containers* in storage areas.

The system developed by *Preussag Noell, GmbH,* Würzberg, in cooperation with the Technical University of Braunschweig, Germany, consists of track-mounted, single-sided, iron-cored armature units and car-mounted movable PM excitation systems [56]. The length of the PM excitation system covers at least two armature units including the distance between them. A group of armature units connected in series is fed from an IGBT VVVF inverter. The position of cars is detected with the aid of special position sensors. Cars of length up to 15 m run on standard gauge railway track. The airgap between the armature core and PMs is 13 to 15 mm. With the pole pitch from 80 to 100 mm and PM height from 9 to 15 mm, the thrust density of 30 to 40 kN/m^2 can be obtained [56].

Another LSM system for container transportation has been developed at Kyushu University, Fukuoka, Japan [149]. The air cored armature coils are distributed along the guidaway beneath the container carrier and the PM excitation system is integrated with the carrier. The air cored LSM produces both the propulsion force (thrust) and normal repulsive force (no armature ferromagnetic core). The normal repulsive force electro dynamic levitation) helps to reduce the mass of the payload by about 85% [149]. By applying the *decoupled control method,* the thrust and normal force can be controlled independently [149]. It is possible not only to reduce the mass of payloads but also to reduce friction, vibration and noise caused by heavy goods.

Horizontal linear motor transportation system can alleviate and simplify duties of medical personnel in hospitals. Clinical charts, X-ray films, chemicals, specimens and documents can be transported by linear motor conveyance systems in special containers. *Shinko Electric Co. Ltd.*, Tokyo, Japan has developed *linear motor conveyance technology* for hospital staff [75]. This system called *LimLinear* can travel both vertically (5 m/s) and horizontally (3 m/s), connects several floors and is controlled by computer.

©2000 CRC Press LLC

Industrial Automation Systems

8.1 Automation of Manufacturing Processes

Manufacturing processes can be classified as follows [26]:

- casting, foundry or molding processes,
- forming or metalworking processes,
- machining (material removal) processes,
- joining (fastening, welding, fitting, bonding) and assembly,
- surface treatments and finishing (cleaning, tumbling, scribing, polishing, coating, plating),
- heat treating,
- other, e.g., inspection, testing, packaging, storaging, etc.

Manufacturing process automation frees the human operator from control functions, i.e., from the need to do certain actions in a particular sequence to carry out an operation in accord with the preset machining conditions.

Automation is the use of energy of nonliving system to control and carry out a process or process operation without direct human intervention [129]. The object of automation is to make the best use of available resources, materials, resources and machine. The human worker's function is limited to machine supervisory control and elimination of possible deviations from the prescribed process (corrective adjustment).

According to *Yardstick for Automation* chart (Table 8.1) presented by G.H. Amber and P.S. Amber in 1962 [7], each level of automation is tied to a human attribute which is being replaced by the machine. Thus the A(O) level of automation, in which no human attribute was mechanized, covers the Stone Age through the Iron Age. So far, levels A(5), A(6) and A(7) have partially been implemented or are subject to intensive research. Levels A(8) and A(9) are still topics of science fiction.

©2000 CRC Press LLC

Table 8.1 Yardstick for Automation [7].

Orders of Automation	Human Attribute Replaced	Examples
A(0)	*None*: Lever, screw, pulley, wedge	Hand tools, manual machines
A(1)	*Energy*: Muscles replaced	Powered machines and tools Whitney's milling machine
A(2)	*Dexterity*: Self-feeding	Single-cycle automatics
A(3)	*Diligence*: No feedback	Repeats cycle; open loop numerical control or automatic screw machine; transfer lines
A(4)	*Judgment*: Positional feedback	Closed loop; numerical control; self-measuring and adjusting
A(5)	*Evaluation*: Adaptive control; deductive analysis; feedback from the process	Computer control, model of process required for analysis and optimization
A(6)	*Learning*: By experience	Limited self-programming; some artificial intelligence (AI); expert systems
A(7)	*Reasoning*: Exhibit intuition; relates causes and effects	Inductive reasoning; Advanced AI in control software
A(8)	*Creativeness*: Performs design unaided	Originality
A(9)	*Dominance* : Super machine, commands others	Machine is master

In automatic systems, actuation components are adapted to moving various mechanisms of machine tools to execute the required step of control, e.g., change the mode of operation, release a work piece, start or stop the machine, etc. One of emerging technologies is the use of linear motors as electrical actuators.

8.2 Casting processes

8.2.1 Metal Casting Machines

In automation of metal casting processes, only LIMs have been utilized so far [80]. In modern, mass production foundries, *automatic pouring*

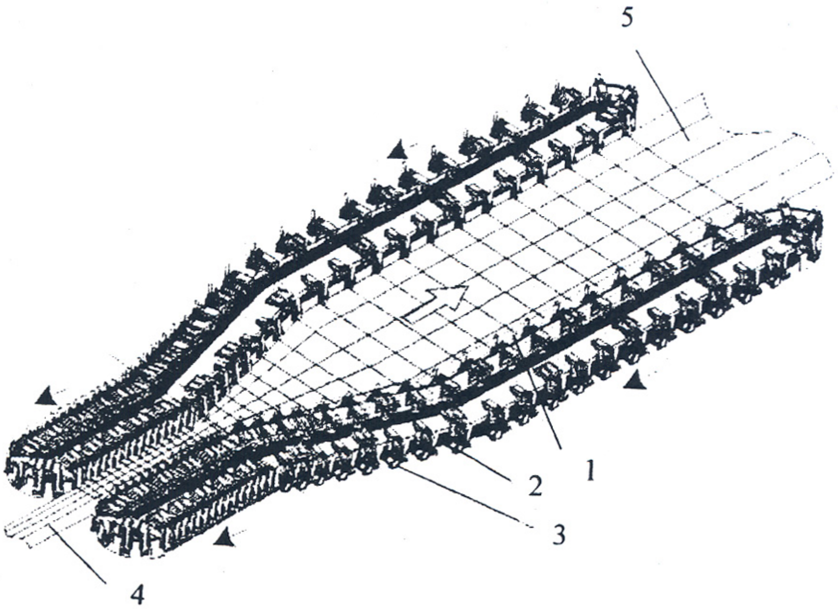

Figure 8.1 Application of LSMs to simultaneous film orientation technology. 1 - LSM, 2 - driven clips, 3 - idle clips, 4 - cast film, 5 - oriented film. Courtesy of Brueckner Maschinenbau GmbH, Siegsdorf, Germany.

systems are used. The molten metal is brought from the main melting furnace to a holding furnace by an overhead crane. Then, the molten metal is poured into the individual pouring ladles from the holding furnace and, in turn, is poured automatically into the corresponding molds [26]. A specially designed *roundabout casting machine* with molds can be driven by LIMs [80]. In addition to propulsion, LIMs also heat the molten metal so that there is efficient conversion of electrical energy into mechanical and thermal energy. An incremental encoder is implemented to control the speed and position of the roundabout casting machine.

8.2.2 2D Orientation of Plastic Films

High quality plastic films can be obtained as a result of *simultaneous orientation technology* in which the film is stretched in two directions [19]. Simultaneous orientation is a process where the distances between clips, i.e., gripping points of the film, are continuously increased as a result of moving clips apart lengthwise and across.

LSMs can be used to move clips forward with adjustable speeds [19]. Driven carriage (clips) with built-in PMs are arranged in a closed circuit to form a roller rail (Fig. 8.1). Armature systems of LSMs are stationary. Additional gripping points for the film are provided by idle carriages which move between driven carriages. Each carriage can move freely along the rail without any mechanical limitations. As many as 900 LSMs with rated thrust of 900 N each can be employed and linear velocities up to 7.5 m/s (450 m/min) can be achieved [19]. The working width of foil is 7.5 m and the length of track is 2 X 126 m. High speeds and flexibility of speed sequences of individual carriages allow for high productivity and adjustable product features.

The thrust of each LSM is proportional to the load (power) angle δ, i.e., $F_{dx} \approx (m_1/v_s)(V_1 E_f / X_{sd}) \sin\delta$. Variation of external forces causes variation of the angle δ and, as a consequence, oscillations are generated. To damp oscillations effectively, an active damping control system is implemented in addition to the damper. An observer estimates the load angle δ from the known currents and sends a feedback to the controller [19].

©2000 CRC Press LLC

8.3 Machining Processes

The seven basic machining processes are *shaping, drilling, turning, milling, sawing, broaching* and *abrasive machining* . To accomplish the basic machining processes, eight basic types of cutting *machine tools* have been developed [26]:

- shapers and planers,
- drill presses,
- lathes, ,
- boring machines,
- milling machines,
- saws,
- broaches,
- grinders.

For example, constructions of milling machines are shown in Fig. 8.2. Most of machine tools are capable of performing more than one of the basic machining processes. This advantage has led recently to the development of machining centers. A *machining center* is a specifically designed and numerically controlled (NC) single machine tool with a single work piece setup to permit several of the basic processes, plus other related processes [26]. Thus, a machining center can perform a variety of processes and change tools automatically while under programmable control. Numerical control is a method of controlling the motion of machine components by means of coded instructions generated by microprocessors or computers.

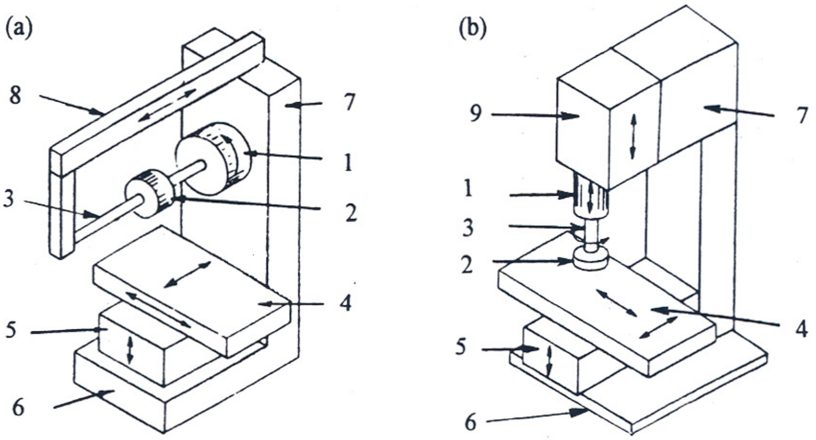

Figure 8.2 Major components of knee type milling machines with: (a) horizontal spindle, (b) vertical spindle. 1 - spindle, 2 - cutter, 3 - arbor, 4 -table, 5 - knee, 6 - base, 7 - column, 8 – over arm, 9 - head.

A part to be machined is fixed to the x-y table of machining center which must provide a movement both in the x and y direction (Fig. 8.3). The vertical z movement is provided by the head, e.g., to control the depth of drilled holes. This can also be achieved by moving the cutting tool in the w direction (Fig. 8.3). To obtain a full flexibility of machining, the vertical cutting tool should rotate around its horizontal axis (α

©2000 CRC Press LLC

direction). Closed loop position control is used in each of five axes. Normally, the rotation of a rotary servo motor, usually PM brushless motor, is converted into linear motion in *x, y, z* or *w* direction with the aid of *ball lead screws* (Fig. 8.4).

The ball lead screw drive is characterized by the following parameters [62];

- maximum linear speed

$$v_{\max} = n_{\max}\tau_l \qquad (8.1)$$

- maximum acceleration

$$a_{\max} = \frac{T_{\max}\tau_l}{2\pi\left[J + m\left(\tau_l/(2\pi)\right)^2\right]} \qquad (8.2)$$

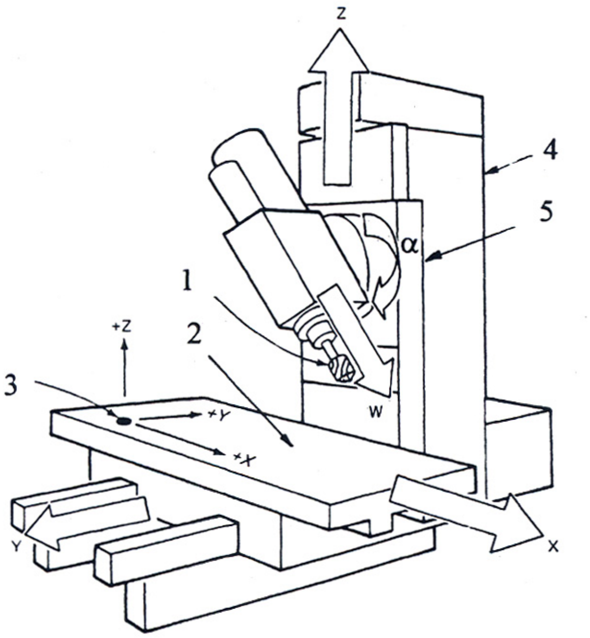

Figure 8.3 Five-axis vertical spindle machining center. 1- cutting tool, 2 - table, 3 - machine zero point, 4 - column, 5 - head.

©2000 CRC Press LLC

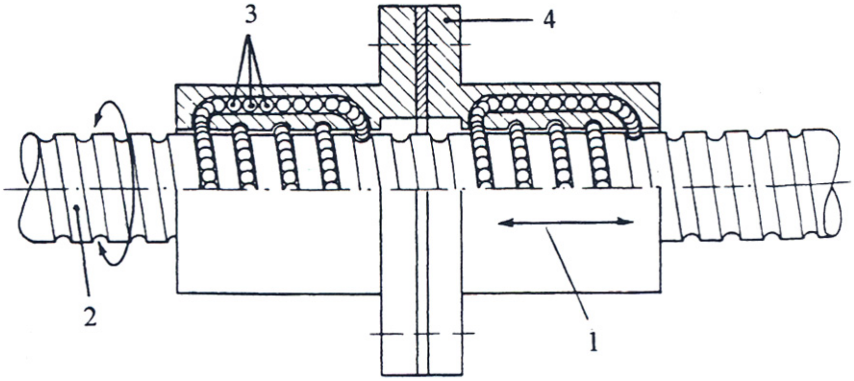

Figure 8.4 Longitudinal section of a ball lead screw. 1 - table movement, 2 - recirculating ball lead screw, 3 - recirculating balls, 4 - ball nut attached to the table.

- static servo stiffness

$$H = aV_g K_p k_T \left(1 + bV_i\right)\left(\frac{2\pi}{\tau_l}\right)^2 \tag{8.3}$$

where $n_{\max}$ is the maximum rotational speed, τ_l is the lead, J is the moment of inertia of servo motor and ball lead screw, *m* is the mass of the slider, V_g is the proportional gain, V_i is the integral gain, K_p is the position loop gain, k_T is the torque constant of the servo motor and a and b are constant parameters. Conventional machining centers use ball screws with leads τ_i = 10 to 14 mm and servo motors with maximum speeds $n_{\max}$ = 2000 to 2500 rpm which gives $v_{\max}$ = 20 to 35 m/min, $a_{\max}$ = 0.2g to 0.3g and $H \approx 23 \times 10^8$ N/m (*x*-axis of the table) [62].

In the early 1990s high speed, modern machining centers have been developed (*Makino Milling Company* and *Comau Company*). Specifications of high speed machining centers are given in Table 8.2 [62]. The maximum speed $v_{\max}$ = 60 m/min is at least twice higher and the maximum acceleration $a_{\max} \approx 1$g is at least three times higher than those of conventional machining centers. On the other hand, the static servo stiffness of high speed machining centers decreases about eighteen times in comparison with conventional machining centers. This is mainly caused by the increase of the lead τ_l and decrease of the rotor moment of inertia J of the servo motor.

Linear motors can successfully replace ball lead screws in machine tools. Fig. 8.5 shows two methods of obtaining high linear speed (feed rate) and high acceleration by using a ball lead screw and linear motor. Rotary servo motors can use either a rotary encoder or linear encoder with table mounted scale while linear motors use only linear encoders. LIMs [38] are not recommended motors for machine tool applications because they emit large amounts of heat and have low efficiency and power factor. PM LSMs or LBMs are much better motors because they are smaller and can provide efficiency over 75%, high power factor and fast response. According to *Shinko Electric* Co. Ltd, Takegahana Ise, Japan, the so-called PM high thrust density linear motor (HDL) has efficiency over 90% at low speed and very high acceleration [63, 100]. A HDL is similar to HLSM, i.e., both have forcer windings and toothed reaction rail; however, the HDL has a different arrangement of PMs (Fig. 8.6). Table 8.3 compares performance of three different linear motors, i.e., LIM, LSM and HDL for applications to machine tools [62, 100].

First machining centers with linear motor propulsion were built by *Ingersoll Milling Machine Company* , Rockford, IL, U.S.A. and LMT *Consortium* , Japan [62] in the mid 1990s. In machining centers built by *Ingersoll* series LF LSMs manufactured by *Anorad* [8] have been

Table 8.2 Specifications of a modern high speed machining center with ball lead screws.

Parameter	x-axis	y-axis	z-axis
Stroke, m	0.56	0.41	0.41
Maximum linear speed (feed rate), m/min	60		
Maximum acceleration	1.0g	1.2g	0.9g
Mass of slider, kg	235	500	425
Ball lead screw Diameter, mm Lead τ_l, mm Type of support	36 20 single		
Type of guidaway	Sliding		
Control	Semi-closed loop		
Resolution of positioning, mm	0.001		
Spindle Diameter, mm Rated output power, kW Rotational speed, rpm	65 30 20,000		

©2000 CRC Press LLC

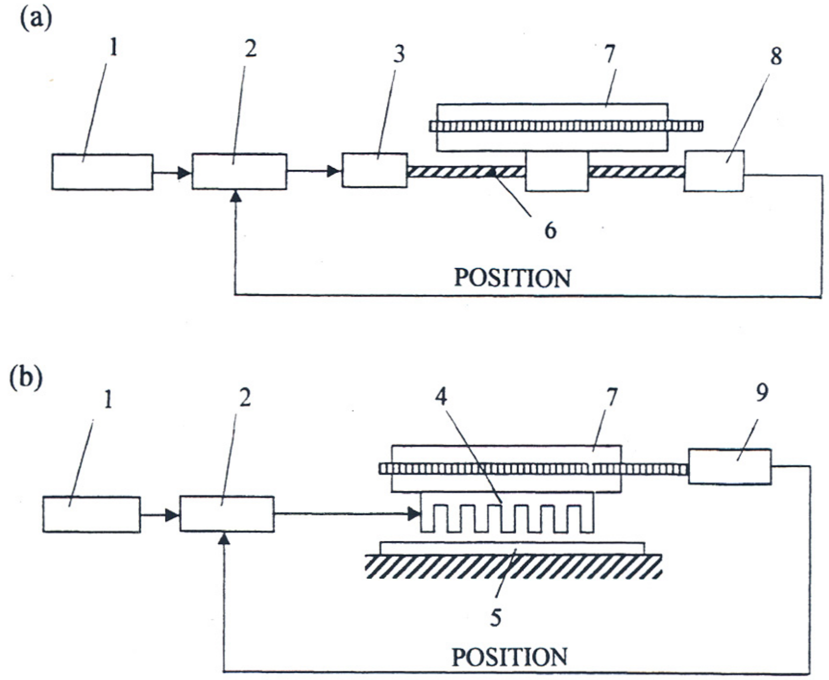

Figure 8.5 Axis drive systems with: (a) ball lead screw, (b) linear motor. 1 - interpolator, 2 - controller, 3 - low inertia servomotor, 4 – armature of a linear motor, 5 - reaction rail of a linear motor, 6 – ball lead screw, 7 - table (guide), 8 - rotary encoder or resolver, 9 - linear sensor.

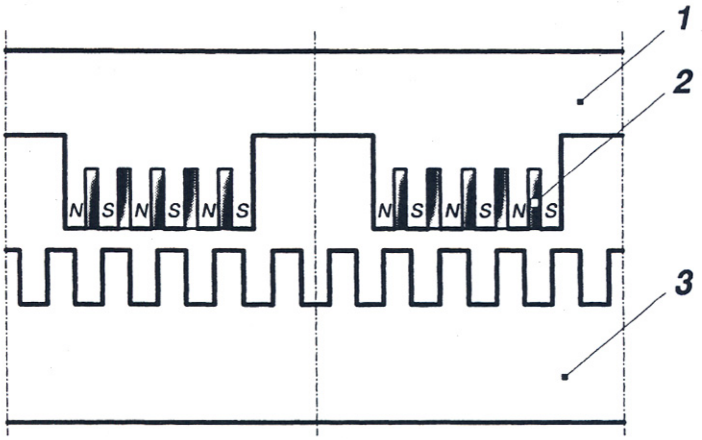

Figure 8.6 High thrust density PM LBM developed by *Shinko Electric Co. Ltd*, Japan. 1 - armature core, 2 - PM, 3 - reaction rail.

©2000 CRC Press LLC

Table 8.3 Comparison of linear motors used in servo drives of machine tools.

Parameter	LIM	LSM	HLD
Dimensions LxWxH mm	222x50x49.5	160x50x27	290x79x40
Mass of armature, kg	4.29	1.89	6.47
Air gap, mm	1.0	0.5	0.2
Resistance per phase, Ω	1.72	26.8	0.193
Inductance per phase, mH	14.4	54.7	5.62
Pole pitch τ , mm	54	33	10
Construction of armature	Winding	Winding	Winding+PMs
Construction of reaction rail	Cu+Fe	PMs+Fe	Fe
Cogging and detent force	nonexisting	exists	exists
Rated current, A	4.0	1.03	16.9
Rated thrust, N	48	139	880
Thrust constant k_F ,N/A	12	135	52
Maximum efficiency, η	0.18	0.77	0.92
Efficiency at rated thrust and v= 1 m/s	0.125	0.60	0.62
Thermal resistance, °c/W	0.87	0.686	0.291

Table 8.4 Specifications of machining center LMT96 manufactured by LMT *Consortium*, Japan.

Mass of machining center, kg	16,000
Dimensions length x width x height, m	4.4x4.4x2.9
Stroke m *x* axis *y* axis *z* axis	 0.8 0.5 0.5
Maximum feed rate $v_{\max}$, m/min *x* axis *y* axis *z* axis	 80 80 80
Maximum acceleration $a_{\max}$ *x* axis *y* axis *z* axis	 1.0*g* 2.0*g* 1.0*g*
Spindle Diameter, mm Rated output power, kW Rotational speed, rpm	 65 15/22 30,000
Tools Number of tools Tool selection Maximum diameter of tool, mm Maximum length of tool, mm Time required to change • tool-to-tool • chip-to-chip	 12 Random 100 250 1.5 s 3.5 s

installed. Table 8.4 shows specifications of LMT96 machining center manufactured by LMT *Consortium* [62].

Machining centers with linear motors are mainly used for machining processes which require high *contouring* accuracy, e.g., manufacturing of dies or molds. Contouring permits two or three axes to be

©2000 CRC Press LLC

controlled simultaneously in two or three dimensions. The price of machining centers with linear motors is almost twice of those with ball lead screws.

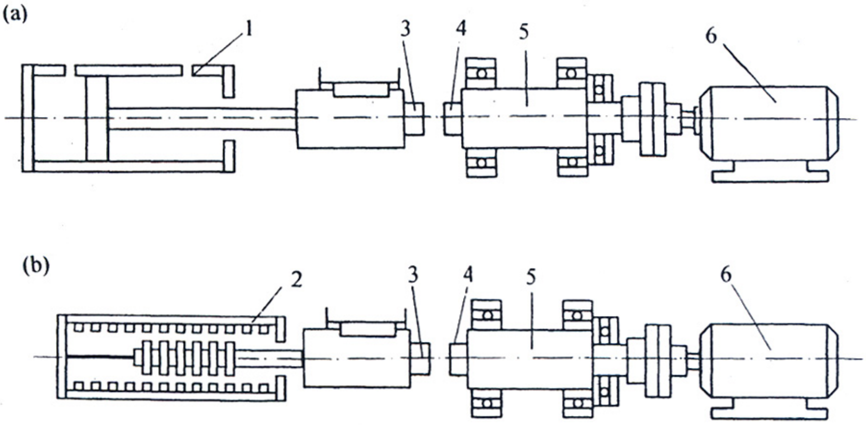

Figure 8.7 Equipment used for friction welding: (a) with hydraulic or pneumatic actuator, (b) with electric linear actuator. 1 - mechanical actuator, 2 - PM actuator or tubular LSM, 3 - chuck for stationary part, 4 – chuck for rotating part, 5 - spindle, 6 - rotary electric motor.

8.4 Welding and Thermal Cutting

8.4.1 Friction Welding

The heat required for *friction welding* is produced as a result of mechanical friction between two pieces of metal to be joined [26]. Those two pieces are held together while one rotates and the other is stationary. The rotating part is held in a motor driven collet while the stationary part is held against it under controlled pressure produced by a hydraulic or pneumatic actuator (Fig. 8.7a). The frictional heat is a function of the rotational speed and applied pressure (linear force). The rotational speed and force depend on the size of the piece of metal to be welded. For example, for welding a 3 mm mild steel stud, a force about 900 N at 20,000 rpm is required [55].

In manufacturing plants where clean atmosphere is required, hydraulic or pneumatic actuator must be replaced by electric linear actuator (Fig.8.7b). PM linear actuators [55] or PM LSMs can successfully be used.

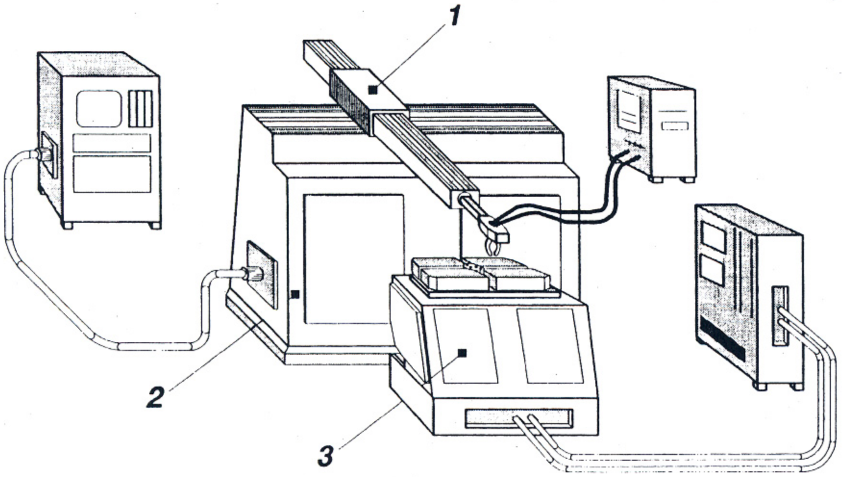

Figure 8.8 Linear motor driven welding robot. 1 - arm driven by two HLSMs in *x*-*y* plane, 2 - base, 3-table.

8.4.2 Welding Robots

HLSMs provide a simple solution to high precision motion control of a torch or electrode of *welding robots*. Fig. 8.8 shows a robot for the resistance spot welding in which the electrode is moved in the *x*-*y* plane with the aid of two HLSMs [144]. The robot is microprocessor controlled.

8.4.3 Thermal Cutting

Most of all *thermal cutting* is done by *oxyfuel gas cutting* where acetylene is used as a fuel [26]. The tip of torch contains a circular array of small holes through which the oxygen-acetylene mixture is supplied for the heating flame. In many manufacturing applications, cutting torches cannot be manipulated manually and electrically driven carriages are used to hold cutting torches. LSMs or LIMs can be used as direct linear drives for torch carriages.

8.5 Surface Treatment and Finishing

8.5.1 Electrocoating

In the *electrocoating* process, a work piece is placed in a tank with paint and water solvent. A d.c. voltage is applied between the tank (cathode) and work piece to be coated (anode). The paint particles are attracted to

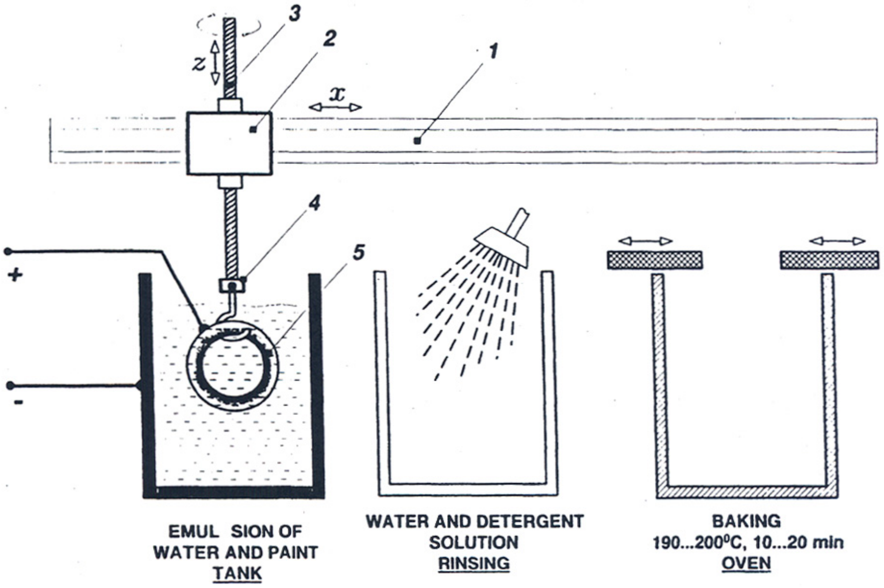

Figure 8.9 Automated electro coating line with linear motor driven work- pieces. 1 - monorail, 2 - LSM or HLSM, 3 - ball lead screw driven by a rotary servo motor, 4 - gripper, 5 – work piece.

the work piece and deposited on it creating a uniform thin coating (0.02 to 0.04 mm) [26]. Then the work piece is removed from the dip tank, rinsed, and baked at about 195°C for 10 to 20 min. This process is especially suitable for complex metal structures, i.e., automobile bodies [26].

Fig. 8.9 shows an automated electro coating line with linear motor driven overhead monorail system for horizontal transfer of bulk work-pieces. Depending on the required thrust, mass of the work piece and travel distance in the *x* direction, either LSMs or HLSMs can be used. To raise or lower a heavy work piece vertically, ball lead screws driven by rotary servo motors are better than linear motors.

8.5.2 Laser Scribing Systems

Aircraft aluminum skin panels are usually scribed manually through templates prior to chemical milling. This costly process can be automated by the use of laser scribers and LSMs [29, 67]. An automatic *laser maskant scriber* with LSMs was built in 1993 for Boeing, Wichita, KS, U.S.A. [29]. *Maskant* is an etched machining process in which the scribed metal surface is coated with polymer material. The polymer is scribed to a desired pattern and then removed from the surface. The

©2000 CRC Press LLC

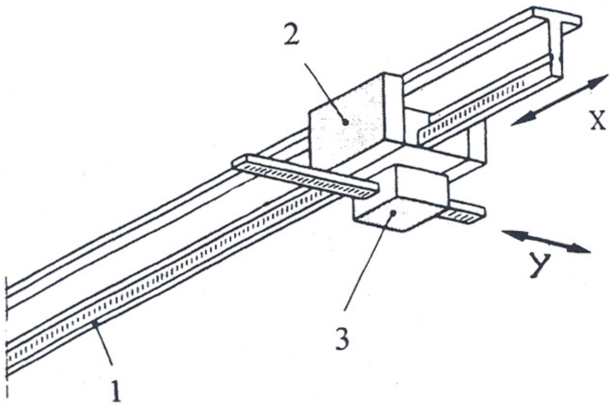

Figure 8.10 Automated monorail system with HLSMs. 1- overhead monorail, 2 - *x* direction forcer of a HLSM, 3 - *y* direction forcer of a HLSM.

metal is then placed in some acid solution which etches out the exposed surfaces.

Two parallel LSMs, (series LF, *Anorad* [8]) which produce the peak thrust up to 9 kN at speed up to 5 m/s have been used [67]. LSMs rapidly and precisely position a huge gantry with CO_2 laser maskant scribing system. Two laser systems have been used: one for scribing and second for position feedback. The use of a laser interferometer for positioning feedback with LSM drive mechanisms results in high accuracy and repeatability.

The advantages of the new LSM driven laser maskant scriber include mass, scrap and inventory reduction, non-contact design, no lubrication and adjustments, elimination of the stress channel and minimizing back bending and repetitive motions. According to *Boeing* , this is the largest automatic laser scriber in the world (33 m long, 3 m wide and 5.1 m tall) which can hold two Boeing 747 wings simultaneously, scribing one while positioning the other and scribe up to 254 mm per 1 s or complete up to four skin panels in 1 h [67].

8.6 Material Handling

8.6.1 Monorail Material Handling System

Fig. 8.10 shows an *overhead monorail* system for material handling with two HLSMs to obtain a linear motion control in the *x* and *y* direction. Such a monorail system can be computer controlled and installed in automated assembly lines or material transfer lines where high precision of positioning or clean atmosphere is required.

©2000 CRC Press LLC

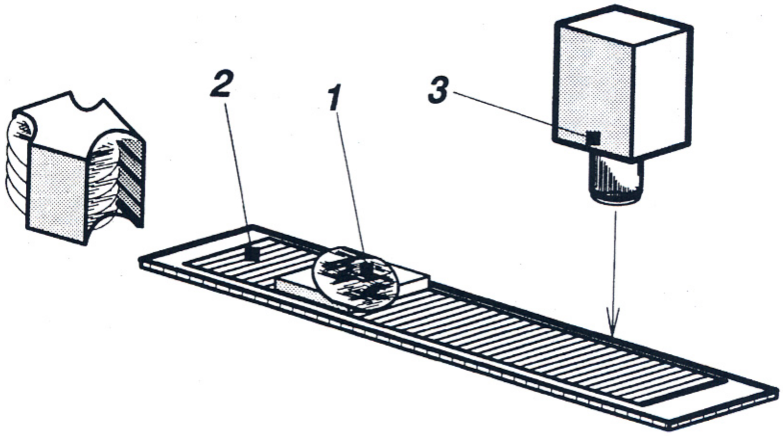

Figure 8.11 Semiconductor wafer transport. 1 - forcer of HLSM used as a carrier for wafers, 2 - platen, 3 - camera or laser. Courtesy of Parker Hannifin Corporation, Rohnert Park, CA, U.S.A.

8.6.2 Semiconductor Wafer Transport

HLSMs simplify the process of semiconductor wafer transport as shown in Fig. 8.11 [21]. The HLSM offers increased throughput and gentle handling of the wafer.

8.6.3 Capsule Filling Machine

To dispense radioactive fluid into a capsule, a HLSM driven machine can be used. Such a solution has the following advantages [21]:

- increased throughput,
- no spilling of radioactive fluid,
- automation in two axes,
- smooth, repeatable motion,
- cost effective solution.

In *capsule filling machine* shown in Fig. 8.12, the forcer of a HLSM moves a tray with empty capsules along a horizontal axis [21]. The filling head driven by a rotary stepping motor and ball lead screw is raised and lowered in vertical axis. A linear motor in vertical axis has also been considered, but with the loss of power, the fill head will drop onto the tray [21]. The simple mechanical construction guarantees a long maintenance-free life.

©2000 CRC Press LLC

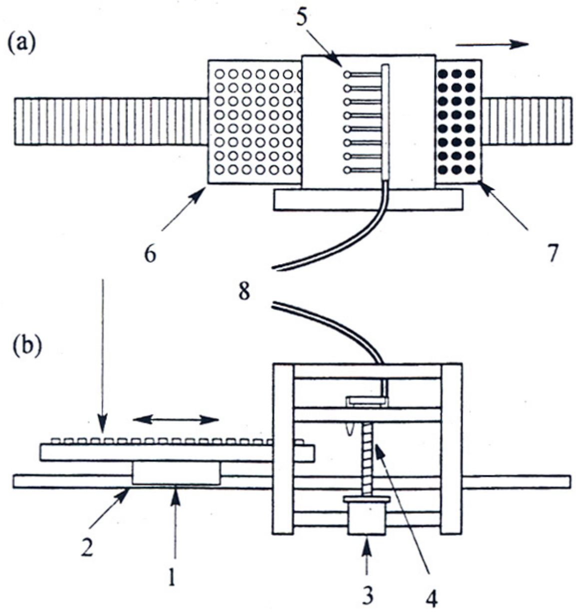

Figure 8.12 Capsule filling machine with a HLSM. 1 - forcer, 2 - platen, 3 - rotary microstepping motor, 4 -lead screw, 5 - filling heads, 6 – tray of empty capsules, 7 - full capsules, 8 - hose. Courtesy of *Parker Hannifin Corporation*, Rohnert Park, CA, U.S.A.

In addition to the above examples of material handling systems, HLSMs offer solutions to a variety of factory automation systems which include [21]:

- printed circuit board assembly,
- industrial sewing machines,
- light assembly automation,
- automatic inspection,
- wire harness making,
- automotive manufacturing,
- gauging,
- packaging,
- medical applications,
- parts transfer,
- pick and place,
- laser cut and trim systems,
- flying cutters,
- semiconductor technology,
- water jet cutting,
- print heads,

- fiber optics manufacture,
- *x-y* plotters.

Speed, distance and acceleration are easily programmed in a highly repeatable fashion.

8.7 Testing

8.7.1 Surface Roughness Measurement

Roughness is measured by the heights of irregularities with respect to an average (center) line [26]. Most instruments for *measuring surface roughness* use a diamond *stylus* that is moved at a constant speed. The vertical movement of the stylus is detected usually with the aid of linear variable differential transformer (LVDT) and as an electrical signal can be processed electronically and stored on the computer disk or recorded on a strip chart. The unit containing the stylus can be driven by two HLSMs in the *x-y* plane (Fig. 8.13). After making a series of parallel offset traces on the tested surface, a two dimensional profile map is obtained.

8.7.2 Generator of Vibration

Analysis and simulation of dynamic behavior of buildings and large-scale constructions requires long stroke and high speed *generators of vibration* . Typical parameters of such a device are: 7.7 kN maximum thrust, 6.5 kN rated thrust, 2 m/s maximum speed, 0.5 m effective stroke and 2000 kg maximum load mass [63]. Oil hydraulic devices are large, need complex maintenance, have low efficiency and nonlinear characteristics. Linear electric actuators or motors are smaller, provide high speed and acceleration, and do not need maintenance. *Shinko Electric Co. Ltd* has built a prototype generator of vibration with HDL [63]. A good response, i.e., thrust versus sinusoidal current signal, has been obtained in vibration domain less than 5 Hz.

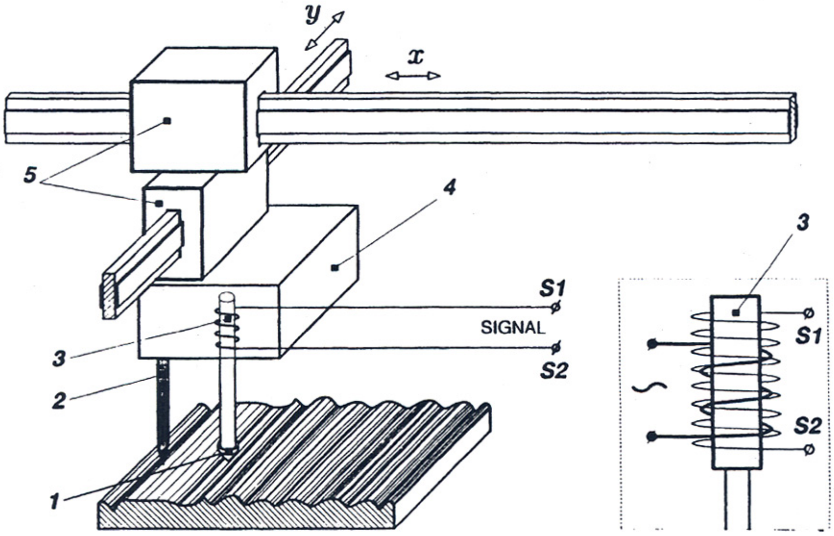

Figure 8.13 Stylus profile device for measuring surface roughness and profile. 1 - diamond stylus, 2 - rider, 3 - LVDT, 4 - head, 5 - HLSM.

©2000 CRC Press LLC

8.8 Industrial Laser Applications

Laser systems driven by LSM *x-y* positioning stages have been success fully applied to *diamond processing*, including sawing, cutting, kerfing and shaping [29]. Advantages of applications of LSMs versus ball lead screws include better quality finished surface, insensivity of LSMs to diamond dust and positioning accuracy of 0.2 μm over travel distances 300 by 100 mm. A multi-task *diamond processing laser system* has been built by *Or-Ziv* , Rehovot, Israel [29].

A linear motor gantry for industrial *laser cutting systems* has been built by CBLT, Starnberg, Germany [29]. High beam quality CO_2 laser together with LBM positioning stages provide smoother cuts, more vertical surfaces and cleaner edges.

A large *laser scribing system* with LSMs has been described in Section 8.5.2.

©2000 CRC Press LLC

appendix A

Magnetic Circuits with Permanent Magnets

A.1 Approximation of Demagnetization Curve and Recoil Line

The most widely used approximation of the demagnetization curve is the approximation using a hyperbola, i.e.,

$$B = B_r \frac{H_c - H}{H_c - a_0 H} \tag{A.1}$$

where B and H are coordinates, and a_0 is the constant coefficient, which can be evaluated as [13]

$$a_0 = \frac{B_r}{B_{sat}} \frac{\sqrt[2]{\gamma} - 1}{\gamma} \tag{A.2}$$

or

$$a_0 = \frac{1}{n} \sum_{i=1}^{n} \left(\frac{H_c}{H_i} + \frac{B_r}{B_i} - \frac{H_c}{H_i} \frac{B_r}{B_i} \right) \tag{A.3}$$

where $\left(B_i, H_i\right)$ are coordinates of points i = 1, 2, . . . n on the demagnetization curve, arbitrary chosen, and n is the number of points on the demagnetization curve.

The recoil magnetic permeability is assumed to be constant and equal to [13]

$$\mu_{rec} = \frac{B_r}{H_c} \left(1 - a_0\right) \tag{A.4}$$

The above equations give a good accuracy between calculated and measured demagnetization curves for Alnicos and isotropic ferrites with low

©2000 CRC Press LLC

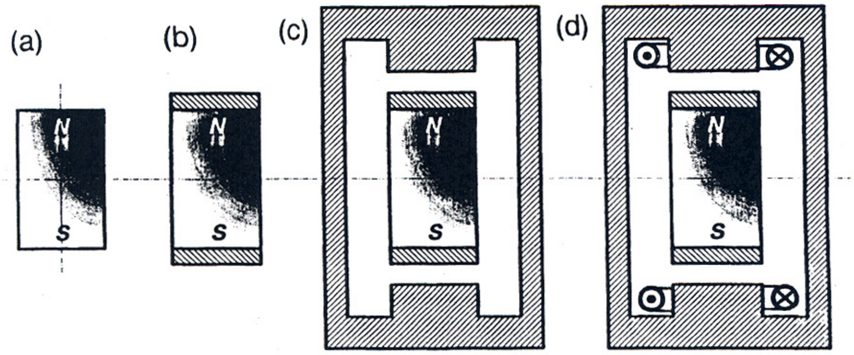

Figure A.1 Stabilization of a PM: (a) PM alone, (b) PM with pole shoes, (c) PM inside an external magnetic circuit, (d) PM with a complete external armature system.

magnetic energy. Application to anisotropic ferrites with high coercivity can in some cases cause errors.

For rare-earth PMs the approximation is simple due to their practically linear demagnetization curves, i.e.,

$$B = B_r \left(1 - \frac{H}{H_c} \right) \tag{A.5}$$

This means that putting $a_0 = 0$ or $\gamma = 0.25$, eqn (A.1) gets the form of eqn (A.5).

A.2 Operating Diagram

A.2.1 Construction of the Operating Diagram

The energy of a PM in the external space only exists if the reluctance of the external magnetic circuit is higher than zero. If a previously magnetized PM is placed inside a closed ideal ferromagnetic circuit, i.e., toroid, this PM does not show any magnetic properties in the external space, in spite of the fact that there is magnetic flux Φ_r corresponding to the remanent flux density B_r inside the PM.

A PM previously magnetized and placed alone in an open space, as in Fig. A.1a generates a magnetic field. To sustain a magnetic flux in the external open space, an MMF developed by the magnet is necessary. The state of the PM is characterized by the point K on the demagnetization curve (Fig. A.2). The location of the point K is at the intersection of the demagnetization curve with a straight line representing the permeance of the external magnetic circuit (open space), i.e.,

$$G_{ext} = \frac{\Phi_K}{F_K}, \qquad \tan\alpha_{ext} = \frac{\Phi_k / \Phi_r}{F_k / F_c} = G_{ext} \frac{F_c}{\Phi_r} \tag{A.6}$$

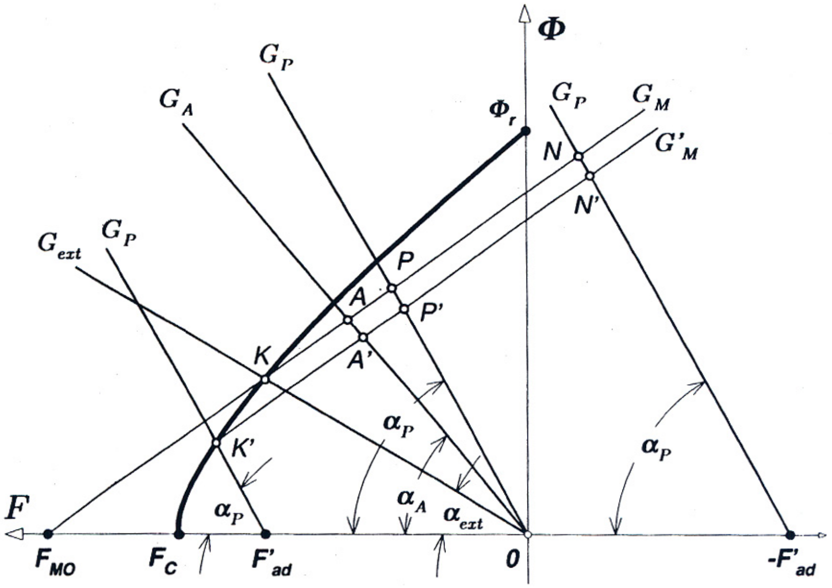

Figure A.2 Diagram of a PM for finding the origin of the recoil line and operating point.

The permeance G_{ext} corresponds to a flux Φ-MMF coordinate system and is referred to as MMF at the ends of the PM. The magnetic energy per unit produced by the PM in the external space is $w_k = B_k H_k / 2$. This energy is proportional to the rectangle limited by the coordinate system and lines perpendicular to the Φ and F coordinates projected from the point K. It is obvious that the maximum magnetic energy is for $B_k = B_{\max}$ and $H_k = H_{\max}$.

If the poles are furnished with pole shoes (Fig. A.1b) the permeance of the external space increases. The point which characterizes a new state of the PM in Fig. A.2 moves along the recoil line from the point K to the point A. The recoil line KG_M is the same as the internal permeance of the PM, i.e.,

$$G_M = \mu_{rec} \frac{w_M l_M}{h_M} = \mu_{rec} \frac{S_M}{h_M} \tag{A.7}$$

The point A is the intersection of the recoil line KG_M and the straight line OG_A representing the leakage permeance of the PM with pole shoes, i.e.,

$$G_A = \frac{\Phi_A}{F_A}, \qquad \tan \alpha_A = G_A \frac{F_c}{\Phi_r} \tag{A.8}$$

The energy produced by the PM in the external space decreases as compared with the previous case, i.e., $w_A = B_A H_A / 2$.

The next stage is to place the PM in an external ferromagnetic circuit as shown in Fig. A.1c. The resultant permeance of this system is

$$G_P = \frac{\Phi_P}{F_P}, \qquad \tan \alpha_P = G_P \frac{F_c}{\Phi_r} \tag{A.9}$$

which meets the condition $G_P > G_A > G_{ext}$. For an external magnetic circuit without any electric circuit carrying the armature current, the magnetic state of the PM is characterized by the point P (Fig. A.2), i.e., the intersection of the recoil line KG_M and the permeance line OG_P.

When the external magnetic circuit is furnished with an armature winding and when this winding is fed with a current which produces an MMF magnetizing the PM (Fig. A.1d), the magnetic flux in the PM increases to the value Φ_N. The d-axis MMF $F_{ad}^{'}$ of the external (armature) field acting directly on the PM corresponds to Φ_N. The magnetic state of the PM is described by the point N located on the recoil line on the right-hand side of the origin of the coordinate system. To obtain this point it is necessary to layoff the distance $OF_{ad}^{'}$ and to draw a line G_p from the point $F_{ad}^{'}$ inclined by the angle αp to the F-axis. The intersection of the recoil line and the permeance line G_p gives the point N. If the exciting current in the external armature winding is increased further, the point N will move further along the recoil line to the right, up to the saturation of the PM.

When the excitation current is reversed, the external armature magnetic field will demagnetize the PM. For this case it is necessary to lay off the distance $OF_{ad}^{'}$ from the origin of the coordinate system to the left (Fig. A.2). The line G_p drawn from the point $F_{ad}^{'}$ with the slope α_p intersects the demagnetization curve at the point k'. This point can be up or down of the point K (for the PM alone in the open space). The point k' is the origin of a new recoil line $k'G'_M$. Now if the armature exciting current decreases, the operating point will move along the new recoil line $k'G'_M$ to the right. If the armature current drops down to zero, the operating point takes the position P' (intersection of the new recoil line $k'G'_M$ with the permeance line G_p drawn from the origin of the coordinate system).

On the basis of Fig. A.2 the energies $w_{p'} = B_{p'}H_{p'}/2, w_p = B_pH_p/2,$ and $wp' < wp$. The locations of the origin of the recoil line as well as the location of the operating point determine the level of utilization of the energy produced by the PM. A PM behaves in a different way than a d.c. electromagnet: the energy of a PM is not constant if the permeance, and exciting current of the external armature changes.

The location of the origin of the recoil line is determined by the minimum value of the permeance of the external armature or the demagnetization action of the external field.

©2000 CRC Press LLC

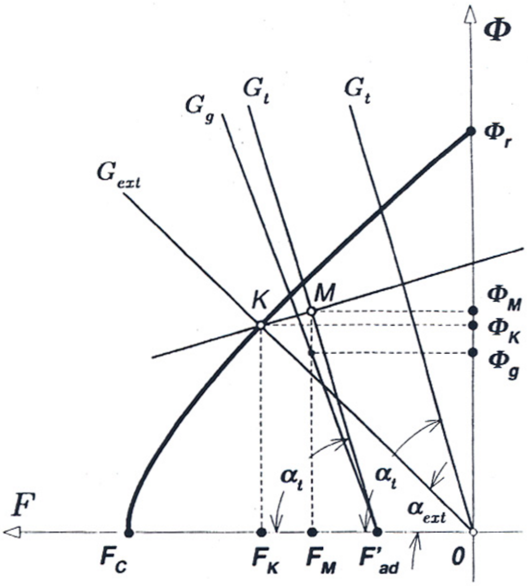

Figure A.3 Location of the operating point for the magnetization without the armature.

To improve the properties of PMs independent of the external fields PMs are stabilized. In magnetic circuits with stabilized PMs, the operating point describing the state of the PM is located on the recoil line. *Stabilization* means the PM is demagnetized up to a value which is slightly higher than the most dangerous demagnetization field during the operation of a system where the PM is installed.

A.2.2 Magnetization without Armature

In most practical applications the PM is magnetized without the armature and then is placed in the armature system with an airgap. In Fig.A.3 the demagnetization curve is plotted in flux Φ -MMF coordinate system. The beginning of the recoil line is determined by the leakage permeance G_{ext} of the PM alone located in open space (Fig. A.3).

For rare-earth PMs the recoil permeability μ_{rec} and the equation of the recoil line is the same as that for the demagnetization line.

The armature field usually demagnetizes the PM so that the line of the resultant magnetic permeance G_t intersects the recoil line between the point K and the magnetic flux axis.

The magnetic flux in the PM is $\Phi_M = G_t \left(F_M - F_{ad}^{'} \right)$. Using the coefficient of leakage flux (2.13), the useful flux density in the airgap can be found as [40]

$$B_g = \frac{\Phi_M}{S_g \sigma_{lM}} = \frac{G_t \left(F_M - F_{ad}^{'} \right)}{S_g \sigma_{lM}}$$

$$= \frac{G_t}{S_g \sigma_{lM}} \left[\frac{\Phi_K + F_K \mu_{rec} \left(S_M / h_M \right) G_t F'_{ad}}{G_t + \mu_{rec} \left(S_M / h_M \right)} - F'_{ad} \right] \qquad \text{(A.10)}$$

where S_g is the surface of the airgap. With the fringing effect being neglected, the corresponding magnetic field intensity is

©2000 CRC Press LLC

$$H_g = H_M = \frac{F_M}{h_M} = \frac{\Phi_K + F_K \mu_{rec} \left(S_M / h_M \right) + G_t F'_{ad}}{h_M \left[G_t + \mu_{rec} \left(S_M / h_M \right) \right]} \tag{A.11}$$

In the general case the resultant permeance G_t of the external magnetic circuit consists of the useful permeance G_g of the airgap and the leakage permeance G_{lM} of the PM, i.e.,

$$G_t = G_g + G_{lM} = \sigma_{lM} G_g \tag{A.12}$$

The useful permeance G_g corresponds to the useful flux in the active portion of the magnetic circuit. The leakage permeance G_{lM} is the referred leakage permeance of a single PM or PM with armature. Consequently, the external energy w_{ext} can be divided into the useful energy w_g and leakage energy w_{lM}. The useful energy per volume in the external space is

$$w_g = \frac{B_g H_g}{2} = \frac{G_g}{V_M} \left[\frac{\Phi_K + F_K \mu_{rec} \left(S_M / h_M \right) + G_t F'_{ad}}{G_t + \mu_{rec} \left(S_M / h_M \right)} - F'_{ad} \right]$$

$$\times \frac{\Phi_K + F_K \mu_{rec} \left(S_M / h_M \right) + G_t F'_{ad}}{G_t + \mu_{rec} \left(S_M / h_M \right)} \tag{A.13}$$

A.2.3 Magnetization with Armature

If the magnet is placed in the external armature circuit and then magnetized by the armature field or magnetized in a magnetizer and then the poles of the magnetizer are in a continuous way replaced by the poles of the armature, the origin K of the recoil line is determined by the resultant magnetic permeance G_t drawn from the point $F'_{ad\max}$ at the F-coordinate. The MMF $F'_{ad\max}$ corresponds to the maximum demagnetizing d-axis field acting directly on the magnet which can appear during the machine operation. In Fig. A.4 this is the intersection point K of the demagnetization curve and the line G_t:

©2000 CRC Press LLC

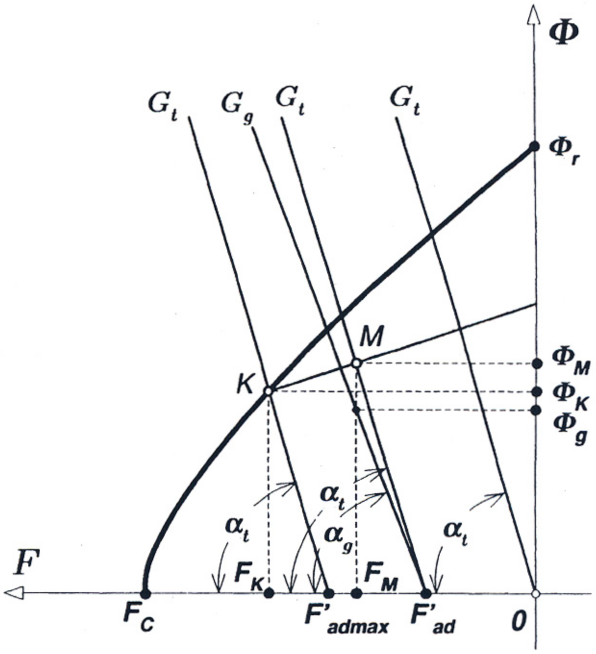

Figure A.4 Location of the operating point for the magnetization with the armature.

$$G_t = \frac{\Phi_K}{F_K - F'_{ad\max}} \tag{A.14}$$

The maximum armature demagnetizing MMF $F'_{ad\max}$ can be determined for the reversal or locked-rotor condition.

The beginning of the recoil line is determined by the resultant permeance G_t of the PM mounted in the armature (Fig. A.4).

The rest of the construction is similar to that shown in Fig. A.3 for the demagnetization action of the armature winding (point M). The beginning of the recoil line is determined by the resultant permeance G_t of the PM mounted in the armature (Fig. A.4).

If $a_0 > 0$ the MMF corresponding to the point K is [40]:

$$F_k = b_0 \pm \sqrt{b_0^2 - c_0} \tag{A.15}$$

where

$$b_0 = 0.5\left(\frac{F_c}{a_0} + F'_{ad\max} + \frac{\Phi_r}{a_0 G_t}\right) \quad \text{and} \quad c_0 = \frac{(G_t F'_{ad\max} + \Phi_r)F_c}{a_0 G_t}$$

If $a_0 = 0$ (for rare-earth PMs), the MMF F_K is [40]:

©2000 CRC Press LLC

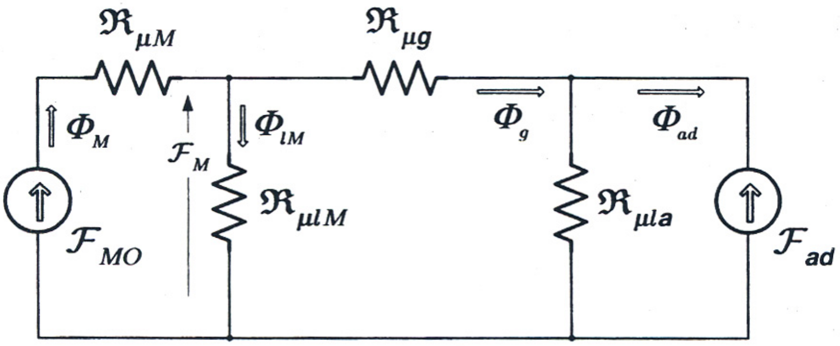

Figure A.5 Equivalent circuit (in the *d*-axis) of a PM system with armature

$$F_K = \frac{\Phi_r + G_t F'_{ad\,\max}}{G_t + \Phi_r / F_c} \qquad \text{(A.16)}$$

The magnetic flux Φ_K can be found on the basis of eqn (A.14).

The rest of the construction is similar to that shown in Fig. A.3 for the demagnetization action of the armature winding (point M).

A.2.4 Equivalent Magnetic Circuit

The *equivalent magnetic circuit of a PM system* with armature is shown in Fig. A.5 The reluctances of pole shoes (mild steel) and armature stack (electro technical laminated steel) are much smaller than those of the airgap and PM and have been neglected. The 'open circuit' MMF acting along the internal magnet permeance $G_M = 1/\Re_{\mu M}$ is $F_{M0} = H_{M0} h_M$, the d-axis armature reaction MMF is F_{ad}, the total magnetic flux of the permanent magnet is Φ_M, the leakage flux of the PM is Φ_{lM}, the useful airgap magnetic flux is Φ_g, the leakage flux of the external armature system is Φ_{la}, the flux produced by the armature is Φ_{ad} (demagnetizing or magnetizing), the reluctance for the PM leakage flux is $\Re_{\mu lM} = 1/G_{lM}$, the airgap reluctance is $\Re_{\mu g} = 1/G_g$, and the external armature leakage reactance is $\Re_{\mu la} = 1/G_{gla}$. The following Kirchhoff's equations can be written on the basis of the equivalent circuit shown in Fig. A.5

$$\Phi_M = \Phi_{lM} + \Phi_g$$

$$\Phi_{la} = \frac{\pm F_{ad}}{\Re_{\mu la}}$$

$$F_{M0} - \Phi_M \Re_{\mu M} - \Phi_{lM} \Re_{\mu lM} = 0$$

$$\Phi_{lM} \Re_{lM} - \Phi_g \Re_{\mu g} \mp F_{ad} = 0$$

The solution to the above equation system gives the airgap magnetic flux:

©2000 CRC Press LLC

$$\Phi_g = \left(F_{Mo} \mp F_{ad} \frac{G_g}{G_g + G_{lM}} \frac{\left(G_g + G_{LM}\right)\left(G_M + G_{lM}\right)}{G_g G_M} \right) \frac{G_g G_M}{G_g + G_{lM} + G_M}$$

or

$$\Phi_g = \left[F_{M0} \mp F_{ad}^{'} \frac{G_t \left(G_M + G_{lM}\right)}{G_g G_M} \right] \frac{G_g G_M}{G_t + G_M} \qquad \text{(A.17)}$$

where the total resultant permeance G_t for the flux of the PM is according to eqn (A.12) and the direct-axis armature MMF acting directly on the PM is

$$F_{ad}^{'} = F_{ad} \frac{G_g}{G_g + G_{lm}} = F_{ad} \left(1 + \frac{G_{lM}}{G_g} \right)^{-1} = \frac{F_{ad}}{\sigma_{lM}} \qquad \text{(A.18)}$$

The upper sign in eqn (A.17) is for the demagnetizing armature flux and the lower sign is for the magnetizing armature flux.

The coefficient of the PM leakage flux can also be expressed in terms of permeances, i.e.,

$$\sigma_{lM} = 1 + \frac{\Phi_{lM}}{\Phi_g} = 1 + \frac{G_{lM}}{G_g} \qquad \text{(A.19)}$$

©2000 CRC Press LLC

appendix B

Calculations of Permeances

B.1 Field Plotting

The procedure to be followed in *field plotting* is simple. On a diagram of the magnetic circuit, several equipotential lines are drawn. Flux lines connecting the surfaces of opposite polarity are then added in such a manner so as to fulfill the following requirements:

- all flux lines and equipotential lines must be mutually perpendicular at each point of intersection,
- each figure bonded by two adjacent flux lines and two adjacent equipotential lines must be a curvilinear square,
- the ratio of the average width to average height of each square should be equal to unity

When the full plot has been completed (Fig. B.1), the magnetic permeance can be found by dividing the number of curvilinear squares between any two adjacent equipotential lines, designated as n_e, by the number of curvilinear squares between any two adjacent flux lines, n_Φ and multiplying by the length l_M of the field perpendicular to the plane of the flux plot, i.e.,

$$G = \mu_0 \frac{n_e}{n_\Phi} l_M \tag{B.1}$$

Permeances of air gaps between poles of different configurations are expressed by the following formulae:

(a) Rectangular poles neglecting fringing flux paths (Fig. B.2a)

$$G = \mu_o \frac{w_M l_M}{g} \tag{B.2}$$

where $g/w_M < 0.1$ and $g/l_M < 0.1$

©2000 CRC Press LLC

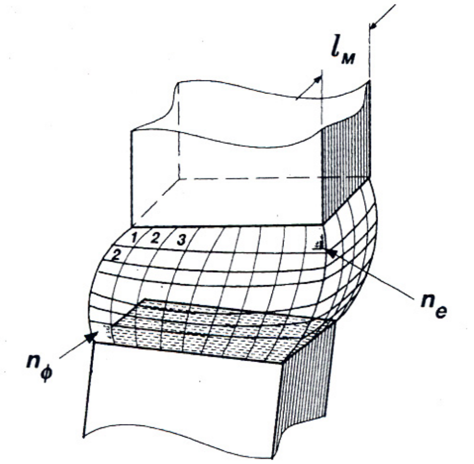

Figure B.1 Permeance evaluation by flux plotting.

(b) Half space and a rectangular pole (Fig. B.2b)

$$G = \mu_0 \frac{1}{g}\left(w_M + 0.614g/\pi\right)\left(l_M + 0.614g/\pi\right) \tag{B.3}$$

(c) Fringe paths originating on lateral flat surfaces (Fig. B.2c)

$$G = \mu_o \frac{w_M x}{0.17g + 0.4x} \tag{B.4}$$

or

$$G = \mu_o \frac{w_M}{\pi} \ln\left[1 + 2\sqrt{\frac{x + \left(x^2 + xg\right)}{g}}\right] \tag{B.5}$$

(d) Cylindrical poles neglecting fringing flux (Fig. B.2d)

$$G = \mu_o \frac{\pi d^2{}_M}{4g} \tag{B.6}$$

More accurate formula for $g/d_M < 0.2$ is

$$G = \mu_o d_M \left[\frac{\pi d_M}{4g} + \frac{0.36 d_M}{2.4 d_M + g} + 0.48\right] \tag{B.7}$$

For fringe paths originating on lateral cylindrical surfaces

$$G = \mu_o \frac{x d_M}{0.22g + 0.4x} \tag{B.8}$$

©2000 CRC Press LLC

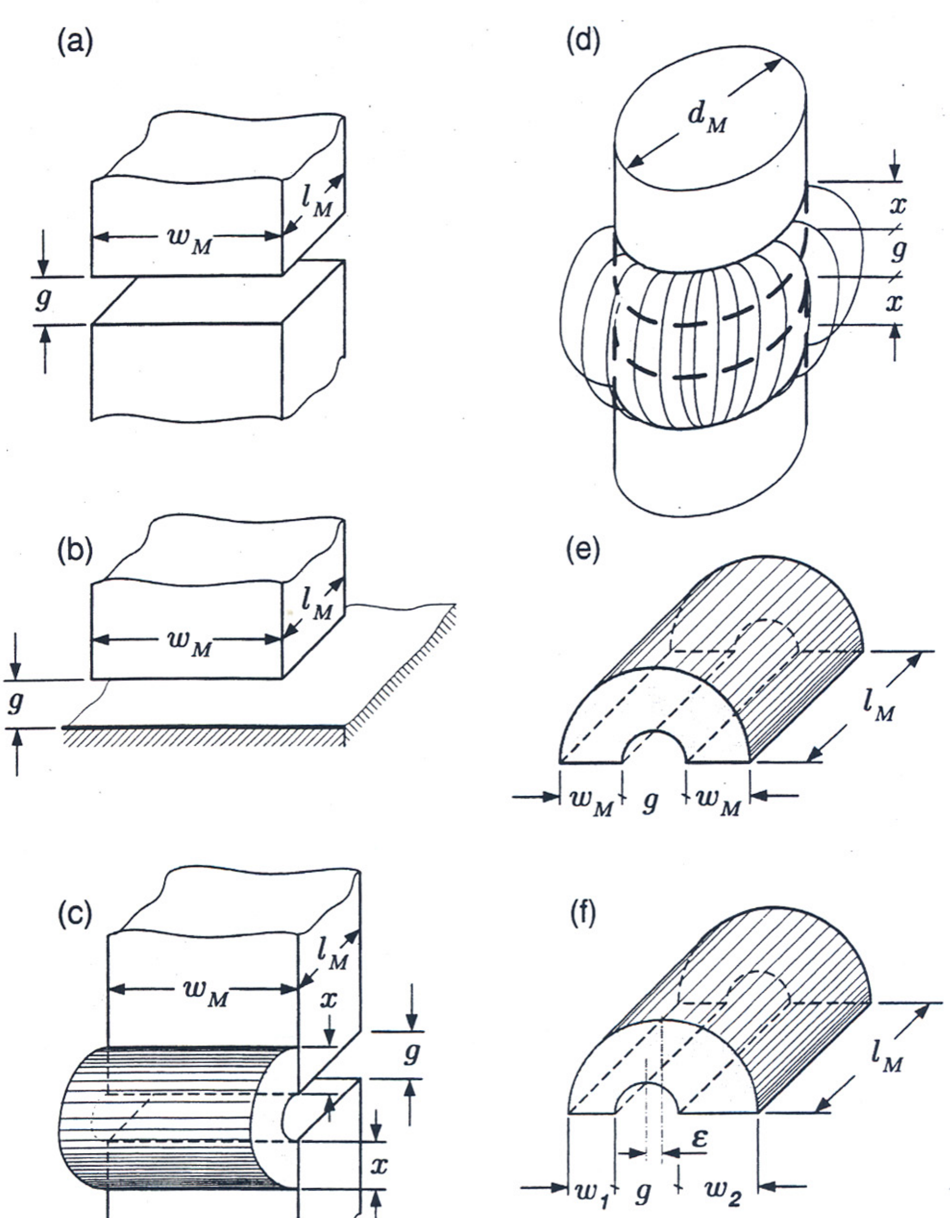

Figure B.2 Configurations of poles and air gaps between them: (a) rectangular poles, (b) half space and a rectangular pole, (c) fringe paths originating on lateral flat surfaces, (d) cylindrical poles, (e) indentical rectangles lying on the same surface, (f) two rectangles of different area lying in the same plane.

(e) Between indentical rectangles lying on the same surface (Fig. B.2e)

©2000 CRC Press LLC

$$G = \mu_o \frac{1}{2\pi} \ln\left[2m^2 - 1 + 2m\sqrt{m^2 - 1}\right] l_M \tag{B.9}$$

or

$$G = \mu_0 \frac{1}{\pi} \ln\left(1 + \frac{2w_M}{g}\right) l_M \tag{B.10}$$

(f) Between two rectangles of different area lying in the same plane (Fig. B.2f)

$$G = \mu_0 \frac{1}{\pi} \ln\left[\frac{\Delta^2 - (\varepsilon + x)^2}{\Delta(g - x)} - \frac{\varepsilon + x}{\Delta}\right] l_M \tag{B.11}$$

where

$$\varepsilon = \frac{w_2 - w_1}{2}\ , \qquad 2\Delta = w_1 + w_2 + g$$

and

$$x = \frac{1}{2\varepsilon}\left(\Delta^2 - (g/2)^2 - \varepsilon^2 - \sqrt{\Delta^2 - (g/2)^2 - \varepsilon^2 - \varepsilon^2 g^2}\right) \tag{B.12}$$

B.2 Dividing the Magnetic Field into Simple Solids

The permeances of simple solids shown in Fig. B.3 can be found using the following formulae:

(a) Rectangular prism (Fig. B.3a)

$$G = \mu_0 \frac{w_M l_M}{g} \tag{B.13}$$

(b) Cylinder (Fig. B.3b)

$$G = \mu_0 \frac{\pi d^2{}_M}{4g} \tag{B.14}$$

(c) Half-cylinder (Fig. B.3c)

$$G = 0.26\mu_0 l_M \tag{B.15}$$

where $g_{av} = 1.22g$ and $S_{av} = 0.322 g l_M$

©2000 CRC Press LLC

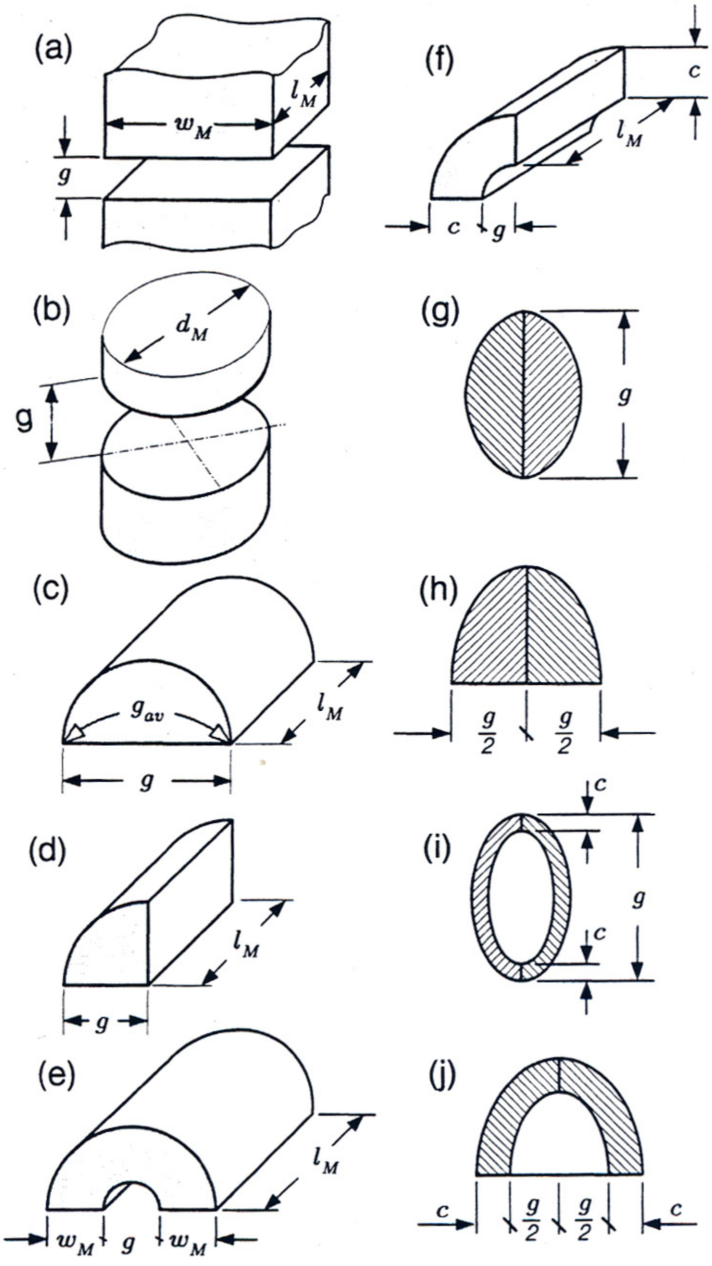

Figure B.3 Simple solids: (a) rectangular prism, (b) cylinder, (c) half-cylinder, (d) one-quarter of a cylinder, (e) half-ring, (f) one-quarter of a ring, (g) one-quarter of a sphere, (h) one-eighth of a sphere, (i) one-quarter of a shell, (j) one-eighth of a shell.

(d) One-quarter of a cylinder (Fig.B.3d)

$$G = 0.52\mu_0 l_M \tag{B.16}$$

(e) Half-ring (Fig. B.3e)

©2000 CRC Press LLC

$$G = \mu_0 \frac{2l_M}{\pi\left(g/w_M + 1\right)} \tag{B.17}$$

For $g < 3w_M$

$$G = \mu_0 \frac{l_M}{2\pi} \ln\left(1 + \frac{2w_M}{g}\right) \tag{B.18}$$

(f) One-quarter of a ring (Fig. B.3f)

$$G = \mu_0 \frac{2l_M}{\pi\left(g/c + 0.5\right)} \tag{B.19}$$

For g < 3c

$$G = \mu_0 \frac{2l_M}{\pi} \ln\left(1 + \frac{c}{g}\right) \tag{B.20}$$

(g) One-quarter of a sphere (Fig. B.3g)

$$G = 0.077\mu_0 g \tag{B.21}$$

(h) One-eighth of a sphere (Fig. B.3h)

$$G = 0.308\mu_0 g \tag{B.22}$$

(i) One-quarter of a shell (Fig. B.3i)

$$G = \mu_0 \frac{c}{4} \tag{B.23}$$

(j) One-eighth of a shell (Fig. B.3j)

$$G = \mu_0 \frac{c}{2} \tag{B.24}$$

©2000 CRC Press LLC

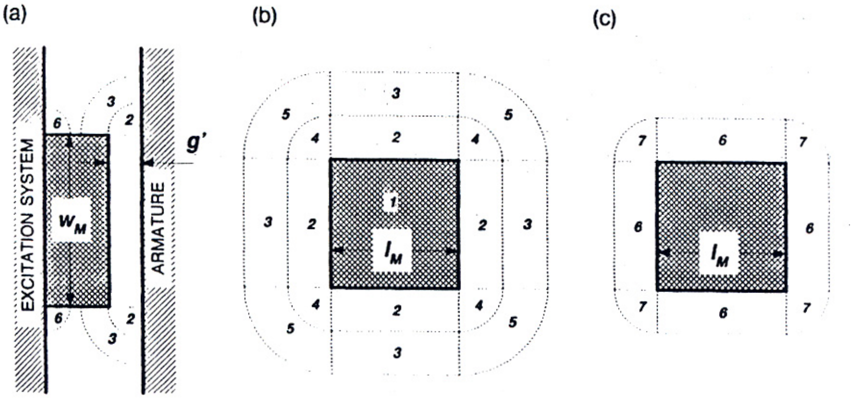

Figure B.4 Electric machine with flat slotless armature and flat PM excitation system - division of the space occupied by the magnetic field into simple solids: (a) longitudinal section, (b) airgap field, (c) leakage field (between the PM and steel yoke). The width of the PM w_M is equal to its length l_M.

Fig. B.4 shows a model of a flat electrical machine with smooth armature core (without slots) and salient-pole PM excitation system. The armature is in the form of a bar made of steel laminations. The PMs are fixed to the mild steel rail (yoke). It is assumed that the width of a PM is equal to its length, i.e., $w_M = l_M$.

The pole pitch is τ, the width of each PM is w_M, and its length is l_M. The space between the pole face and the armature core is divided into a prism (1), four quarters of a cylinder (2), four quarters of a ring (3), four pieces of 1/8 of a sphere (4), and four pieces of 1/8 of a shell (5). Formulae for the permeance calculations are found on the assumption that the permeance of a solid is equal to its average cross section area to the average length of the flux line. Neglecting the fringing flux, the permeance of a rectangular airgap per pole (prism 1 in Fig. B.4) is

$$G_{g1} = \mu_0 \frac{w_M l_M}{g'} \tag{B.25}$$

The equivalent airgap g' is only equal to the nonferromagnetic gap (mechanical clearance) g for a slotless and unsaturated armature. To take into account slots (if they exist) and magnetic saturation, the airgap g is increased to $g' = g\, k_C\, k_{sat}$, where $k_C > 1$ is Carter's coefficient taking into account slots, and $k_{sat} > 1$ is the saturation factor of the magnetic circuit defined as the ratio of the MMF per pole pair to the airgap magnetic voltage drop taken twice, i.e.,

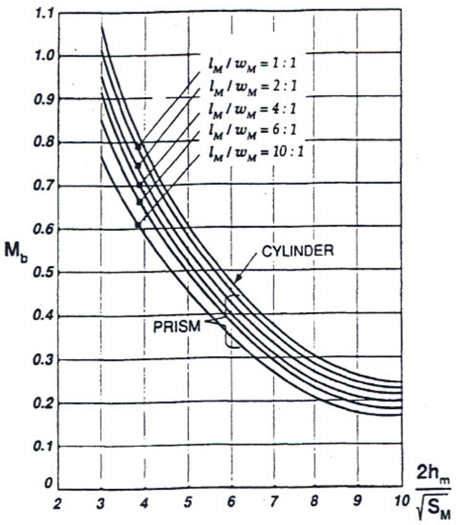

Figure B.5 Ballistic coefficient of demagnetization M_b for cylinders and prisms of different ratios of l_M / w_M (experimental curves).

$$k_{sat} = 1 + \frac{2\left(V_{1t} + V_{2t}\right) + V_{1y} + V_{2y}}{2V_g} \tag{B.26}$$

where V_g is the magnetic voltage drop (MVD) across the airgap, V_{1t} is the MVD along the armature teeth (if they exist), V_{2t} is the MVD along the PM pole shoe teeth (if there is a pole shoe and cage winding), V_{1y} is the MVD along the armature yoke, and V_{2y} is the MVD along the excitation system yoke.

To take into account the fringing flux it is necessary to include all paths for the magnetic flux coming from the excitation system through the airgap to the armature system (Fig. B.4), i.e.,

$$G_g = G_{g1} + 4\left(G_{g2} + G_{g3} + G_{g4} + G_{g5}\right) \tag{B.27}$$

where G_{g1} is the airgap permeance according to eqn (B.25) and G_{g2} to G_{g5} are the airgap permeances for fringing fluxes. The permeances G_{g2} to G_{g5} can be found using eqns (B.16), (B.19), (B.22) and (B.24).

In a similar way the resultant permeance for the leakage flux of the PM can be found, i.e.,

$$G_{lM} = 4\left(G_{l6} + G_{l7}\right) \tag{B.28}$$

where G_{l6} (one-quarter of a cylinder) and G_{l7} (one-eight of a sphere) are the permeances for leakage fluxes between the PM and rotor yoke according to Fig. B.4c - eqns (B.16) and (B.22).

©2000 CRC Press LLC

B.3 Prisms and Cylinders Located in an Open Space

In the case of simple shaped PMs, the permeance for leakage fluxes of a PM alone can be found as:

$$G_{ext} = \mu_0 \frac{2\pi}{M_b} \frac{S_M}{h_M} \tag{B.29}$$

where M_b is the ballistic coefficient of demagnetization. This coefficient can be estimated with the aid of graphs as shown in Fig. B.5 [13]. The cross section area is $S_M = \pi d_M^2/4$ for a cylindrical PM and $S_M = w_M l_M$ for a rectangular PM. In the case of hollow cylinders (rings), the coefficient M_b is practically the same as that for solid cylinders. For cylindrical PMs with small h_M and large cross sections $\pi d_M^2/4$ (button-shaped PMs), the leakage permeance can be calculated using the following equation [13]

$$G_{ext} \approx 0.716 \mu_0 \frac{d_M^2}{h_M} \tag{B.30}$$

Eqns (B.29) and (B.30) can be used for finding the origin K of the recoil line for PMs magnetized without an armature (Fig. A.3).

©2000 CRC Press LLC

Calculations for PM LSMs

The *Case Study* in Chapter 3 deals with the performance calculations for a LSM with surface PMs. Let us make similar calculation for the same armature system and equivalent reaction rail with buried configuration of PMs. The line *voltage-to-frequency* ratio should be V_{1L-L}/f = 10 ($V_{1L-L=200}$ V at 20 Hz) and calculations should be done for f = 20 Hz and f = 5 Hz.

All specifications are the same as for PM surface configuration except the airgap which in the d-axis is equal to that in the *q*-axis, i.e., g = g_q = 2.5 mm, depth of the reaction rail slot for the PM h_2 = 21 mm and width of the reaction rail slot for the PM b_2 = 8 mm. The axial length of the PM l_M = 84 mm and pole pitch τ = 56 mm

The height of a surface PM per pole is h_M = 4 mm and its width is w_M = 42 mm. The equivalent height of a buried PM is $2h_M$ and its width is 0.5 w_M (Fig. C.l). In both two cases the volume V_M of PM materials is the same, i.e.,

- for surface magnets

$$V_M = p\times 2h_M \times w_M \times l_M = 4\times(2\times 4.0)\times 42.0\times 84.0 = 112{,}896 \ \ \text{mm}^2$$

- for buried magnets

$$V_M = p\times 2h_M \times 2\frac{w_M}{2}\times l_M = 4\times(2\times 4.0)2\times\frac{42.0}{2}\times 84.0 = 112{,}896 \ \ \text{mm}^2$$

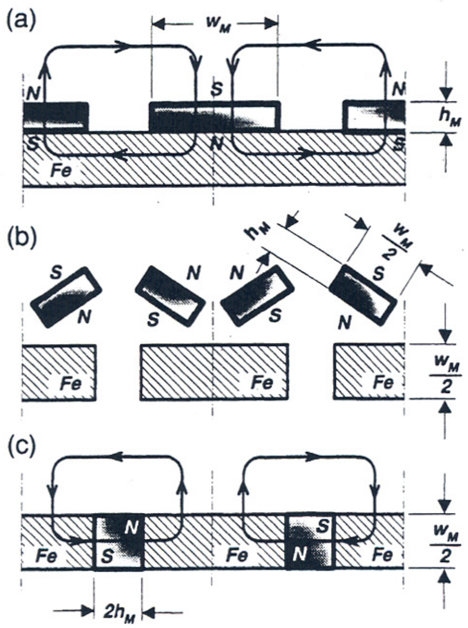

Figure C.1 Comparison between surface and buried magnets configurations: (a) reaction rail with surface PMs, (b) surface PMs are cut in half, (c) reaction rail with buried PMs of the same volume.

©2000 CRC Press LLC

The width of the reaction rail slot for a buried PM is $b_2 = 2h_M$ and its depth is $h_2 = 0.5\,w_M$ or $w_M = 2\,h_2$.

The width of the pole shoe of the reaction rail with buried PMs

$$b_p = \tau - 2h_M = 56.0 - 2\text{x}4.0 = 48 \text{ mm}$$

For f = 20 Hz the line-to-line voltage V_{1L-L} = 200 V and synchronous speed υ_s = 2.24 m/s. For f = 5 Hz the line-to-line voltage V_{1L-L} = 50 V and synchronous speed υ_s = 0.56 m/s.

Parameters independent of the frequency, voltage and load angle are as follows:

- number of slots per pole per phase q_1 = 1
- winding factor k_{w1} = 1.0
- *pole shoe-to-pole pitch* ratio α = 0.8571
- pole pitch in slots = 3
- coil pitch in slots = 3
- coil pitch in millimeters w_c = 56 mm
- armature slot pitch t_1 = 18.7 mm
- width of the armature slot b_{11} = b_{12} = 10.3 mm
- number of conductors in each slot N_{sl} = 280
- conductors area-to-slot area k_{sl} = 0.2252
- Carter's coefficient k_C = 1.46703
- form factor of the excitation field k_f = 1.2413
- form factor of the d-axis armature reaction k_{fd} = 0.9126
- form factor of the q-axis armature reaction k_{fq} = 0.7190
- reaction factor in the d-axis k_{ad} = 0.7352
- reaction factor in the q-axis k_{aq} = 0.5793
- coefficient of leakage flux σ_l = 1.2469
- permeance of the airgap G_g = $0.1633 \text{ X } 10^{-5}$ H
- permeance of the PM G_M = $0.1213 \text{ X } 10^{-5}$ H
- permeance for leakage fluxes G_{lM} = $0.4032 \text{ X } 10^{-6}$ H
- magnetic flux corresponding to remament magnetic flux density Φ_r = 0.3881×10^{-2} Wb
- relative recoil magnetic permeability μ_{rrec} = 1.094

©2000 CRC Press LLC

- PM edge line current density A_M = 800,000.00 A/m
- mass of the armature yoke m_{y1} = 5.56 kg
- mass of the armature teeth m_{t1} = 4.92 kg
- mass of the armature wires m_{Cu} = 15.55 kg
- friction force F_r = 1.542 N

Resistances and reactances independent of magnetic saturation are

- armature winding resistance R_1 = 2.5643 Ω at 75°C
- armature winding leakage reactance X_1 = 4.6532 at f = 20 Hz
- armature winding leakage reactance X_1 = 1.1633 at f = 5 Hz
- *d*-axis armature reaction reactance X_{ad} = 8.8093 at f = 20 Hz
- *d*-axis armature reaction reactance X_{ad} = 2.2090 at f = 5 Hz
- *q*-axis armature reaction reactance X_{aq} = 6.9411 at f = 20 Hz
- *q*-axis armature reaction reactance X_{aq} = 1.7353 at f = 5 Hz
- specific slot leakage permeance λ_{1s} = 1.3918
- specific leakage permeance of end connections λ_{1e} = 0.2192
- specific tooth-top leakage permeance λ_{t1} = 0.1786
- specific differential leakage permeance λ_{1d} = 0.4477
- coefficient of differential leakage τ_{d1} = 0.0965

The steady state performance characteristics (Table C.1) have been calculated as functions of the load angle δ and corresponding value of the angle Ψ between the phasor of the armature current I_a and the q-axis (or the phasor of the EMF E_f). Magnetic saturation due to the main flux and leakage fluxes has been included. The maximum efficiency corresponds to the angle Ψ ≈ 0 at which the current in the *d*-axis I_{ad} ≈ 0 (theoretically Ψ = 0° and I_{ad} = 0). A LSM should operate with maximum efficiency and its rated parameters are usually for Ψ ≈ 0. This gives a linear thrust F_x versus the armature current I_a.

Calculation results for Ψ ≈ 0° (approximately maximum efficiency) with magnetic saturation taken into account are given in Table C.2. The electric and magnetic loadings for Ψ ≈ 0 and I_{ad} ≈ 0 are rather low, i.e., A_{m1} = 41,460 A/m, J_1 = 2.411 A/mm^2, B_{mg} = 0.4833 T for 20 Hz and A_{m1} = 18,140 A/m, J_1 = 1.054, B_{mg} = 0.4832 T for 5 Hz. Those values are higher for $|\Psi| > 0°$ ($\delta > 0°$). Because the armature winding current density J_1 is low, the LSM can operate as a continuous duty motor. The airgap

©2000 CRC Press LLC

magnetic flux density B_{mg} is independent of the input frequency f, because for V_1/f = *const* the airgap magnetic flux Φ_g = *const*.

The thrust constant k_F is practically independent of the input frequency, i.e.,

- for 20 Hz

$$k_F = \frac{F_x}{I_a} = \frac{501.6}{3.91} = 128.29 \quad \text{N/A}$$

- for 5 Hz

$$k_F = \frac{F_x}{I_a} = \frac{218.5}{1.71} = 127.8 \quad \text{N/A}$$

©2000 CRC Press LLC

Table C.1 Steady state characteristics of a flat three phase four pole LSM with τ = 56 mm and buried PM configuration.

δ deg	Ψ deg	P_{out} W	F_x N	F_z N	I_a A	η –	$\cos\phi$ –
f = 20 Hz, V_{1L-L} =200 V , υ_s = 2.24m/s							
-20	34.01	-830.1	-371.6	1301	3.59	0.8796	0.5877
-10	58.63	-345.6	-159.7	1293	2.44	0.8921	0.3644
-5	77.98	-105.4	-54.6	1298	2.05	0.8219	0.1222
1	72.30	141.1	69.8	1320	1.88	0.7555	0.2873
5	52.31	320.4	151.5	1340	2.00	0.8581	0.5402
10	31.78	540.7	251.9	1373	2.36	0.8853	0.7457
15	16.73	756.1	350.2	1414	2.89	0.8873	0.8505
18	9.69	882.5	407.9	1443	3.26	0.8838	0.8854
20	5.62	965.5	445.7	1464	3.51	0.8804	0.9017
22	1.94	1047.0	483.1	1486	3.77	0.8763	0.9140
23	**0.21**	1088.0	501.6	1499	3.91	**0.8741**	0.9190
24	-1.42	1128.0	519.9	1511	4.05	0.8718	0.9234
25	-2.98	1168.0	538.1	1522	4.18	0.8694	0.9271
30	-10.01	1362.0	626.7	1592	4.89	0.8560	0.9397
35	-15.95	1546.0	710.9	1666	5.61	0.8411	0.9452
40	-21.17	1719.0	790.0	1750	6.36	0.8251	0.9465
45	-25.87	1880.0	863.4	1841	7.11	0.8081	0.9448
60	-38.02	2271.0	1043.0	2167	9.40	0.7523	0.9273
80	-51.63	2525.0	1161.0	2694	12.46	0.6650	0.8799
f = 5Hz, V_{1L-L} = 50 V , υ_s = 0.56 m/s							
-20	63.99	-82.8	-151.2	1254	2.76	0.3026	0.1046
-10	87.20	-3.6	-12.8	1313	1.85	0.1791	0.1254
-5	73.84	26.3	51.5	1352	1.52	0.5554	0.3609
1	42.91	65.9	123.8	1406	1.35	0.7832	0.7205
5	21.42	90.5	168.6	1447	1.43	0.8148	0.8956
6	16.52	96.4	179.4	1457	1.48	0.8164	0.9237
7	11.89	102.2	190.0	1468	1.53	0.8162	0.9461
8	7.54	107.9	200.3	1479	1.59	0.8146	0.9635
9	3.47	113.4	210.5	1490	1.65	0.8117	0.9764
9.8	**0.42**	117.8	218.5	1498	1.71	**0.8086**	0.9841
10	-0.33	118.9	220.5	1503	1.72	0.8077	0.9858
15	-15.70	144.5	267.3	1562	2.15	0.7768	0.9999
20	-26.67	167.1	308.6	1627	2.64	0.7347	0.9932
25	-34.98	186.4	343.8	1697	3.18	0.6873	0.9849
30	-41.64	202.1	372.7	1771	3.74	0.6376	0.9794
35	-47.24	214.1	394.6	1849	4.31	0.5870	0.9773
40	-52.12	222.0	409.3	1931	4.89	0.5364	0.9777
45	-56.51	225.8	416.3	2015	5.47	0.4862	0.9799
60	-67.79	210.2	388.6	2280	7.22	0.3393	0.9908
80	-80.48	123.6	231.8	2632	9.46	0.1509	0.9999

©2000 CRC Press LLC

Table C.2 Calculation results for minimum angle Ψ ($I_{ad} \approx 0$) with magnetic saturation taken into account.

Quantity	f = 20 Hz	f = 5 Hz
Load angle δ	23^0	9.8^0
Angle between the armature current I_a and q axis Ψ	0.21^0	0.42^0
Output power P_{out} ,W	1088	118
Output power-to-armature mass, W/kg	41.80	4.53
Input power P_{in} , W	1245	146
Electromagnetic thrust F_{dx} , N	503.1	220.1
Thrust F_x , N	501.6	218.5
Normal force F_z , N	1499	1498
Electromagnetic power P_g , W	1127	123
Efficiency η	0.8741	0.8086
Power factor $\cos\phi$	0.9190	0.9841
Armature current I_a , A	3.91	1.71
d-axis armature current I_{ad} , A	0.01	0.01
q-axis armature current I_{aq} , A	3.91	1.71
Armature line current density, peak value, A_{m1} , A/m	41,460	18,140
Current density in the armature winding J_1 , A/mm^2	2.411	1.054
Airgap magnetic flux density, maximum value B_{mg} , T	0.4833	0.4832
Per phase EMF excited by PMs E_f , V	96.07	24.02
Magnetic flux in the airgap Φ_g , Wb	0.1950×10^{-2}	0.1950×10^{-2}
Armature winding loss ΔP_{1w} , W	117.6	22.5
Armature core loss ΔP_{1fe} , W	13.88	2.19
Mechanical losses ΔP_m , W	3.45	0.86
Additional losses ΔP_{ad} , W	21.8	2.4
Armature leakage reactance X_1 , Ω	4.6103	1.1572
d-axis synchronous reactance X_{sd} , Ω	13.326	3.336
q-axis synchronous reactance X_{sq} , Ω	11.551	2.892
Magnetic flux density in the armature tooth, B_{1t} , T	1.1188	1.1185
Magnetic flux density in the armature yoke B_{1y} , T	0.6044	0.604
Saturation factor of the magnetic circuit k_{sat}	1.0107	1.0107

For $I_{ad} \approx 0$ the buried PM LSM has lower thrust and higher efficiency than its surface PM counterpart (Chapter 3, Table 3.3). It also draws less current from the power supply, so that the temperature rise of the stator winding will be lower. By increasing the input voltage to obtain similar electromagnetic loadings, the thrust can be close to that developed by the surface PM LSM.

©2000 CRC Press LLC

Symbols and Abbreviations

$\vec{A}$	magnetic vector potential
A	line current density
a	instantaneous value of the line current density; number of parallel current paths of the a.c. armature winding
$\vec{B}$	vector magnetic flux density
B	magnetic flux density
b	width of slot
b_p	pole shoe width
c	tooth width
c_E	armature constant, 1/m
c_F	thrust constant, N/ (VAs)
D	diameter
d	thickness; diameter
E	EMF, *rms* value
E_f	EMF per phase induced by the excitation system without armature reaction
E_i	internal EMF per phase
e	instantaneous EMF
F	force
F_x	thrust
f_r	thrust ripple
F	MMF
F_{exc}	MMF of the rotor excitation system
F_a	armature reaction MMF
G	permeance
g	airgap (mechanical clearance)
g'	equivalent airgap $g' = gk_C k_{sat}$
$\vec{H}$	vector magnetic field intensity
H	magnetic field intensity
h	height
h_M	height of the PM
I	current
I_a	armature current
i	instantaneous value of current or HLSM current
J	electric current density
J_a	current density in the armature winding
k	coefficient, general symbol

©2000 CRC Press LLC

k_{1R}	skin effect coefficient for armature resistance
k_{1X}	skin effect coefficient for armature leakage reactance
k_C	Carter's coefficient
k_{ad}	reaction factor in d-axis
k_{aq}	reaction factor in q-axis
k_{d1}	distribution factor
k_E	armature constant, Vs/m
k_F	thrust constant, N/A
k_{end}	end effect coefficient
k_f	form factor of the field excitation $k_f = B_{mg1} / B_{mg}$
k_F	thrust constant, N/A
k_i	stacking factor of laminations
k_{p1}	pitch factor
k_s	spring constant
k_{sat}	saturation factor of the magnetic circuit due to the main (linkage) magnetic flux
k_{w1}	winding factor $k_{w1} = k_{d1} k_{p1}$
L	inductance; length
L_i	armature stack effective length
l_{1e}	length of the one-sided end connection
l_M	axial length of PM
$\vec{M}$	magnetization vector
M_b	ballistic coefficient of demagnetization
m	number of phases; mass
N	number of turns per phase
P	active power
P_{elm}	electromagnetic power
ΔP	active power losses
$\Delta p_{1/50}$	specific core loss in W/kg at 1T and 50 Hz
p	number of pole pairs (number of poles is 2 p)
R	resistance
R_1	armature winding resistance of a.c. motors
$\Re$	reluctance
$\Re_{\mu M}$	permanent magnet reluctance
$\Re_{\mu g}$	airgap reluctance
$\Re_{\mu la}$	external armature leakage reluctance
r	radius
S	apparent power; surface
S_M	cross section area of PM $S_M = w_M L_M$ or $S_M = b_p L_M$

©2000 CRC Press LLC

s	cross section area; displacement
t	time; slot pitch
V	electric voltage; volume
υ	instantaneous value of electric voltage; linear velocity
W	energy, J
w	energy per volume, J /m^3
w_M	width of PM
X	reactance
X_1	armature leakage reactance
X_{ad}	d-axis armature reaction (mutual) reactance
X_{aq}	q-axis armature reaction (mutual) reactance
X_{sd}	d-axis synchronous reactance
X_{sq}	q-axis synchronous reactance
Z	impedance $Z = R + jX$; $\lvert Z \rvert = Z = \sqrt{R^2 + X^2}$
z_1	number of armature teeth or slots
α_i	effective pole arc coefficient $\alpha_i = b_p / \tau$
β	propagation constant ($\beta = \pi / \tau$)
χ	magnetic susceptibility
γ	form factor of demagnetization curve of PM material
δ	power (load) angle
η	efficiency
ϑ	temperature
λ	coefficient of leakage permeance (specific leakage permeance)
μ_0	magnetic permeability of free space $\mu_0 = 0.4\pi \times 10^{-6}$ H/m
μ_r	relative magnetic permeability
μ_{rec}	recoil magnetic permeability
μ_{rrec}	relative recoil permeability $\mu_{rrec} = \mu_{rec} / \mu_0$
ρ	specific mass density
σ	electric conductivity
τ	pole pitch
Φ	magnetic flux
Φ_f	excitation magnetic flux
Φ_l	leakage flux
ϕ	power factor angle
Ψ	flux linkage $\Psi = N\Phi$; angle between I_a and E_f
Ψ_{sd}	total flux linkage in d-axis
Ψ_{sq}	total flux linkage in q-axis
ω	angular frequency $\omega = 2\pi f$

ε force angle (angle between phasors of the excitation flux Φ_f in the d-axis and the armature current I_a)

©2000 CRC Press LLC

Subscripts

a	armature
av	average
c	counterweight; core
Cu	copper
d	direct axis; differential; developed
e	end connection; eddy-current
elm	electromagnetic
eq	equivalent
exc	excitation
ext	external
Fe	ferromagnetic
f	field
g	airgap
h	hysteresis
$hoist$	hoist
in	inner
l	leakage
M	magnet
m	peak value (amplitude)
n, t	normal and tangential components
out	output, outer
q	quadrature axis
r	rated; remanent
rec	recoil
rel	reluctance
s	synchronous; slot
sat	saturation
sh	shaft
st	starting
syn	synchronous or synchronizing
t	teeth
y	yoke
x, y, z	Cartesian coordinate system
1	armature; stator; fundamental harmonic
2	reaction rail

Abbreviations

A/D	analog-to-digital
AMG	active magnetic guidance
a.c.	alternating current
BCD	binary coded decimal
CAD	computer aided design
DSP	digital signal processor
d.c.	direct current
EMF	electromotive force
EMI	electromagnetic interference
FEM	finite element method
HLSM	hybrid linear stepping motor
HTS	high temperature superconductor

©2000 CRC Press LLC

IC	integrated circuit
IPT	inductive power transfer
LBM	linear brushless motor
LCX	leaky coaxial cable
LED	light-emitting diode
LIM	linear induction motor
LSM	linear synchronous motor
LTS	low temperature superconductor
LVDT	linear variable differential transformer
MMF	magnetomotive force
MR	magneto-resistive
MVD	magnetic voltage drop
NBC	natural binary code
PLC	programmable logic controller
PM	permanent magnet
PWM	pulse width modulation
RFI	radio frequency interference
RNA	reluctance network approach
TTL	transistor-transistor logic
VVVF	variable voltage variable frequency

©2000 CRC Press LLC

References

[1] *Accucore Components,* information brochure, Magnetic International Inc., Burns Harbor, IN, U.S.A., 1997, www.inland.com/mii

[2] Afonin, A., *The Application of Metal Powder Technology for Linear Motors,* 1st Int. Symp. on Linear Drives for Industry Applications LDIA '95, Nagasaki, Japan, 1995, pp. 271-274.

[3] Afonin, A., Szymczak, P. and Bobako, S., *Linear Drives with Controlled Current Layer,* 1st Int. Symp. on Linear Drives for Industry Applications LDIA '95, Nagasaki, Japan, 1995, pp. 275-278.

[4] Adamiak, K., Barlow, D., Choudhury, C.P., Cusack, P.M., Dawson, G.E., Eastham, A.R., Grady, B., Ho, E., Yuan Hongpin, Pattison, L. and Welch, J., *The Switched Reluctance Motor as a Low Speed Linear Drive,* Int. Conf. on Maglev and Linear Drives, Las Vegas, U.S.A., 1987, pp. 39-43.

[5] Akmese, R. and Eastham, J.F., *Design of Permanent Magnet Flat Linear Motors for Standstill Applications,* IEEE Trans. on Magnetics, vol. 28, 1992, No.5, pp. 3042-3044.

[6] Albicini, F., Andriollo, M., Martinelli, G. and Morini, A., *General Expressions of Propulsion Force in EDS-Maglev Transport Systems with Superconducting Coils,* IEEE Trans. on Applied Superconductivity, vol. 3, 1993, No.1, pp 425-29.

[7] Amber, G.H. and Amber, P.S., *Anatomy of Automation*, Prentice Hall, Englewood Cliffs, NJ, 1962.

[8] *Anorad Linear Motors* information brochure), Anorad, Hauppauge, NY, U.S.A. 1998, www.anorad.com

[9] Atherton, D.L. et al, Design, Analysis and Test Results for a Superconducting Linear Synchronous Motor, Proc. IEE, vol. 124, No.4, 1977, pp. 363-372.

[10] Atzpodien, H.C., *Magnetic Levitation System on Route from Berlin to Hamburg - Planning, Financing, State of Project,* 14th Int. Conf. on Magnetically Levitated Systems Maglev '95, Bremen, Germany, 1995, pp. 25-29.

[11] Ayoma, H., Araki, H., Yoshida, T., Mukai, R. and Takedoni, S., *Linear Motor System for High Speed and High Accuracy Position Seek,* 1st Int. Symp. on Linear Drives for Industry Applications LDIA'95, Nagasaki, Japan, 1995, pp. 461-464.

[12] Azukizawa, T., *Optimum Linear Synchronous Motor Design for High Speed Ground Transportation,* IEEE Trans. on PAS, vol. 102, 1983, No. 10, pp. 3306-3314.

[13] Balagurov, V.A., Galtieev, F.F. and Larionov, A.N., *Permanent Magnet Electrical Machines* (in Russian), Energia, Moscow, 1964.

[14] Beakley, B., *Linear Motors for Precision Positioning,* Motion Control, October 1991.

[15] *Magnetic Sensors,* BEl Sensors & System Company, Goleta, CA, U.S.A., 1998.

[16] Blaugher, R.D., *Low-Calorie, High-Energy Generators and Motors,* IEEE Spectrum, vol. 34, 1997, No.7, pp. 36-42.

[17] Bocarov, V.I. and Nagorsky, V.D., *High-Speed Ground Transport with Linear Propulsion and Magnetic Suspension System* (in Russian), Transport, Moscow, 1985.

[18] What *Every Engineer Should Know About Finite Element Analysis,* edited by J.R. Brauer, Marcel Dekker Inc., New York, 1988.

[19] Breil, J., Oedl, G. and Sieber, B., *Synchronous Linear Drives for many Secondaries with Open Loop Control,* 2nd Int. Symp. on Linear Drives for Ind. Appl. LDIA '98, Tokyo, Japan, 1998, pp. 142-146.

[20] Chai, H.D., *Permeance Model and Reluctance Force between Toothed Structures,* in *Theory and Applications of Step Motors.* edited by Kuo B.C., West Publishing, 1974, pp.141-153.

[21] *Compumotor Digiplan: Positioning Control Systems and Drives,* Parker Hannifin Corporation, Rohnert Park, CA, U.S.A., 1996.

©2000 CRC Press LLC

[22] Cruise, R.J. and Landy, C.F., *Design Considerations of Linear Motor Hoists for Underground Mining Operations*, 7th South African Universities Power Engineering Conf. SAUPEC'98, Stellenbosch, RSA, 1998, pp. 65-68.

[23] Cruise, R.J. and Landy, C.F., *Linear Synchronous Motor Propelled Hoist for Mining Applications*, The 31st IEEE Ind. Appl. Conf., San Diego, CA, 1996.

[24] *Concise Encyclopedia of Traffic and Transportation Systems,* edited by M. Papageorgiu, Pergamon Press, 1991, pp. 36-49.

[25] Coulomb, J. and Meunier, G., *Finite Element Implementation of Virtual Work Principle for Magnetic and Electric Force and Torque Computation*, IEEE Trans. on Magnetics, vol. 20, No.5, 1984, pp.1894-1896.

[26] DeGarmo, E.P., Black, J.T. and Kohser, R.A., *Materials and Processes in Manufacturing, Macmillan,* New York - London, 1988.

[27] Deng, Z., Boldea, I. and Nasar, S.A., *Forces and Parameters of Permanent Magnet Linear Synchronous Machines,* IEEE Trans. on Magn., vol. MAG-23, No. 1, 1987, pp. 305-309.

[28] Ishii, T., *Elevators for Skyscrapers,* IEEE Spectrum, No.9, 1994, pp. 42-46.

[29] Eidelberg, B., *Linear Motors Drive Advances in lndsutrial Laser Applications,* Industrial Laser Review, 1995, No.1, pp. 15-18.

[30] Eidelberg, B., *Simulation of Linear Motor Machines,* 2nd Int. Symp. on Linear Drives for Ind. Appl. LDIA '98, Tokyo, Japan, 1998, pp. 30-33.

[31] Ellerthorpe and J. Blaney, J., *Force Estimation for Linear Step Motor with Variable Airgap,* 25th Annual Symposium on Incremental Motion Control Systems and Devices, San Jose, CA, U.S.A., 1996, pp. 327-335.

[32] Everes, W., Henneberger, G., Wunderlich, H. and Selig, A., *A Linear Homopolar Motor for a Transportation System*, 2nd Int. Symp. on Linear Drives for Ind. Appl. LDIA '98, Tokyo, Japan, 1998, pp. 46-49.

[33] Ficheux R. and Pavoz M., *Self-Powered Elevator Using a Linear Electric Motors as Counterweight*, U.S. Patent 4, 402, 386, 1983.

[34] Fitzgerald, A.E. and Kingsley, C., *Electric Machinery,* McGraw-Hill Book Company, New York, 1990.

[35] Gagnon E., Jamminet J. and Olsen E., *Elevator Driven by a Flat Linear Motor,* U.S. Patent 5, 086, 881, 1991.

[36] Gieras, J.F., *Electrodynamic Forces in Electromagnetic Levitation systems,* Acta Technica CSAV, 1982, No.5, pp. 532-535.

[37] Gieras, J.F. and Miszewski, .M., *Performance Characteristics of the Air-Core Linear Synchronous Motor* (in Polish), Rozprawy Elektrot. PAN, Warszawa, Poland, vol. 29, 1983, No.4, pp. 1101-1124.

[38] Gieras, J.F., *Linear Induction Drives*, Clarendon Press, Oxford, U.K., 1994.

[39] Gieras, J.F., Spannenberg, A., Wing, M. and Yamada, H., *Analysis of a Linear Synchronous Motor with Buried Permanent Magnets,* 1st Int. Symp. on Linear Drives for Industry Applications LDIA '95, Nagasaki, Japan, 1995, pp. 323-326.

[40] Gieras, J.F. and Wing, M., *Permanent Magnet Motors Technology: Design and Applications,* Marcel Dekker, Inc., New York, U.S.A., 1996.

[41] Gieras, J.F. and Wang, R., *Calculation of Forces in a Hybrid Linear Stepping Motor for Machine Tools,* 7th European Conf. on Power Electronics and Applications EPE'97, Trondheim, Norway, 1997, vol. 3, pp. 591-595.

[42] Gieras, J.F., Santini, E. and Wing. M. *Calculation of Synchronous Reactances of Small Permanent-Magnet Alternating-Current Motors: Comparison of Analytical Approach and Finite Element Method with Measurements*, IEEE Trans. on Magnetics, vol. 34, 1998, No.5, pp. 3712-3720.

[43] Guderjahn, C.A., Wipf, S.I., Fink, H.J., Boom, R.W., MacKenzie, K.E., Williams, D. and Downey, T., *Magnetic Suspension and Guidance for High Speed Rockets by Superconducting Magnets,* Journal of Appl. Physics, vol. 40 (1998), No. 5, pp. 3519-3521.

[44] Hakala, H., *Application of Linear Motors in Elevator Hoisting Machines*, Thesis for the Doctor Degree, Publication No. 157, Tampere University of Technology, Finland, 1995.

[45] Halbach, K., *Design of Permanent Multipole Magnets with Oriented Rare Earth Cobalt Material,* Nuclear Instruments and Methods, vol. 169, 1980, pp. 1-10.

©2000 CRC Press LLC

[46] Hamler, A., Trlep, M. and Hribernik, B., *Optimal Secondary Segment Shapes of Linear Reluctance Motors Using Stochastic Searching,* IEEE Trans. on Magn., vol. 34 (1998), No.5, pp. 3519-3521.

[47] Hannakam, L., *Wirbelströme in dünnen leitenden Platten infolge bewegter stromdurchflossener Leiter*, etz-a, vol. 86, 1965, No. 13, pp.427-431.

[48] Hashimoto, M., Kitano, J., Inden, K., Tanitsu, H., Kawaguchi, I., Kaga, S., Nakashima, T., Koike, S., Migiya, Y. and Sogihara, H., *Driving Control Characteristic Using the Inverter System at Yamanashi Maglev Test Line,* 15th Int. Conf. on Magnetically Levitated Systems and Linear Drives Maglev'98, Mt. Fuji, Yamanashi, Japan, 1998, pp. 287-291.

[49] *Heidenhein General Catalogue: Linear Encoders,* Heidenhain, GmbH, Traunreut, Germany, 1998, http://www.heidenhain.com

[50] Heller, B. and Hamata, V., *Harmonic Field Effects in Induction Motors,* Academia, Prague, 1977.

[51] Henneberger, G. and Reuber, C., *A Linear Synchronous Motor for a Clean Room Conveyance System*, 1st Int. Symp. on Linear Drives for Industry Applications LDIA '95, Nagasaki, Japan, 1995, pp. 227-230.

[52] Hinds, W. and Nocito, B., *The Sawyer Linear Motor, Theory and Applications of Step Motors* edited by Kuo, B.C., 1974, pp. 327-340.

[53] Hippner, M. and Piech, Z., *Ripple Free Linear Synchronous Motor,* Int. Conf. on Electr. Machines ICEM'98, Istanbul, Turkey, 1998, pp. 845-850.

[54] Hor, P.J., Zhu, Z.Q., Churn, P.M., Howe, D. and Rees-Jones, J., *Design and Analysis of a Novel Long-Stroke Tubular Permanent Magnet Linear Motor,* 2nd Int. Symp. on Linear Drives for Ind. Appl. LDIA'98, Tokyo, Japan, 1998, pp. 34-37.

[55] Howe, D. and Zhu, Z.Q., *Status of Linear Permanent Magnet and Reluctance Motor Drives in Europe,* 2nd Int. Symp. on Linear Drives for Ind. Appl. LDIA '98, Tokyo, Japan, 1998, pp. 1-8.

[56] Huth, E., Canders, W.R. and Mosebach, H., *Linear Motor Transfer Technology (LMTT) for Container Terminals*, 2nd Int. Symp. On Linear Drives for Ind. Appl. LDIA '98, Tokyo, Japan, 1998, pp. 38-41.

[57] Ishii, T., *Elevators for Skyscrapers,* IEEE Spectrum, No.9, 1994, pp. 42-46.

[58] Jahns, T.M., Kliman, G.B. and Neumann, T.W., *Interior PM Synchronous Motors for Adjustable-Speed Drives,* IEEE Trans. on Industry Applications, vol. 22, 1986, No.4, pp. 738-747.

[59] Jahns, T.M., *Motion Control with Permanent-Magnet a.c. Machines*, Proc. IEEE, vol. 82, 1994, No.8, pp. 1241-1252.

[60] Jahns, T.M. *Variable Frequency Permanent Magnet a.c. Machine Drives, in Power Electronics and Variable Frequency Drives,* edited by B.K. Bose, IEEE Press, New York, 1997.

[61] Kajioka, M., Torii, S. and Ebihara, D., *A Comparison of Linear Motor Performance Supported by Air bearings,* 2nd Int. Symposium on Linear Drives for Industry Applications, LDIA '98, Tokyo, Japan, 1998, pp.252-255.

[62] Kakino, Y., *Tools for High Speed and High Acceleration Feed Drive System of NC Machine Tools* 2nd Int. Symposium on Linear Drives for Industry Applications, LDIA '98, Tokyo, Japan, 1998, pp. 15-21.

[63] Karita, M., Nakagawa, H. and Maeda, M., *High Thrust Density Linear Motor and its Applications, 1st Int. Symp. on Linear Drives for Industry Applications LDIA '95*, Nagasaki, Japan, 1995, pp. 183-186.

[64] Kawanishi, T., *Linear Motor Application for Architecture,* 1st Int. Symposium on Linear Drives for Industry Applications, LDIA '95, Nagasaki, Japan, 1995, pp. 239-242.

[65] Khan, S.A. and Ivanov, A.A., *Methods of Calculation of Magnetic Fields and Static Characteristics of Linear Step Motor For Control Rod Drives of Nuclear Reactors*, IEEE Trans. on Magnetics, vol.28, No.5, 1992, pp. 2277-2279.

[66] Khan, S.H. and Ivanov, A.A., *An Analytical Method for the Calculation of Static Characteristics of Linear Step Motor For Control Rod Drives in Nuclear Reactors,* IEEE Trans. on Magnetics, vol.31, No.3, 1995, pp.2324-2330.

[67] King, R., *Precision Laser Scribes Aircraft Skins,* Design News, 1994, No. 5-9, pp. 66-67.

©2000 CRC Press LLC

[68] Kitamori, T., Inoue, A., Yoshimura, M., Matsudaira, Y. and Hosaka, S., *Outline of the Second Train Set for the Yamanashi Maglev Test Line*, 15th Int. Conf. on Magnetically Levitated Systems and Linear Drives Maglev'98, Mt Fuji, Yamanashi, Japan, 1988, pp. 220-224

[69] *Kollmorgen Linear Motors Aim to Cut Cost of Semiconductors and Electronics Manufacture*, Kollmorgen, Radford, VA, U.S.A., 1997.

[70] Kostenko, M. and Piotrovsky, L., *Electrical Machines, Vol. 2: Alternating Current Machines*, Mir Publishers, Moscow, 1974.

[71] Kudermann, K., *Eletrischer Antrieb fur Lastenforderer,* Deutsches Patentamt Offenlegungsschrift, 1970.

[72] Kurobe, H., Kaminishi, K., Miyamoto, S. and Seki, A., *Current Test Status of the Superconducting Maglev System on the Yamanashi Test Line*, 15th Int. Conf. on Magnetically Levitated Systems and Linear Drives Maglev'98, Mt. Fuji, Yamanashi, Japan, 1998, pp. 56-61.

[73] Kwon, B.I., Woo, K.I., Rhyu, S.H. and Park, S.C., *Analysis of Direct Thrust Control in Permanent Magnet Type Linear Synchronous Motor by FEM*, 2nd Int. Symposium on Linear Drives for Industry Applications, LDlA'98, Tokyo, Japan, 1998, pp.404-407.

[74] Kyutoku, S., Shinya, T., *Development of Linear Synchronous Motor for Air Suspension Table,* 1st Int. Symp. on Linear Drives for Industry Applications LDIA '95, Nagasaki, Japan, 1995, pp. 223-226.

[75] Linear Motor Conveyance System for Hospitals, Shinko Electric Co. Ltd., Tokyo, Japan, 1999, www.shinko-elec.co.jp

[76] *Linear-Motor-Driven Vertical Transportation System,* Elevator Word, September, 1996, pp. 66-72, www.elevator-world.com

[77] *Linear Synchronous Motors,* MagneMotion, 1999, www.magnemotion.com/linear.html

[78] *Linear Step Motor* (information brochure), Tokyo Aircraft Instrument Co., Ltd., Tokyo, 1998.

[79] *LinMot Design Manual,* Sulzer Electronics, Ltd, Zürich, Switzerland, 1999.

[80] Laugis, J. and Lehtla, T, *Control of Special Purpose Linear Drives,* 7th European Conf. on Power Electronics and Applications EPE'97, Trondheim, Norway, vol. 3, pp. 541-546.

[81] Lingaya, S. and Parsch, C.P., *Characteristics of the Force Components on an Air-Core Linear Synchronous Motor with Superconducting Excitation Magnets,* Electric Machines and Electromechanics, Hemisphere Publishing Corp., No.4, 1979, pp. 113-123.

[82] Locci, N. and Marongiu, I., *Modelling and Testing a New Linear Reluctance Motor,* Int. Conf. on Electr. Machines ICEM'92, vol.2, Manchester, U.K., pp. 706-710.

[83] Luukko, J., Kaukonen, J., Niemelää, M., Pyrhönen, O., Tiitinen, P. and Väänänen, J., *Permanent Magnet Synchronous Motor Drive Based on Direct Flux Linkage Control,* 7th European Conf. on Power Electronics and Applications EPE'97, Trondheim, Norway, 1997, vol. 3, pp. 683-688.

[84] Mangan, J. and Warner, A., *Magnet Wire Bonding,* Joyal Product, Inc., Linden, NJ, U.S.A., 1998, www.joyalusa.com

[85] Marshall, S.V., Skitek, G.G., *Electromagnetic Concepts and Applications,* Prentice-Hall, Englewood Cliffs, NJ, 1987.

[86] Masada, E., *Linear Drives for Industry Applications in Japan -History, Existing State and Future Prospects,* 1st Int. Symp. on Linear Drives for Industry Applications LDIA '95, Nagasaki, Japan, 1995, pp. 9-12.

[87] Masada, E., *Development of Maglev and Linear Drive Technology for Transportation in Japan,* 14th Int. Conf. on Magnetically Levitated Systems Maglev'95, Bremen, Germany, 1995, pp. 11-16.

[88] Masada, E *High Power Converters and their Future Applications,* 7th Int. Power Electronics and Motion Control Conference PEMC'96, Budapest, Hungary, vol. 3, 1996, pp. K1-K4.

[89] Matsui, N, Nakamura. M. and Kosaka, T., *Instantaneous Torque Analysis of Hybrid Stepping Motors,* IEEE Trans. on IA, vol.32, No.5, 1996, pp.1176-1182.

[90] Matsuoka, K. and Kondou, K., *Development of Permanent Magnet Linear Motor for the Next Generation High Speed Railways,* Symp. on Power Electronics, Electr. Drives, Adv. Electr. Machines SPEEDAM'94, Taormina, Italy, 1994, pp. 237-242.

[91] Menden, W., Mayer, W.J. and Rogg, D., *State of Development and Future Prospects on the Maglev System Transrapid, M-Bahn and Starlim,* Int. Conf. Maglev'89, Yokohama, Japan, 1989, pp. 11-18.

[92] *Metglas Amorphous Magnetic Alloys,* information brochure, AlliedSignal Inc., Morristown, NJ, U.S.A., 1999, www6.alliedsignal.com/metglas/magnetic/

©2000 CRC Press LLC

[93] Miller, L., *Superspeed Maglev System Transrapid: System Description*, 14th Int. Conf. on Magnetically Levitated Systems Maglev'95, Bremen, Germany, 1995, pp. 37-43.

[94] Miller, L. and Löser, F., *System Characteristics of the Transrapid Superspeed Maglev System*, 15th Int. Conf. on Magnetically Levitated Systems and Linear Drives Maglev'98, Mt. Fuji, Yamanashi, Japan, 1998, pp. 19-24.

[95] Mishler, W.R., *Test Results on a Low Loss Amorphous Iron Induction Motor*, IEEE Trans. on PAS, vol. 100, 1981, No.6, pp.860-866.

[96] Miyatake, M., Koseki, T. and Sone, S., *Design and Traffic Control of Multiple Cars for an Elevator System Driven by Linear Synchronous Motors*, 2nd Int. Symp. on Linear Drives for Ind. Appl. LDIA '98, Tokyo, Japan, 1998, pp. 94-97.

[97] Mizuno, T. and Yamada, H., *Magnetic Circuit Analysis of a Linear Synchronous Motor with Permanent Magnets*, IEEE Trans. On Magn., vol. 28, No.5, 1992, pp. 3027-3029.

[98] Mosebach, H., *Direct Two-Dimensional Analytical Thrust Calculation of Permanent Magnet Excited Linear Synchronous Machines*, 2nd Int. Symp. on Linear Drives for Ind. Applications LDIA '98, Tokyo, Japan, 1998, pp. 396-399.

[99] Mosebach, H. and Canders, W.R., *Average Thrust of Permanent Magnet Excited by Linear Synchronous Motors for Different Stator Current Waveforms*, Int. Conf. on Electr. Machines ICEM'98, Istanbul, Turkey, 1998, vol. 2, pp. 851-865.

[100] Muraguchi, Y., Karita, M., Nakagawa, H., Shinya, T. and Maeda, *M., Method of Measuring Dynamic Characteristic for Linear Servo Motor and Comparison of their Performance*, 2nd Int. Symp. On Linear Drives for Ind. Appl. LDIA '98, Tokyo, Japan, 1998, pp. 204-207.

[101] Nai K., Forsythe W., Goodall R.M., *Improving ride quality in high speed elevators*, Elevator World, 1997, No 6, pp.80-93.

[102] Nakao, H., Takahashi, M., Sanada, Y., Yamashita, T., Yamaji, M., Miura, A., Terai, M., Igarashi, M., Kurihara, T. and Tomioka, K., *Development of the New Type On-board GM Refrigeration System for the Superconducting Magnet in Maglev Use*, 15th Int. Conf. on Magnetically Levitated Systems and Linear Drives Maglev'98, Mt. Fuji, Yamanashi, Japan, 1998, pp. 250-255.

[103] Nakashima, H. and Seki, A., *The Status of the Technical Development for the Yamanashi Maglev Test Line*, 14th Int. Conf. on Magnetically Levitated Systems MAGLEV'95, Bremen, Germany, 1995, pp. 31-35.

[104] Nakashima, H. and Isoura, K., *Superconducting Maglev Development in Japan*, 15th Int. Conf. on Magnetically Levitated Systems and Linear Drives Maglev'98, Mt. Fuji, Yamanashi, Japan, 1998, pp. 25-28

[105] *Northern Magnetics Linear Motors Technology*, Normag (Baldor Electric Company), Santa Clarita, CA, U.S.A., 1998.

[106] Osada, Y., Gotou, H., Sawada, K. and Okumura, F., *Outline of Yamanashi Maglev Test Line and Test Schedule*, 15th Int. Conf. on Magnetically Levitated Systems and Linear Drives Maglev'98, Mt. Fuji, Yamanashi, Japan, 1998, pp. 50-55.

[107] Otis, G. E., *Improvement in Hoisting Apparatus*, US Patent 1, 128, 1861.

[108] Parker, R.J., *Advances in Permanent Magnetism*, John Wiley & Sons, 1990.

[109] *Platinum^{TL} DDL Direct Drive Linear Motors*, Kollmorgen, Radford, VA, U.S.A., 1998, www.kollmorgen.com

[110] Preston, M. and King, R., *Noise-Cancelating Quadrature Magnetic Position, Speed and Direct Sensor*, U.S. Patent 5, 486, 844, 1996.

[111] Rajagopal, K., Krishnaswamy. M, Singh, B. and Singh, B.P., *High Thrust Density Linear Motor and its Applications*, LDIA '95, Nagasaki, Japan, 1995, pp. 183-186.

[112] Raschbichler, H.G. and Miller, L., *Readiness for Application of the Transrapid Maglev System*, RTR Railway Technical Review, vol. 33, 1991/92, pp. 3-7.

[113] *RG2 Linear Encoder System*, Renishaw plc, New Mills, Gloucestershire, U.K., 1998, www.renishaw.com

[114] Rees, J.J., *Dynamic Consideration and Candidacy Requirements for Linear Servo-Driven Motors in Factory Automation*, 1st Int. Symp. on Linear Drives for Industry Applications LDIA '95, Nagasaki, Japan, 1995, pp. 255-258.

[115] Rosenmayr, M., Casat, Glavitsch, A. and Stemmler, H., *Swissmetro - Power Supply for a High-Power-Propulsion System with Short Stator Linear Motors*, 15th Int. Conf. on Magnetically Levitated Systems and Linear Drives Maglev'98, Mount Fuji, Yamanashi, Japan, 1998, pp. 280-286.

©2000 CRC Press LLC

[116] Sanada, M., Morimoto, S. and Takeda, Y., *Interior PermanentcMagnet Linear Synchronous Motor for High-Performance Drives,* IEEE Trans. on IA, vol. 33, No.4, 1997, pp. 966-972.

[117] Sanada, M., Morimoto, S. and Takeda, Y., *Reluctance Equalization Design of Multi Flux Barrier Construction for Linear Synchronous Reluctance Motors,* 2nd Int. Symp. on Linear Drives for Ind. Appl.LDlA'98, Tokyo, Japan, 1998, pp. 259-262.

[118] Seki, K., Watada, Torii, S. and Ebihara, D., *Experimental Device of Long Stator LSM with Discontinuous Arrangement and Result,* 7th European Conf. on Power Electronics and Applications EPE'97, Trondheim, Norway, 1997, vol. 3, pp. 532-536.

[119] Seki, K., Oka, K., Watada, M., Torii, S. and Ebihara, D., *Synchronization of Discontinuously Arranged Linear Synchronous Motor for Transportation System*, 2nd Int. Symp. on Linear Drives for Ind. Appl. LDIA '98, Tokyo, Japan, 1998, pp. 82-85.

[120] Seok-Myeong, J. and Sang-Sub, J., *Design and Analysis of the Linear Homopolar Synchronous Motor for Integrated Magnetic Propulsion and Suspension,* Int. Symp. on Linear Drives for Ind. Appl.LDlA'98, Tokyo, Japan, 1998, pp. 74-77.

[121] Setbacken, R., *Feedback Devices in Motion Control Systems*, RENCO Encoders, Fiftian Press, Santa Barbara, CA, U.S.A., 1997.

[122] Shiraki, M., Song, R., Itoh, A., Mizuno, T. and Yamada, H., *High Speed High Accuracy Positioning System for Industrial Printer by LDM,* 2nd Int. Symp. on Linear Drives for Ind. Appl. LDIA '98, Tokyo, Japan, 1998, pp. 98-101

[123] Skalski, C.A., *The Air-Core Linear Synchronous Motor: An Assessment of Current Development,* MITRE Technical Report, VA, U.S.A., 1975.

[124] Smith, A.C., *Magnetic Forces on a Misaligned Rotor of a PM Linear Actuator*, Int. Conf. on Electrical Machines ICEM'90, Boston, MA, U.S.A., 1990, pp. 1076-1081.

[125] Stec, T.F., *Amorphous Magnetic Materials Metglass 2605S-2 and 2605TCA in Application to Rotating Electrical Machines, NATO* ASI Modern Electrical Drives, Antalya, Turkey, 1994.

[126] Suwa, H., Turuga, H., Iida, T., Tujimoto, S., Kobayashi, Y. and Itabashi, Y. , *Features of Ground Coils for Yamanashi Maglev Test Line,* 15th Int. Conf. on Magnetically Levitated Systems and Linear Drives Maglev'98, Mt. Fuji, Yamanashi, Japan, 1998, pp. 292-296.

[127] Sykulski, J.K., *Computational Magnetics,* Chapman & Hall, London, 1995.

[128] Takahashi, Y., Yoshihiro, J., Hidenari, A., Motoaki, T. Motohiro, I. and Masatoshi, S., *Vibration Characteristics and Mechanical Heat Load of superconducting Magnets of Maglev Trains,* 15th Int. Conf. on Magnetically Levitated Systems and Linear Drives Maglev'98, Mt. Fuji, Yamanashi, Japan, 1998, pp. 244-249.

[129] Tergan, V., Andreev, I. and Liberman, B., *Fundamentals of Industrial Automation,* Mir Publishers, Moscow, 1986

[130] *The LIM Elevator Drive,* Elevator World, 1991, No 3, pp.34-41.

[131] *Transrapid Maglev System* edited by K. Heinrich and R. Kretzschmar, Hestra- Verlag, Darmstadt, Germany, 1989.

[132] *PM Linear Motors,* Trilogy Systems Corp., Webster, TX, U.S.A., 1999, www.trilogysystems.com

[133] Tsuchishima, H., Mizutani, T., Okai, T., Nakauchi, M., Terai, M., Inadama, S. and Asahara, T., *Characteristics of Superconducting Magnets and Cryogenic System on Yamanashi Test Line,* 15th Int. Conf. on Magnetically Levitated Systems and Linear Drives Maglev'98, Mt. Fuji, Yamanashi, Japan, 1998, pp. 237-243.

[134] Turowski, J., Turowski, M. and Kopec, M., *Method of Fast Analysis of 3D Leakage Fields in Large Three-Phase Transformers,* Compel, James & James Scie Publishers, Vol. 9, 1990, London, U.K., pp. 107-116.

[135] Turowski, J., *Technical Electrodynamics* (in Polish), WNT, Warsaw, 1993.

[136] Utsumi, T. and Yamaguchi, I., *Thrust Characteristics of a Rectangular Core LIM*, 2nd Int. Symp. on Linear Drives for Industry Applications LDIA'98, Tokyo, 1998, pp. 248-251.

[137] *The Contactless Power Supply System of the Future,* Wampfler AG, Weil am Rhein-Maerkt, Germany, 1998.

[138] Wang, R. and Gieras, J.F., *Performance Calculations for a PM Hybrid Linear Stepping Motor by the Finite Element and Reluctance Network Approach,* 2nd Int Symp. on Linear Drives for Industry Applications LDIA '98, Tokyo, 1998, pp. 400-403.

[139] Wang, R. and Gieras, J.F., *Analysis of Characteristics of a Permanent Magnet Hybrid Linear Stepping Motor,* Int. Conf. on Electr. Machines ICEm'98, Istanbul, Turkey, 1998, pp. 835-838.

[140] Wegerer, K., Ellman, S., Becker, P., and Hahn, W., *Requirements, Design and Characteristics of the Maglev Vehicle Transrapid 08,* 15th Int. Conf. on Magnetically Levitated Systems and Linear Drives Maglev'98, Mt. Fuji, Yamanashi, Japan, 1998, pp. 202-208.

[141] Weglinski, B., *Soft Magnetic Powder Composites – Dielectromagnetics and Magnetodielectrics,* Reviews on Powder Metallurgy and Physical Ceramics, vol. 4, 1990, No.2, pp. 79-153.

[142] Wiescholek, U., *High-Speed Magnetic Levitation System Transrapid,* 14th Int. Conf. on Magnetically Levitated Systems Maglev'95, Bremen, Germany, 1995, pp. 17-23.

[143] *Yamanashi Maglev Test Line - Guide of Electric Facilities,* Central Japan Railway Company, Tokyo, 1992.

[144] Yamada, H., *Handbook of Linear Motor Applications* (in Japanese), Kogyo Chosaki Publ. Co. Ltd, 1986.

[145] Yamazaki, M., Gotou, Y., Aoki, S., Hashimoto, S. and Sogabe, M., *Guideways and Structures on the Yamanashi Maglev Test Line and their Dynamic Response Characteristics,* 15th Int. Conf. on Magnetically Levitated Systems and Linear Drives Maglev'98, Mt. Fuji, Yamanashi, Japan, 1998, pp. 178-183.

[146] Yoshida, K., Takaki, T. and Muta, H., *System Dynamics Simulation of Controlled PM LSM Maglev Vehicles,* 10th Int. Conf. on Maglev and Linear Motors, MAGLEV'88, Hamburg, Germany, 198, pp. 269-278.

[147] Yoshida, K., Muta, H. and Teshima, N., *Underwater Linear Motor Car,* Int. Journal of Appl. Electromagnetics in Materials, vol. 2, Elsevier, 1991, pp. 275-280

[148] Yoshida, K., Liming, S., Takami. H. and Sonoda, A., *Repulsive Mode Levitation and Propulsion Experiments of an Underwater Travelling LSM Vehicle ME02,* 2nd Int. Symp. on Linear Drives for Industry Applications LDIA '98, Tokyo, 1998, pp. 347-349.

[149] Yoshida, K., Takami. H., Kong, X. and Sonoda, A., *Mass Reduction and Propulsion Control of PM LSM Test Vehicle for Container Transportation,* IEEE Int. Electr. Machines and Drives Conf. IEMDC'99, Seattle, WA, U.S.A., 1999, pp. 72-74

[150] Yoshioka, H., Suzuki, E., Seino, H., Azakami, M., Oshima, H. and Nakanishi, T., *Results of Running Tests and Characteristics of the Dynamics of the MLX0l Yamanashi Maglev Test Line Vehicles,* 15th Int. Conf. on Magnetically Levitated Systems and Linear Drives Maglev'98, Mt. Fuji, Yamanashi, Japan, 1998, pp. 225-230.

[151] Zolghadri, M.R., Diello, D. and Roye, D., *Direct Torque Control System for Synchronous Motor,* 7th European Conf. on Power Electronics and Applications EPE'97, Trondheim, Norway, 1997, vol. 3, pp. 694-699.